2014

Transient and steady-state Mobile Air Conditioning operation with the Inclusion of and Internal Heat Exchanger

Stephen Gemin
University of Windsor

Transient and Steady-state Mobile Air Conditioning Operation with the Inclusion of an Internal Heat Exchanger

By

Stephen Gemin

A Thesis
Submitted to the Faculty of Graduate Studies
through the Department of Mechanical, Automotive, and Materials Engineering
in Partial Fulfillment of the Requirements for
the Degree of Master of Applied Science
at the University of Windsor

Windsor, Ontario, Canada

2014

Transient and Steady-state Mobile Air Conditioning Operation with the Inclusion of an Internal Heat Exchanger

by

Stephen Gemin

APPROVED BY:

_____

Dr. X. Xu
Civil and Environmental Engineering

_____

Dr. G. Reader
Mechanical, Automotive and Materials Engineering

_____

Dr. M. Zheng
Mechanical, Automotive and Materials Engineering

21 May 2014

AUTHOR'S DECLARATION OF ORIGINALITY

I hereby certify that I am the sole author of this thesis and that no part of this thesis has been published or submitted for publication.

I certify that, to the best of my knowledge, my thesis does not infringe upon anyone's copyright nor violate any proprietary rights and that any ideas, techniques, quotations, or any other material from the work of other people included in my thesis, published or otherwise, are fully acknowledged in accordance with the standard referencing practices. Furthermore, to the extent that I have included copyrighted material that surpasses the bounds of fair dealing within the meaning of the Canada Copyright Act, I certify that I have obtained a written permission from the copyright owner(s) to include such material(s) in my thesis and have included copies of such copyright clearances to my appendix.

I declare that this is a true copy of my thesis, including any final revisions, as approved by my thesis committee and the Graduate Studies office, and that this thesis has not been submitted for a higher degree to any other University or Institution.

ABSTRACT

This thesis investigates the change in power consumption for a mobile air conditioning (MAC) system from the introduction of an internal heat exchanger (IHX). The internal heat exchanger is so named since it is a simple heat exchanger that is placed internally into the AC system. It serves to transfer heat from the high to low pressure refrigerant to maximize the system cooling capacity. The work investigates how other performance parameters such as the pressure drops, IHX capacity, evaporator capacity, coefficient of performance and the absolute efficiency ratio change from the introduction of the IHX. The steady-state simulation results are compared to data available in the literature and transient experimental tests including the cabin cool-down, and the simulation results from the New European Driving Cycle.

The results from the simulations show a reduction in power consumption of up to 2% in high ambient temperatures but an increase in power consumption of up to 1.5% for low ambient temperatures. The power consumed by the MAC system is largely by the compressor. Placing the thermal sensing bulb (TSB) of the thermal expansion valve downstream of the internal heat exchanger yielded higher MAC coefficient of performance, lower suction line pressure drops and compressor power consumption compared to placing the TSB upstream of the internal heat exchanger.

Dedication

To my family,

thank you so very much for providing your unconditional love and support throughout my whole life and especially during my post graduate studies.

To Dr. Peter Frise and Jeannette Stewart,

I would not be where I am today if it were not for your support and guidance, thank you very much.

Acknowledgements

This two year Double Degree Master program represents the organization and collaboration efforts of two universities, University of Windsor and Politecnico di Torino and two automotive companies, Chrysler LLC and Fiat Group Automobile.

I would like to express my innermost appreciation to the persons who were responsible for creating and coordinating this two year Double Degree Master program, Dr. Peter Frise, Prof. Giovanni Belingardi, Edoardo Rabino and Mohammed Malik.

I offer my sincere gratitude to my academic advisors Dr. Ming Zheng and Prof. Marco Masoero who have supervised my activities and supported me throughout my time in this program. A special thanks to Marco Jeftic and Kelvin Xie for the time, dedication and guidance which they have shown me.

I also offer my sincere gratitude to my technical advisors, both at Chrysler and Fiat. So I am grateful to Sadek Rahman, Carloandrea Malvicino and Matteo Rostagno for their patience and assistance throughout this project.

These people were not my direct advisors but were very influential in helping me in my daily activities and Chrysler and Fiat and their kindness and experience have allowed me to develop as an engineer and a person, Shankar Natarajan, Ling Xiao, Antonio Mancina, Andrea Perosino, Federica Bettoja, Fausto Di Sciulo, Fabrizio Mattiello, Riccardo Seccardini, Walter Ferraris and especially Francesco Lovuolo.

A special thanks goes to Mike Houston, Jeannette Stewart for the tremendous help that they have provided during my time in Windsor and to Raffaella Fiora for her tremendous help during my time in Torino.

I would like to thank my committee members, Dr. Graham Reader and Dr. Xiaohong Xu whose work have helped me to greatly improve the quality of my work.

I am extremely thankful to my family, who have been an anchor for me, both morally and economically throughout my life. Without their love and dedication as parents, I would not be where I am today.

TABLE OF CONTENTS

LIST OF FIGURES

LIST OF TABLES

LIST OF ABBREVIATIONS

- AC—air conditioning
- AER—absolute efficiency ratio
- ah—absolute humidity
- ASCII—American Standard Code for Information Interchange
- BLW—blower activation level
- COP—coefficient of performance
- GHG—green house gas
- HEAT—Heat Exchangers Assembly Tool
- HP—high-pressure
- IHX—internal heat exchanger
- IHXa—AC system configuration where the IHX suction line is **downstream** of the TXV temperature sensing bulb.
- IHXb—AC system configuration where the IHX suction line is **upstream** of the TXV temperature sensing bulb.
- LL—liquid line
- LP—low-pressure
- MAC—mobile air conditioning
- NTU—Number of transfer units
- RH—Relative humidity
- Rpm—revolutions per minute
- SAE—Society of Automotive Engineers
- SL—suction line
- TSB—thermal sensing bulb
- TXV—thermal expansion valve

LIST OF NOMENCLATURE

Upper and Lower Case

A	Area [m^2]
a	Nusselt number constant
B	Nusselt number constant
C	Nusselt Number Constant; Natural Nusselt constant
c_p	Constant pressure specific heat [kJ/kg·K]
D	Diameter [m]
f	Darcy-Weisbach friction factor
h	Hours
k	Thermal conductivity [W/m·K]
L	Length [m]
P	Pressure [kPa]
h	Specific enthalpy [kJ/kg]
ħ	Convection coefficient [$W/m^2 \cdot K$]
Q	Heat transfer [kJ]
q	Heat transfer per unit mass [kJ/kg]
T	Torque [N-m]
T	Temperature [^oC]
t	Thickness [m]
g	Gravitational acceleration [m/s^2]
m	Mass [kg]
$\dot{m}$	Mass flow rate [kg/s]
U	Overall heat transfer coefficient
V	Velocity [m/s]
W	Work [kJ]
w	Work per unit mass [kJ/kg]
x	Refrigerant quality [%]

Greek

α	Thermal diffusivity [m^2/s]
β	coefficient of volume expansion, 1/K (Beta= 1/T for ideal gases)

δ	user-specified temperature constant
Δ	Finite change in quantity
ε	Error
η	Efficiency
μ	Dynamic viscosity [kg/m·s]
ν	Kinematic viscosity [m^2/s]
ρ	Density [kg/m^3]

Subscrips

amb	Ambient parameter
c	Characteristic length
dis	Discharge side of compressor
eq, setpt	Equilibrium set point temperature for the NEDC blower control system
Evap	Evaporator
ext	External property
IHX	Internal heat exchanger
int	Internal property
L	indication of a surface length
l	Liquid
m	Mechanical
s	Isentropic
suc	Suction side of compressor
Suction	Suction line of air conditioning system
TPF	Two-phase flow
v	Vapour
vol	Volumetric parameter

Superscripts

′ (prime)	System with an IHX

CHAPTER 1
INTRODUCTION

For the near future, the world focuses on the need to address global climate change, greenhouse gas emissions and fuel consumption. Enacted in 1975 by the U.S. Congress as a result of the Organization of Petroleum Exporting Countries (OPEC) Oil Embargo, the Corporate Average Fuel Economy (CAFE) standard was established to legislate fuel economy standards for automobiles and light trucks [1]. On May 19, 2009 President Barack Obama proposed a program to increase vehicle fuel economy and reduce greenhouse gas emissions [2]. The May 2010 CAFE standards apply to passenger cars, light-duty trucks and medium-duty passenger vehicles and covers the model years 2012 through 2016 [3]. Further increases to the CAFE standard are presently under negotiations for the 2015-2016 period [3].

Air conditioning (AC) is a parasitic load on the transmission system and increases vehicle fuel consumption [4-7]. When the industry made the change from R12 to the R134a refrigerant, several other changes were made to the mobile air conditioning (MAC) system. To use the same compressor design, higher capacity condensers were introduced to maintain the same operating pressures, thermal expansion valve (TXV) settings were adjusted to maintain evaporator capacities and synthetic lubricants replaced the mineral lubricants used in the R12 systems [8]. To measure the contribution of air conditioning system operation to overall vehicle fuel consumption, the supplemental Federal Test Procedure, known as SC03, has been added as a requirement for the label fuel economy in North America [3].

Over the past two decades, numerous researchers have investigated the concept of introducing an internal heat exchanger (IHX) into a MAC system [9-17]. Theoretically, the IHX increases evaporator capacity, allowing for more heat extraction from the air that will be entering the cabin [9-17]. Thus, at equivalent capacities, the introduction of an IHX should also decrease the power input to the compressor due to the load reduction on the AC system.

An IHX transfers heat from the sub-cooled liquid refrigerant exiting the condenser to the superheated refrigerant vapour entering the compressor. The reduced evaporator inlet enthalpy increases the specific cooling capacity. This concept is explained in further detail in Chapter 2. Therefore, the warmer suction gas has a lower density, resulting in a lower mass flow rate and a higher specific compressor work [9].

Research has shown for the refrigerant R134a that implementing an IHX increases system coefficient of performance (COP) at an equivalent evaporator capacity [9-17]. A well designed IHX will maximize heat transfer between the liquid and suction line and minimize suction side pressure drop in the refrigerant flow [11]. The increased temperature of the suction side refrigerant assists to eliminate the possibility of "wet" compression and minimizes the effect of flash gas as the refrigerant passes through the TXV on the liquid side. In this thesis, the terms suction side and low-pressure side are used interchangeably, as are the terms liquid line and high-pressure line.

Automotive manufacturers have become especially interested in the IHX due to the switch from the refrigerant R134a to HFO-1234yf or R1234yf [18]. Studies for the new refrigerant have shown that by implementing an IHX, the AC system will have a cooling capacity similar to R134a [12]. Implementation of an IHX in a MAC automatically earns the manufacturer air conditioning related credits of 1.1 g/mi (0.7 g/km) of CO_2 toward the Light-Duty Vehicle Greenhouse Gas Emission Standards and CAFE standards [3].

Due to the potential benefits of including an IHX in an MAC system, and the air conditioning credits offered to automotive manufacturers that include this technology, it is important to quantify the expected benefits. One must determine if the benefits of the IHX introduction outweigh the increased costs to implement this system. It is also important to understand how an MAC system will react under steady-state and transient scenarios. This information will help automotive manufacturers meet the strict demands of future vehicle fuel economy and legislation of emissions.

1.1 The Vapour-Compression Cycle

The vapour-compression cycle is a more practical solution to the idealized Carnot cycle [19]. The popularity of this method arises from the practical considerations as opposed to its performance and thermal efficiency. It is a modified version of the classical reversed Carnot cycle, which is an idealized model for the most efficient refrigeration cycle [19]. The reversed Carnot cycle, shown in Figure 1-1, consists of four processes, which are:

1-2 Isothermal addition of heat

2-3 Isentropic compression

3-4 Isothermal rejection of heat

4-1 Isentropic expansion

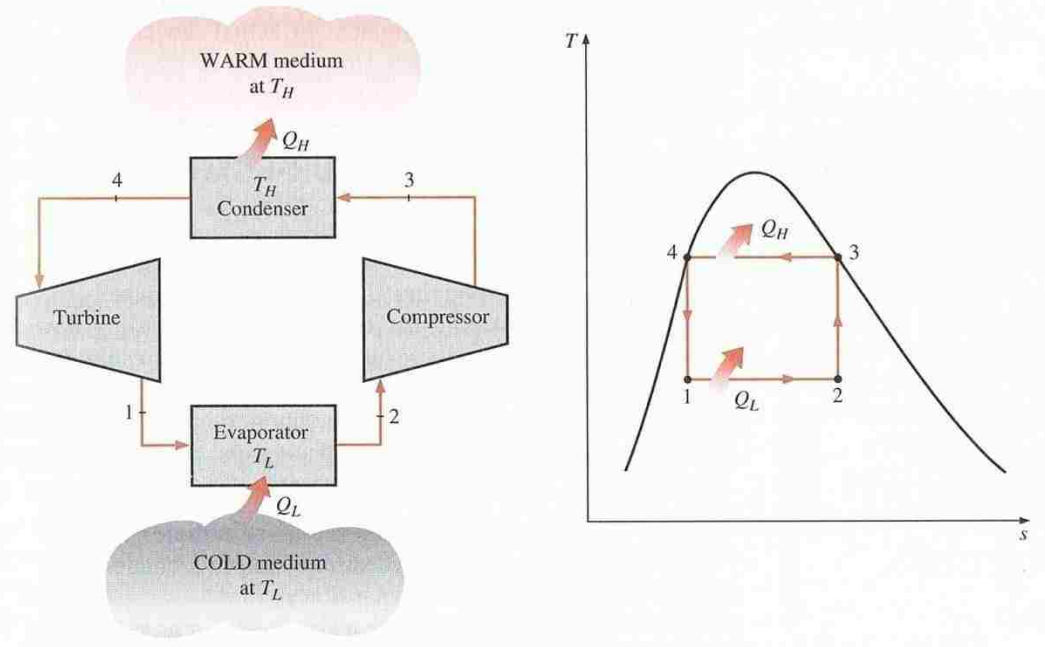

Figure 1-1: Schematic of a Carnot refrigerator and the corresponding T-s diagram of the reversed Carnot cycle. The four processes listed above correspond to the numbered states in this figure. The enclosed area on the T-s diagram represents the net work of the refrigeration process and the box enclosed by vertical lines from points 1 and 2 extending to the abscissa axis represents the useful refrigeration. Copied from Cengel, [19].

However, there are practical restrictions associated with the Carnot cycle. The first obstacle is the adiabatic compression process, 2-3, which involves a two-phase liquid-vapour mixture. During wet compression, the liquid droplets may wash away the compressor lubricating oil, accelerating mechanical wear [20]. Also, compressed liquid droplets are vaporized by an internal heat-transfer process occurring during a finite time interval [20]. With a compressor speed of 1000RPM, one single compression process is 0.06 seconds, which is too short for liquid vaporization to occur [20]. The liquid droplets may increase erosion, again accelerating wear [21]. Therefore dry compression, using only superheated refrigerant fluid is preferable to wet compression.

The second obstacle is the adiabatic expansion, which involves a turbine recovering work from a low-quality two-phase refrigerant. A low-quality refrigerant has a high moisture content. The liquid droplets impinging on the turbine blades cause erosion, accelerating wear. The cost to power recover ratio of implementing a turbine is high, so currently it is not a cost-effective solution [19].

The impracticalities of the reversed Carnot cycle are eliminated by dry compression and using a throttling device rather than a turbine. This resulting process is the ideal vapour-compression refrigeration cycle. The vapour-compression refrigeration cycle, shown in Figure 1-2, consists of four processes:

1-2 Isentropic compression in a compressor

2-3 Constant-pressure heat rejection in a condenser

3-4 Throttling in an expansion device

4-1 Constant-pressure heat absorption in an evaporator

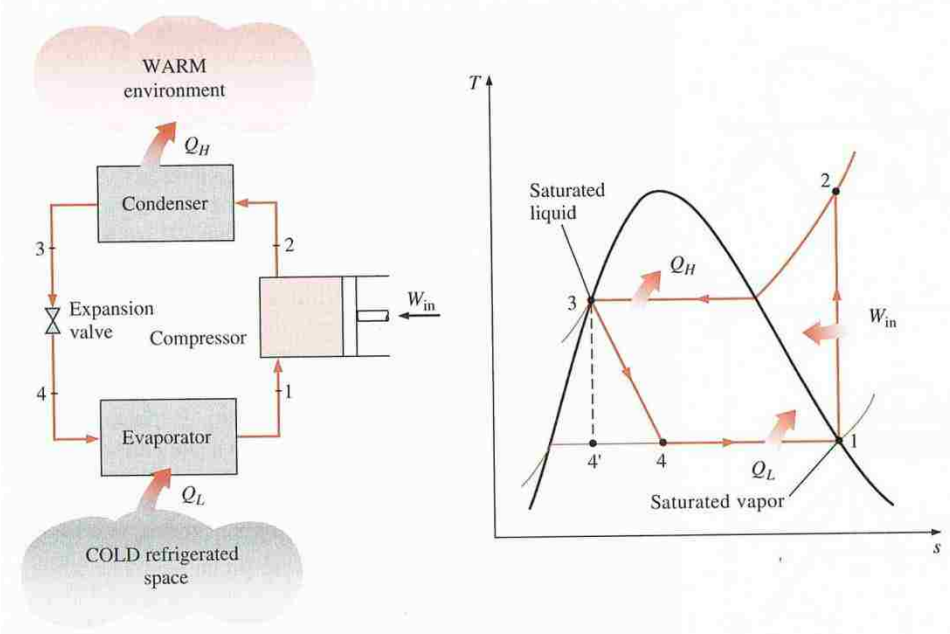

Figure 1-2: Schematic of an ideal vapour-compression refrigeration cycle and corresponding T-s diagram. The variables T and s represent the temperature and entropy values. The four processes listed above correspond to the numbered states in this figure. The enclosed area on the T-s diagram represents the net work of the refrigeration process. Copied from Cengel, [19].

The components that make up a vapour-compression system in the present thesis, which will be referred to as an AC system, are as follows:

- compressor;
- condenser with integrated receiver/dryer;
- thermostatic expansion valve (TXV);
- evaporator;
- internal heat exchanger (IHX), not shown and may or may not be a part of the AC system.

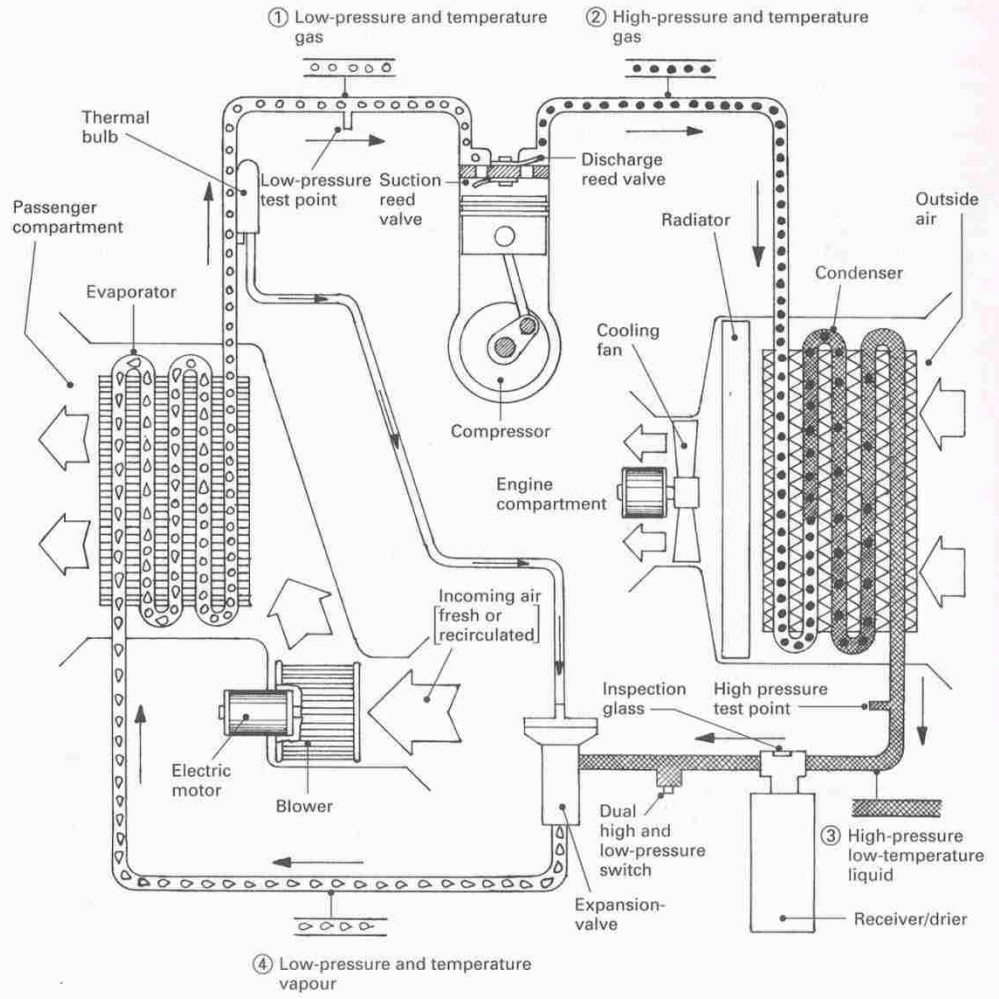

Figure 1-3: Air conditioning (AC) system displaying the essential components. . Note that the internal heat exchanger is not included in this in this AC system. The numbered refrigerant states also do not correspond to the numbered states shown in the previous figures of the different heating and cooling cycles. Copied from Heisler, [22].

Figure 1-3 displays an example of the AC system studied in the present thesis. In this figure, the receiver/dryer is a separate component rather than integrated with the condenser. The engine-driven compressor takes the low-pressure and temperature refrigerant and compresses it, increasing both the temperature and pressure. Recall that the refrigerant is in a superheated vapour state as it passes through the compressor. Ideally, the compression process is isentropic, however due to irreversibilities such as heat transfer with the surroundings this is not always the case. The compressor type for the AC system of the present thesis is a swash-plate compressor, which is discussed in Appendix G. The suction and discharge pressures of a compressor are very important as they control the refrigeration capacity and power requirement of a compressor operating

at constant speed [21]. Changing the suction and discharge pressures changes the refrigerant state and consequently the enthalpy of the refrigerant.

The condenser and evaporator are both heat exchangers and serve a common purpose within the AC system. The condenser rejects heat from the high pressure and high temperature refrigerant to the ambient surroundings, changing from superheated vapour to subcooled liquid as the refrigerant passes through the condenser. Within the evaporator, the low pressure and low temperature refrigerant absorbs heat from the air that will be entering the refrigerated space. As the refrigerant passes through the evaporator, it changes from a sub-cooled liquid to a superheated vapour. If there is any flash gas as the refrigerant passes through the thermal expansion valve (TXV) it decreases the range where the refrigerant heat is transferred to the refrigerant while it is changing state. The AC model in the present thesis uses a parallel flow, horizontal, tube and fin condenser and a parallel flow, vertical , tube and fin evaporator. The refrigerant flows through the tubes and air through the fins. The laws governing the flow of the liquid through the tubes and fins are the same for the evaporator and condenser, however the heat exchange mechanisms of refrigerant condensation are very different from those of refrigerant boiling.

The air-side heat transfer limits the performance of the condenser and evaporator due to the properties of air. Equation (2.13) in Section 2.2, which represent Newton's law of cooling, display the rate of heat transfer by convection from the air and refrigerant, respectively. The convection heat transfer coefficient, ħ, is of particular importance since it is an experimentally determined parameter based on the fluid properties, velocity, motion and surface geometry. Typical values of ħ, in W/m^2-K are in the range of 2-25 for the free convection of gases, 50-1,000 for the free convection of liquids, 25-250 for the forced convection of gases, 50-20,000 for the forced convection of liquids, and 2,500-100,000 for the convection in boiling and condensation processes [10]. The amount of heat exchanged during a phase change process is much greater compared to free or forced convection. The convection coefficient is explained in more detail in Section 2.1.

The AC model in the present thesis uses a superheated-controlled thermal expansion valve (TXV). The TXV serves two purposes: it reduces the pressure of the liquid

refrigerant, bridging the gap between the high and low pressure sides of the AC system and it regulates the flow of the refrigerant to the evaporator. The TXV control is actuated by the magnitude of the superheated refrigerant leaving the evaporator [21]. For further information, please see Section 3.2.6.

The receiver/dryer separates water moisture and filters any debris from the refrigerant with a filter screen and drier desiccant crystals. Filtering water that leaks into the pipes of the AC system prevents partial freezing in the expansion valve during engine start-up. The receiver-dryer also stores refrigerant, which compensates for any leakage that occurs during the lifespan of the AC system. There is a fusible safety plug at the top of the receiver-dryer that melts when the refrigerant reaches a critical temperature. Melting of the fusible safety plug allows for some of the refrigerant to discharge to the atmosphere. Figure 1-4 displays a schematic of the receiver-dryer.

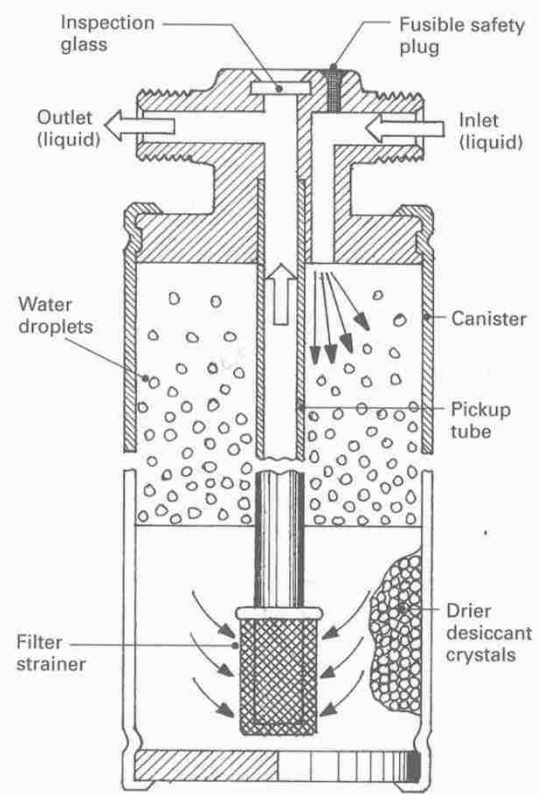

Figure 1-4: Schematic of the receiver-dryer. Copied from Heisler [22].

The reversed Carnot and vapour-compression refrigeration cycles shown in Figure 1-1 and Figure 1-2 represent idealized processes. An actual AC system performance differs from these idealized processes due to irreversibilities. Common sources of irreversibilities are pressure drops caused by fluid friction and heat transfer to or from the surroundings [10]. The T-s diagram for an actual vapour compression refrigeration cycle is shown in Figure 1-5. Note the difference in the T-s diagrams from the inclusion of the irreversibilities between Figure 1-2 and Figure 1-5.

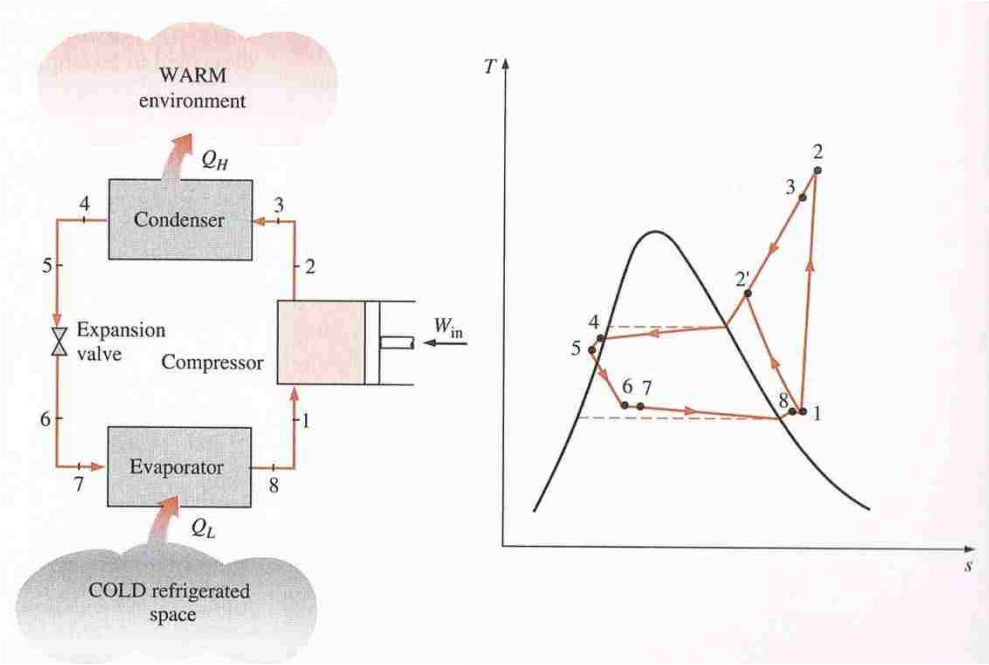

Figure 1-5: Schematic and T-s diagram for the actual vapour-compression refrigeration cycle. The variables T and s represent the temperature and entropy values. The four processes listed above correspond to the numbered states in this figure. The enclosed area on the T-s diagram represents the net work of the refrigeration process. Copied from Cengel, [19].

1.2 Project Overview

The MAC model used in the present thesis was originally developed and calibrated by Fiat. The original model includes the AC system without an IHX and the cabin model. The word calibration represents the process of minimizing the error between specific experimental measurements and their corresponding values from the simulation model.

This process involves tuning specific model parameters in order to minimize the error between the simulation and experimental values. Figure 1-2: below shows the project layout of the full Heating, Ventilation and Air Conditioning (HVAC) simulation model. This includes any previous work as well as the studies investigated by this thesis.

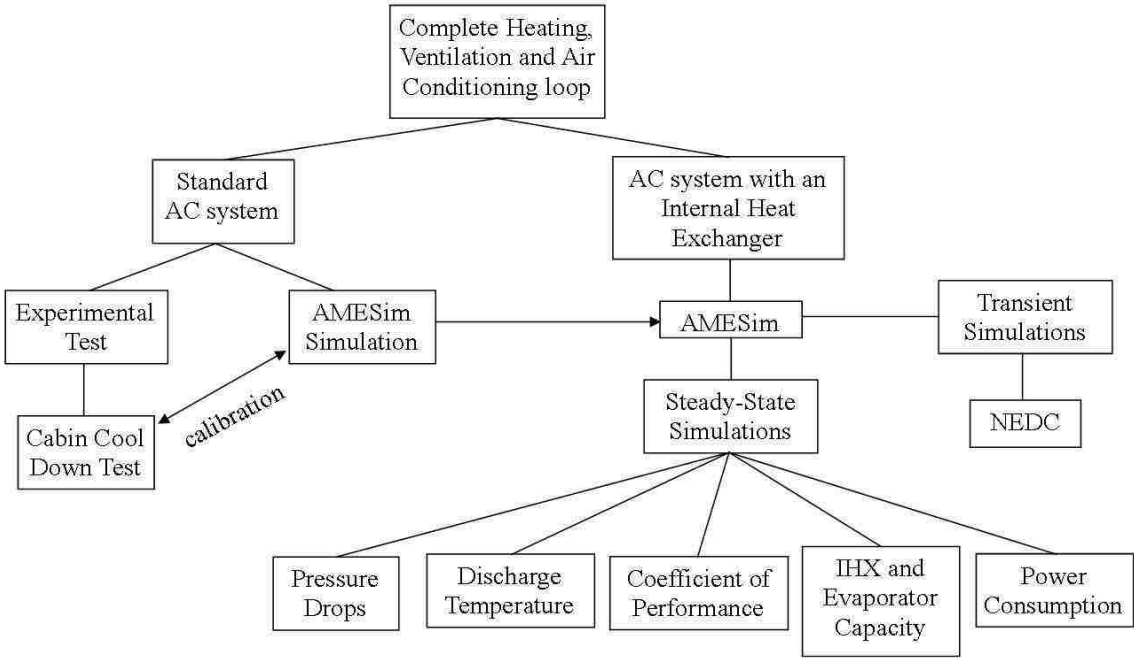

Figure 1-6: Overall project layout for the work presented in this thesis.

The simulation model was calibrated by Fiat using the cabin cool down (CCD) test. The literature also refers to the CCD test as a pulldown test [14]. The data from the experiment is for a Fiat Grande Punto, shown in Figure 1-7, a third generation design of the Fiat Punto. It is based on a vehicle platform developed from a collaboration between General Motors (GM) and Fiat. The vehicle uses a 1.2L Fully Integrated Robotized Engine (FIRE) inline-four cylinder Otto cycle engine. It is a B-segment vehicle with the following dimensions:

- Wheelbase 2510mm (98.8in)
- Length 4030mm (158.7in)

- Width 1687mm (66.4in)
- Height 1490mm (58.7in)
- Weight 1015-1040kg (2240-2300lb)

Figure 1-7: Photo of the Fiat Grande Punto. This photo is included to provide a visual reference for the reader [23].

The vehicle used R134a refrigerant for the experiment. From the experimental data the AMESim model was calibrated by Fiat. AMESim is a commercial simulation software used to conduct one dimensional (1D) analyses for the AC system in the present thesis. As such, this thesis offers a simulation-based approach to study the effect of an IHX on AC system performance.

The IHX model developed and calibrated by the author is included in the HVAC model originally developed and calibrated by Fiat. Steady state and transient simulations are conducted to determine how the IHX influences specific AC performance parameters.

1.2 Focus of Research Work

The work completed in the present thesis focuses on two specific points of interest, listed below, regarding the inclusion of a co-axial smooth double pipe IHX in the MAC model initially created by Fiat.

The first point includes the introduction of an IHX as a "drop-in" component into a single evaporator MAC system and conduct simulations for steady-state AC operating conditions. The steady-state simulations will serve as a baseline for determining the best suction line plumbing configuration and the corresponding change in AC performance. The two plumbing configurations consider the placement of the IHX before (also named IHXb) and after (also named IHXa) the inlet to the thermal sensing bulb of the thermal expansion valve (TXV). For further explanation regarding the two different configurations please see Section 3.6.3. There are component and system level performance comparisons of interest which include:

1. Suction and liquid line pressure drops in the IHX and the AC system
2. IHX capacity
3. The compressor power consumption
4. Evaporator capacity
5. Coefficient of performance (COP)
6. Absolute efficiency ratio
7. Compressor discharge temperature.

The second point investigates two transient driving cycles, the CCD test and New European Driving Cycle (NEDC). The analysis for the transient driving cycles includes the effect of suction line plumbing configurations and IHX length on system performance and power usage. The results assume a direct relationship between the AC power and vehicle fuel consumption. Increased power consumption increases the parasitic load on the engine, thus increasing the fuel consumption to provide the additional power for this ancillary load. The power required to run the compressor is directly taken from the engine since it is mechanically connected to the engine.

1.3 Major Assumptions

The key assumptions for the modelling of the AC system in the present thesis are included in the bullet points listed below.

- The packaging requirements of the IHX in the vehicle are not considered. Findings in the literature suggested that the pipe length and bending angle should be taken into consideration when designing the IHX [10]. There are no studies conducted in this thesis to quantify how much this assumption affects the accuracy of the presented results.
- When solving the energy equation, the effects of potential and kinetic energy are ignored because their influence is small compared to the change in enthalpy [24].
- Internal interference that may occur due to vehicle vibration is neglected. It was found that to ensure that no internal interference occurs at vehicle vibration up to 500Hz, the length of any straight portion should be less than 340mm [10].
- IHX is assumed to be straight in all of the simulations. Therefore, the IHX will transfer much more heat energy and will have a lower pressure drop than an IHX in a production vehicle.

CHAPTER 2
THEORY AND LITERATURE REVIEW

Initial studies by Preissner et al., 2001, for an automotive IHX in an mobile air conditioning (MAC) system with a TXV reported a performance improvement of 8-10% for the evaporator capacity and 5-7% for the coefficient of performance (COP) [9]. Friction within the pipes leads to irreversible pressure drops. The experimental results from this paper also found that the pressure drop on the high-pressure side had almost no effect on the system performance whereas the low side pressure drop significantly affected the system performance [9] [11].

The equation for the pressure drop along a pipe is given in Equation (2.1), expressed in a manner to represent all types of fully developed internal flows: laminar or turbulent flows, circular or noncircular pipes, smooth or rough surfaces, horizontal or inclined pipes [20].

$$\Delta P_{loss} = f \frac{L}{D} \frac{\rho V^2}{2} \qquad \textbf{(2.1)}$$

In the equation above, *f* represents the Darcy-Weisbach friction factor and $\frac{\rho V^2}{2}$ is the dynamic pressure. The value of *f* depends on many different factors and is the variable that can significantly influence the pressure drop, next to the fluid velocity influence. The variables L, D and V correspond to the characteristic length, hydraulic diameter and fluid velocity, respectively. Determining the friction factor is critical to calculating the correct pressure loss. The calculation of the friction factor depends on the state of the refrigerant, that is, one phase or two phases.

Only one study, performed by Zhang et al, 2002, could be found where the TXV was placed downstream of the IHX. Hereafter, this configuration will be referred to as IHXb. For further clarification of this AC configuration please see Section 3.5. In this experiment the IHX as a “drop-in” component, was evaluated with the TXV controlling the refrigerant superheat at the compressor suction port. Environmental chamber testing yielded improved capacity and increased COP by 15%. Achieving the same evaporator

cooling capacity required 20% less refrigerant [14]. The results of the study showed the following benefits [14]:

1. Equal or higher cooling capacity with higher COP
2. Equal or better AC system performance with less charge
3. Lower compressor discharge pressure
4. Better compressor protection from cavitation from any liquid state refrigerant present on the suction side upstream of the compressor.
5. "Flooded" evaporator in a TXV system

The term "flooded" signifies that the refrigerant leaves the evaporator in a non-superheated state. In this condition, the refrigerant flowing through the evaporator absorbs a majority of the heat from the passing air while it is in two-phase form. This maximizes the evaporator capacity and the COP of the AC system. Once the refrigerant is in a superheated state, its heat transfer ability is greatly diminished.

Kurata, Suzuke and Ogura, 2007, from the Denso Corporation studied the effect of a double-pipe IHX in a mid-size car during idling. With a length of 400mm the results yielded an increase in cooling performance by 5-12% at equivalent power consumption levels and an increase in COP by 10-15% at equivalent cooling performance [10] [14]. A method for tuning the TXV is explained in this paper to further improve AC system performance that includes an IHX.

Initial studies of AC systems with an IHX did not always yield results of increased capacity, COP and decreased compressor power consumption. Determining whether the IHX has a positive or negative influence on the system performance requires a comparison of the COP values. Based on Figure 2-1 and Figure 2-2, the equations for the COP with and without an IHX are shown in Equation (2.2) and Equation (2.3). In these equations q_{evap} and w_{in} correspond to the specific capacity of the evaporator and specific work input to the compressor, respectively. The variable *h* corresponds to the specific enthalpy of the refrigerant at its numbered state corresponding to Figure 2-1 and Figure 2-2, respectively. The prime symbol, ′, in Equation (2.3) signifies an AC system with an IHX.

If the ratio, COP′/COP is greater than one, the use of an IHX improves system performance. A study by Mastrullo et al, 2007, devised a method to predict the post IHX installation behaviour of the system based on the operating conditions and type of refrigerant [15]. In this study, the refrigerant evaporating temperature was varied for different condensation temperature values. The study found that use of an IHX with refrigerant R-134a was always advantageous since the ratio of COP′/COP was always greater than unity.

Both figures represent idealized AC systems, and pressure losses in the pipes are neglected. Inclusion of pipe pressure losses requires the refrigerant state at the inlet and outlet of every AC component. In Figure 2-1 and Figure 2-2, the refrigerant state is only specified at the outlet of every AC component.

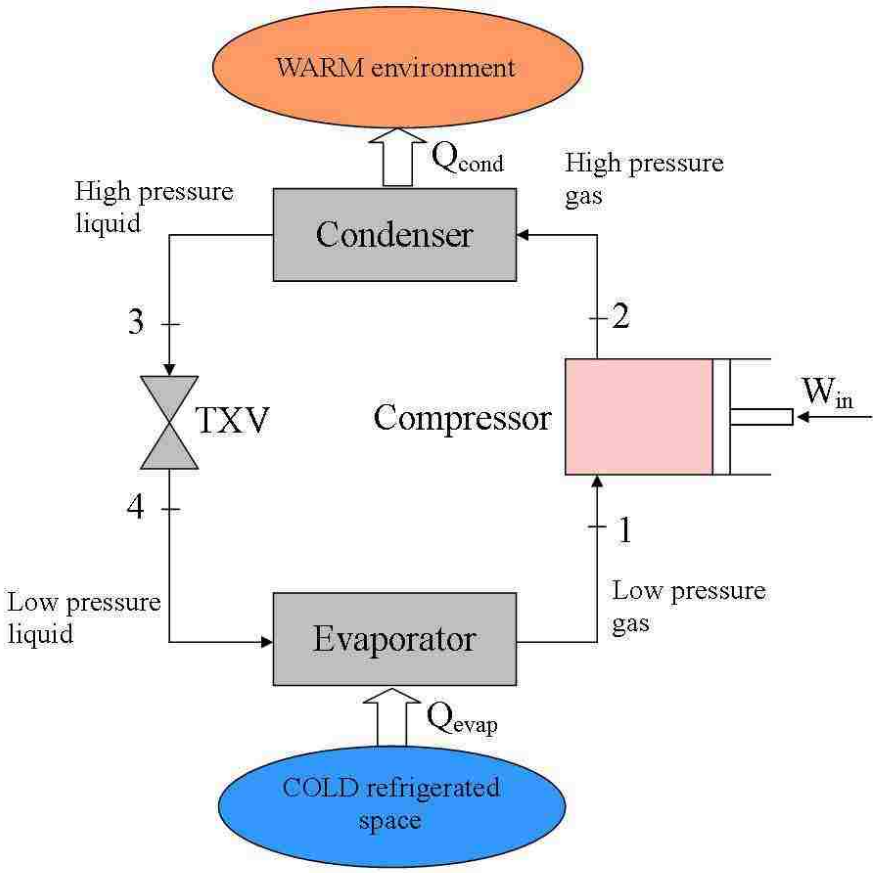

Figure 2-1: Ideal air conditioning (AC) system. The parameter Q_{evap} represents the system capacity. W_{in} represents the work input to the compressor. The system efficiency is measured using the coefficient of performance, which is the ratio of Q_{evap} to W_{in}.

$$COP = \frac{Q_{evap}}{W_{in}} = \frac{h_1 - h_4}{h_2 - h_1} \quad (2.2)$$

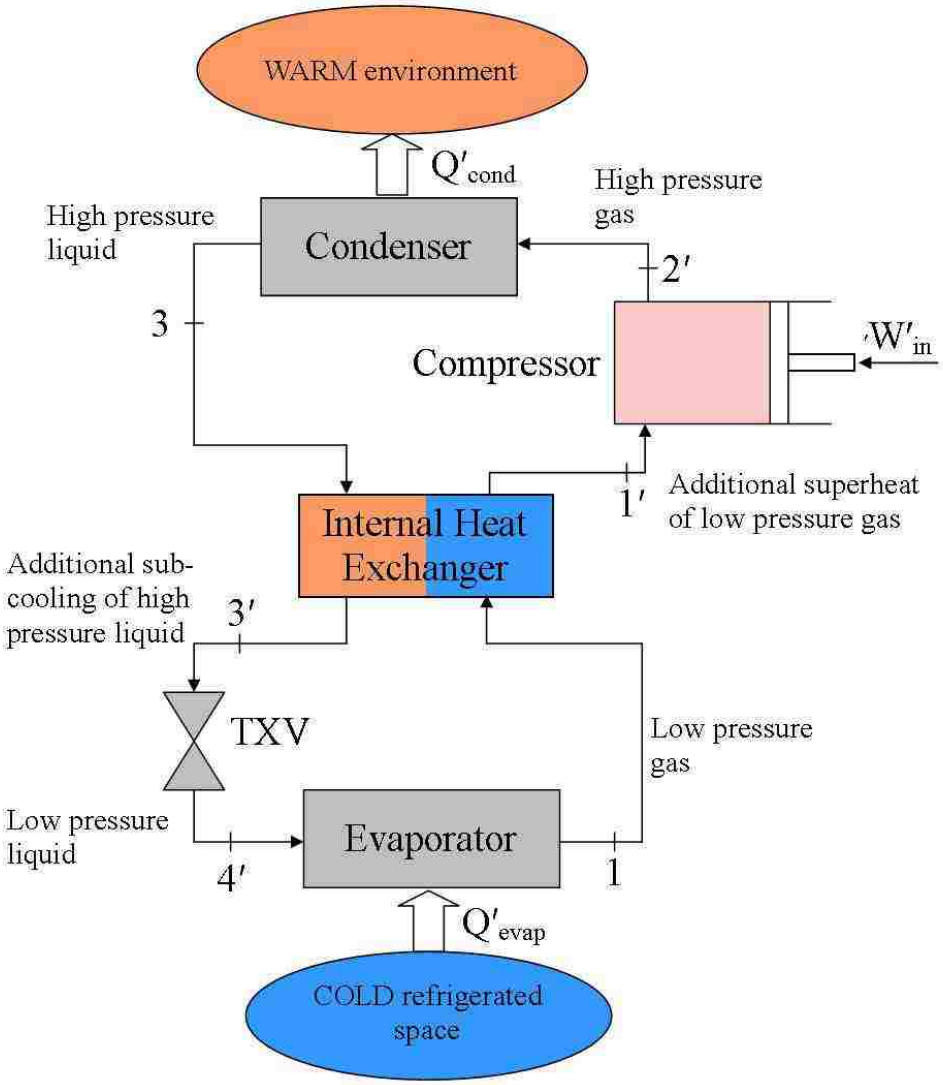

Figure 2-2: Ideal air conditioning system with the inclusion of an internal heat exchanger.

$$COP = \frac{Q'_{evap}}{W'_{in}} = \frac{h_1 - h_{4'}}{h_{2'} - h_{1'}} \quad (2.3)$$

As compressor superheat increases, the density of the refrigerant entering the compressor decreases The density decrease of the refrigerant means that the compressor volumetric efficiency decreases as well. This represents a drawback to including an IHX in an AC system as this will increase power consumption and reduce the benefits obtained from an IHX [15].

An ideal IHX has the highest possible effectiveness and zero suction side pressure drop. Since an ideal IHX is only theoretically possible, a real IHX design must include high heat transfer, minimized suction pressure drop, and limited liquid pressure drop, although this effect is not as significant as the suction pressure drop.

Factors to consider when studying the design and performance criteria of an IHX include pressure drop, heat transfer, length, internal surface area, the effect of oil circulation and how these factors impact the effectiveness of the heat exchanger [11]. In this study, by Seybold et al, 2010, all of the measurements are made for the IHX at a component level, rather than at a system level.

As previously described, the suction pressure drop significantly affected the system COP and it did increase exponentially with increased refrigerant mass flow rate according to Equation (2.1). The authors (Seybold et al) of this study also introduced a method to make a fair evaluation of the positive and negative effects of an IHX on a component level, called the absolute IHX efficiency ratio, shown in Equation (2.4) [11]. The variables Q_{IHX} and Δp_{lp} represent the average heat exchange rate of the IHX and suction side pressure drop, respectively. Only the pressure drop of the refrigerant as it passes through the IHX is considered for this equation.

$$\text{Absolute efficiency ratio} = \frac{\dot{Q}_{IHX}}{\sqrt{\Delta p_{lp}}} \qquad \textbf{(2.4)}$$

Seybold et al., 2011, suggests that to make a comparison of different IHX types at the component level and to predict the effect of an IHX on a MAC system level requires the definition of another efficiency ratio, which is shown by Equation (2.5) [12]. Contrary to the pressure drop in Equation (2.4), the pressure drop of the entire suction line is considered for this equation. Both Equation (2.4) and Equation (2.5) are used in Chapter 4 of this document.

$$\text{System Absolute Efficiency Ratio} = \frac{\dot{Q}_{IHX}{}^{2}}{\sqrt{\Delta p_{suction}}} \qquad \textbf{(2.5)}$$

The effect of increased oil concentration within the refrigerant improved heat transfer in the IHX up to a saturated value of 2-3% oil concentration. However, the efficiency ratio of the IHX decreased with increasing oil concentration due to a higher suction pressure drop [11]. By increasing the length of an IHX there is a trade off between increased heat transfer and increased suction line pressure drop. Increasing the length of an IHX past 600mm led to reduced IHX efficiency due to increased suction line pressure drop [11]. Of all the different type of IHXs available on the market today, the smooth tube double pipe IHX has the lowest effectiveness [16].

An IHX may reduce the refrigerant mass flow rate due to the increased heat transfer and pressure drop on the suction side. The purpose of the compressor displaces a finite volume for every revolution. The heating of the suction side refrigerant results in a decrease of the specific density. Therefore, for the refrigerant mass flow rate through the compressor to remain unchanged, the volumetric displacement must increase. This increases the specific work of the compressor since it must work harder to maintain an equivalent mass flow rate. The increased superheat of the suction gas also increases the compressor discharge temperature. One of the IHX plumbing configurations, IHXb, in the present thesis serves to eliminate this drawback, but the effects on the AC power consumption are unknown. For further information on the different plumbing configurations studied of the present thesis, please see Section 3.5.

An important consideration of whether implementation of an IHX will be beneficial is the ambient air temperature. One study found for ambient temperatures of 25°C and 15°C with the compressor in variable mode, the system capacity did not increase with the IHX addition. The evaporator capacity was fixed in this study resulting in reduced IHX heat transfer at these cooler temperatures [16]. For smooth-tube IHXs the authors, Seybold et al., stated that these IHX types provide an ultra-low-pressure drop but do not deliver significant heat transfer per unit length. They are most suitable where compressor discharge temperature is limited and/or a long co-tube can be packaged between the evaporator and compressor [16].

Increased heat transfer is good for system capacity and efficiency, it results in hotter compressor discharge temperatures. Include cost, packaging and the impact on compressor discharge temperature to the list of considerations and it becomes clear that when choosing an IHX, one size does not fit all [16].

2.1 Internal Heat Exchanger Studies for Transient Driving Cycles

The open literature contains very little information regarding AC performance with an IHX for transient driving processes. One study, by Zhang et al, 2002, investigates the cabin cool-down (CCD) test cycle with the IHXb configuration for a compact vehicle in a wind tunnel. The test compared the average interior temperature at breath level to the vent discharge temperature. The testing chamber maintained the ambient air temperature and humidity at 38-43°C and 20-30%, respectively. For more information regarding the CCD testing procedures, see Appendix J and K.

The results from this test revealed a lower compressor discharge pressure, reduced refrigerant superheat at the compressor suction pipe and the compressor discharge temperature remained unchanged. The evaporator always remained in a non-superheated or flooded state, resulting in improved system capacity [14].

2.2 Important Correlations and Coefficients

There are a number of non-dimensional correlations and coefficients to describe and calculate the heat transfer processes of the AC system.

The first is the non-dimensional heat transfer coefficient called the Nusselt number, Nu. This parameter represents the enhancement of heat transfer through a fluid layer as a result of convection relative to conduction across the same fluid layer. A Nusselt number of one for a fluid layer represents heat transfer across the layer by pure conduction [25]. This value is especially important when calculating the forced convection heat transfer by the heat exchangers of the AC system. The Nusselt number in the turbulent regime is determined using the correlation from Equation (3.3) in Appendix F. Where k is the thermal conductivity of the fluid, L_C is the characteristic length and ħ is the heat transfer coefficient. Knowing the Nusselt number allows AMESim to calculate the heat transfer coefficient, ħ ,which is an experimentally determined value. The equation for the Nusselt number is shown in Equation (2.6) below.

$$Nu = \frac{ħ \cdot L_c}{k} \qquad \textbf{(2.6)}$$

A non-dimensional ratio, called the Reynolds number (Re), describes the external flow regime. It describes whether the fluid flow is laminar, turbulent or the laminar-turbulent transition regime. Determining the type of flow regime requires the comparison of the inertia forces to the viscous forces in the fluid. For large Reynolds numbers, such as values greater than $5x10^5$, the inertial forces are much greater than the viscous forces [24]. Thus, the viscous forces cannot prevent rapid and random fluctuations, or turbulence in the flow. The critical Reynolds number defines the boundary where the flow transitions from laminar to turbulent. This value is highly dependent on the geometry and flow conditions. The calculation for the Reynolds number is shown below in Equation (2.7). This number describes the flow regime for internal and external fluid flow. If $Re<Re_{crit}$ the flow is laminar, if $Re>Re_{crit}$ the flow is turbulent. There also exists

a range where laminar-turbulent flow exists, so Re_{crit} gives the engineer an idea of when this transition occurs.

$$Re = \frac{\text{inertial force}}{\text{viscous force}} = \frac{VL_c}{\nu} = \frac{\rho VL_c}{\mu} \quad \textbf{(2.7)}$$

In external and internal fluid flow, where the fluid and the surface are at the same temperature, there is a velocity boundary layer that forms. The velocity of the fluid varies as a function of the boundary layer height, until it reaches the free stream velocity at the edge of the boundary layer. When heat transfer occurs between the surface and the fluid, there is a thermal boundary layer, the flow region over the surface in which the temperature variation in the direction normal to the surface is significant [25]. The Prandtl number (Pr), a dimensionless parameter, describes the relative thickness of the velocity and the thermal boundary layers. Typical Prandtl number ranges for gases are 0.7-1.0 and for water 1.7-13.7. For fluids with Pr much less than unity heat diffuses very quickly relative to momentum and very slowly for Pr much greater than unity. Equation (2.8) below shows the calculation for the dimensionless Prandtl number.

$$Pr = \frac{\text{viscous diffusion}}{\text{thermal diffusion}} = \frac{\nu}{\alpha} = \frac{\mu c_p}{k} \quad \textbf{(2.8)}$$

Another important and sometimes overlooked phenomenon is the heat transfer due to free convection. An example of free convection heat transfer is the heating of a cold can of pop in a room with zero forced air movement. The air in the room circulates naturally due to the density variation with temperature. Warm air will transfer heat to the pop can, decreasing its temperature and increasing its density. As a result, the warm air temperature decreases and it naturally move to the ground and displace air that was previously occupying that volume. If there is no natural air movement, the heat transfer process occurs by conduction only which lowers the heat transfer rate. Two non-

dimensional parameters that describe natural convection heat transfer and flow regime are the Grashof number, Gr, and Rayleigh number, Ra.

The Grashof number which represents the ratio of the buoyancy force to the viscous force acting on the fluid describes the natural convection fluid flow. The value of the Grashof number describes whether the fluid flow is turbulent or laminar in natural convection. The significance of the Grashof number to natural convection is the same as the Reynolds number is to forced convection. For external fluid flow the ratio of the Grashof number to the Reynolds number shows which type of fluid flow dominates. Equation (2.9) below displays the calculation for the Grashof number.

$$\mathrm{Gr} = \frac{\text{Buoyancy force}}{\text{Viscous force}} = \frac{g\beta(T_s - T_\infty)L_c{}^3\rho^2}{\mu^2} \qquad \textbf{(2.9)}$$

Where:

- G gravitational acceleration, m/s^2
- β coefficient of volume expansion, 1/K (Beta= 1/T for ideal gases)
- T_s temperature of the surface, ^oC
- T_∞ temperature of the fluid sufficiently far from the surface, ^oC
- L_c characteristic length of the geometry, m
- ν kinematic viscosity of the fluid, m^2/s

Natural convection heat transfer on a surface depends on the geometry of the surface, its orientation, temperature variation along the surface and the thermo-physical properties of the fluid [25]. The following two equations below are used to describe heat transfer processes that occur within the cabin. Due to the complexity of the fluid motions, it is difficult to obtain analytical solutions for natural convection heat transfer with the exception of a few simple geometries with simplifying solutions. Therefore, heat transfer relations for natural convection are often obtained experimentally. There are simple empirical relations for the average Nusselt number which are in the general form shown

in Equation (2.10) below. This equation represents a simple empirical format used to calculate the Nusselt number for specific geometries with simplifying assumptions, which is accurate for a specific Rayleigh number range. C and n represent a constant coefficient and constant exponent value, specific to one geometry case. The subscript *L* indicates that the dimensionless coefficient is for a surface of length L. The established empirical relations are valid with minimized error for certain simple geometries for a specific range of Rayleigh numbers.

$$\mathrm{Nu_{free}} = \frac{\hbar \cdot \mathrm{L_c}}{\mathrm{k}} = \mathrm{C} \cdot (\mathrm{Gr_L Pr})^{\mathrm{n}} = \mathrm{C Ra_L}^{\mathrm{n}} \qquad \textbf{(2.10)}$$

The non-dimensional number, Ra, is the Rayleigh number, which is the product of the Grashof and Prandtl numbers. The value of the constants C and n depend on the geometry of the surface and flow regime. Equation (2.11) below shows the calculation to determine the Rayleigh number. The variables in this equation have been described previously for Equation (2.10). The subscript *L* indicates that the dimensionless coefficients are for a surface of length L. The magnitude of the Rayleigh number describes whether the heat transfer process is dominated by conduction or natural convection [25].

$$\mathrm{Ra_{free_L}} = \mathrm{Gr_L Pr} = \frac{\mathrm{g\beta(T_s - T_\infty)L_c}^3}{\nu^2}\mathrm{Pr} \qquad \textbf{(2.11)}$$

To analyze a two-phase mixture it is important to know the proportion of liquid and vapour phases. The quality, *x*, is the ratio of the mass of vapour to the total mass of the mixture. A value of zero (0) corresponds to saturated liquid and one corresponds to a saturated vapour. This is an intensive, independent property as changing the mass of the refrigerant does not change its quality. Equation (2.12) below shows the calculation for the mixture quality.

$$x = \frac{\mathrm{m_{vapour}}}{\mathrm{m_{vapour}} + \mathrm{m_{liquid}}} \qquad \textbf{(2.12)}$$

Newton's law of cooling, shown in Equation (2.13), expresses the convection heat transfer. This equation calculates the heat transfer from convection. It is possible to experimentally determine or calibrate a value for ħ that accounts for conduction and convection. However, the heat transfer ability via conduction is usually much smaller than convection. This equation is very critical as the condenser, evaporator and internal heat exchanger models use this equation to calculate the heat transfer of the simulations in the present thesis.

$$Q = \hbar A_s (T_s - T_\infty) \quad \textbf{(2.13)}$$

The most important and difficult parameter to accurately establish in Equation (2.13) is the convection heat transfer coefficient, h(cross), which is defined as the rate of heat transfer between a solid surface and a fluid per unit surface area per unit temperature difference [25]. Variables that can affect the heat transfer coefficient include dynamic viscosity (μ), thermal conductivity (K), density (ρ), constant pressure specific heat (c_p), fluid velocity (V), geometry and roughness of the solid surface and the fluid flow regime. There are relations that can approximate the convection coefficient for specific cases with simplifying assumptions, but this value is largely determined experimentally. In the case of the simulation in the present thesis, the convection coefficient is obtained through calibration of the Nusselt number. AMESim then uses Equation (2.6) to obtain the convection coefficient.

CHAPTER 3
METHODOLOGY

3.1 Simulation Software

There are a variety of commercial software packages on the market today that offer one dimensional (1D) simulation capabilities. A common assumption for 1D modeling is homogeneous material properties, neglecting any property variations along the other two dimensions. The mass and energy conservation equations are written as a function of one

dimension, d*x*, the flow direction. This allows for large spatial resolution and calculation methods that are faster than 2D or 3D models. The 1D model requires user-specified boundary and topographical data. The boundary conditions may include information about material state properties, component efficiencies, and maximum/minimum flow displacements. The topographical data includes information about component geometry and cross-sectional areas. One-dimensional modeling provides the user with base knowledge of a system and to understand system response under various conditions. This knowledge is useful when designing experiments, and when creating higher order models which take much longer to obtain results.

AMESim is the software package used to create and run the AC model. It is very similar to Simulink within Matlab, however the pre-established models within the program help to standardize how the models are created. With Simulink, the design, layout and construction of the model is unique to each engineer, thus making it very difficult for others who are not familiar with such a specific model. It also helps different automotive companies, such as Chrysler and Fiat to share model information easier, since they are using the same simulation platform.

AMESim is a software tool developed by LMS for engineers in the automotive, aerospace and other advanced manufacturing industries. Selection of the correct software requires accurate refrigerant and solid material properties, steady-state and transient simulation capabilities and the ability of applying different boundary conditions for different tests. Although this feature is not included in this thesis, connecting the front-end heat exchanger models to study the air flow and heat exchanged from one component to the other offers the interesting ability to investigate the complete vehicle thermal management. Appendix F.5 presents further information regarding the front end heat exchanger connection.

A complete AC model requires the inclusion of solid material properties and two-phase material modeling. The two-phase refrigerant material requires an accurate estimation of the thermodynamic state of the fluid, based on two independent, intensive properties. Intensive properties are those that are independent of the mass of a system such as temperature, pressure and density. Temperature and pressure are independent properties

for single-phase systems, but dependent properties for multi-phase systems. In other words, temperature is a function of pressure, or vice versa during a phase change process. Therefore specifying the temperature and pressure are not sufficient to describe the state of the material, but one can be specified with another intensive property [19].

Steady-state simulations are important to study changes in system performance under controlled conditions. Changing specific parameters and viewing their effect on the measured output value can highlight ways of improving system and component performance. However, it is also important to understand how the AC will function when subjected to transient conditions, such as varying compressor RPM and the condenser and evaporator air inlet conditions. Transient cycles help engineers understand the margin of benefit for new technology introductions under realistic usage.

The software package AMESim, meets all of the above criteria. It is popular within the automotive industry and it is a very versatile program due to the large range of libraries containing pre-established models for multi-body dynamics, electronics, hydraulics, thermal, electromechanical and others. Refer to the next section regarding the AMESim libraries required to model the AC system. A detailed description of the libraries used for the work in the present thesis is located in Appendix E.

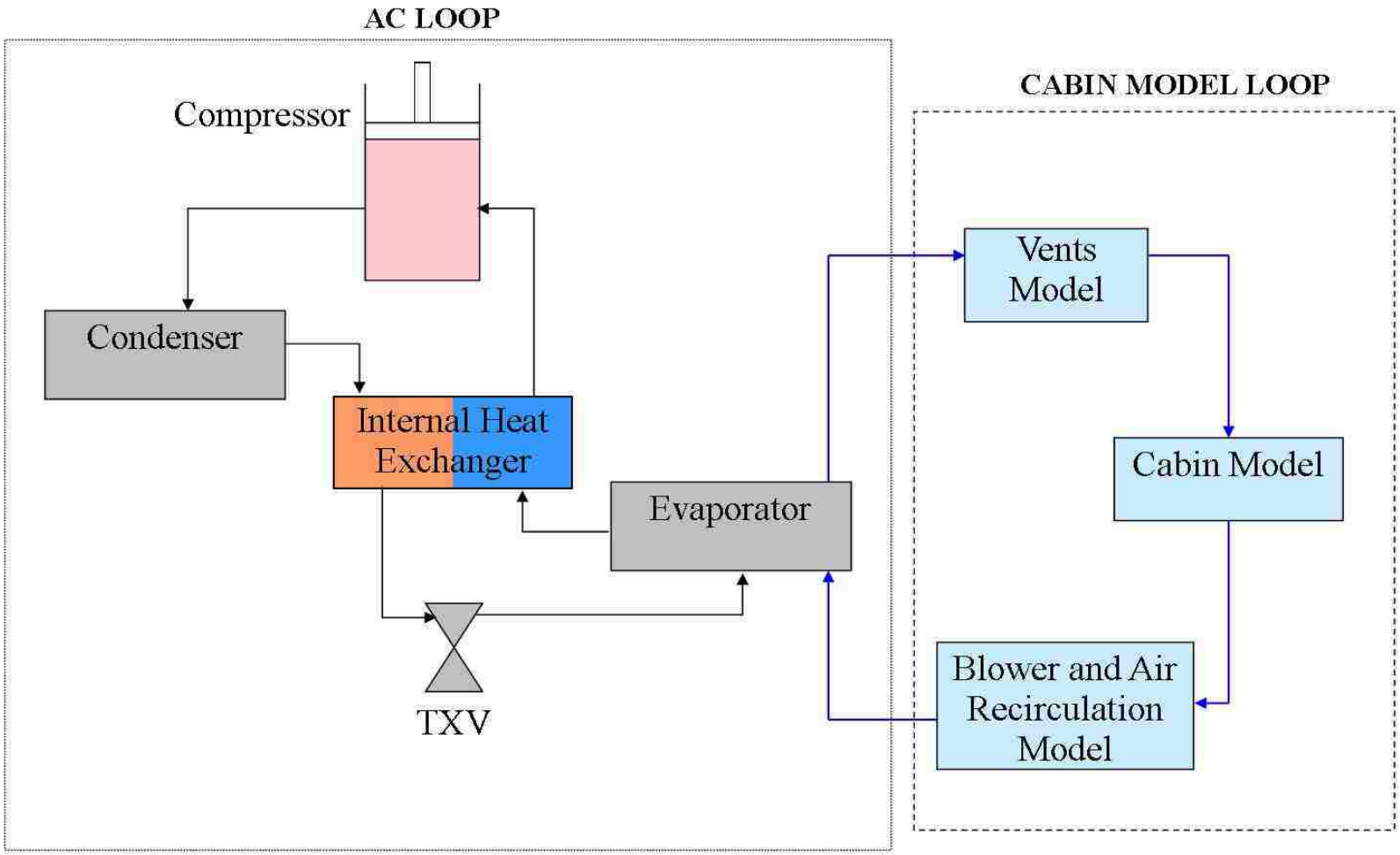

Figure 3-1: Diagram of the complete air conditioning (AC) loop. It is comprised of the major AC components as well as the cabin model, vents model and the blower and air recirculation model.

3.2 Model Components

All of the components in this section have been previously developed by other engineers or are pre-established models within AMESim. This section serves to briefly introduce the major components of the AC system. For an in-depth discussion of the AMESim modeling methods please see Appendices G, H, I and J.

3.2.1 Compressor

All simulations, both steady-state and transient, have a variable displacement compressor with an internal control. The experimental AC system used an axial piston swash-plate compressor. Figure 3-2, obtained from reference 19, shows a cross section as well as labelling for the important components for this type of compressor. The compressor model is pre-built into AMESim, and requires the user-specified to function properly.

Calibration of the compressor sub-model involves specifying the volumetric, isentropic and mechanical efficiencies. For all three efficiencies, zero and one are the lowest and highest possible values respectively. The volumetric and isentropic efficiencies are input as functions of the compressor rotary speed. Please see Appendix D. for the input map files for the volumetric and isentropic efficiencies and their corresponding formatting to meet the input requirements for the compressor sub-model. The mechanical efficiency remains constant for all simulations, with a value of 0.9.

Finally, the compressor sub-model calculates the torque with the user-specified mechanical efficiency. Equation (3.1) represents shows the equation used to calculate the compressor torque. The units of this equation are N-m/revolution.

$$T = \frac{\dot{m}_{dis} \cdot (h_{dis} - h_{suc})}{\eta_s \cdot N} \quad \textbf{(3.1)}$$

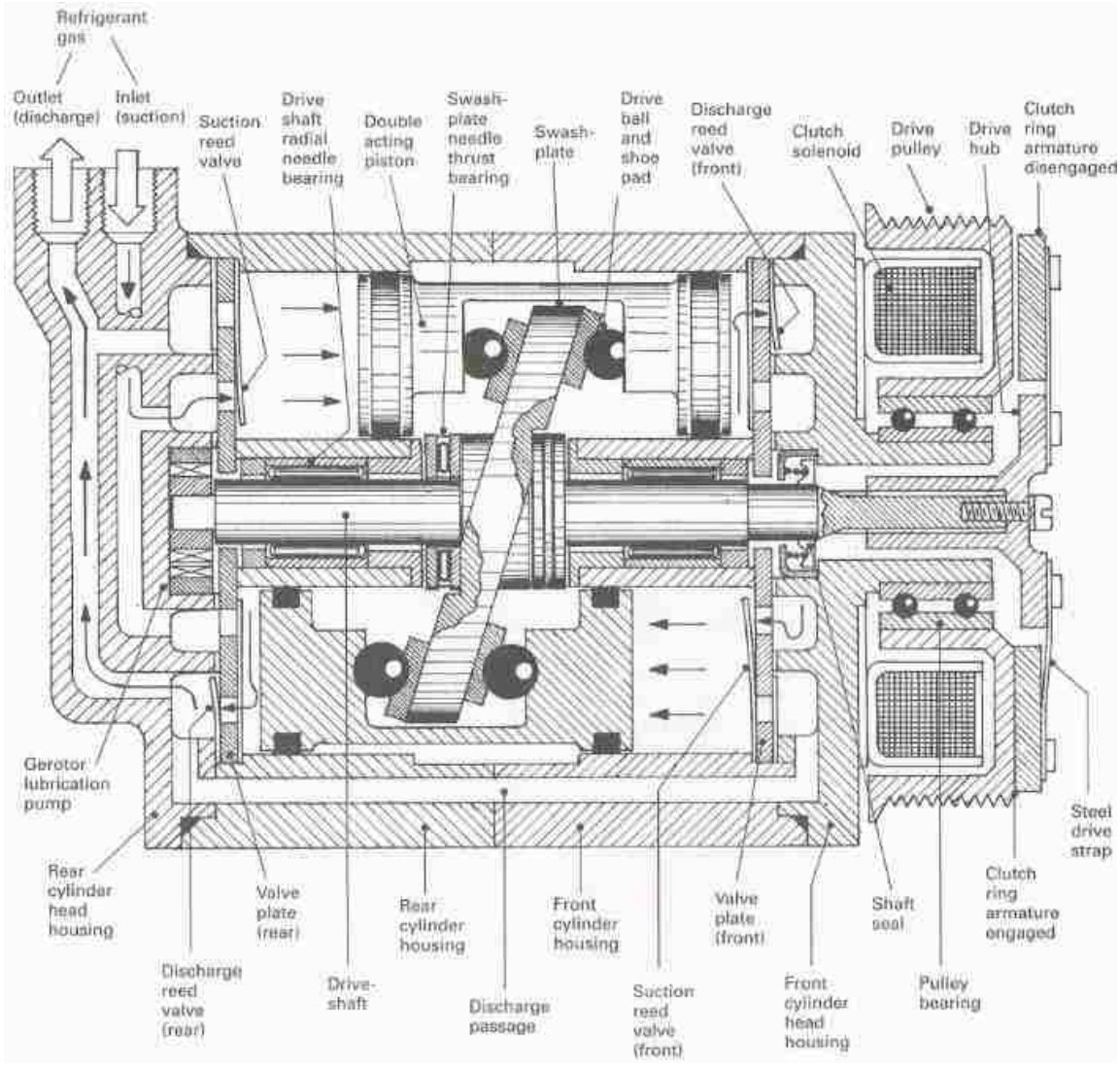

Figure 3-2: Cross section of a double acting axial piston swash-plate driven compressor [22]. This schematic is for a fixed displacement compressor, whereas the compressor in the present thesis has an internal regulation valve which changes the angle of the swash plate. Increasing the angle increases the refrigerant volumetric displacement per revolution and decreasing does the opposite.

3.2.2 Condenser and Evaporator

The condenser and evaporator perform the same function in the sense that they transfer heat to or from the refrigerant to an external air source. The AC loop contains a four pass vertical tube and fin evaporator with the plates and collectors treated separately.

All simulations in the present thesis model a parallel flow tube and fin condenser. Figure F-6, obtained from reference 21, shows a cross section for such a condenser along with labels for the important condenser parameters. There are three passes for the condenser shown in Figure F-6. They are the superheating, condensing and sub-cooling passes. The convention, first pass, second pass, etc., will be used instead for the explanations in the present thesis. The condenser for the simulations has a built in receiver/dryer, which helps reduce and simplify the system packaging requirements.

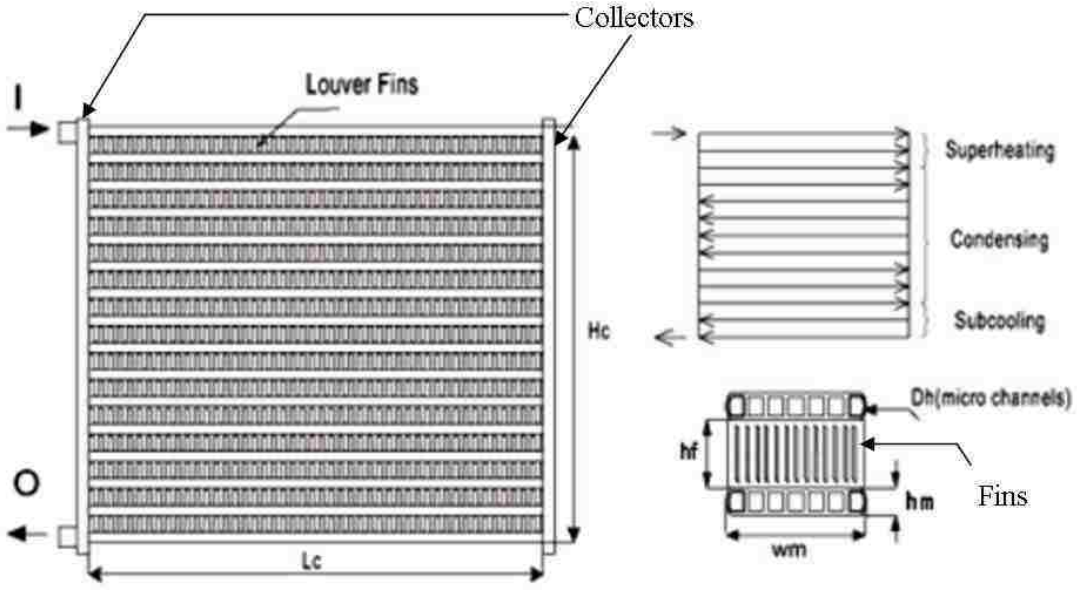

Figure 3-3: Representation of a parallel flow micro channel condenser. The measurements in this figure are not relevant to the present thesis. This figure only serves to illustrate the concept of a parallel flow condenser with micro channel tubing for the refrigerant. Although not discussed in the present thesis, louvred fins serve to increase the turbulence of air flowing through the condenser, thus improving the condenser heat transfer capability [26]. On the left side of the figure, I and O represent the inlet and outlet of the refrigerant flowing through the condenser. L_c and H_c represent the width and height of the condenser. The measurements for the fins in the bottom right corner of the figure are not important, since AMESim has its own way of describing the fin geometry, which will be discussed in detail later on in this section.

The external air side heat transfer coefficient and the corresponding heat transfer is computed using the Nusselt formulation, Equation 3.3. The coefficients a and *B* are used to calibrate the heat exchanger heat transfer to match the experimental data. An optimization tool within AMESim determines the best values for *A* and *B* yielding the lowest difference between the simulation and the experimental heat transfer and pressure

drop combination of the heat exchangers. The user specifies a range of possible values for A and B, the increment between different iterations and the allowable tolerance. The coefficient *C* remains constant with a value of 0.4 since the simulations are all for cooling cases [25]. This equation is very important for the heat exchanger since this is how AMESim is able to calculate the amount of heat transfer between the refrigerant and external air.

$$\text{laminar regime: } \mathrm{Nu} = \text{constant}$$
$$\text{tubulent regime: } \mathrm{Nu} = a \cdot \mathrm{Re}^{B} \cdot \mathrm{Pr}^{C} \quad \textbf{(3.3)}$$

3.2.3 Thermal Expansion Valve (TXV)

The purpose of a thermal expansion valve (TXV) is to regulate the refrigerant superheat leaving the evaporator. In a standard MAC system, the refrigerant exiting the evaporator passes through a feedback loop where it enters the thermal sensing bulb (TSB) of the TXV. There is fluid in the bulb, called the power fluid, which partially fills the TSB in Figure F-12. The pressure of the power fluid applies a force to the top of the diaphragm and the evaporator pressure applies a force on the bottom of the diaphragm. An increase in the refrigerant superheat, increases the temperature and pressure of the gas in the TSB. The pressure increase causes the ball valve to open against the return spring, increasing the refrigerant flow rate through the evaporator. The increase in refrigerant superheat is usually an indication of either a decrease in the air velocity passing through the evaporator or an increase in the ambient air temperature. By increasing the refrigerant mass flow rate, this causes a discrete quantity of refrigerant to exchange less heat with the passing air as it passes through the evaporator. This reduces the refrigerant exiting temperature if it is superheated and the refrigerant quality if it exits in a saturated mixture state. However, overall the amount of heat transferred will increase since more refrigerant is passing through the evaporator. The refrigerant exiting as a saturated mixture will only occur when the IHX is introduced into the AC system because the compressor is not designed to handle a saturated mixture.

Figure F-12 displays a cross-sectional diagram of a TXV and includes labelling of the important components. In the figure, the outlet component screws into the main housing

providing a method to calibrate the TXV. Screwing the outlet component up or down will change the super heat spring tension, thus changing the opening and max opening points of the ball valve. The super heat spring is calibrated to open at a specific refrigerant pressure from the evaporator outlet to control the temperature of the liquid refrigerant entering the evaporator. It is crucial that the temperature of the refrigerant is firstly low enough to be able to meet the cooling requirements of the refrigerated space, and secondly not too high which would deteriorate the compressor life.

3.3 Internal Heat Exchanger (IHX)

Despite the complexity of modeling the complete air conditioning system and the focus of this thesis being the internal heat exchanger (IHX), the model concept is simple. It is composed of two lines exchanging heat with one another through an aluminum medium. The complex nature of the IHX is calculating the performance parameters such as heat transfer, pressure drop, temperature profiles and convective heat transfer coefficients for a two-phase refrigerant in various flow conditions. Figure 3-4 below shows a simple schematic for an IHX.

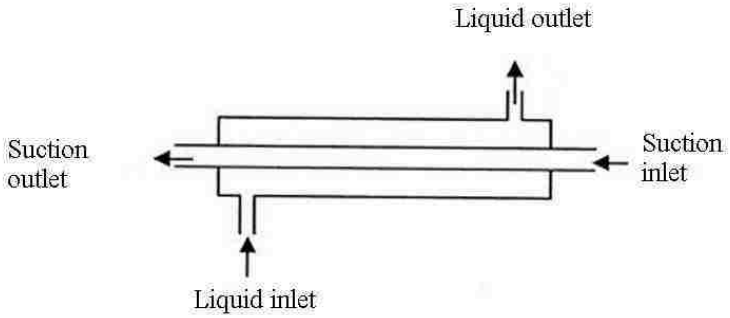

Figure 3-4: Schematic of an internal heat exchanger. This figure displays a cross flow double pipe heat exchanger. Note that the geometry of the IHX is not limited to the design in this figure, but this type of schematic which can be found in any heat transfer textbook accurately represents the heat transfer process between the liquid and suction lines.

The length of the IHX is discretized into sections representing a portion of the heat transfer and pressure drop along the IHX. Each section contains two pipe sub-models for

the liquid and suction lines and a material model representing the aluminum mass. The term “thermal masses” is also used when referring the degree of discretization for a model in the present thesis. Therefore an IHX with three degrees of discretization has three thermal masses. Discretization of the IHX allows the model to predict the transient changes in heat transfer, pressure drop, temperatures, etc., with greater accuracy. The appropriate degree of discretization as it relates the model’s ability to predict the performance of the IHX will be further explained in Section 4.1.

Two-phase flow pipes with heat transfer capabilities model the liquid and suction lines of the IHX. This sub-model is named TPFPHE000 in AMESim. It acts in the exact same way as the two-phase flow pipe described previously in Section 3.2.5. The pipe sub-models of the liquid and suction lines connect to an aluminum thermal mass sub-model. This sub-model, named THC000 in AMESim, computes the temperature profile and energy stored as a function of the simulation time. Figure 3-5 shows a visual representation of the IHX model built within AMESim.

In the figure below, there is a power sensor, named TPFPOT0 within AMESim, that calculates the power of the refrigerant flow at the inlet and exit of the liquid and suction lines. By measuring the power difference and integrating it with respect to the simulation time, AMESim calculates the total heat transfer of the liquid and suction lines. These values also correspond to the IHX capacity. The pressure sensors, named TPFGS010 within AMESim, measure the refrigerant flow-pressure at the entrances and exits of the liquid and suction lines. The summing junction calculates the pressure difference.

In Figure 3-5 there is no connection between the discretized aluminum masses. Simulations with and without the connection showed little to no difference in the heat transfer calculations for the IHX. This is not realistic from an experimental standpoint, but the assumption reduces simulation time. The results for these simulations will also be shown and explained in Section 4.1.

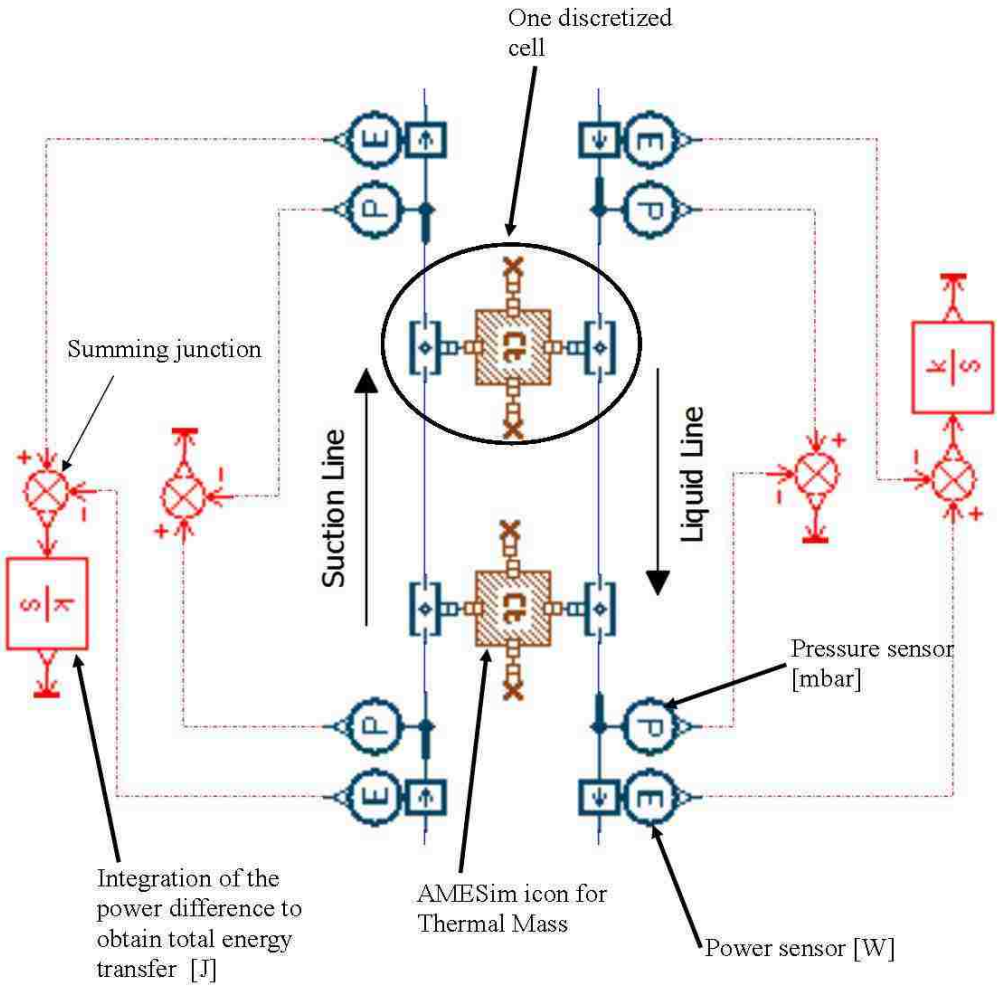

Figure 3-5: AMESim model of the IHX. The literature also uses the names low-pressure and high-pressure lines when referring to the suction and liquid lines, respectively. The red summing junctions calculate the pressure drop and enthalpy flow rate difference between the outlets and inlets of the liquid and suction pipes.

There are pressure and energy sensors placed at the entrance and exit for both the liquid and suction lines. This allows for the measurement of the pressure drop through both pipes as well as the total heat transferred by each line. The energy sensor measures the power difference of each line. This value is integrated for the whole simulation time to obtain the total heat transfer value in units of energy.

3.4 Internal Heat Exchanger (IHX) Calibration

Calibration of the internal heat exchanger (IHX) involves matching the capacity and the pressure drop in the liquid and suction lines with the results provided by the supplier. For

the complete data sheet provided by the supplier, please see Appendix C. The supplier , also referred to as the original equipment manufacturer (OEM) conducts tests for five operating points:

- low load;
- idle;
- idle II;
- high load;
- high load II.

In Figure 3-6, the numbers correspond to inlet and outlet of the high and low-pressure lines of the IHX, or the liquid and suction lines, respectively;

1. High-pressure inlet conditions described by the mass flow rate and specific enthalpy
2. High-pressure outlet conditions described by the pressure and specific enthalpy
3. Low-pressure inlet conditions described by the mass flow rate and specific enthalpy
4. Low-pressure outlet conditions described by the pressure and specific enthalpy

Table 3-1 provides the geometrical parameters of the IHX. The supplier data does not specify IHX geometry information, except for the IHX length. The mass of aluminum is an approximated value. Varying the aluminum mass of the IHX only changes the heat transfer performance for transient operation. An IHX with a mass of 0.5kg or 100kg will perform the same under steady-state operation. The outer diameter of the IHX is not specified, which is not relevant for the one-dimensional modeling in the present thesis, however future experimental tests, 3D simulations and packaging design will require the IHX outer diameter.

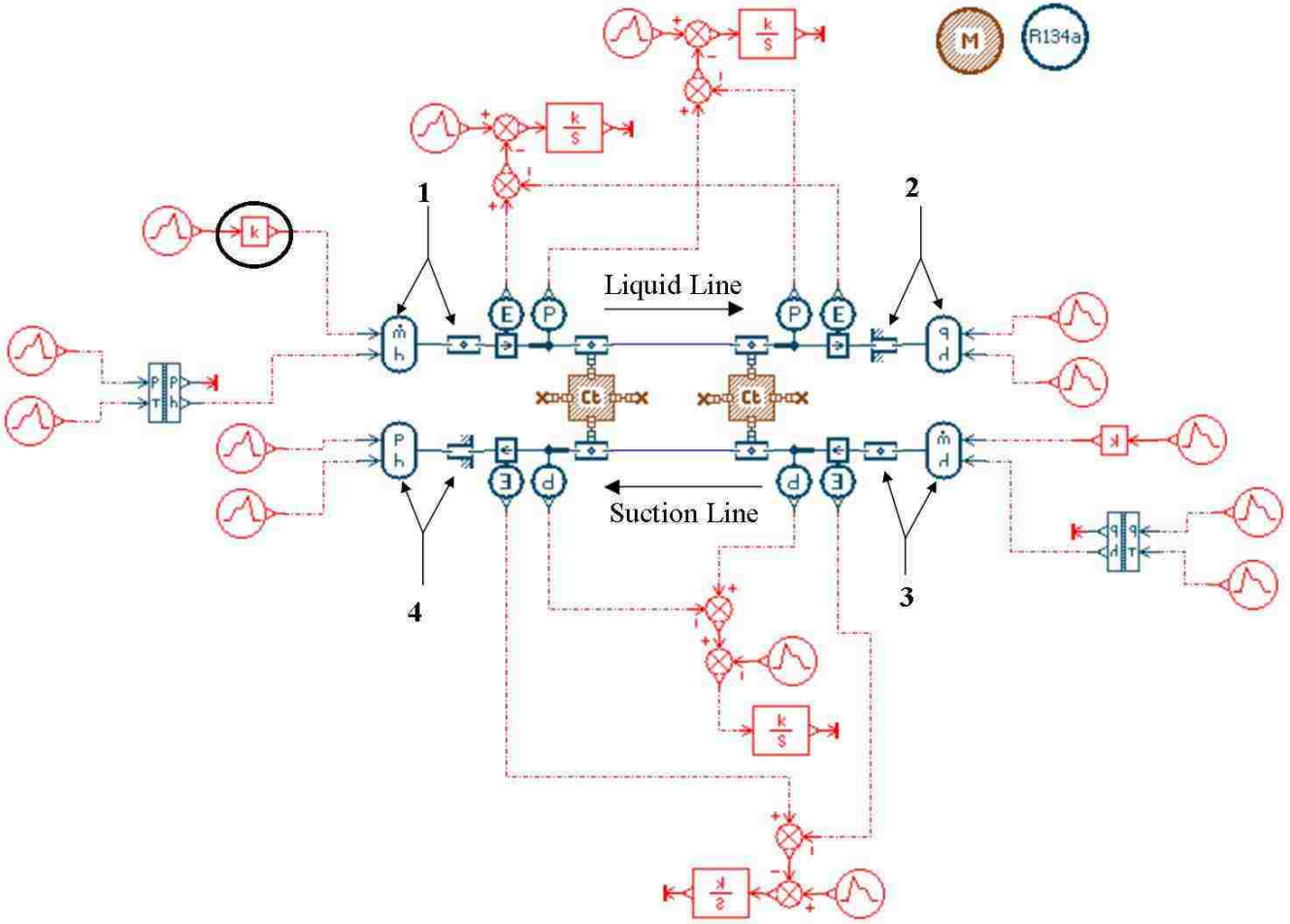

Figure 3-6: IHX calibration model included in AMESim.

The hydraulic diameters and cross sectional areas of the high and low-pressure lines (liquid and suction lines, respectively) are calibrated using an AMESim optimization program. The program iterates through a range of diameter and cross-sectional values to minimize the error of the high-pressure drop, low-pressure drop, and IHX capacity between the simulation and experimental results.

Table 3-1: IHX geometrical parameters. The acronyms LP and HP stand for low-pressure and high-pressure, respectively.

IHX PARAMETER	UNIT	VALUE
Length	mm	900
Mass of Aluminum	kg	0.5
Outer Diameter	mm	unknown
Hydraulic Diameter LP	mm	calibrated
Cross-Sectional Area LP	mm^2	calibrated
Hydraulic Diameter HP	mm	calibrated
Cross-Sectional Area HP	mm^2	calibrated

All of the inlet and outlet conditions are inputs to the model using piecewise linear signal sources. There are five step inputs in each signal source corresponding to the five different test cases. Table 3-2 and Table 3-3 display the boundary conditions for the five different cases.Table 3-3 displays the supplier test points for the inlet and outlet conditions of the IHX, respectively. The initialization values used for the refrigerant piping sub-models correspond to the average inlet temperature and pressure values in Table 3-2. The sub-model in Figure 3-6, which is circled in black, converts the mass flow rate from g/s to kg/s.

Table 3-2: Inlet temperature, pressure and mass flow conditions for the HP and LP lines

Parameter Name	Unit	OEM Test Parameters Requirement				
		Low Load	Idle II	Idle	Highload	Highload II
Temp. OUT LP	°C	19.6	35.3	29.5	24.4	25.8
Pressure OUT LP	bar	3.5	3.5	3.5	2.9	2.9
Specific enthalpy OUT LP	kJ/kg	415	429.5	424.2	420.6	422.1
Temp. OUT HP	°C	22	56	41.3	37	41.1
Pressure OUT HP	bar	7.5	25	16	13	15.9
Specific enthalpy OUT HP	kJ/kg	230.8	282	259.1	252.6	258.8

Table 3-3: Outlet temperature, pressure and specific enthalpy for the HP and LP lines

Parameter Name	Unit	OEM Test Parameters Requirement				
		Low Load	Idle II	Idle	Highload	Highload II
Temp. IN HP	°C	25	70	50	45	50
Pressure IN HP	bar	7.5	25	16	13	16
Temp. IN LP	°C	15	10	15	11	11
Pressure IN LP	bar	3.5	3.5	3.5	3	3
Mass Flow	g/s	10	28	28	45	65

3.5 IHXa vs. IHXb as drop-in Component

Previously discussed in Chapter 2, only one study was found in the literature [13]. All of the other studies consider only IHXa, thus the present thesis attempts to determine the benefits and drawbacks of each configuration in an effort to determine the best plumbing configuration of the suction line.

Figure 3-7 and Figure 3-8 illustrate the difference between the two suction line plumbing configurations. In Figure 3-7, the suction line of the IHX is located *after* the thermal sensing bulb (TSB) of the thermal expansion valve (TXV). This configuration will be hereafter referred to as IHXa. In Figure 3-8, the suction line of the IHX is located *before* the TSB of the TXV. This configuration will be referred to as IHXb for the duration of the thesis.

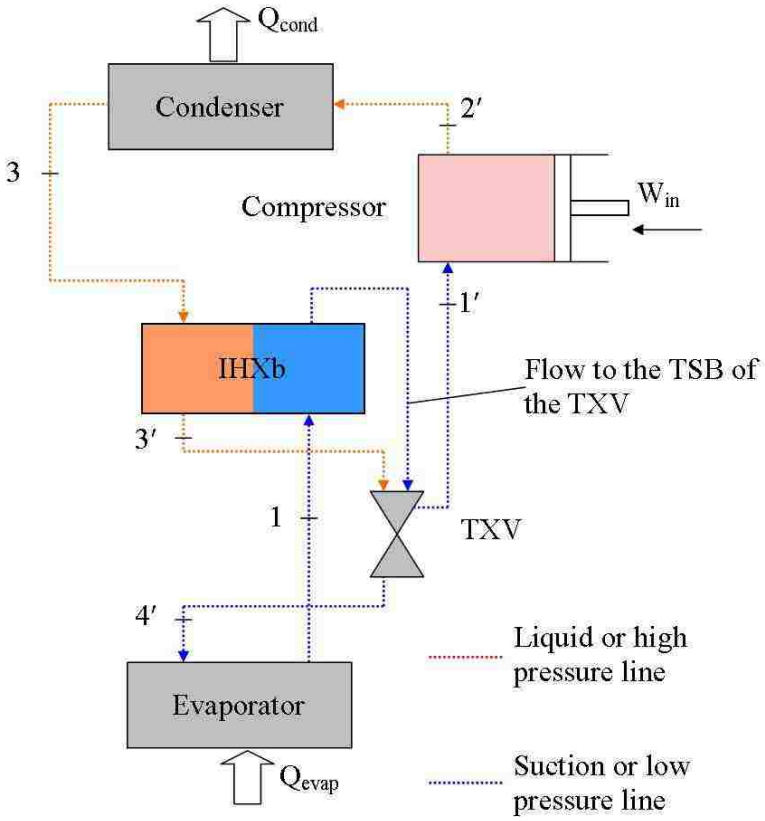

Figure 3-7: Representation of IHXa configuration where the IHX suction line is located downstream of the TXV. Here the TSB does not sense the increase in refrigerant superheat from the IHX. The refrigerant superheat entering the compressor is much higher in the IHXa configuration as compared to IHXb. The colour scheme of the IHX highlights the high and low pressure sides, rather than the temperature of the refrigerant.

For the IHXa configuration, the TXV regulation of the increased refrigerant temperature leaving the suction line of the IHX is delayed. The refrigerant must pass through the system another time to be sensed by the TSB. However, the TXV for IHXa should not influence the refrigerant flow rate through the evaporator compared to the IHXb configuration.

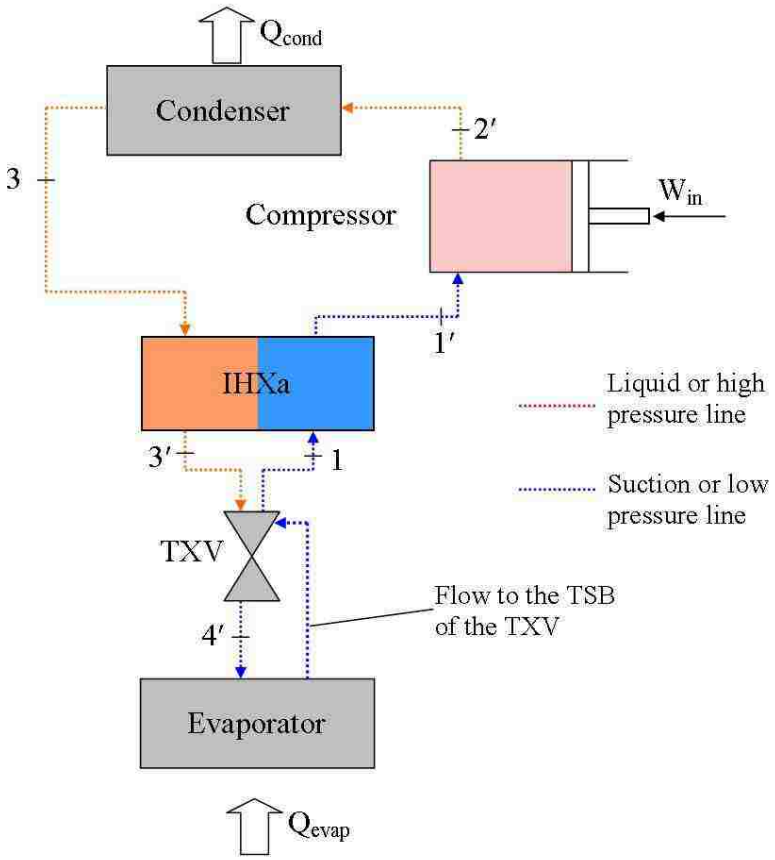

Figure 3-8: Representation of IHXb configuration where the IHX suction line is located upstream of the TXV. Here the TSB senses the increase in refrigerant superheat from the IHX. The TXV is able to regulate the refrigerant temperature before entering the compressor. The colour scheme of the IHX highlights the high and low pressure sides, rather than the temperature of the refrigerant.

In an AC system without an IHX, the TSB calibration ensures that the refrigerant temperature is a few degrees above the saturated vapour curve to ensure superheated refrigerant flow through the compressor. If there is any liquid within the refrigerant, this will alter the performance of the compressor and lead to cavitation, significantly diminishing the compressor life. Thus, the engineer can alter the TSB calibration to allow a lower refrigerant temperature exiting the evaporator. The effect of altering the TXV settings is not considered in the work of the present thesis since there is no experimental data to provide a possible range of adjustments within the simulation.

The influence of the TXV on the refrigerant mass flow rate through the evaporator should be less than an AC system without an IHX. This should lead to decreased pressure drop

between the high and low-pressure lines and consequently decrease the compressor work. One significant drawback of this configuration is the increased refrigerant temperature through the compressor. The material of the compressor may not be designed to withstand the increased refrigerant temperature or the resulting temperature will significantly reduce the life of the compressor. The work in the present thesis does not consider compressor damage and life span as a function of the refrigerant superheat temperature, however, the engineer should always consider this factor when designing an AC system.

With IHXb, the TSB will sense the increased refrigerant temperature and overcompensate by lifting the ball valve to increase the refrigerant mass flow rate through the evaporator. Increased refrigerant flow through the evaporator from a greater ball valve lift means a smaller pressure drop between the high and low-pressure lines. The TXV will influence the refrigerant mass flow rate through the evaporator more than the IHXa configuration, but it is uncertain whether this influence will lead to increased or decreased compressor work. It is believed that the evaporator capacity of IHXb should be significantly greater than IHXa. The temperature of the refrigerant through the compressor should be equivalent or similar to the temperature profile of an AC system without an IHX since the TSB is located downstream of the IHX.

3.6 Steady-State Simulations

To understand whether the IHX model in AMESim actually functions as intended and how its introduction into the AC system actually makes a difference, it was necessary to conduct two types of steady-state simulations. Therefore, the present thesis includes simulations studying the IHX performance at a component and system level.

Component level testing involved varying certain IHX dimensions and evaluating the subsequent response. Changed parameters included the IHX length and aluminum thermal mass. Since the aluminum mass was not specified by the supplier, it was necessary to investigate its influence on the heat transfer capabilities of the IHX. This is discussed further in

System level testing involves the effect of an IHX included in an AC system. In the steady-state tests, the compressor speed and evaporator and condenser inlet air conditions are kept constant. There is no control for the superheat exiting the evaporator and the sub-cooling leaving the condenser, thus the evaporator capacity is allowed to change for each of the testing states. For information regarding the input parameters for the compressor, condenser and evaporator please see Appendix F.

One of the major drawbacks for the steady-state simulations in the present thesis, is the lack of experimental data for model validation. Therefore to circumvent this issue, testing conditions and results were compared to a paper published by Seybold et al., 2012, reference [13]. This was the only available method to ensure that the model was providing accurate results, adhering to the general performance of a similar AC system published in the literature.

3.6.1 Component Level Testing

Studies found in the literature have already investigated the effect of varying the IHX length on the IHX performance parameters, which are provided below. The purpose of the component level testing in the present thesis serves to look at the IHX length and the corresponding component performance changes. The following list shows all of the considered performance parameters for the IHX length investigation.

- Evaporator capacity ratio as a function of compressor power ratio
- Compressor discharge temperature
- Evaporator capacity ratio vs. IHX length at 45^{o}C and 25^{o}C
- Compressor power consumption ratio vs. IHX length at 45^{o}C and 25^{o}C
- Coefficient of Performance (COP) ratio vs. IHX length at 45^{o}C and 25^{o}C

3.6.2 System Level Testing — Boundary Conditions

The testing parameter selection, shown in Table 3-4, originates from a SAE technical paper, by Seybold et al., 2012 [13]. These parameters cover a wide range of AC usage for light-duty vehicles. The steady-state testing condition, utilized 11 of the 14 operating points from the SAE paper. The three omitted operating conditions where ones that only varied the ambient relative humidity at a temperature of 25°C.

The SAE paper specifies an air inlet mass flow rate for the condenser. However, the condenser in the SAE study and the present thesis are not the same thus this boundary condition is not imposed on the condenser. The pre-established AMESim condenser model requires an air speed input from the user or some other input source, and from there determines the air mass flow rate based on the user-specified geometry values.

The first column of Table 3-4 specifies the naming convention for each test. The numbers correspond, from left to right, to the evaporator air inlet temperature, relative humidity (RH) and the compressor speed. For example, 40/40/4850 corresponds to the following testing conditions: 40°C, 40% RH and 4850 revolutions per minute (RPM). From this point forwards, reference to a specific operating condition in the present thesis will use the format in the column labelled *Test Number*.

Table 3-4: Steady-state test conditions for MAC system. These test conditions are obtained from the AC system level testing conducted in the SAE paper by Seybold et al [13]. These parameters cover a wide range of AC usage for light-duty vehicles.

Test Number	Compressor	Condenser		Evaporator		Remark
	Compressor Speed [rev/min]	Air inlet temp [°C]	Air speed [m/s]	Temp [°C] / Air rel. humidity inlet [%]	Air inlet mass flow [kg/h]	
40/40/4850	4850	38	4	40 / 40	520	max performance
45/25/900	900	45	1.5	45 / 25	520	40 km/h
45/25/2500	2500	45	3	45 / 25	520	80 km/h
45/25/4000	4000	45	4	45 / 25	520	100 km/h
45/25/6000	6000	45	5	45 / 25	520	140 km/h
35/40/900	900	35	1.5	35 / 40	520	40 km/h
35/40/2500	2500	35	3	35 / 40	520	80 km/h
35/40/4000	4000	35	4	35 / 40	520	100 km/h
25/80/900	900	25	1.5	25 / 80	390	40 km/h
25/80/2500	2500	25	3	25 / 80	390	80 km/h

3.6.3 System Level Testing—Performance Comparison

The comparison of the AC performance from the system level testing literature data provides a way of checking if the model is providing accurate results. Since experimental data from bench tests was not available, this method is used as a replacement. The simulation of the two cases, IHXa and IHXb, will be compared and evaluated based on the performance parameters listed below:

- compressor power consumption;
- compressor discharge temperature;
- coefficient of performance (COP);
- evaporator capacity;
- IHX capacity;
- suction line pressure drop;
- absolute efficiency ratio of the two IHX configurations;
- suction line pressure drop for all steady-state operating points in Table 3-4;
- absolute efficiency ratio for all steady-state operating points in Table 3-4;

With the exception of the compressor discharge temperature and suction line pressure drop, the comparison is based on the percent difference between IHXa or IHXb and the baseline AC system without an IHX. For example, Equation (3.4) displays the calculation below, where W represents the comparison parameter. By normalizing the difference between an AC system with and without an IHX the strengths and weaknesses of the two suction line plumbing configurations is more apparent.

$$\text{Percent Difference (\%)} = \frac{W_{\text{a or b}} - W_{\text{no IHX}}}{W_{\text{no IHX}}} * 100 \qquad \textbf{(3.4)}$$

The configuration of the feedback loop to the TXV is not specified, therefore the IHXa and IHXb configurations will be compared to the experimental results from the SAE paper, reference [13]. The following are comparison parameters shown as a function of refrigerant mass flow rate:

- IHX capacity
- Suction line pressure drop
- Efficiency ratio
- Liquid line pressure drop

The following are comparison parameters shown as a function of compression ratio:

- Volumetric efficiency
- COP

Finally, the last comparison made between the simulation results and the SAE paper is the compressor discharge temperature.

3.7 Transient Simulations

The following sub-sections will describe the boundary conditions imposed on the AMESim model to mimic the way the experiment is conducted in the climatic testing chambers. For a general description of these government testing cycles please refer back to Section 1.1.

These transient cycles will provide a more realistic feedback on the value of implementing an IHX in an AC system. The studies conducted in the literature all study the inclusion of an IHX under steady-state conditions with the exception of one study for a CCD test by Zhang et al., 2002 which was mentioned previously in Section 2.1.

The compressor controls for the NEDC simulations are not changed from the CCD simulations. The only difference is the compressor RPM map. Figure 3-9 displays a plot of the vehicle velocity and the compressor RPM as a function of time. In this simulation, the input RPM map includes the fluctuations from gear changing. The original NEDC ASCII text files containing the compressor and velocity maps had data points every 0.25 seconds. Due to the large size of the data files, this led to very long simulation times. Changing the print period between the data points to five seconds significantly decreased computation time.

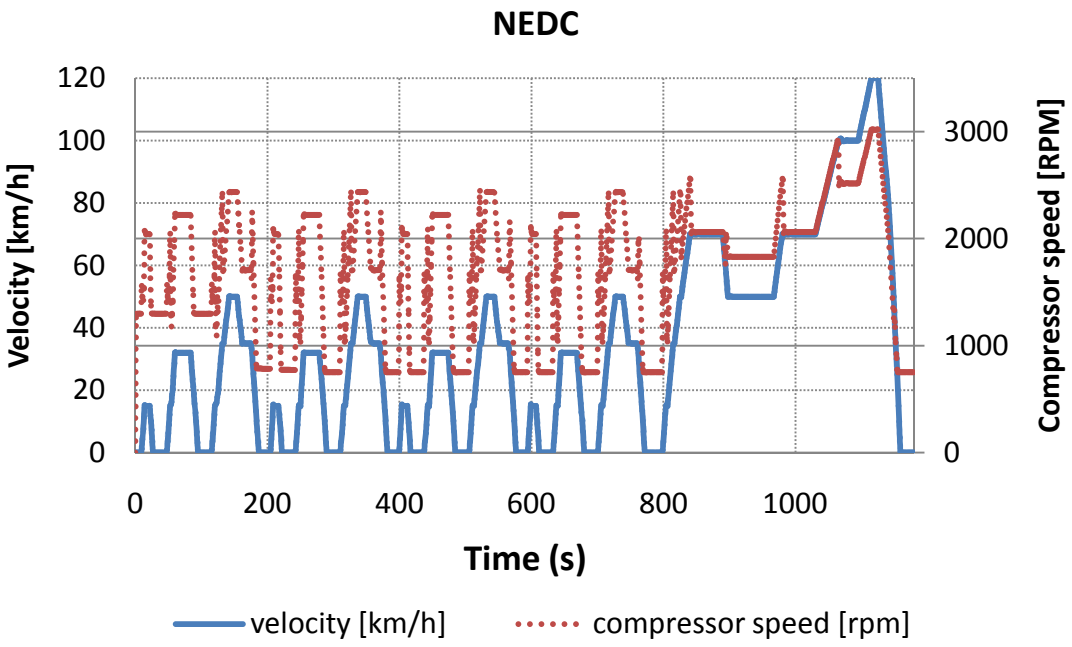

Figure 3-9: Vehicle velocity and compressor RPM plot for the NEDC test. The vehicle velocity is input into the cabin model for the external convection sub-models and the compressor RPM map is input into the compressor sub-model.

Figure 3-10 displays the blower control system for the NEDC simulations. This control system collects three feedback temperatures and changes the blower activation level accordingly. An explanation of the numbered controls in Figure 3-10, allows for a complete understanding of how this control system functions.

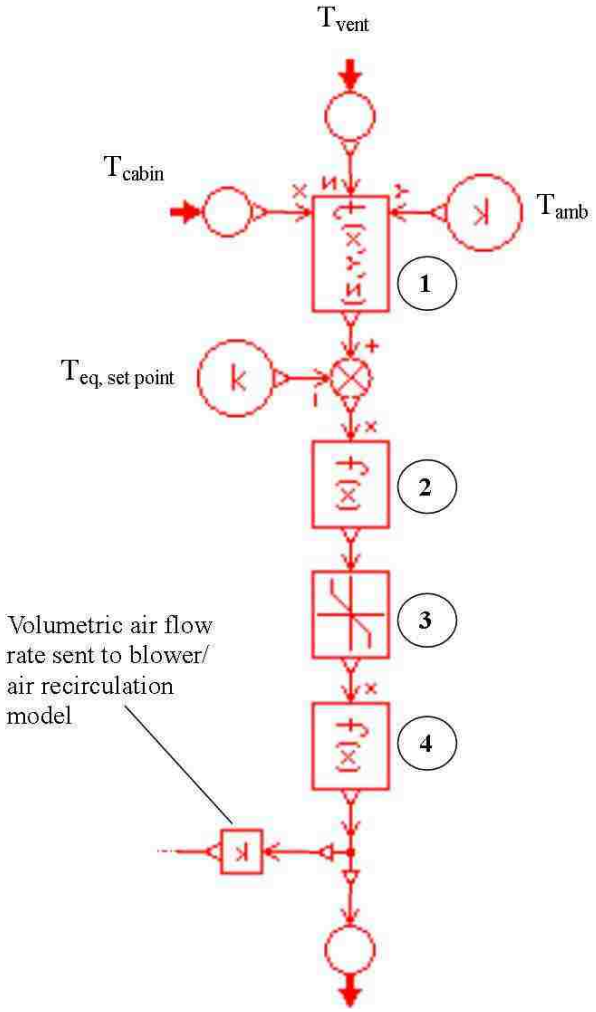

Figure 3-10: Blower control system for the NEDC simulations. The numbers correspond to the different sub-models/user-specified functions that are explained in the list below.

1. This function contains an equation that gives a weighting value to the three feedback temperatures of the blower control system, the cabin air temperature, T_{cabin}, the vent outlet temperature, T_{vent}, and the ambient temperature, T_{amb}. In Figure 3-10, the variable *delta* is used to increase the vent temperature. A value of 6°C is used based on Fiat recommendations. Equation (3.5) displays the calculation for the weighted temperature based on the feedback values of the cabin, vent and ambient air temperatures.

$$T_{weighted}[°C] = 0.6 \cdot T_{cabin} + 0.2 \cdot (T_{vent} + \delta) + 0.2 \cdot T_{amb} \quad \textbf{(3.5)}$$

2. Before the second function the error between $T_{weighted}$ and the equilibrium set point temperature of the cabin, $T_{eq,\ setpt}$ is calculated. $T_{eq,\ setpt}$ specifies the desired cabin temperature for the AC system. The error between these two temperatures is represented by the parameter $T_{diff_{eq}}$.

   In the second function, a linear equation relates $\Delta T_{control}$ to the blower activation level, which represents the percentage of the maximum blower volumetric capacity. Equation (3.6) is unique to Fiat's design specifications for blower control. This function is an internal control method used by Fiat to control the airflow through the evaporator inlet for the NEDC test.

$$\text{BLW } [\%] = 14.5 + 12.8 \cdot T_{diff_{eq}} \qquad \textbf{(3.6)}$$

3. The third function is a saturation control ensuring the output value is between a minimum allowable value of 5% and a maximum value of 100%. A minimum value is specified to avoid AMESim error crashes from zero air mass flow rate. Also, in actual operating conditions there will always be some air flow through the blower, therefore a non-zero value for the blower capacity is justified.
4. The fourth function converts the blower capacity percentage into a volumetric air flow rate. This equation is used by Fiat, with the number 400 corresponding to the maximum volumetric flow rate of the blower installed on the testing vehicle.

$$\text{volumetric air flow rate } \left[\frac{m^3}{h}\right] = 400 \cdot \frac{\text{blower } \%}{100} \qquad \textbf{(3.7)}$$

Having described the air mass flow control for the blower, the other input parameters for the blower remain constant for the entire NEDC simulation. Table 3-5, shows the other ambient conditions of the NEDC. Three different NEDC cycles corresponding to different ambient temperatures and relative humidities are conducted in the present thesis. In Table 3-5, the parameters with more than one value provide the different values that correspond to each of the three tests.

Table 3-5: Other input conditions for the NEDC blower control. The parameters with more than one value have different values for each of the three tests.

NEDC Blower Control Parameter	Value
Temperature [^{o}C]	25, 28, 35
Pressure [kPa]	1.01
Relative Humidity [%]	50, 50, 60
Recirculation [%]	0

Figure 3-11 shows the condenser fan NEDC control system. An explanation of the numbered controls in Figure 3-11, will allow for a complete understanding of how this control system functions.

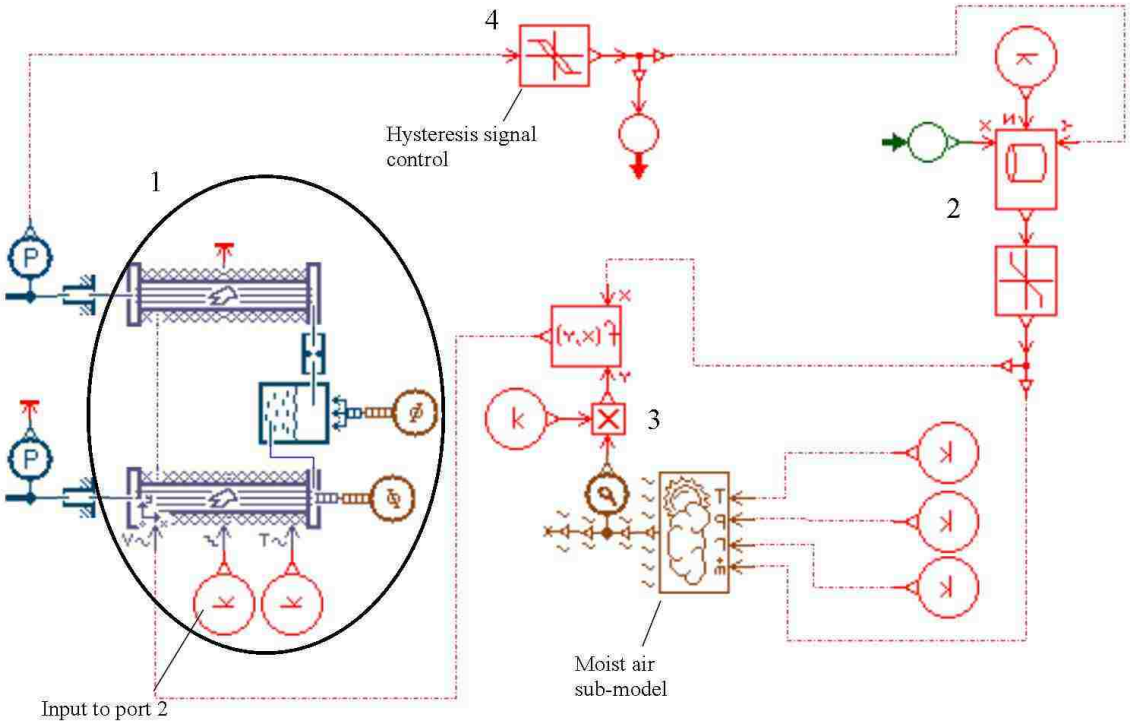

Figure 3-11: Condenser fan control for the NEDC.

1) Section one, circled in black in Figure 3-11, represents the pre-existing AMESim condenser model, discussed in Appendix F.4. The *homogeneous variable* option is used for the velocity data since this value is varied based on the input from an air flow file, shown in Appendix B. For the temperature data option ambient constant is chosen since the ambient temperature is kept constant for the whole

test. These two options for the condenser sub-model, HEATCONDREF120, are explained in Section 3.2.5. This option is used because the temperature remains at ambient, whereas the vehicle velocity is changing with respect to simulation time.

The input to port 2, labelled in Figure 3-11, of the reference condenser is set at a constant value of 1 and is only used when switching between two or more different air velocity profiles for the condenser. Since there is only one velocity profile for this test, a value of 1 is set for this port.

2) The air mass flow rate [kg/s] into the condenser is calculated from an air flow file provided by Fiat. In this file, the air mass flow rate through the condenser is a function of the vehicle velocity [km/h], fan activation level [no units] and ambient temperature [^{o}C]. Again, see Appendix B for a copy of this file.
   There is a saturation sub-model ensuring the air mass flow rate never reaches 0 kg/s. The condenser model uses the NTU method to calculate the amount of heat transfer, thus a zero mass flow rate would lead to a simulation error. The minimum value allowed is 0.001 kg/s.
3) The third function calculates the velocity of the air entering the condenser in meters per second. Based on the density of the air, the mass flow rate of air is established from the air flow file and the frontal area of the condenser. The density of air is calculated based on the temperature, pressure and relative humidity of the ambient air. This calculation occurs in the moist air sub-model, and displayed below by Equation (3.8). This calculation is important since it allows AMESim to compute the air mass flow rate through the condenser. The variables in the equation are as follows: ah is the absolute humidity, P is the pressure in PaA, T is the temperature ^{o}C, R_{da} is the perfect gas constant for dry air in J/kg-K, R_{mv} is the perfect gas constant for water vapour in J/kg-K.

$$\rho_{ma} = \frac{1 + ah}{R_{da} + ah \cdot R_{wv}} \cdot \frac{P}{T} \qquad \textbf{(3.8)}$$

4) The inlet condenser pressure controls the fan activation level input, which is an input parameter to the air flow file. The activation level responds differently depending if the pressure is increasing or decreasing, and therefore requires a hysteresis sub-model. Table 3-6 displays the inputs for the increasing and decreasing control curves. Figure 3-12, is a plot of the numbers in Table 3-6. There were AMESim rules regarding the creation of the increasing and decreasing curves. This is the reason for the ordinate and abscissa values not corresponding to whole numbers.

Table 3-6:NEDC hysteresis feedback response of the inlet condenser pressure for the condenser fan.

INCREASING CURVE		DECREASING CURVE	
Condenser Inlet Pressure [barA]	**Activation Level**	**Condenser Inlet Pressure [barA]**	**Activation Level**
0	0.1	0	0.1
14.9	0.2	10.9	0.3
15	49.8	11	50.1
19.9	49.9	15.9	50.2
20	100	16	100

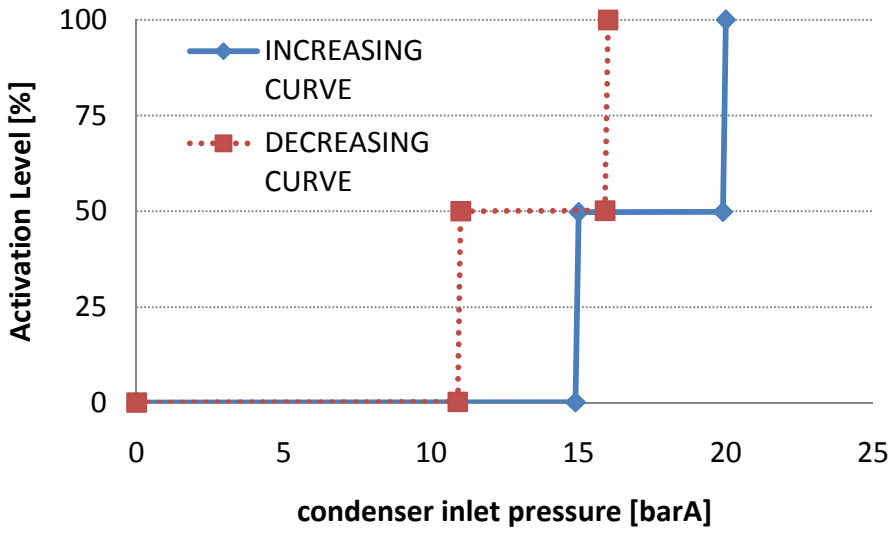

Figure 3-12: Graphic representation of the NEDC hysteresis feedback response for the condenser fan. When the inlet condenser pressure is in an increasing condition, the activation signal corresponds to the blue curve. When the inlet condenser pressure is in a decreasing condition, the activation signal corresponds to the red curve.

For the legislative transient testing cycles, the important parameter will be the overall power consumption of the AC system. In order to meet the strict fuel economy standards of the future, it is important that the incorporation of IHX results in an overall reduction in power consumption. The simulation considers three components responsible for the AC power consumption: compressor, blower and fan.

A time-averaged power consumption will be specified for the three transient cycles, providing a quantitative comparison. When the time-averaged power consumption value is multiplied by the test time the area is equivalent to total power consumption of the compressor, blower and fan.

The calculation for the compressor power consumption uses the refrigerant mass flow rate and the enthalpy difference between the inlet and outlet of the compressor.

The calculation of the condenser fan power consumed depends on the fan activation level, which represents the level the fan is running relative to its maximum capability. Calculation of the blower power consumed depends on the mass flow rate of the fresh and re-circulated air. At maximum capacity, the condenser fan and blower power consumption correspond to 300W and 250W, respectively. The power consumption relations for the blower and condenser fan are shown in Figure 3-13 and Figure 3-14 below, respectively.

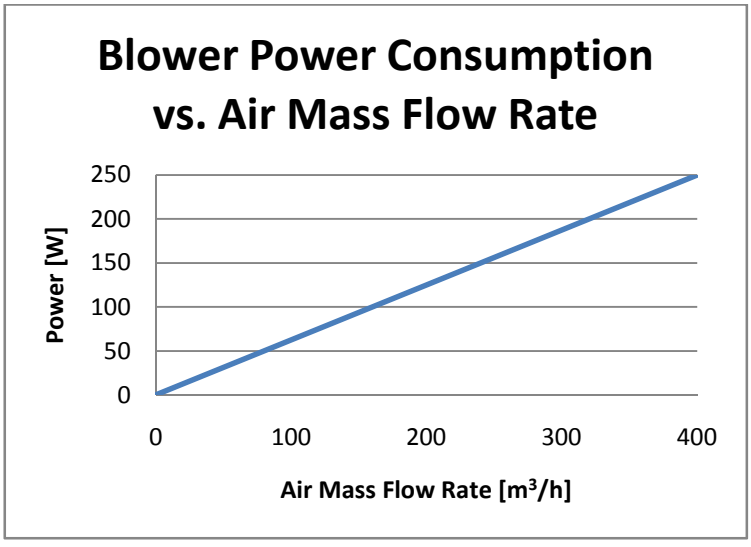

Figure 3-13: Blower power consumption as a function of the air mass flow rate.

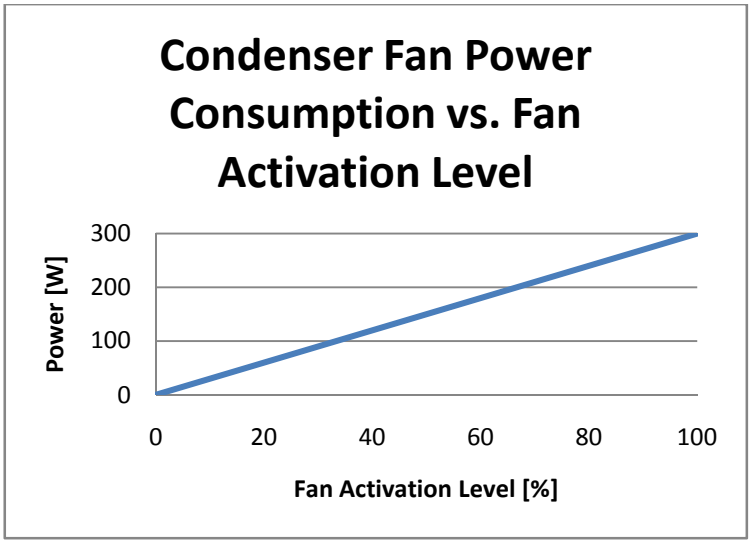

Figure 3-14: Condenser Fan Power Consumption as a function of the fan activation level.

The AC power consumption for the CCD test only accounts for the contribution from the compressor. For this test the AC is set to the maximum, so the blower constantly runs at maximum capacity of 400 m^3/h. From Figure 4-39 in Section 4.3 the contribution of the blower power is small in comparison to the compressor. The condenser fan contribution is not present in this test. The air flow is only a function of the vehicle velocity.

CHAPTER 4
RESULTS AND DISCUSSION

4.1 Internal Heat Exchanger (IHX) Calibration

The following results illustrate the effect of internal heat exchanger (IHX) discretization on the IHX capacity and pressure drop error. Three models, are studied where the IHX is partitioned into two, three and four thermal masses, hereinafter named 2mass, 3mass and 4mass, respectively. The number of thermal masses are equivalent to the degree of discretization. Two pipe sub-models for the liquid and suction sides and a thermal mass sub-model constitute one discretized cell of the IHX. Refer back to Figure 3-5 in Section 3.3 for a graphical representation of a one discretized cell for the IHX.

The IHX calibration was carried out using the optimization software in AMESim. The optimization run was set up to minimize the flow pressure drop and IHX heat transfer capacity errors. The calibrated parameters include the cross-sectional areas and hydraulic pipe diameters of the high and low-pressure lines. The initializing values for the areas and diameters influence the final results. Consequently, they also affect the capacity and pressure drop calculations . This was determined from running many IHX calibration iterations within AMESim. The model selects values that minimize the simulation error mathematically, based on the user-specified allowable range.

The goal of this set of simulations was to minimize the error of the IHX suction side pressure drop due to its suggested importance found in the literature. Figure 4-1, Figure 4-2, Figure 4-3, and Figure 4-4 display the error for the LP and HP pressure drops and capacities. Each figure displays the error of one parameter for the 2mass, 3mass and 4mass calibration models with respect to the specifications supplied by the manufacturer. The experimental data from the supplier shows that there is a variation in the HP and LP capacities, however these two values are the same for the AMESim IHX model.

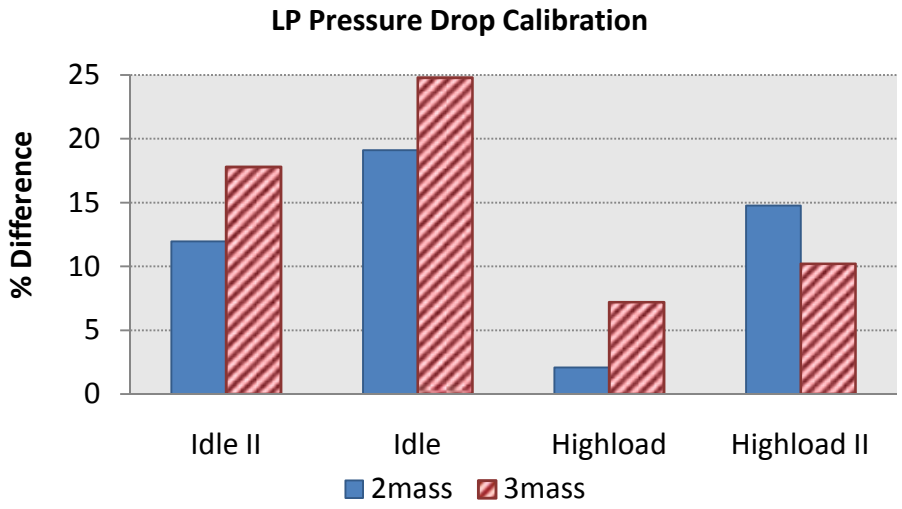

Figure 4-1: Low-side pressure drop calibration of the internal heat exchanger (IHX). These are the results of the component level simulations of the IHX to determine the appropriate degree of discretization for the model.

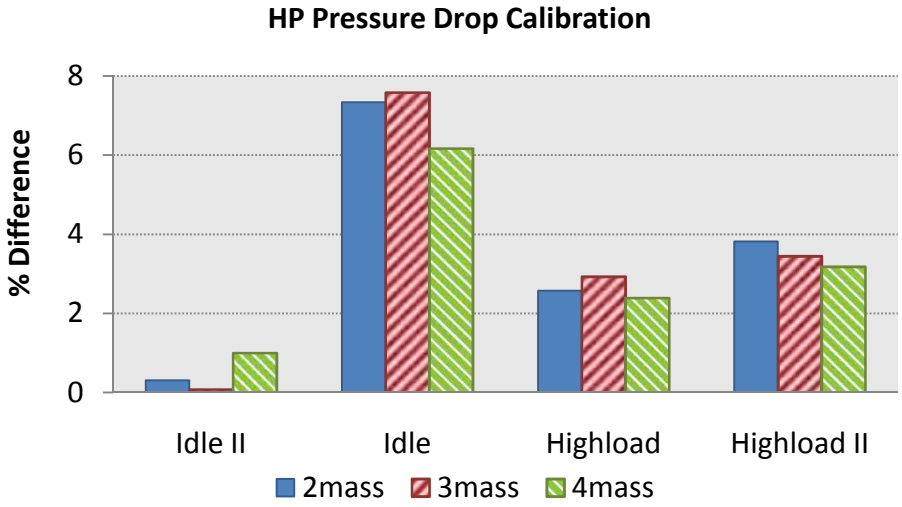

Figure 4-2: High-side pressure drop calibration of the internal heat exchanger (IHX). These are the results of the component level simulations of the IHX to determine the appropriate degree of discretization for the model.

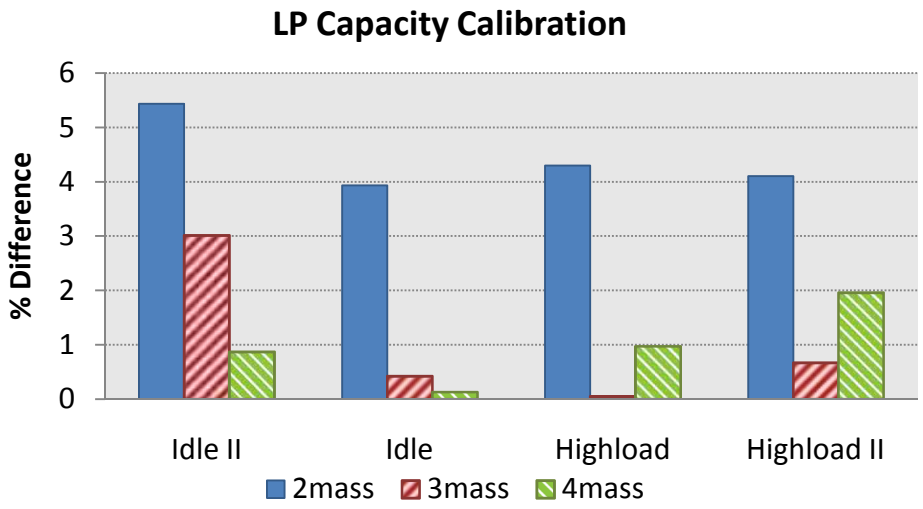

Figure 4-3: Low-side heat transfer, or capacity, calibration of the internal heat exchanger (IHX). These are the results of the component level simulations of the IHX to determine the appropriate degree of discretization for the model.

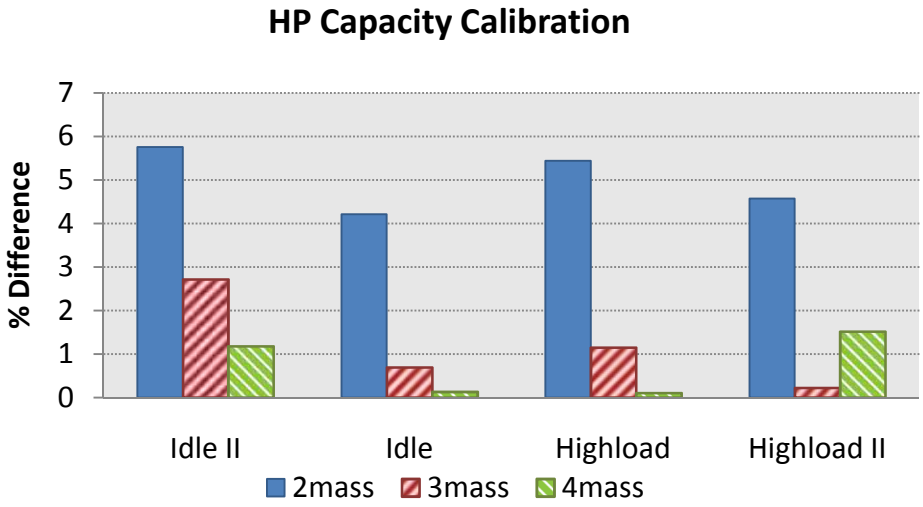

Figure 4-4: High-side heat transfer, or capacity, calibration of the internal heat exchanger (IHX). These are the results of the component level simulations of the IHX to determine the appropriate degree of discretization for the model.

The results from the calibration model show a trade-off between the predictive abilities of the IHX capacity and the LP pressure drop accuracy. As the accuracy of one increases, the other decreases. In Figure 4-1, the 4mass model results are not included since the

pressure drop error was very large compared to the 2mass and 3mass models. Also in Figure 4-1, the Low Load results for the 2mass and 3mass models are -78.5% and -85%, respectively and have been omitted in Figure 4-1 so to allow the results for the other four operating points to be plotted. The 2mass model predicts the low side pressure drop better than the 3mass and 4mass models, with the exception of the operating point High Load II.

From Figure 4-2, the 4mass model predicts the high side pressure drop better than the other two. As is the case for all of the calibration results, the Low Load has the highest error and has been omitted from Figure 4-2. The errors for the 2mass, 3mass and 4mass models for the Low Load operating point are -28.5%, -27.5% and -16%, respectively.

From the results in Figure 4-3 and Figure 4-4, the IHX model predicts the capacity with higher accuracy than the pressure drop results. The Low Load operating points are omitted due to the large errors compared to the other operating points. For Figure 4-3, the Low Load error for the 2mass, 3mass and 4mass models correspond to 5.81%, 7.91% and 10.00%, respectively. For Figure 4-4, the Low Load error for the 2mass, 3mass and 4mass models correspond to -3.57%, -5.71% and -7.86%, respectively. With the exception of the Low Load operating point, the 2mass model predicts the IHX capacity with the worst accuracy compared to the other two models, however it does predict the low-side pressure drop with smaller errors.

Another important factor to consider when deciding on the most appropriate model is the simulation time. The best model offers the lowest error between the simulation results and the experimental measurements with the smallest simulation time. There is often a trade-off between these two objectives , therefore it is up to the engineer to decide which is most important.

The simulation times for the 2mass, 3mass and 4mass models are shown in the list below:

- 2mass 3.336 seconds
- 3mass 2.863 seconds
- 4mass 3.703 seconds

The simulation times for the component level IHX are very small, however due to the complexity of the full AC model, any simplifications may lead to decreased simulation times. This is especially true for the evaporator model discussed in Appendix M. From the small discretization samples there is no direct relation with the simulation time.

Due to the importance of the LP pressure drop, the 2mass model was selected since it had the lowest error of the three models, with the exception of the Highload II operating point. This is the model that will be used in all of the upcoming analyses in the present thesis, both for the component and system level simulations.

4.2 Steady-State Simulations

Due to the lack of experimental data for steady-state AC performance, the results from Seybold et al, [13], 2012 were compared to the simulation results in the present thesis. The research paper is from the Society of Automotive Engineers (SAE) technical paper series. All figures from the SAE reference compare IHX and AC performance variables against either the mass flow rate or the compressor compression ratio. The investigations in this section determine if the AC model performs similar to the experimental results of the SAE reference. They will also display if the AMESim model responds to the IHX introduction similarly to the AC system in the SAE paper. The system response trend of the simulation as compared to the experimental data is the key focus point here. The SAE paper studies different types of IHX geometries, however the focus for the present thesis is only the coaxial IHX results, labelled by "*Coax*" in all of the SAE reference graphs. The authors of the SAE paper study the IHXa configuration. The thermal sensing bulb (TSB) of the TXV is located upstream of the IHX suction side. Refer back to Section 3.5 for further clarification.

In Section 5.4.1, all of the system level simulation are conducted with a 500mm length IHX. Despite the OEM IHX being 900mm, using the same IHX length as that of the SAE paper allows for a more meaningful comparison.

4.2.1 Internal Heat Exchanger (IHX) Capacity and Pressure drop

This sub-section will investigate performance related to the IHX from system level, steady-state simulations. The IHX capacity, pressure drops and Absolute Efficiency Ratio will be investigated and displayed similarly to the method used in the SAE paper. This means that the independent parameter is the refrigerant mass flow rate in units of kg/h.

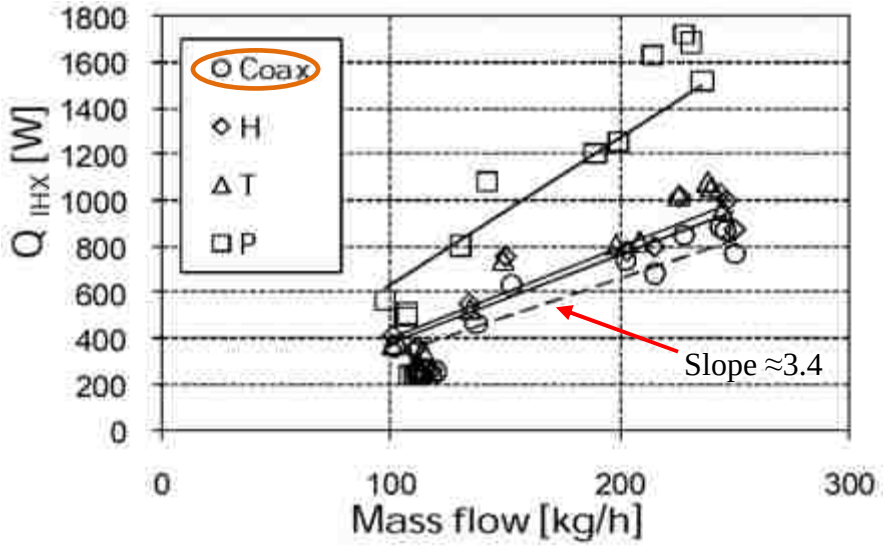

Figure 4-5: Experimental results for the steady-state internal heat exchanger (IHX) heat transfer (capacity) as a function of the refrigerant mass flow rate from the SAE paper. As the IHX capacity increases, the refrigerant enthalpy entering the evaporator decreases, which should lead to increased evaporator capacity. The dashed line and hollow circular points correspond to the double pipe co-axial IHX results copied from Seybold et al. [13].

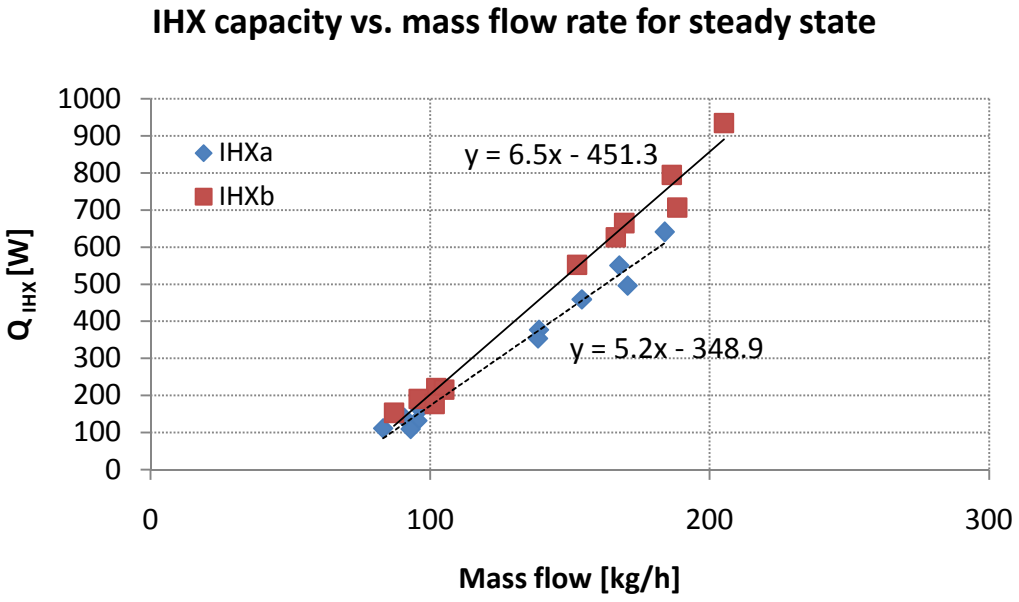

Figure 4-6: Simulation results for the steady-state internal heat exchanger (IHX) heat transfer (capacity) as a function of the refrigerant mass flow rate. A greater IHX capacity allows for a lower refrigerant enthalpy at the evaporator inlet, increasing the evaporator capacity. System level test results for IHX capacity vs. mass flow rate

Comparing the simulation results of Figure 4-6 to Figure 4-5, both show that the heat exchanged by the IHX is a direction linear function of the refrigerant mass flow rate. Figure 4-6 displays the linear relationship for the simulation results and the relationship for the experimental results is obtained from interpolation. The approximate interpolated points used to calculate the slope in Figure 4-5, taken from the co-axial line of best fit represented by the dashed line, are (120 kg/h, 400 W) and (180 kg/h, 600W). For the IHXa configuration, the model capacity is approximately 1.5 times greater than the experimental IHX from Seybold et al., at an equivalent refrigerant mass flow rate. The IHXb capacity is almost double the experimental IHX capacity.

The reason for the mass flow rate differences between the two AC systems is due to the differences between the variable compressors, the TXV settings and the fact that the simulations do not control the refrigerant outlet temperatures of the condenser and evaporator.

Both the IHXa and IHXb simulation performance results over perform compared to the SAE IHX results. However, relationship between the IHX capacity and the refrigerant mass flow rate are the same for the simulation and experimental results.

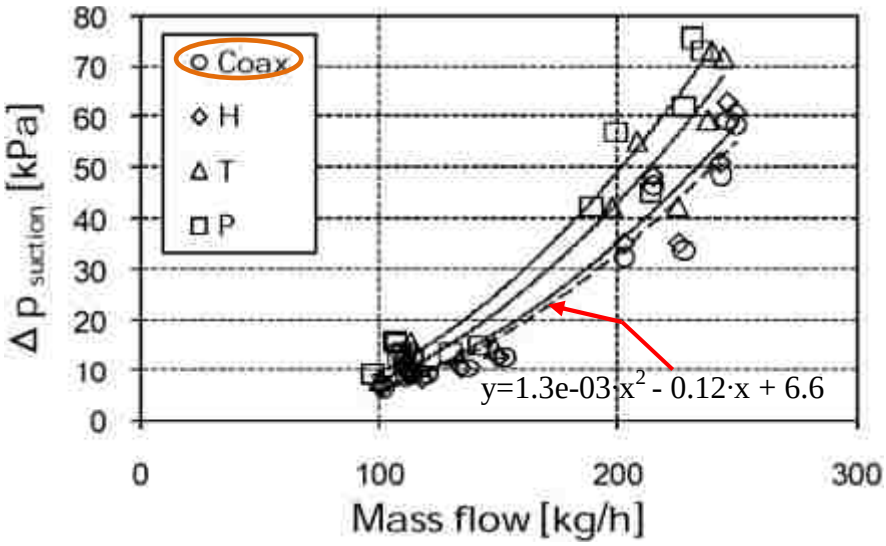

Figure 4-7: Experimental results for the steady-state suction side pressure drop as a function of the refrigerant mass flow rate from the SAE paper. The suction pressure drop accounts for the pressure drop from the evaporator inlet to the compressor inlet. The dashed line and hollow circular points correspond to the double pipe co-axial IHX results [13].

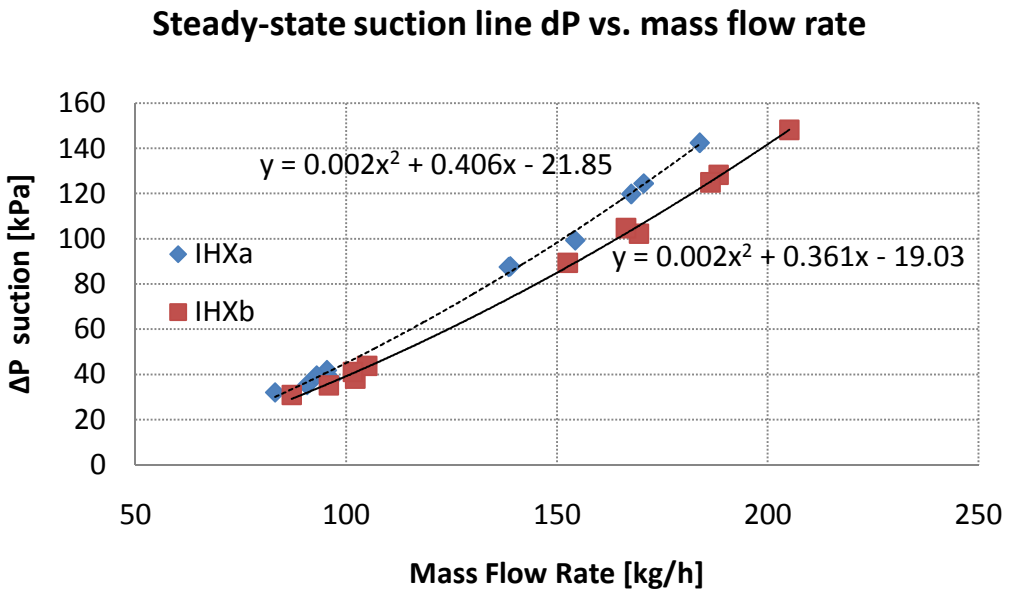

Figure 4-8: Simulation results for the steady-state suction side pressure drop as a function of the refrigerant mass flow rate from the SAE paper. The suction pressure drop accounts for the pressure drop from the evaporator inlet to the compressor inlet.

In Figure 4-7 and Figure 4-8 above, the pressure drop corresponds to the whole suction side pressure drop, from the TXV outlet to the compressor inlet. Comparing the simulation results from Figure 4-7 to Figure 4-8, there is a significant difference between the suction side pressure drops in the higher mass flow rate regions, where the simulation pressure drops are more than double the experimental values. The difference could be attributed to bends, extra piping present in the simulation AC system. The simulation represents an AC system in a Fiat Grande Punto, whereas the SAE paper uses an AC system designed to mimic an automotive setup. As such there may be crimped hoses, extra tubing, deposit build-up within the hoses for the vehicle testing conducted by Fiat that may not be present in the experimental setup from the SAE paper. The simulation high and low pressures are calibrated with the measurements from the transient CCD test, shown in Appendix K.

From Figure 4-7 there is a weak quadratic relationship between the refrigerant mass flow rate and the suction side pressure drop. An approximate equation for the line of best fit for the co-axial IHX is also included in Figure 4-7. This equation was obtained by

interpolating points along the existing line of best fit, the dashed line. The interpolated points are as follows: (120kg/h, 10kPa), (160kg/h, 20kPa), (200kg/h, 32kPa) and (240kg/h, 50kPa). Equation (2.1) supports these measurements, since there exists a direct exponential relationship between the pressure drop and fluid velocity.

The results in Figure 4-8 also displays a weak quadratic between the suction line pressure drop and the refrigerant mass flow rate. The coefficient value next to the squared variable determines the strength of the quadratic relationship. A very small value indicates that the relationship is linear more than it is quadratic in nature.

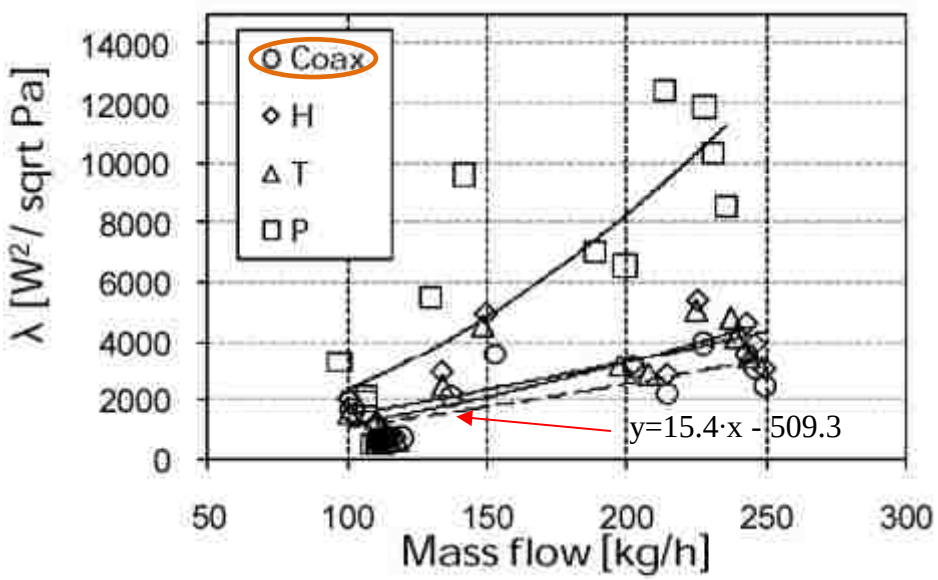

Figure 4-9: Experimental results for the steady-state system level Absolute Efficiency Ratio as a function of the refrigerant mass flow rate from the SAE paper. The Absolute Efficiency Ratio compares the internal heat exchanger (IHX) capacity to the increased suction-side pressure drop. The dashed line and hollow circular points correspond to the double pipe co-axial IHX results [13].

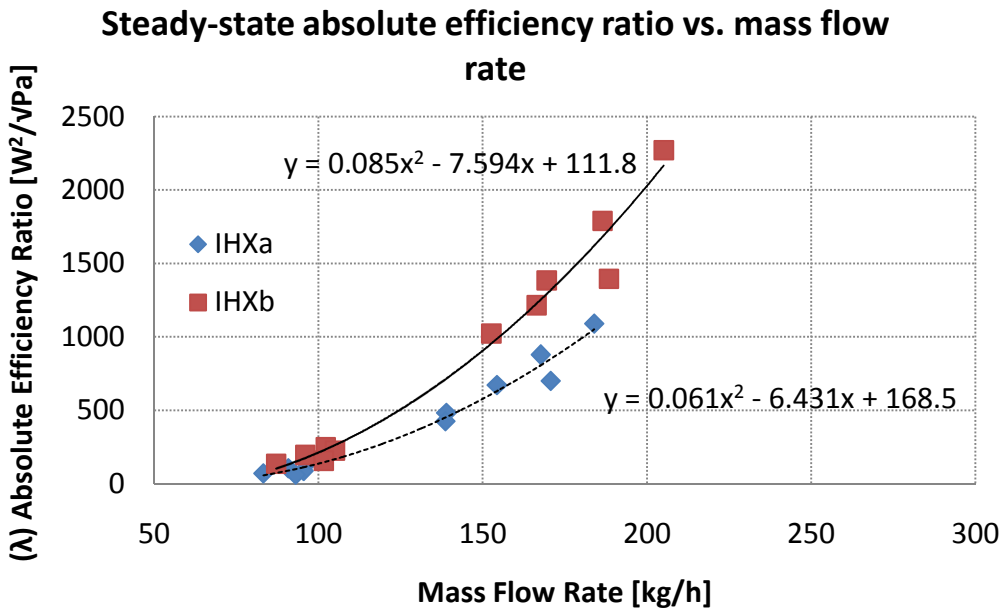

Figure 4-10: Simulation results for the steady-state system level Absolute Efficiency Ratio as a function of the refrigerant mass flow rate from the SAE paper. The Absolute Efficiency Ratio compares the internal heat exchanger (IHX) capacity to the increased suction side pressure drop.

The results for Figure 4-9 and Figure 4-10 present the system level Absolute Efficiency Ratio (A.E.R.), which utilizes the entire suction line pressure drop rather than just the pressure drop for the suction side of the IHX. The simulation A.E.R's are slightly smaller than the experimental measurements at equivalent mass flow rates. One significant difference between the simulation and experimental results is the relationship between the A.E.R. and the mass flow rate. The simulation result show a weak quadratic relation, whereas the interpolation of the co-axial results from Figure 4-9 resulted in a linear relation.

The IHXa Absolute Efficiency results are closer to the experimental results than the IHXb configuration. However, the absolute efficiency values are similar for smaller refrigerant mass flow rates than the experimental results. The simulation efficiencies are much higher due to the significant difference in the suction line pressure drop from Figure 4-7 and Figure 4-8. From the simulation results in Figure 4-10, the IHX is used much more efficiently in the IHXb configuration compared to the IHXa configuration,

however the ultimate goal of the work in the present thesis is to see if the overall AC power consumption can be reduced. Just because the IHX capacity is greater and more efficient does not necessarily result in reduced power consumption. This is shown by the compressor power consumption results for the steady-state tests in Figure 4-23 in Section 4.2.3, where IHXb is higher than IHXa even though the IHXb capacity and absolute efficiency ratio is greater than IHXa.

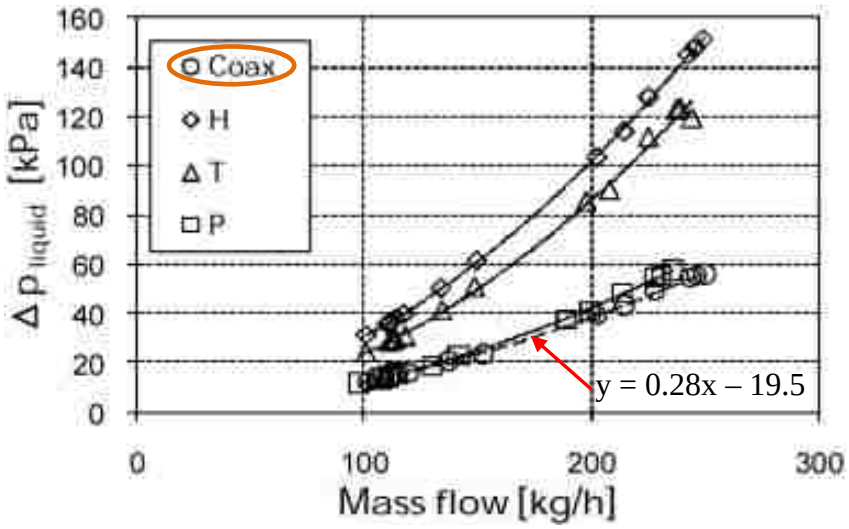

Figure 4-11: Experimental results for the steady-state liquid side pressure drop as a function of the refrigerant mass flow rate from the SAE paper. The liquid pressure drop accounts for the pressure drop from the compressor outlet to the TXV inlet. The dashed line and hollow circular points correspond to the double pipe co-axial IHX results for [13].

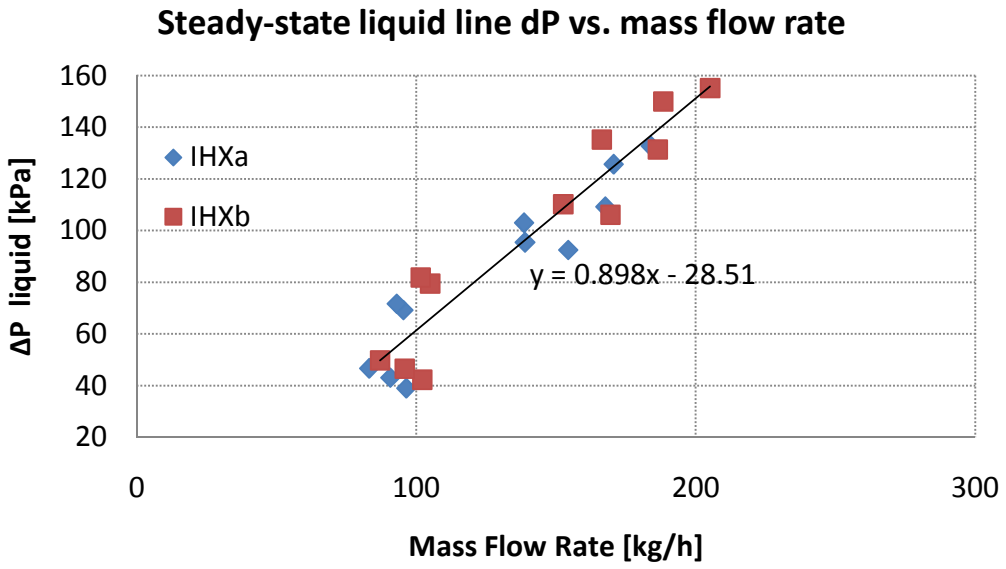

Figure 4-12: Simulation results for the steady-state liquid side pressure drop as a function of the refrigerant mass flow rate. The liquid pressure drop accounts for the pressure drop from the compressor outlet to the TXV inlet. The figure only includes one line of best fit since the IHXa and IHXb data points overlap.

Figure 4-11 and Figure 4-12 display the liquid side pressure drop from the SAE experiment and the simulation in the present thesis. The liquid side pressure drop of the simulations are more than double at equivalent mass flow rates compared to the SAE experimental results. Unlike the suction line pressure drop results from Figure 4-7, the two IHX configurations have very similar liquid line pressure drops. This result is expected because the compressibility of the liquid phase is very small compared to the gas phase. The line of best-fit slope is greater for Figure 4-12 than Figure 4-11, indicating that the increase of the liquid side pressure drop is greater for the AC model within AMESim.

Despite the experimental and simulation results both having a linear relationship with the mass flow rate, this result is unexpected based on the calculation for the pressure drop in Equation (2.1).

The differences can be attributed to differences in the liquid side plumbing configuration. The liquid side pressure is calibrated with the measurements from the transient CCD test.

The CCD test involves testing the AC system already installed in a vehicle, whereas the SAE experiment studies an AC system built specifically for the IHX performance study.

In summary, the introduction of an IHX into the AC system for the AMESim model responds similarly when compared to the experimental results from the SAE paper. The magnitudes of the changed responses are not completely similar, but the two AC systems use different components which are calibrated using different processes. The AC model performance was compared to the SAE paper results for a double pipe co-axial IHX.

For the IHX capacity there is a linear relationship with the mass flow rate for both AC systems. The line of best fit slope is greater for the simulation than the experimental system. For the suction side pressure drop there is a weak quadratic relationship with the mass flow rate for both AC systems. The suction side pressure drop of the simulation model is greater than the experimental results. For the system level A.E.R. there is a quadratic relationship with the mass flow rate for the simulation and a linear relationship with the experimental results. The results from the simulation seem more plausible based on the calculation for the system level A.E.R. in Equation (2.5). The system level A.E.R. is greater for the experimental results than the simulation. For the liquid side pressure drop there is a linear relationship with the mass flow rate for both AC systems. The simulation pressure drop is greater than the experimental results.

4.2.2 Compressor Efficiency and Compressor Discharge Temperature

This sub-section focuses on the response of the compressor from the introduction of the internal heat exchanger (IHX). Both the IHXa and IHXb configurations are displayed from the simulation results and compared to the double pipe co-axial IHX from the SAE paper by Seybold et al [13]. The TSB of the TXV is located upstream of the IHXa for IHXa and downstream for IHXb, refer back to Section 3.6.3 for a detailed description of the two configurations. Recall that the experimental measurements from the SAE paper all correspond to an AC system with an IHXa configuration. The relationship of the compressor volumetric efficiency and the coefficient of performance with the compression ratio are explored. The refrigerant discharge temperatures for all of the steady-state operating points included in the present thesis are compared to the experimental measurements.

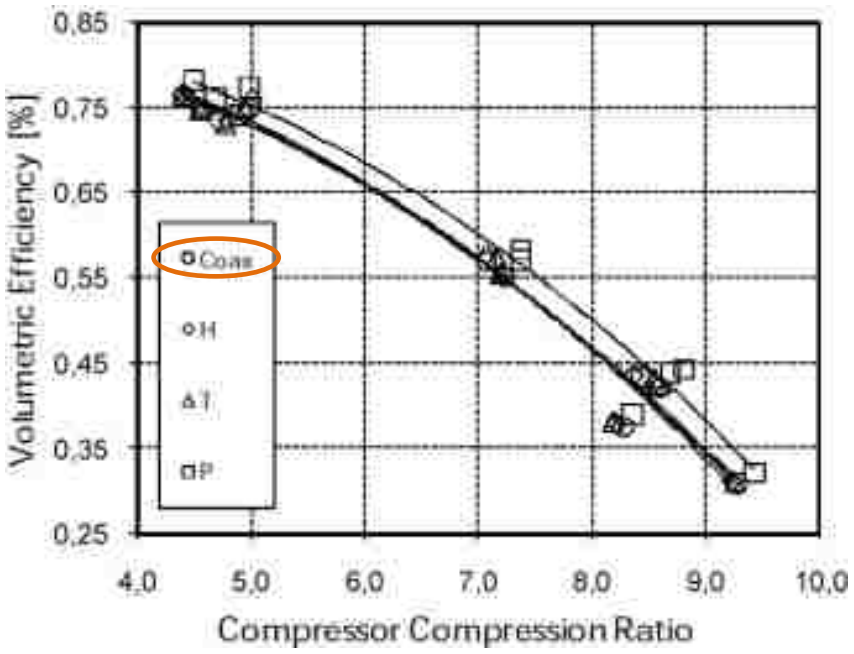

Figure 4-13: Experimental results for the steady-state compressor volumetric efficiency as a function of the compressor compression ratio from the SAE paper. The volumetric efficiency shows how effectively the compressor displaces refrigerant tot eh high pressure side of the AC system based on the pressure difference ratio of the high and low pressure sides. The co-axial heat exchanger line of best fit is the dark black line, since the correlation is very close to two other internal heat exchanger (IHX) geometries studied in [13].

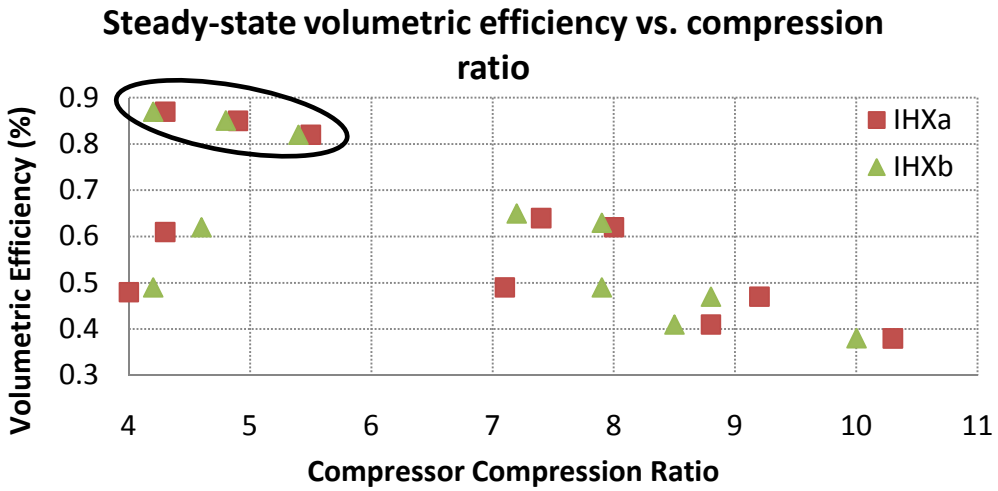

Figure 4-14: Experimental results for the steady-state compressor volumetric efficiency as a function of the compressor compression ratio. The TSB of the TXV is located upstream of the IHX for IHXa and downstream for IHXb. The two outlier points, just below the black circle are a result of the internal regulation compressor control of the user-specified pressure regulation curve in Figure 4-15. The simulation results are compared to the experimental ones from Figure 4-13.

Figure 4-13 and Figure 4-14 display the compressor volumetric efficiency vs. the compression ratio for all of the steady-state operating points. The results from the SAE paper show an inverse increasing relationship between the two variables. Lower volumetric efficiency coincides with higher compression ratios, which correspond to high load conditions of the AC system. The three points in the top left corner with low compression ratios and high volumetric efficiencies, in Figure 4-14, correspond to the operating points where the compressor speed is 900RPM. The volumetric efficiency is smallest for the highest compressor speeds. The two outliers correspond to the 25°C/80% RH/2500 RPM & 25°C/80% RH/4000 RPM operating points. Refer back to Table 3-4 in Section 3.6.2 which describes the naming convention for the steady-state operating points for the simulations in the present thesis. These two points correspond to low load conditions for the AC system due to the low ambient temperature. In these two cases the compression ratio is too low, and the internal regulation valve reduces the volumetric displacement in an effort to maintain a desirable suction pressure, since the compressor speed is too great for the required cooling load. This indicates that the AC system is oversized for similar operating points of low ambient temperature and high compressor speeds.

Figure 4-15 displays the steady-state compressor suction and discharge pressures against the user-specified pressure regulation curve for the variable control sub-model. This graphical representation of the internal compressor regulation valve shows why the two outlier points in Figure 4-14 and Figure 4-17 occur. The regulation valve changes the compressor volumetric displacement to stay within the user-specified pressure regulation curve requirements. The pressure regulation curve was previously discussed in Section 3.2.3 by Figure F-5. The user-specified pressure offset is not included in Figure 4-15 since the tolerance for this value is very small.

Points that lie above the curve signify maximum compressor displacement. The two operating points between the 11 and 13 barA range, lying on the pressure regulation curve, correspond to the two outlier points from Figure 4-14. These two points are circled in black in Figure 4-15 for the reader's convenience. In these two cases, the internal valve control decreases the compressor displacement to maintain the desired

suction to discharge pressure ratio. It is important to regulate the suction pressure to ensure that wet compression does not occur. If the suction pressure is too low, there is risk that some of the superheated refrigerant will condense. The negative effects of wet compression were previously discussed in Section 3.2.3.

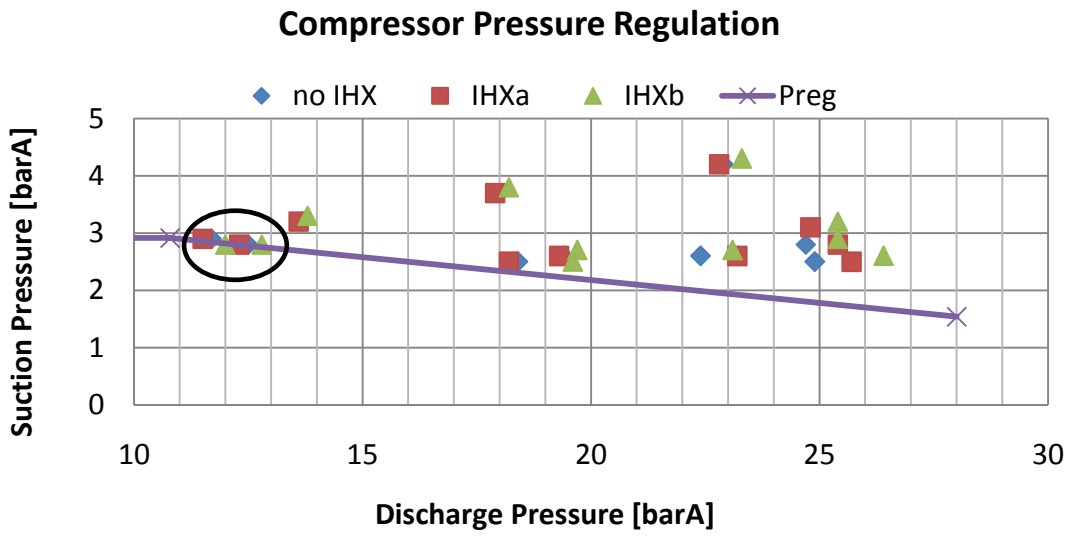

Figure 4-15: Pressure regulation curve with the compressor suction and discharge data points. The curve Preg corresponds to the user-specified pressure regulation curve. Points above the line correspond to maximum displacement and points on or below the line correspond to cases where the internal control sub-model modifies the displacement to regulate the suction pressure.

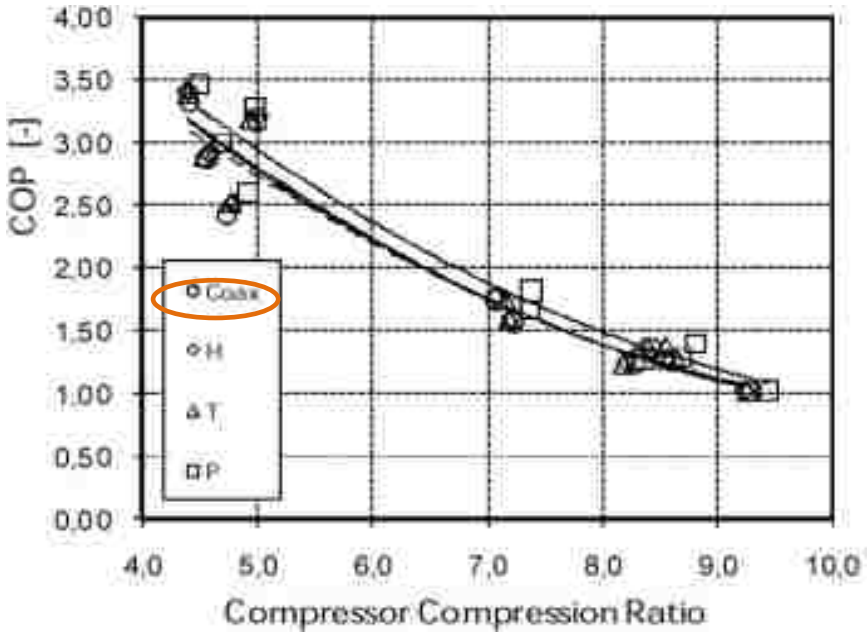

Figure 4-16: Experimental results for the coefficient of performance (COP) as a function of the compressor compression ratio from the SAE paper. The co-axial heat exchanger line of best fit is the dark black line, since the correlation is very close to two other internal heat exchanger (IHX) geometries studied in [13].

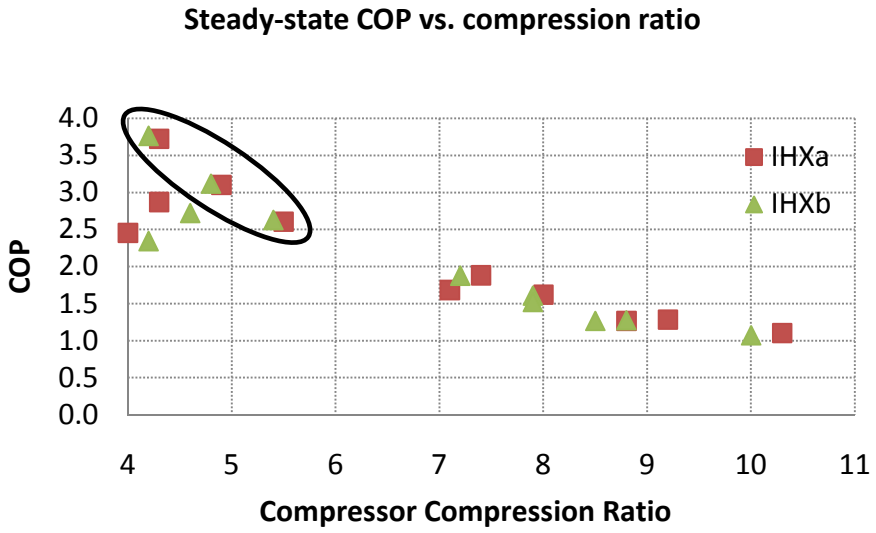

Figure 4-17: Simulation results for the steady-state coefficient of performance (COP) as a function of the compressor compression ratio from the SAE paper. The six points circled in black correspond to the operating points with a compressor speed of 900RPM. The two outlier points, just below the black circle are a result of the internal regulation compressor control of the user-specified pressure regulation curve in Figure 4-15. The simulation results are compared to the experimental ones from Figure 4-16.

Figure 4-16 and Figure 4-17 display the coefficient of performance (COP) vs. the compression ratio. Both figures show an inverse decreasing relationship between the two variables. Similar to the results from Figure 4-14, the operating points with a 900RPM compressor speed are represented by the three points circled in black. They have the lowest compression ratio and highest COP, when the compressor is operating at maximum displacement. Similar to Figure 4-14, the two outlier points correspond to 25°C/80% RH/2500 RPM & 25°C/80% RH/4000 RPM conditions, which are located just below the black circle in the top left corner of Figure 4-17. These are two low loading conditions for the AC system with high compressor speeds. For a mechanically connected compressor, its speed is directly proportional to the engine speed. For steady-state operation, higher engine speed corresponds to higher vehicle speed. In this condition, the air mass flow rate passing through the evaporator is much greater, so there is a greater capacity for the refrigerant flowing through the evaporator to absorb heat from the passing air. Therefore, the compressor must decrease the volumetric displacement per stroke and maintain suction and discharger pressures according to the user-specified pressure regulation curve.

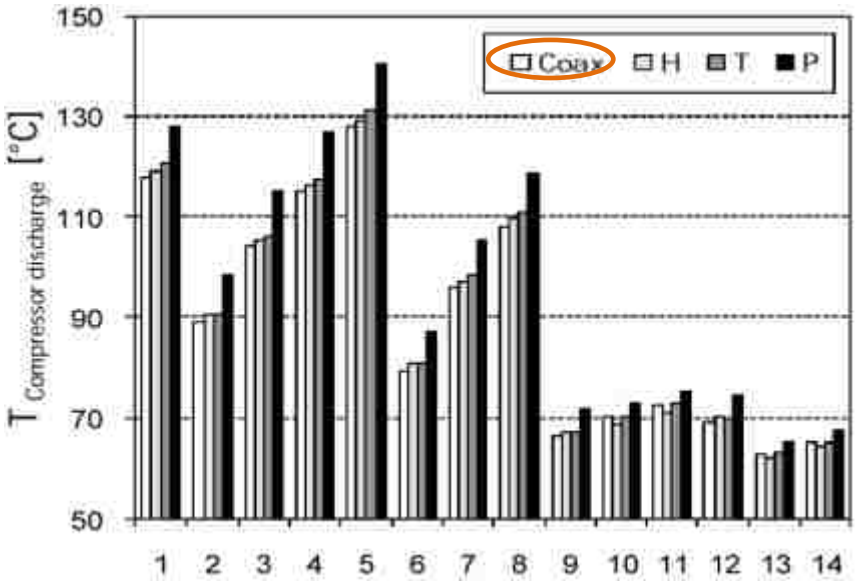

Figure 4-18: Experimental results for the compressor discharge temperature of the steady-state operating points from the SAE paper. High compressor discharge temperatures can cause damage and decrease the life-span of the compressor. The co-axial internal heat exchanger (IHX) results are the first column of each operating point [13].

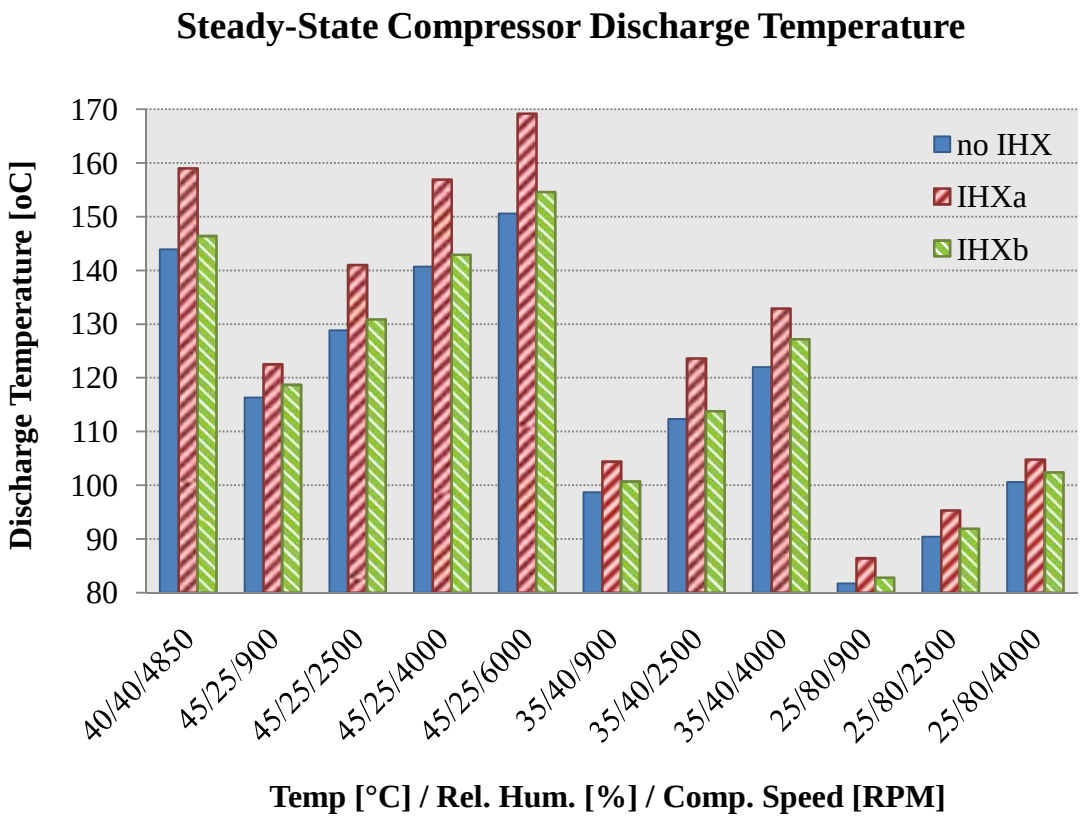

Figure 4-19: System level tests for compressor discharge temperature. The horizontal axis label correspond to the conditions specified in Table 3-4 from Section 3.6.2. As an example, the first operating point corresponds to a temperature of 40°C, a relative humidity of 40% and a compressor speed of 4850 RPM.

Note that the operating points 12-14 in Figure 4-18 were not included in the simulations. Therefore, the results from Figure 4-19 correspond only to the first 11 operating points in Figure 4-18.

The discharge temperatures from the simulation results are significantly higher than the experimental measurements from the SAE paper. For the IHXb configuration, all of the temperatures are 25°C or more than the experimental measurements, and an even larger difference is present with the IHXa configuration. The difference can be attributed to the comparison of the IHX capacities for the experimental results in Figure 4-5 and the simulation results in Figure 4-6. The IHX for the AC model in AMESim transfers more heat than the IHX from the SAE paper, which corresponds to higher refrigerant

temperature at the suction and discharge sides of the compressor. The difference can also be attributed to the differing components between the two AC systems.

The IHXb compressor discharge temperature is lower than IHXa due to the location of the thermal sensing bulb (TSB). The TSB senses the increased superheat of the refrigerant exiting the suction side of the IHX, therefore there should be little difference between the discharge temperatures of an AC system without an IHX compared to IHXb. This is explored in further detail in the next sub-section by Figure 4-25, which compares IHXa and IHXb to an AC system without an IHX.

In summary, the AC compressor model response to the IHX introduction is similar to the experimental results. There is an inverse increasing relationship for the volumetric efficiency and an inverse decreasing relationship for the COP as a function of the compression ratio for both of the AC systems. For the SAE experimental AC system and the IHXa configuration there is a significant difference in the compressor discharge temperatures. The AMESim model predict a discharge temperature that is approximately 20^{o}C than the SAE paper.

4.2.3 IHXa vs. IHXb—System Performance Comparison

The section above compares AC performance to the results obtained from an SAE paper. This comparison method determined, in absence of experimental data, if the AMESim model displayed similar results for steady-state operation, and responded appropriately to the IHX introduction. No experimental data for AC system bench tests with and without an IHX was available from Fiat, and a comparison method was required to make sure that the results were within reasonable ranges and followed trends to similar AC systems. Remember that Section 3.6.3 explains the difference between the two suction line configurations, IHXa and IHXb.

The results from this sub-section will compare strictly the results from the simulations in the present thesis. The comparison uses an AC system without an IHX as the baseline to compare the IHXa and IHXb configuration. The simulations compare the results from the steady-state operating points. All results below will be compared to the baseline AC

system without an IHX and will correspond to the 11 operating points outlined by Table 3-4 in Section 3.6.2. The comparisons included in this sub-section are as follows:

- Heat transferred by the IHX
- Suction line pressure drop
- Compressor power
- Evaporator capacity
- Coefficient of Performance (COP)
- Compressor discharge temperature
- Absolute efficiency ratio

The performance of the two configurations in this section are compared to a baseline AC system without an IHX. Calculating the percent difference from the AC system without an IHX creates a normalized comparison, which the difference between the two configurations more clearly than presenting only the absolute performance values. The percent difference calculation, previously shown by Equation (3.4) from Section 3.6.4 is displayed below for the reader's convenience.

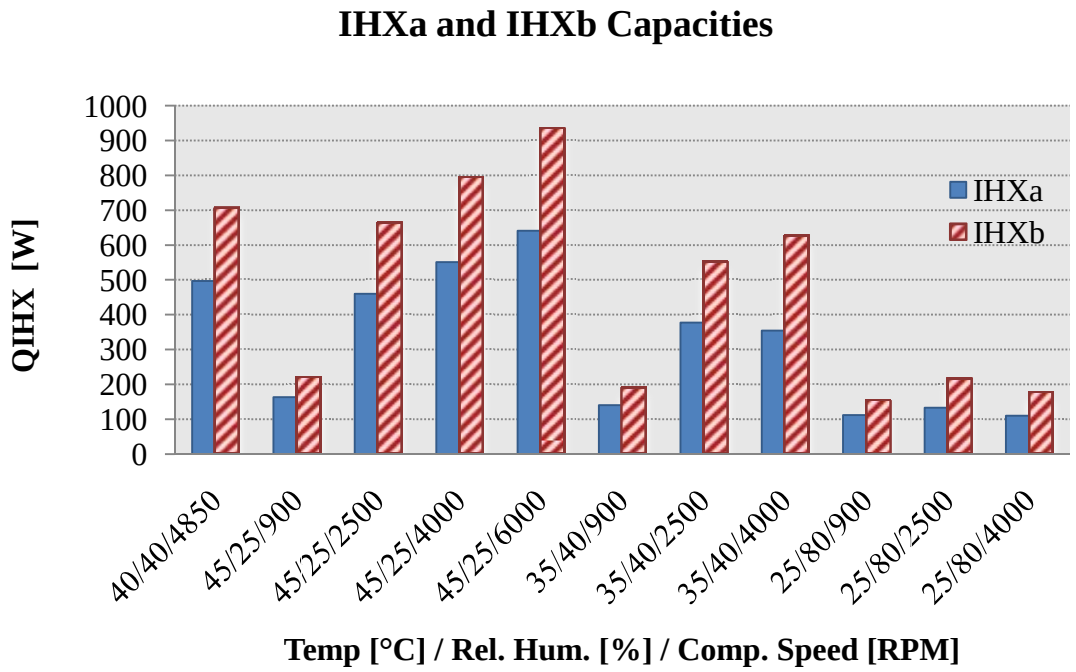

Figure 4-20: IHX capacity for the different steady-state operating points from Table 3-4. The IHXb configuration yields a much higher capacity than IHXa.

From Figure 4-20, the IHXb configuration transfers more heat to the suction side compared to IHXa. This is the case because with the IHXb configuration, the thermal sensing bulb (TSB) location is downstream of the suction side of the IHX. Thus, the TXV treats the heat exchanged by the IHX as an extension of the evaporator performance. Therefore, for the IHXb configuration, the refrigerant may leave the evaporator in a saturated state, allowing for a greater capacity to absorb heat from the liquid side. The energy required for a substance to change its state is much greater than the energy required to increase the temperature of the substance in a single phase state. Other results in this sub-section will provide other arguments for the IHX capacity differences between the two configurations. Variables such as the mass flow rate through the suction side and the temperature gradient between the refrigerant and the ambient air also affect the ability of the suction side to absorb heat from the liquid side. These variables and their influence on the evaporator are explored in further detail in Section 4.2.6.

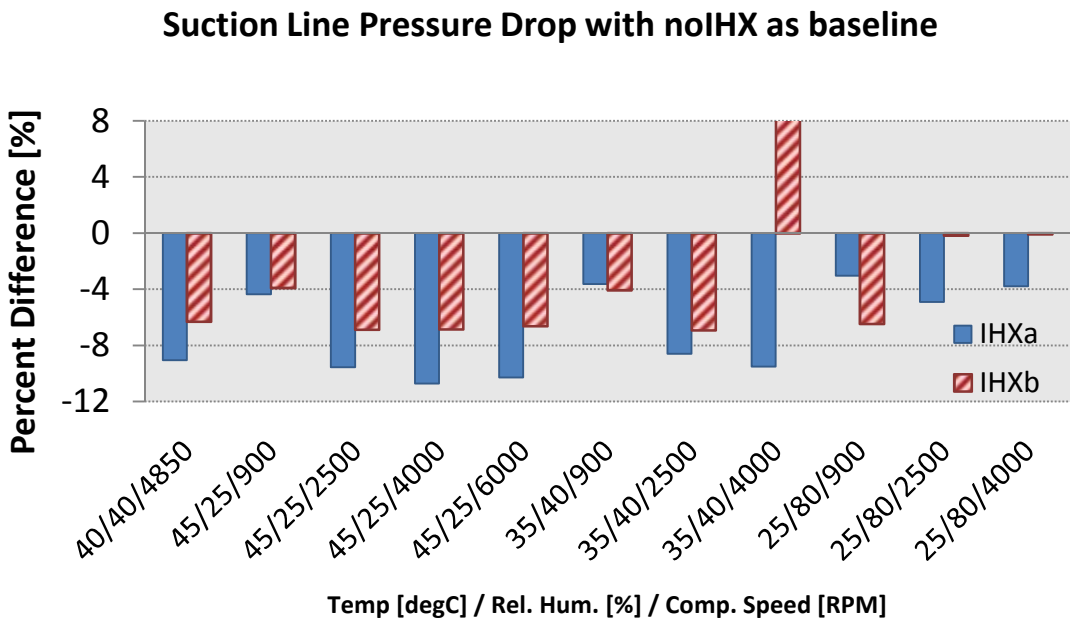

Figure 4-21: Suction line pressure difference compared to baseline AC system without an IHX for the different steady-state operating points from Table 3-4. The percent difference is calculated according to Equation (3.4).

From the results in Figure 4-21, the IHXb configuration results in higher suction line pressure drops compared to IHXa. The TSB temperature for IHXb is greater since it includes the combined heat transfer of the evaporator and the IHX. The increased refrigerant superheat exerts a greater pressure on the TSB, which increases the force acting on the ball valve, increasing the valve lift. This increases the cross-sectional area and refrigerant mass flow rate through the TXV ball valve. The increased mass flow rate results in a greater pressure drop in the suction line of IHXb as compared to IHXa. Recall that the TXV operation was previously discussed in Section 3.2.6 which includes a diagram in Figure F-12. From Equation (2.1), the pressure drop is directly proportional to the square of the fluid velocity. Higher refrigerant velocity coincides with higher mass flow rate.

Another explanation for the pressure drop difference is the differences in densities of the refrigerant for both configurations. Figure N-2 and Figure 4-8, previously shown, display the pressure drop in the suction line of the IHX and the entire suction side, respectively. By comparing the magnitudes of the pressure drop values from these two figures, the majority of the suction side pressure drop occurs in the evaporator rather than the IHX. The temperature of the refrigerant exiting the evaporator is lower for IHXb than IHXa, meaning that the density of the refrigerant for IHXb is greater than IHXa. Recall from Equation (2.1) that a direct linear relationship exists between the pressure drop of a fluid along a pipe and the fluid's density. Therefore, the higher density of the refrigerant in IHXb, due to the lower temperature of the refrigerant exiting the evaporator, will lead to a greater pressure drop through the evaporator. This is another explanation for the larger suction side pressure drop of IHXb compared to IHXa.

As an aside note, do not confuse this concept with the temperature difference sensed by the TSB. At this location, the refrigerant superheat of IHXa is lower than IHXb, since the refrigerant has already passed through the IHX in the latter case. So, the refrigerant temperature for the IHXb configuration is lower at the evaporator outlet and higher at the TSB compared to IHXa. An explanation of the temperature differences for the two IHX configurations is located after Figure 4-22, below.

The increased pressure drop in the IHXb configuration could potentially lead to greater compressor power consumption, since the compressor has to work harder to compress the refrigerant to the required discharge value. The power consumption for the two configurations is explored in Figure 4-23.

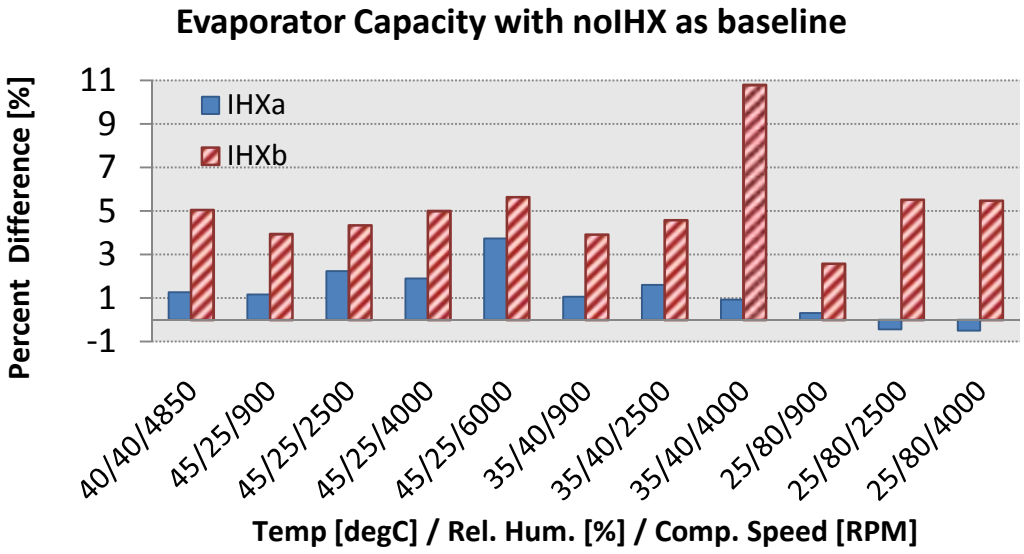

Figure 4-22: Evaporator capacity difference compared to baseline AC system without an IHX for the different steady-state operating points from Table 3-4. The percent difference is calculated according to Equation (3.4).

The steady-state tests in this sub-section do not control the condensing and evaporating temperatures of the refrigerant. This allows the evaporator capacity to vary over the different operating points. This is an effective way to highlight how the evaporator capacity responds to the introduction of an IHX. Figure 4-22 displays the percent difference between the two IHX configurations and an AC system without an IHX. IHXb yields higher evaporator capacity than IHXa.

The reason for the evaporator capacity difference between the two configurations is again attributed to the TXV operation. Previously established, the IHXb configuration has higher refrigerant mass flow rates on the suction side, due to the larger TXV ball valve lift. The higher refrigerant mass flow rate will lead to overall increased evaporator capacity, however a discrete quantity of refrigerant mass absorbs less heat since it spends less time in contact with the structural tubing.

Another benefit of the higher refrigerant mass flow rate is that the temperature of the refrigerant exiting the evaporator in the IHXb configuration will be lower than IHXa. This means the heat transfer process is more efficient due to the larger temperature difference between the refrigerant and the ambient air being cooled.

From Figure 97, the refrigerant superheat exiting the evaporator is much higher for IHXa than IHXb due to the TSB location. In the cases where the refrigerant exits the evaporator in a two-phase state, liquid and gas mixture, the quality of the refrigerant is higher for IHXa than IHXb. The amount of energy absorbed or released during a phase change process is much greater than the energy required to increase or decrease the temperature of that substance in a single-phase state. Since the refrigerant passing through the evaporator remains in a saturated-mixture state for IHXb more than IHXa, this is the reason for the evaporator capacity difference between the two configurations. Recall that the quality, or vapour mass fraction, is the ratio of the mass of vapour to the total mass of the refrigerant, previously discussed in Section 2.2.

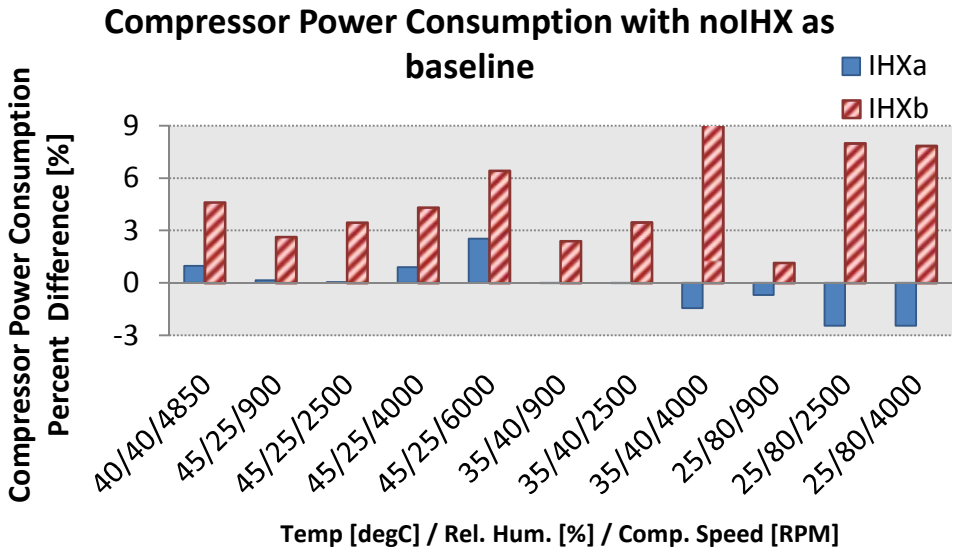

Figure 4-23: Compressor power consumption compared to baseline AC system without an IHX. For the operating point 35/40/4000 the compressor power difference for IHXb is 19.2. The ordinate axis is cut-off at 9% to show the differences between the two configurations for the other operating points more clearly. The percent difference is calculated according to Equation (3.4).

The compressor accounts for a significant portion of the total power consumption of an AC system. The results from Figure 4-23 display the compressor power consumption compared to an AC system without an IHX. For all of the steady-state operating points, the IHXb configuration increases the compressor power consumption. The IHXa configuration increases the power consumption slightly for the high load conditions, high ambient temperature combination, but decreases the power consumption slightly for low load conditions, low ambient temperature operation condition.

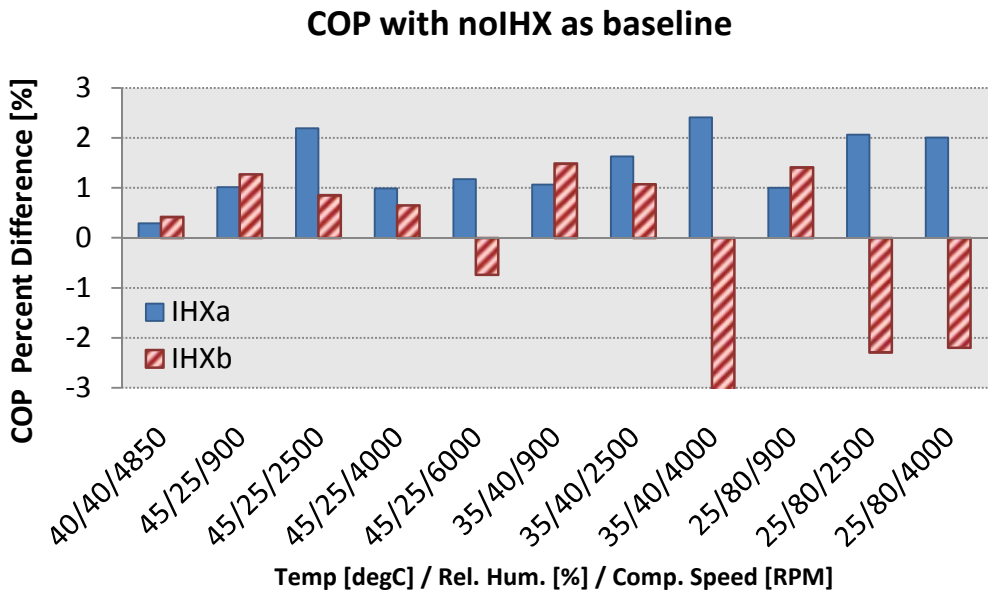

Figure 4-24: COP compared to baseline AC system without an IHX for the different steady-state operating points from Table 3-4. The COP percent difference for the operating point 35/40/4000 is -7%. The ordinate axis is cut-off at -3% to show the differences between the two configurations for the other operating points more clearly. The percent difference is calculated according to Equation (3.4).

Figure 4-24 displays the change of the coefficient of performance (COP) compared to an AC system without an IHX. The IHXa configuration yields increased COP for all of the operating points. The IHXb configuration for the majority of the operating points increases the COP, but there is a decrease for some of the higher compressor speeds. The improvement in the COP from introducing the IHX is less than 3%, when the evaporator capacity is allowed to vary.

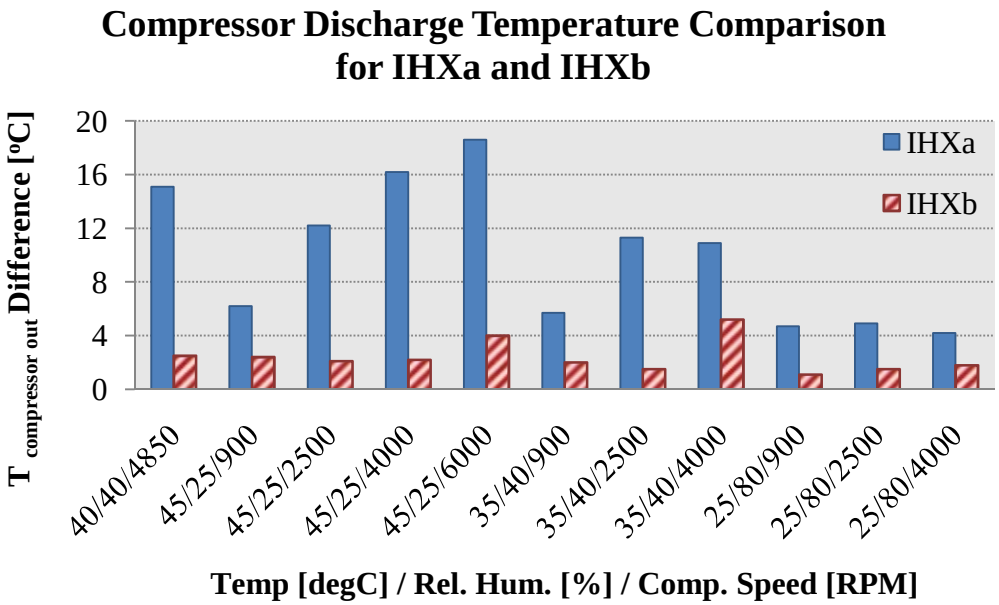

Figure 4-25: Compressor discharge temperature compared to baseline AC system without an IHX for the steady-state operating conditions from Table 3-4. The percent difference is calculated according to Equation (3.4).

The results for Figure 4-25 serve to supplement the compressor discharge temperature results previously shown in Figure 4-19. This figure displays the change in the compressor discharge temperature due to the introduction of the IHX rather than the absolute discharge temperature values. Similar to the results from Figure 4-19, the IHXa configuration significantly increases the discharge temperatures, especially for high load conditions. Due to the placement of the TSB downstream of the IHX in the IHXb configuration, the compressor discharge temperatures increase only slightly compared to the AC system without an IHX.

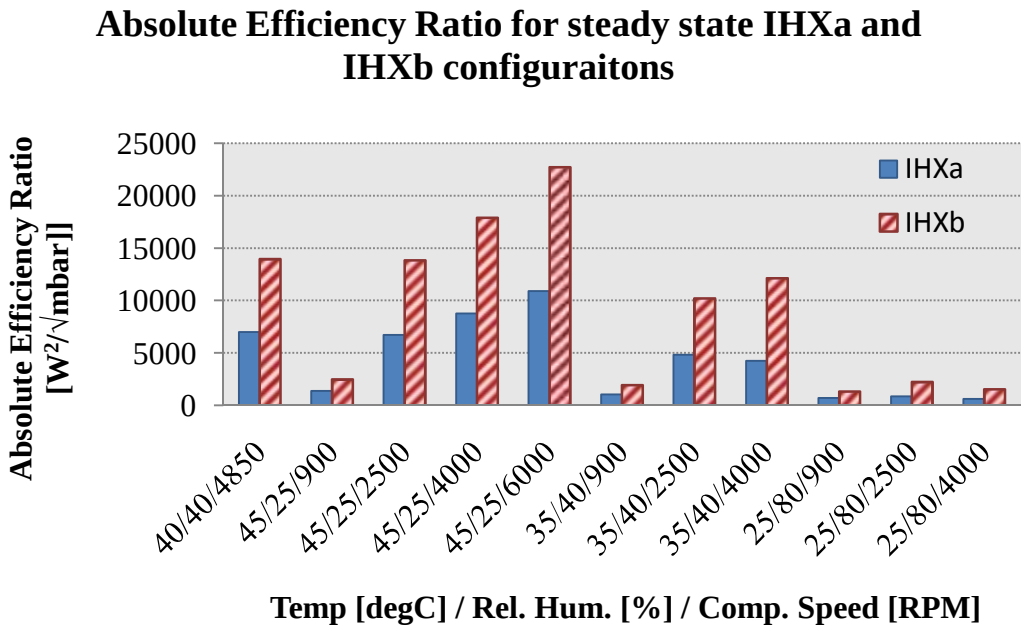

Figure 4-26: Absolute efficiency ratio for IHXa and IHXb using the complete suction line pressure drop. The testing conditions correspond to the steady-state operating conditions from Table 3-4. The percent difference is calculated according to Equation (3.4).

Figure 4-26 supplements the results previously shown in Figure 4-10. Instead of showing the absolute efficiency ratio as a function of the mass flow rate, it is shown as a function of the different operating points. From Figure 4-26 the IHX has a higher A.E.R. in the IHXb configuration.

The IHXb configuration improves the evaporator and IHX capacity much more than the IHXa configuration. Also with the IHXb configuration the compressor discharge temperatures are similar to an AC system without an IHX therefore there is no need to worry about possible compressor damage from this configuration. The benefits of increased capacity to the drawbacks of high suction side pressure drops are greater for the IHXb configuration as well.

However, based on the goals of the present thesis, the IHXa configuration yields lower compressor power consumption and increased COP over an AC system without an IHX. The main goal of the present thesis is to investigate the extent to which an IHX may reduce the overall AC power consumption for both steady-state and transient test cycles.

Towards this end, the IHXa configuration performs better than the IHXb configuration. The next sub-section investigates the ambient air influence for the IHXa configuration only.

4.2.4 Evaporator Capacity Response

This section will discuss the changes in evaporator performance due to the introduction of the IHX. This information included in this section provides supplemental data for the explanations given in Section 4.2.3, for the AC performance of the two IHX configuration. The graphs displayed in this sub-section include information for IHXa, IHXb and/or noIHX. The refrigerant superheat exiting the evaporator will shown for the cases IHXa, IHXb and noIHX. The effect of the suction line plumbing on the refrigerant mass flow rate and ball valve opening of the TXV will be explored as well. Finally, the point where heat transfer with superheated refrigerant within the evaporator is explored to show why it is necessary to tune the AC system after introducing the IHX. As with the other steady-state investigations, the IHX length is 500mm.

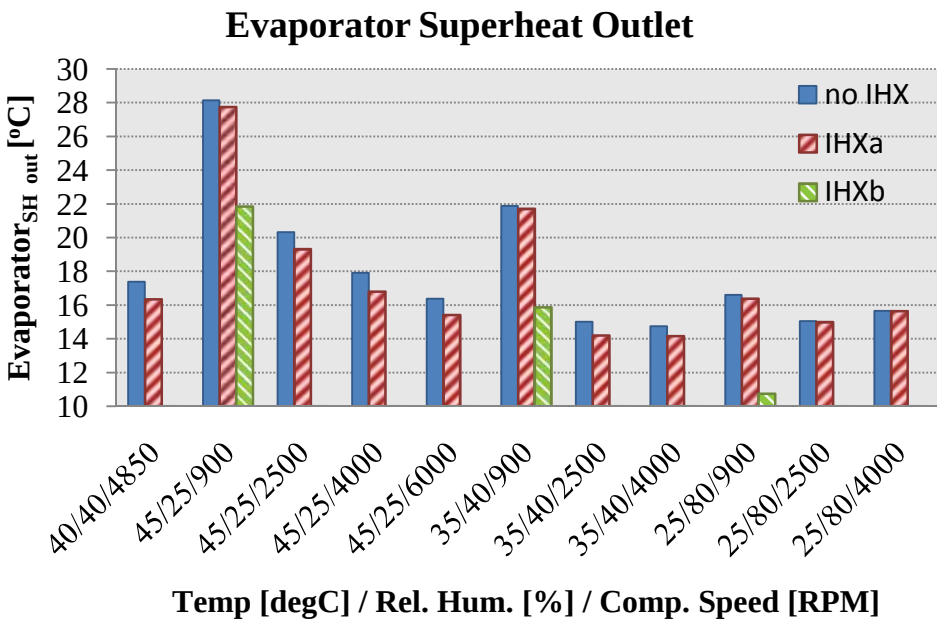

Figure 4-27: Refrigerant superheat exiting the evaporator for AC system without an IHX, IHXa and IHXb. The cases where no value appears for IHXb indicates that the refrigerant leaves the evaporator as a saturated mixture rather than a superheated vapour. This is desirable since it maximizes evaporator capacity and the refrigerant will be superheated as it passes through the IHX before entering the compressor.

The results from Figure 4-27 above is included to show how the suction line plumbing configurations greatly affect the refrigerant superheat exiting the evaporators. The results from the cases noIHX and IHXa yield very similar refrigerant superheat values. Since the TXV does not "see" the superheat increase in the suction line of the IHX this response from the simulations is expected. For IHXb there is a significant difference in the exiting refrigerant superheat. In this case, the TXV treats the evaporator and IHX as a single evaporator. Many of the operating points have zero (0) superheat for IHXb, indicating that the refrigerant leaves the evaporator as a saturated mixture. Compressor speeds of 900RPM are the only three operating points where the refrigerant leaves the evaporator superheated. This is because the refrigerant has a longer time period to absorb heat from the ambient air since the mass flow rate is lowest for this operating point.

Figure 4-28 displays the refrigerant mass flow rates for the steady-state operating points. The IHXa mass flow rates decrease from the AC system with no IHX because of the TXV ball valve lift decreasing. This occurs due to the lower superheat values shown previously in Figure 4-27 and consequently from lower TSB temperatures. The mass flow rate of IHXb increases from the base AC system because the refrigerant temperature entering the TSB is higher. Again, because in IHXb the evaporator and IHX are treated as a single, fictitious evaporator by the TXV. The results from Figure 4-29 support this statement. Due to the increased capacity of the fictitious evaporator, the TXV operation differs from IHXa and noIHX. This will be explored in Figure 4-29 and Figure N-6.

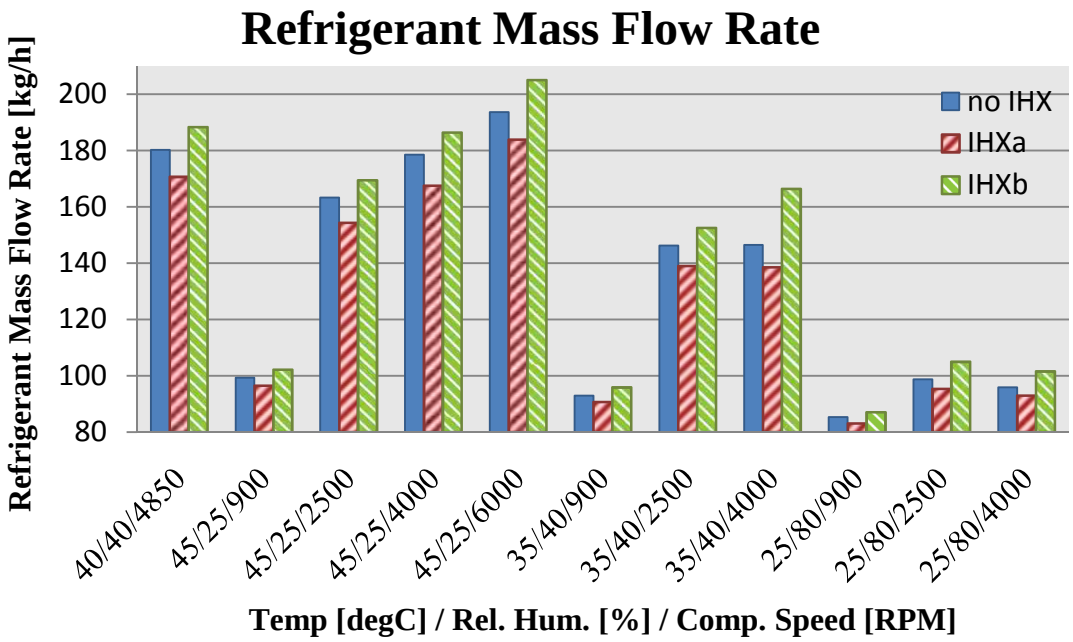

Figure 4-28: Refrigerant mass flow rate for steady-state operating points previously shown in Table 3-4.

Figure N-6 compares the ball valve lift percentages of the TXV IHXa and IHXb. The larger valve lift percentage explains why the evaporator capacity increase for IHXb is much larger than IHXa. The higher refrigerant superheat temperature for IHXb causes the force exerted on the lift rod by the TSB to increase. This increases the cross sectional area the refrigerant flows through, thereby increasing the mass flow rate. The increased mass flow rate allows for increased evaporator capacity.

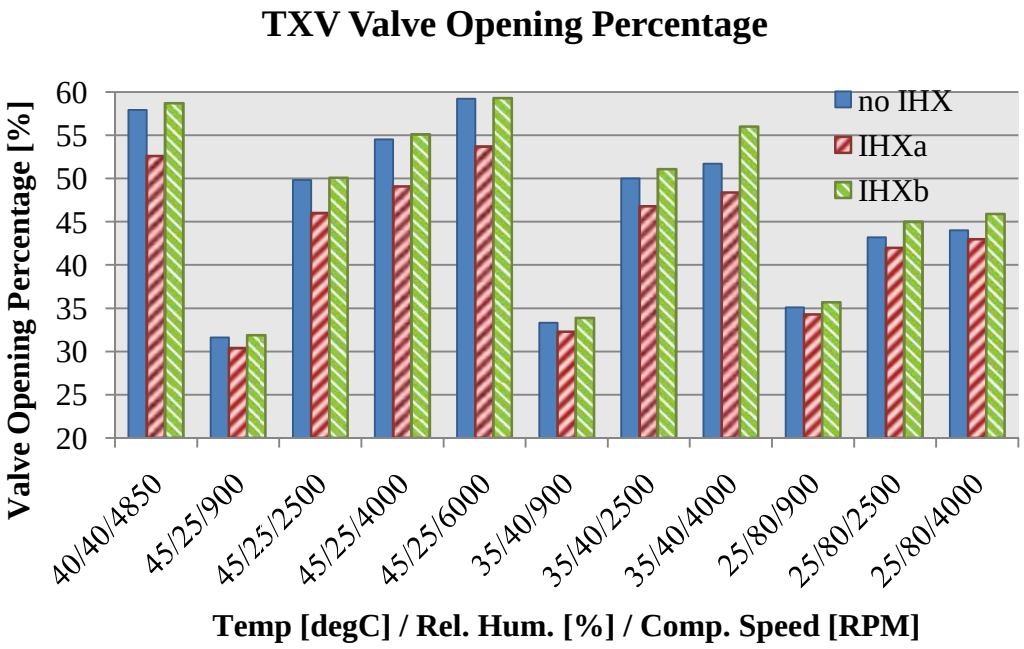

Figure 4-29: TXV opening percentage for the no IHX, IHXa and IHXb configurations. This information serves to validate the simulation results previously shown in Figure 4-27 and Figure 4-28.

Figure 4-30, Figure 4-31 and Figure 4-32 below display the evolution of the refrigerant gas mass fraction as it passes through the evaporator. The information in these figures serves to compliment Figure 4-27, Figure 4-28 and Figure 4-29 previously shown in this sub-section. Only three of the eleven operating points for the steady simulations are compared, which include: 45°C/25% RH/4000RPM, 25°C/25% RH/4000RPM, and 35°C/25% RH/4000RPM. Recall that the definition of the refrigerant quality, Equation (2.12) from Section 2.2, which corresponds to the refrigerant gas mass fraction. Therefore, the former term will be used as opposed to the latter.

There are a couple of observations that can be taken from these three figures below. First, as the ambient temperature increases, the amount of flash gas entering the evaporator increases. The sudden drop in pressure significantly decreases the saturation temperature and allows for rapid expansion of the refrigerant. Flash gas refers to the amount of refrigerant that is vaporized after it passes through the TXV. It is important to reduce the amount of flash gas since it significantly diminishes the evaporator capacity.

Second, the AC system without an IHX has the highest refrigerant quality throughout all of the refrigerant passes, with the exception of the fourth pass. This effect increases with increasing ambient temperature. This finding is supportive with Figure 4-22 in Section 4.2.3, which displayed the percent difference of the evaporator capacity of IHXa and IHXb compared to an AC system without an IHX. The only two cases that resulted in a decrease in evaporator capacity were for the operating points 25°C/80%/2500RPM and 25°C/80%/4000RPM for IHXa. From Figure 4-32, the refrigerant quality for IHXa is very similar to noIHX and is slightly higher for the third pass. These figures also display why the refrigerant exiting the evaporator has a much higher superheat value for noIHX and IHXa compared to IHXb. The refrigerant exiting the evaporator in IHXb is either slightly superheated or a saturated mixture. This also indicates why the IHX capacity, from Figure 4-20, is larger for IHXb than IHXa. The temperature difference of the suction line refrigerant and liquid line refrigerant is greater for IHXb than IHXa.

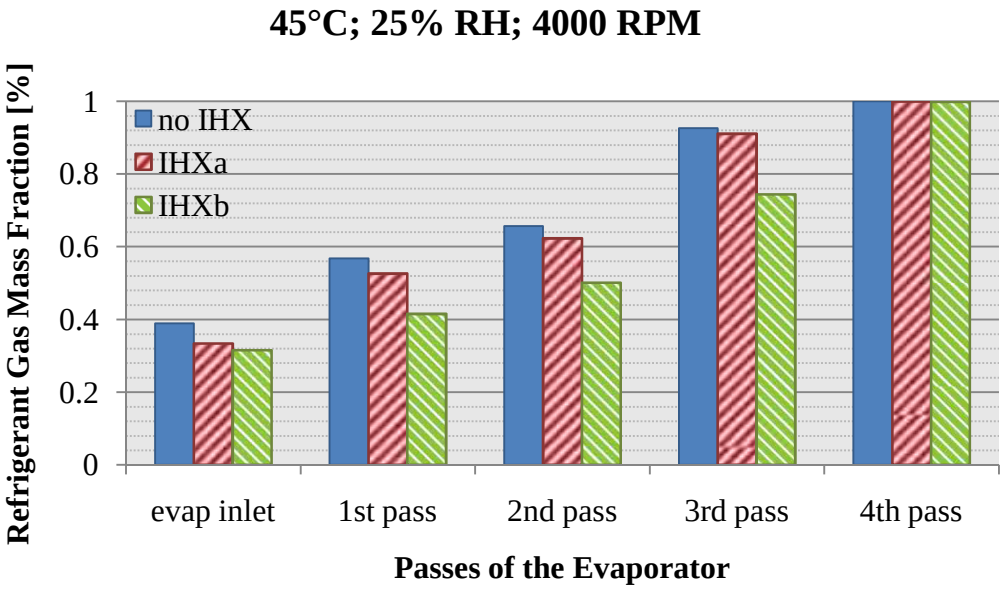

Figure 4-30: Refrigerant quality for the different passes of the evaporator. The evaporator is operating during steady-state where the boundary conditions imposed on the AC system are 45°C, 25% RH and 4000 RPM.

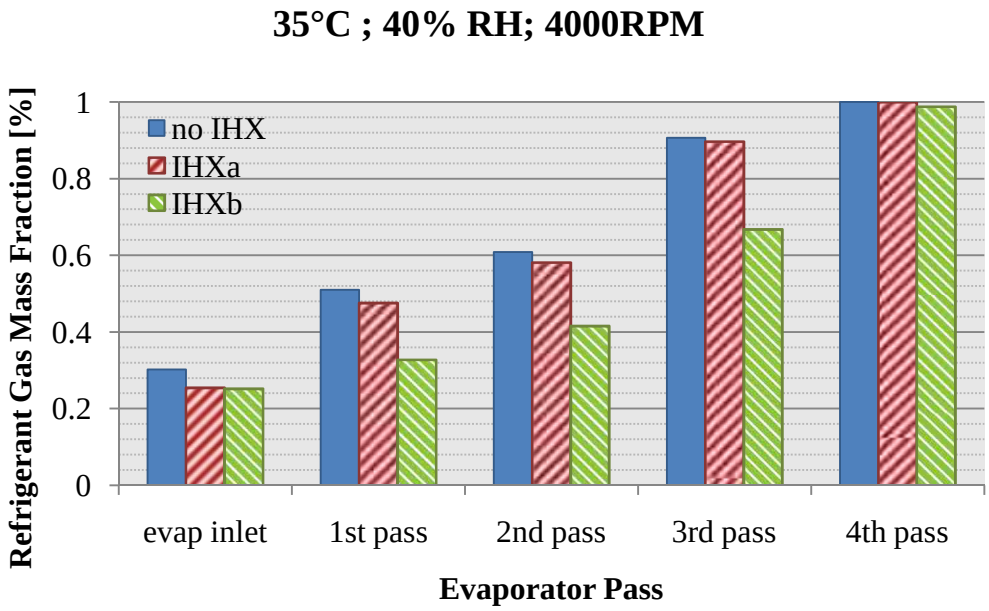

Figure 4-31: **Refrigerant quality for the different passes of the evaporator. The evaporator is operating during steady-state where the boundary conditions imposed on the AC system are 35°C, 40% RH and 4000 RPM.**

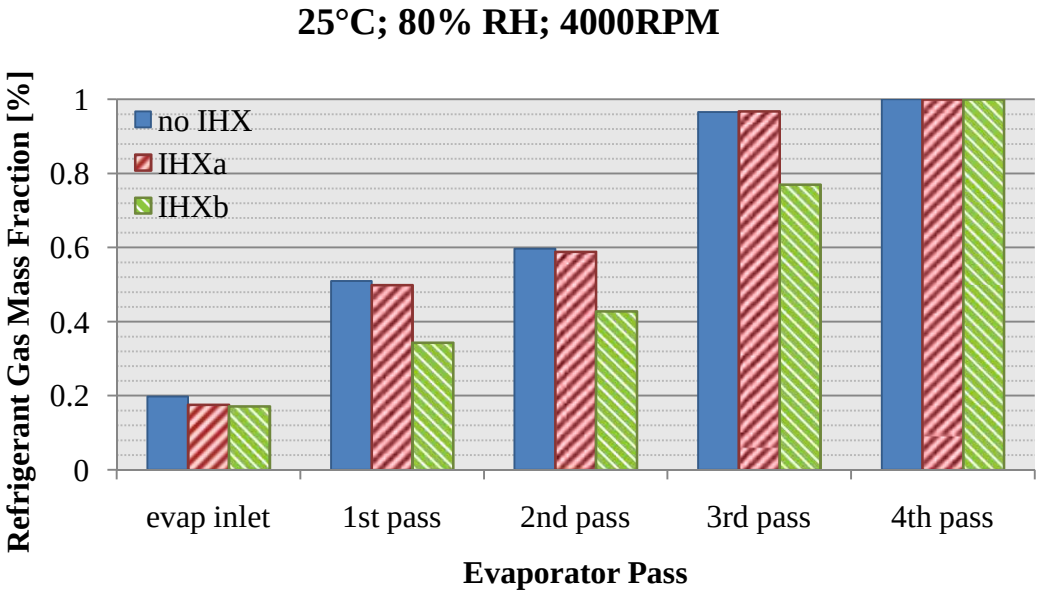

Figure 4-32: **Refrigerant quality for the different passes of the evaporator. The evaporator is operating during steady-state where the boundary conditions imposed on the AC system are 25°C, 80% RH and 4000 RPM.**

4.2.5 IHXa—Influence of the Ambient Conditions

This subsection investigates how the ambient conditions influence IHX performance. The investigation will vary the relative humidity (RH) and temperature of the ambient air only, as the atmospheric pressure only changes with altitude. First, the relative humidity is varied from 0% to 100% at a constant ambient temperature of 40^{o}C. Second, the ambient temperature is varied from 25 to 45^{o}C in increments of 10^{o}C. The naming convention for the operating points is temperature/relative humidity. For example 40/0 corresponds to an ambient air temperature of 40^{o}C and 0% relative humidity.

All of the simulations in this sub-section have a compressor speed of 4850 RPM, condenser air inlet velocity of 4 m/s and an evaporator air mass flow rate of 520 kg/h. These operating points were selected because they represent AC performance under high load conditions. These values correspond to the first operating point for the steady-state investigations. From the discussion in the previous subsection, only the results from IHXa configuration will be shown due to its performance superiority for the compressor power consumption and COP over the entire operating range versus the IHXb configuration. Also, the purpose of this section is not to compare the functioning differences between the two configurations, but to investigate the IHX response to the changing ambient conditions. The four performance parameters of interest include:

- Compressor power consumption;
- Evaporator capacity;
- COP;
- IHX capacity.

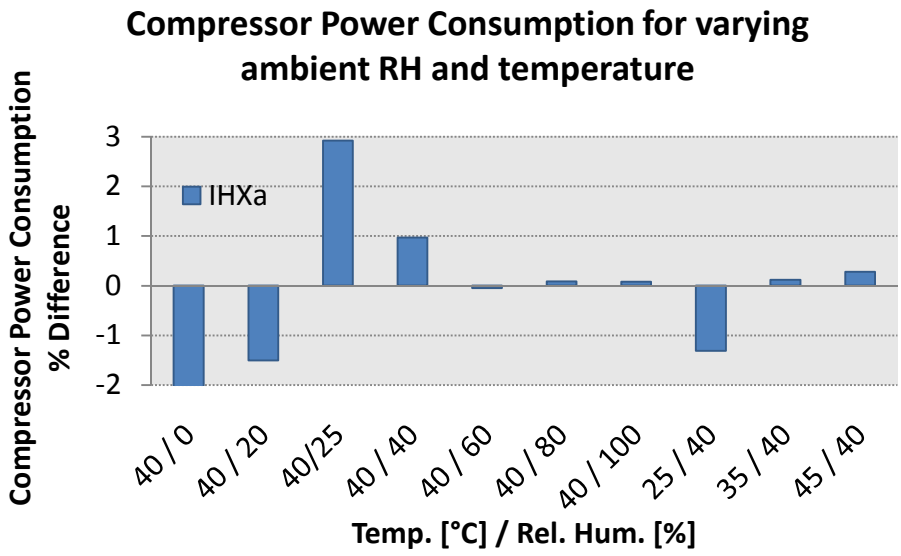

Figure 4-33: Compressor power consumption for variation in ambient relative humidity and temperature. The percent difference is calculated according to Equation (3.4).

The results for the constant temperature and varying relative humidity in Figure 4-33 indicate that the compressor power consumption is slightly affected by the relative humidity. The highest power consumption value occurs at 25% relative humidity however it is only an increase of 3%. With the addition of the IHX, the change in relative humidity appears to affect the compressor power consumption. However, there is not a discernable pattern as the relative humidity increases or the ambient temperature increases.

From the results of Figure 4-34, there is no discernable relationship with the ambient relative humidity and the change in the evaporator capacity. However, there is a clear relationship with the ambient temperature. For the 35^{o}C and 45^{o}C cases, change in evaporator capacity increases with increasing ambient temperature. For the 25^{o}C case, the change in evaporator capacity is negative, but still stays true to the pattern.

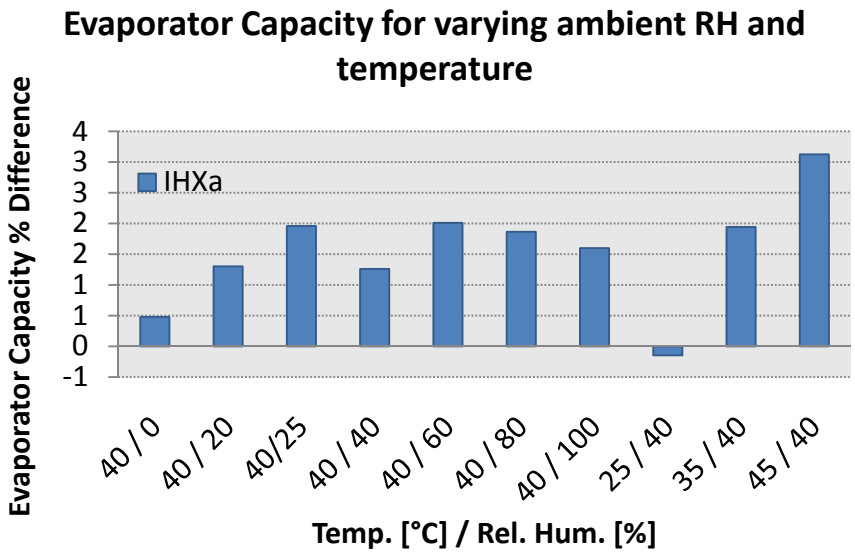

Figure 4-34: Evaporator capacity for variation in ambient relative humidity and temperature. The percent difference is calculated according to Equation (3.4).

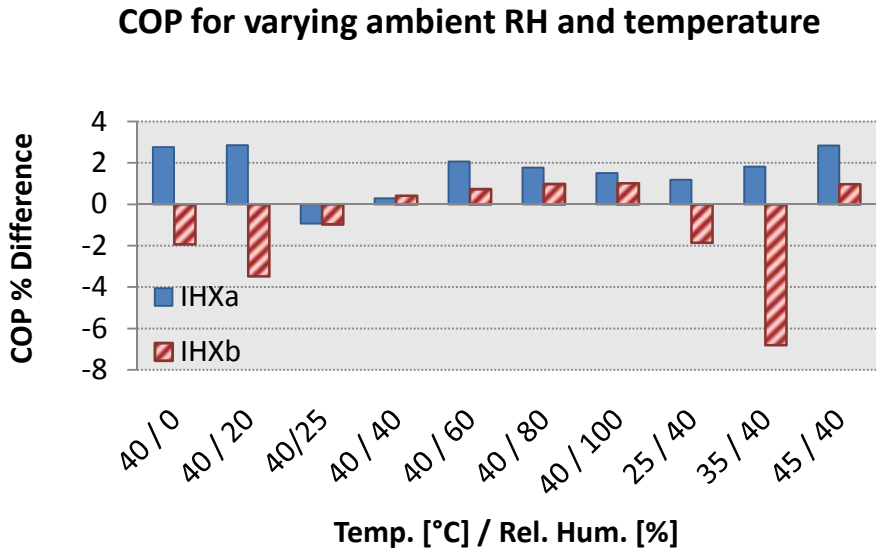

Figure 4-35: COP for variation in ambient relative humidity and temperature. The percent difference is calculated according to Equation (3.4).

From the results of Figure 4-35, again there is no discernable relationship with the ambient relative humidity and the change in the evaporator capacity. There is only one

operating point, 40/25, where the IHX decreases the COP for the AC system. There is a direct relationship between the change in COP and the ambient temperature.

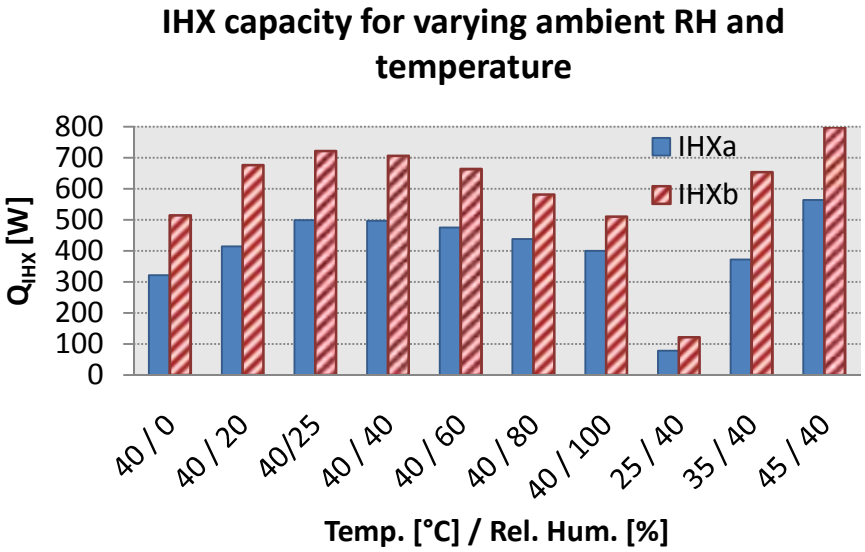

Figure 4-36: IHX capacity for variation in ambient relative humidity and temperature. The percent difference is calculated according to Equation (3.4).

Figure 4-36 above, displays the performance of the IHXa configuration for the ambient operating points. For the varying ambient relative humidity there appears to be a saturation point at 25%. An increase or decrease of the relative humidity from this point results in a smaller IHX capacity. As the ambient temperature of the IHX increases, the IHX capacity increases.

Figure 4-37, shows the COP as a function of ambient temperature for different compressor speeds. These results to provide the reader with another way to see how varying the compressor speed affects the AC performance under different ambient temperature conditions. This graph also served as a comparison to a study by, Mathur, 2011, which investigated the COP of an AC system with an IHX for the refrigerant HFO-1234yf [17]. The relationship of the COP with the ambient temperature and compressor speed was similar to the experimental findings from this SAE paper.

As with the other results in this sub-section, only the IHXa configuration simulations are displayed. Figure 4-38 also shows the percent increase in COP with the inclusion of an IHX, in order to compliment the results from Figure 4-37. The baseline comparison is an

AC system without an IHX. All of the tests for the results in Figure 4-37 and Figure 4-38 have an ambient relative humidity of 40%, a condenser air inlet velocity of 4m/s and an evaporator air mass flow rate of 520 kg/h.

From Figure 4-37, as the compressor speed increases, the COP of the AC system decreases. Also at equivalent compressor speed, the COP decreases as the ambient temperature increases. Recall from Equation (2.2), that the COP is the ratio of the evaporator capacity to the compressor input power. Thus for increasing compressor speeds and ambient temperatures, which both represent increased load on the AC system, the increase in compressor power consumption is greater than the increase in the evaporator capacity.

From the supplemental results in Figure 4-38, there is no discernable pattern with the change in COP as a function of the ambient temperature and compressor speed. As a special note, do not confuse the results from Figure 4-38 to the previously shown COP results from Figure 4-24, with the exception of the 35^{o}C, 40% relative humidity, 4000RPM case. With all of the other operating points in Figure 4-38, there will be variations in the condenser air face velocity, refrigerant mass flow rate or the relative humidity.

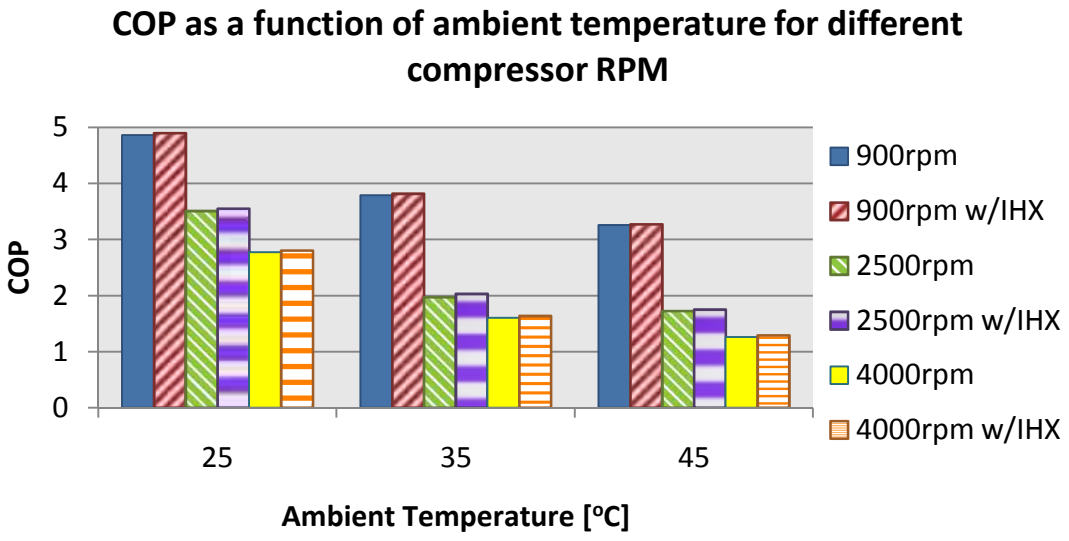

Figure 4-37: COP as a function of ambient temperature. AC system with and without an IHX are shown for different compressor RPM at each ambient temperature

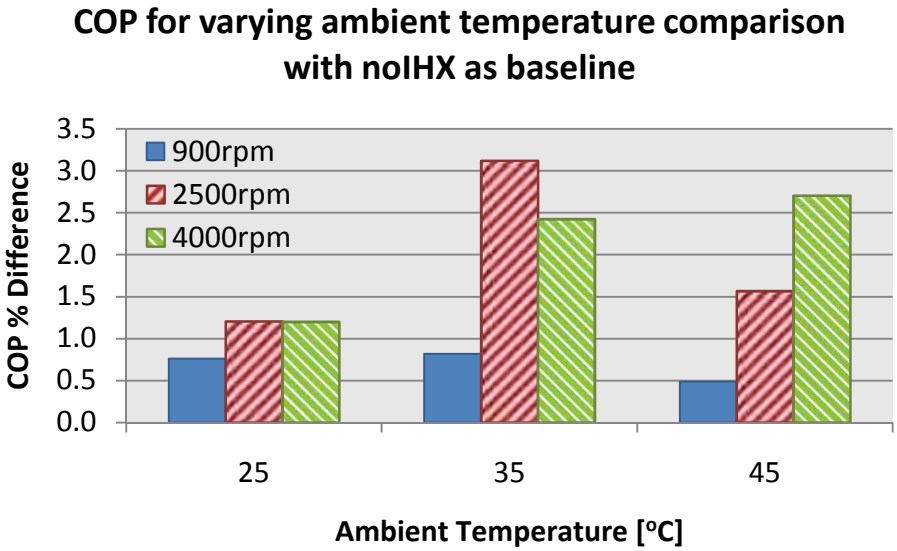

Figure 4-38: COP percent difference as a function of ambient temperature. The difference is calculated based on the results from Figure 4-37.

4.3 New European Driving Cycle (NEDC) with Internal Heat Exchanger (IHX)

This section will show the results for the transient NEDC with an IHX. Figure 4-39 displays how significantly the compressor, blower and fan influence the power consumption of an AC system. This figure was generated from an NEDC test for an AC system without an IHX, however the percentages should not be significantly influenced by the introduction of an IHX. Figure 4-39 shows that the compressor power consumption contributes 84% of the total consumption, thus decreasing the power consumption will lead to results that are more significant.

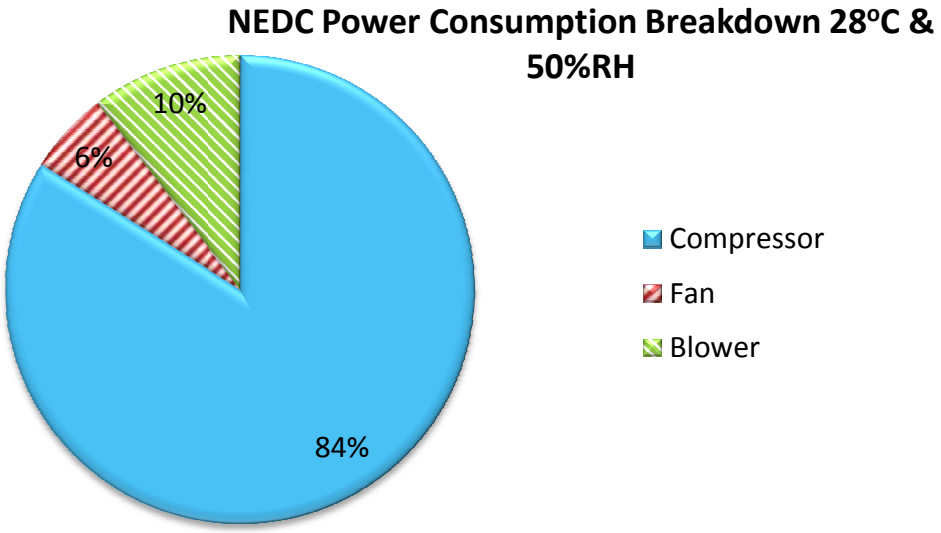

Figure 4-39: Breakdown of the compressor, blower and condenser fan contributions to the overall AC power consumption

Figure 4-40, Figure 4-42 and Figure 4-44 show the individual power consumption for the compressor, fan and blower, respectively. Figure 4-41 shows the percent difference of the compressor power consumption from Figure 4-40. For the low load case, both IHXa and IHXb lead to increased power consumption. For the compressor power consumption, for IHXa is better than IHXb. However, in Figure 4-41 and Figure 4-42, there is a larger power consumption decrease for IHXb. For the 28°C and 35°C cases, IHXa decreases the power consumption where as IHXb only decreases the power consumption for the 35°C case.

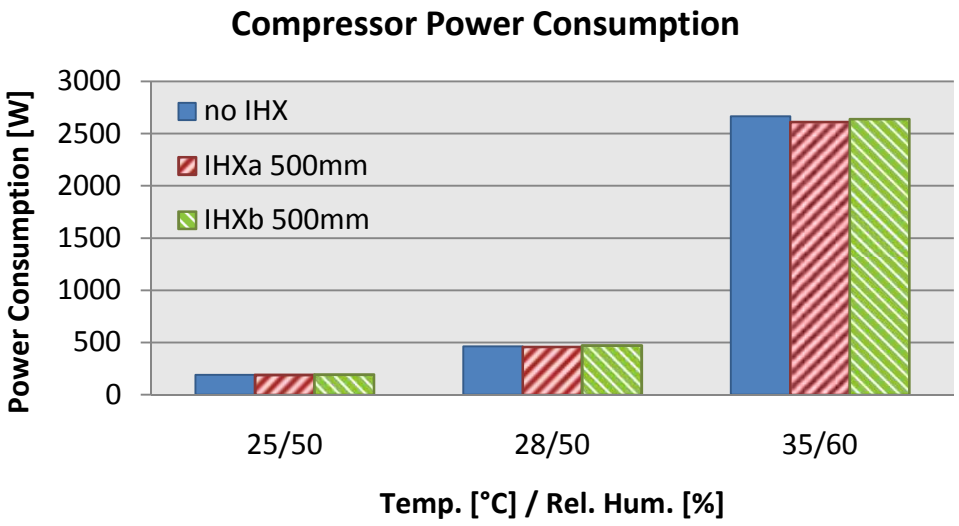

Figure 4-40: Compressor power consumption for noIHX, IHXa and IHXb.

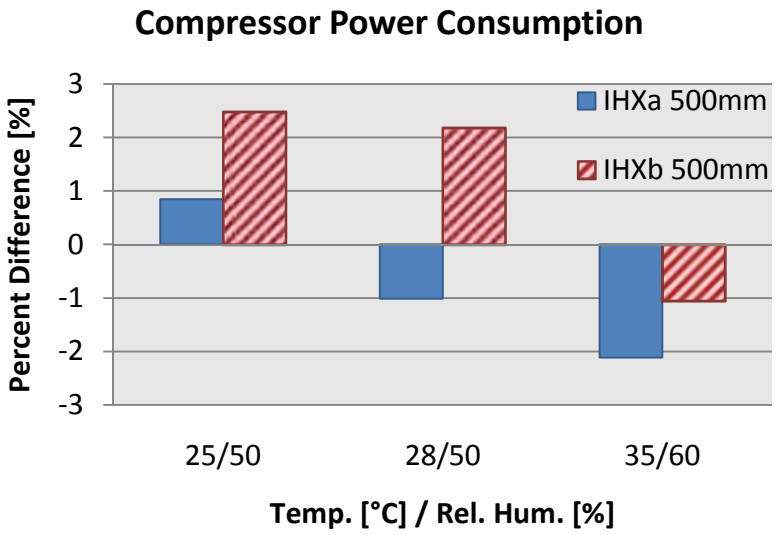

Figure 4-41: Percent difference for the compressor power consumption from the results of Figure 4-40. An AC system without an IHX is used as the baseline comparison.

Figure 4-43 shows the percent difference of the fan power consumption from Figure 4-42. There is a significant increase in the fan power consumption as the temperature of the ambient air increases for Figure 4-42. This is a reasonable response since an increase in air temperature will require an increase in the air mass flow rate to maintain equivalent

heat transfer capability. In Figure 4-43, IHXb decreases the power consumption more than IHXa for the 28°C and 35°C cases.

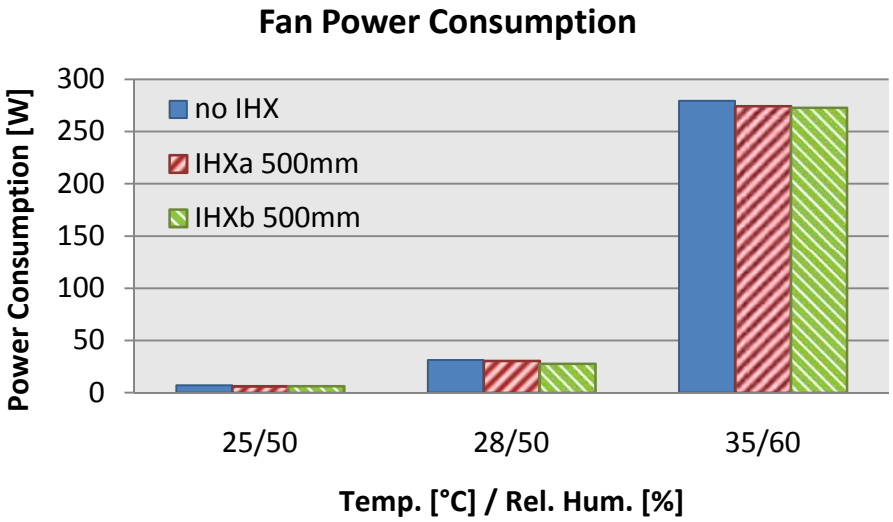

Figure 4-42: Fan power consumption for noIHX, IHXa and IHXb.

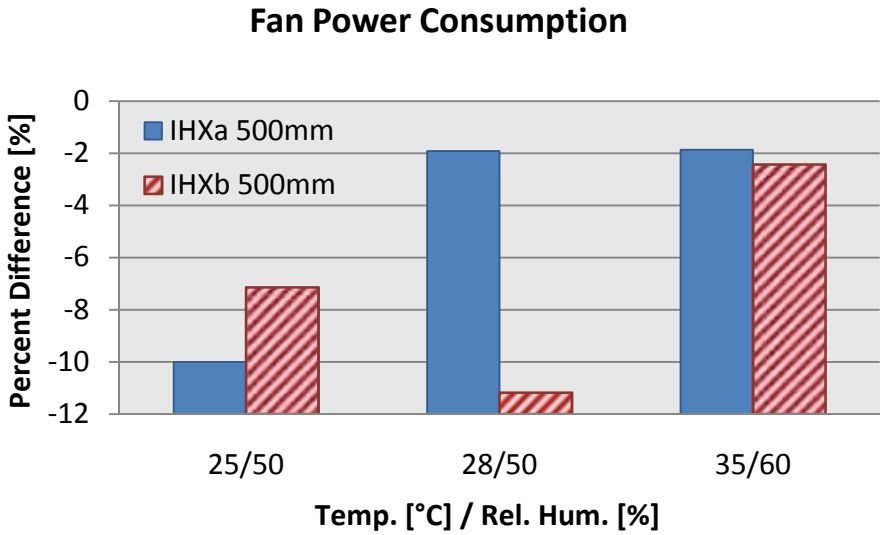

Figure 4-43: Percent difference of the fan power consumption. An AC system without an IHX is used as the baseline comparison.

Figure 4-45 shows the percent difference of the blower power consumption from Figure 4-44. There is a significant increase in the fan power consumption as the temperature of the ambient air increases for Figure 4-44. This is a reasonable response since an increase in air temperature will require an increase in the air mass flow rate to maintain equivalent heat transfer capability. For the blower power consumption IHXa outperforms IHXb.

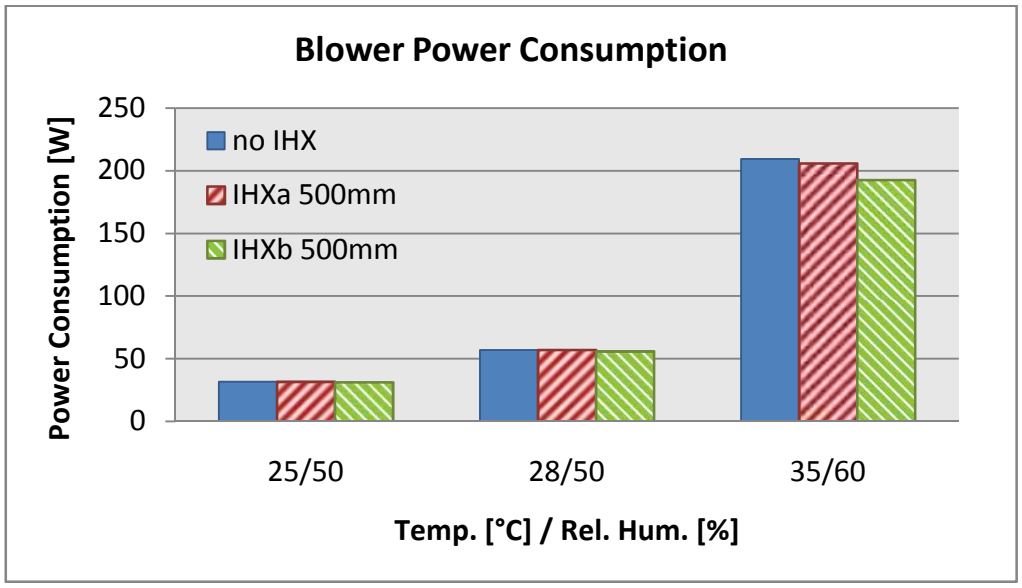

Figure 4-44: Blower power consumption for noIHX, IHXa and IHXb.

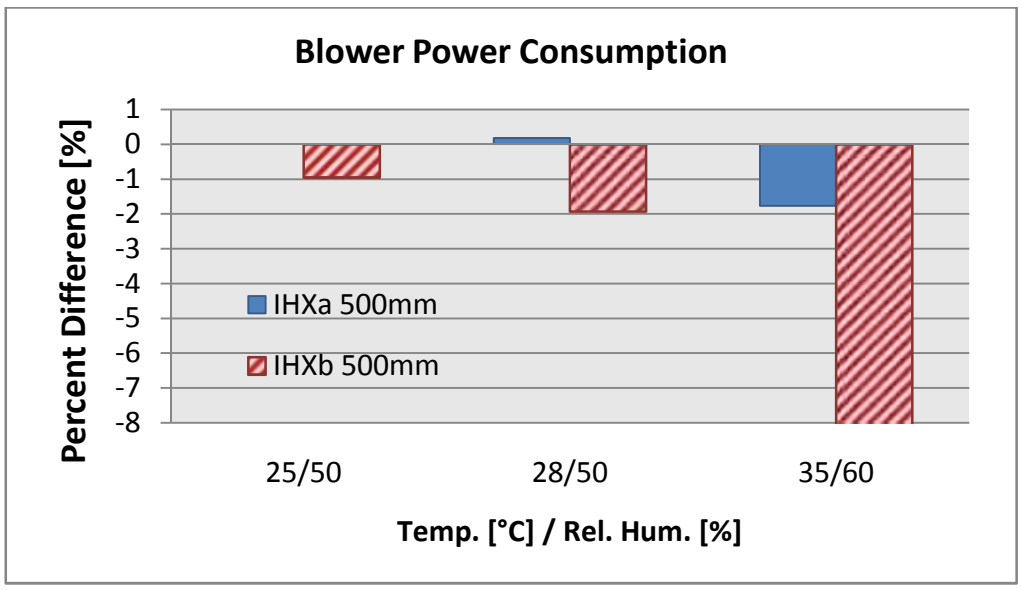

Figure 4-45: Percent difference for the blower power consumption. An AC system without an IHX is used as the baseline comparison.

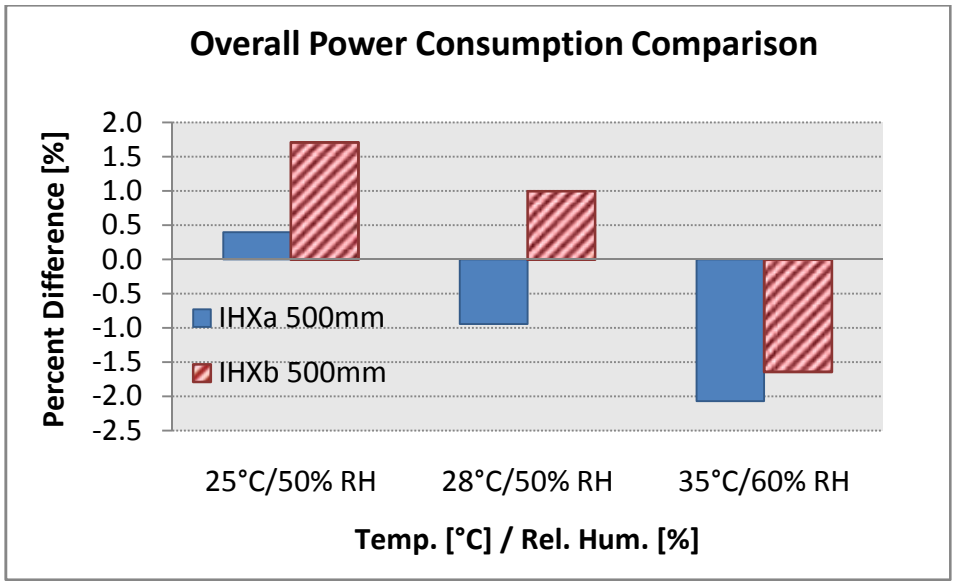

Figure 4-46: Overall power consumption comparison for three NEDC simulations. The baseline for the comparison is an AC system without an IHX

Figure 4-46 shows the change in overall AC power consumption due to the introduction of an IHX. For an ambient temperature of 25^{o}C there is an increase in power consumption, while a power reduction for IHXa in the other two tests. There is only an overall power reduction for IHXb in the 35^{o}C ambient temperature. The improvements in power consumption are not as much as those reported in the literature, however the power consumption decreases for IHXa are very similar to those from the steady-state simulation [11] [14] [16] [17].

CHAPTER 5
CONCLUSIONS

5.1 Inclusion and Analysis of Internal Heat Exchanger in Mobile Air Conditioning System

The internal heat exchanger model predicts the suction side pressure drop with up to 20% error and the liquid side pressure drop with up to 8% error. Since the prediction of the suction side pressure drop was of greater importance than the capacity prediction, due to the findings from various literature studies, the 2mass model was used to conduct all steady-state and transient simulations.

The steady state simulations yielded similar results to the data presented in the study conducted by Seybold et al [13]. The relationships are not exactly similar since the components for the simulation and experimental system are not identical. However, the relationships between the variables of the ordinate and abscissa axes are similar for the simulation and experimental results.

The IHXa configuration outperformed the IHXb configuration for the change in compressor power consumption, coefficient of performance (COP) and suction line pressure drop. For mobile air conditioning (MAC) systems where the compressor discharge temperature is a concern, using IHXb will yield similar temperatures to a MAC system based on the simulation results presented in this thesis. The IHXb configuration also yielded higher increases in IHX capacity, evaporator capacity and system level absolute efficiency ratios. However, the performance response of the suction line pressure drop, COP and compressor power consumption were of greater importance to the author of this thesis.

The calibration of the simulation using the cabin cool-down experimental results from Fiat, showed an average error of less than 3.2% for the following parameters:

- Evaporator outlet pressure
- Evaporator outlet temperature
- Condenser inlet pressure

- Condenser outlet temperature
- Vent air outlet temperature
- Recirculation air temperature
- Cabin cool-down temperature curve

The only parameter outside of the 3.2% error range was the condenser inlet temperature with an error of 23.3%. This is a very large error, but the author was not responsible for the calibration of the AMESim model, only the calibration of the IHX model.

For the NEDC transient cycle, the simulations showed up to a 3% decrease in AC power consumption for ambient temperatures of 35^{o}C and 45^{o}C. For the ambient temperature case of 25^{o}C, there was an increase in AC power consumption. Thus the inclusion of an IHX is only beneficial for higher ambient temperature conditions based on the simulation results in the present thesis.

5.2 Recommendations for Future Work

- To calibrate the cabin model, it would be best to first perform steady-state testing with the three tests in the list below.
    1. A cool-down test with no solar loading, while the vehicle is idle
        - This enables the determination of the internal heat transfer between all of the cabin components without the influence of solar heat being transmitted, absorbed and reflected by the glass.
    2. A cool-down test for steady-state vehicle velocity with no solar loading.
        - This will help calibrate the external heat transfer models between the ambient and the exterior of the vehicle. Excluding solar radiation eliminates another set of parameters that require calibration
    3. A cool-down for steady-state vehicle velocity with solar loading.
- With the majority of automotive manufacturers switching to HFO-1234yf creating a model with this refrigerant would be very beneficial. This would require more experimental data for a vehicle using this refrigerant.
- Steady-state experimental data to help with the calibration of the AMESim model.

APPENDIX A Cabin Model Thermal Mass Significance

Version	Description	Experimental	
		Avg Error (degC)	Val Metric
V0	**Original Fiat model**	**3.1**	**0.969**
V1	recreation of original Fiat model	3.5	0.965
V2	Cut complete roof/roof liner	4.5	0.955
V2a	Cut conduction & roof liner	5.5	0.946
V3	Cut complete Fwind/Dash	13.7	0.864
V3a	Cut Fwind	7	0.93
V3b	Cut Dash convection	4.7	0.954
V3c	Cut Dash radiation	5.6	0.944
V3d	Cut complete Dash	7.8	0.922
V4	Cut complete Swind/Fseat	18.1	0.821
V4a	Cut Swind	9.9	0.902
V4b	Cut Fseat convection	4.4	0.957
V4c	Cut Fseat radiation	3.6	0.964
V4d	Cut complete Fseat	8	0.92
V5	Cut complete Rwind/Rseat	7.2	0.928
V5a	Cut Rwind	4.6	0.954
V5b	Cut Rseat convection	3.8	0.962
V5c	Cut Rseat radiation	4.6	0.954
V5d	Cut complete Rseat	4.7	0.953
V6	Cut complete underbody/floor	4.2	0.958
V6a	Cut conduction & carpet floor	10.8	0.893
V7	Cut complete door/door panel	5.4	0.946
V7a	Cut air gap & door panel	20.2	0.803

APPENDIX B NEDC Airflow File

```
# Table format: 3D
#Car speed [km/h]
#Activation Level [-]
#External Temperature [°C]
#Air Flow [kg/s]
14
3
2

0.000 5.000 10.000     15.000     20.000     25.000     30.000
      36.000     40.000     50.000     64.000     80.000
      96.000     120.000
0     50    100
25    35

0     0.001 0.074 0.119 0.157 0.196 0.236 0.286 0.32  0.407 0.535 0.685
      0.841 1.078
0.314 0.317 0.325 0.339 0.359 0.399 0.438 0.478 0.505 0.575 0.684 0.822
      0.971 1.209
0.547 0.549 0.554 0.563 0.576 0.591 0.611 0.639 0.661 0.75  0.851 0.97
      1.101 1.314
0     0.001 0.071 0.114 0.151 0.188 0.227 0.279 0.307 0.391 0.514 0.659
      0.809 1.037
0.302 0.305 0.313 0.327 0.346 0.385 0.422 0.46  0.485 0.553 0.658 0.79
      0.934 1.163
0.527 0.529 0.534 0.543 0.555 0.57  0.588 0.615 0.637 0.724 0.82  0.935
      1.06  1.265
```

APPENDIX C IHX 500mm supplier data information

TI AUTOMOTIVE

Internal Heat Exchanger Laboratory
Measurement
R134a, 900mm, AE0313
Oil ND8 < 1%

Parameter Name	Para Code	Unit	Test Parameters Requirement OEM				
			Low Load	Idle II	Idle	Highload	Highload II
Temp. IN High Pressure		°C	25	70	50	45	50
Pressure IN High Pressure		bar	7.5	25	16	13	16
Temp. IN Low Pressure		°C	15	10	15	11	11
Pressure IN Low Pressure		bar	3.5	3.5	3.5	3	3
Mass Flow		g/s	10	28	28	45	65
			Test Parameters SET UP on bench				
Mass Flow		g/s	10	28	28	45	65
Temp. IN Low Pressure		°C	15	10	15	11	11
Pressure IN Low Pressure		bar	3.5	3.5	3.5	3	3
spez. Enthalpie IN Low Pressure		kJ/kg	410.7	406.2	410.8	408.3	408.3
Temp. OUT Low Pressure		°C	19.6	35.3	29.5	24.4	25.8
Pressure OUT Low Pressure		bar	3.5	3.5	3.5	2.9	2.9
spez. Enthalpie OUT Low Pressure		kJ/kg	415	429.5	424.2	420.6	422.1
Pressure DROP Low Pressure		**mbar**	**2**	**20**	**19**	**61**	**138**
Enthalpiedelta Low Pressure		kJ/kg	4.3	23	13.4	12.3	14
Heat Capacity Low Pressure		kW	0.043	0.653	0.376	0.554	0.892
Temp. In High Pressure		°C	25	70	50	45	50
Pressure IN High Pressure		bar	7.5	25	16	13	16
spez. Enthalpie IN High Pressure		kJ/kg	235	305.3	272.5	264.8	272.5

Temp. OUT High Pressure		°C	22	56	41.3	37	41.1
Pressure OUT High Pressure		bar	7.5	25	16	13	15.9
spez. Enthalpie OUT High Pressure		kJ/kg	230.8	282	259.1	252.6	258.8
Pressure Drop High Pressure		**mbar**	**2**	**13**	**12**	**28**	**56**
Enthalpiedelta High Pressure		kJ/kg	4.2	23.3	13.4	12.2	13.7
Heat Capacity High Pressure		kW	0.042	0.651	0.375	0.548	0.888
Theoretical spez. Enthalpie		kJ/kg	420	462.6	443.4	439.6	444.4
Theoretical isobare spez. Enthalpie		kJ/kg	415	429.5	424.2	420.5	421.8
Exchange (Enthalpie)		--	0.46	0.41	0.41	0.39	0.38
Exchange (Temperature)		--	0.46	0.42	0.41	0.39	0.38
Temperature delta IN Low Pressure		K	7.1	46	26.3	26	30.1
Temperature delta IN High Pressure		K	5.4	34.8	20.5	20.6	24.2
Temperature delta average		K	6.2	40.4	23.4	23.3	27.1
kxA - Value		W/K	6.8	16.2	16.1	23.7	32.8

APPENDIX D Compressor Map Information

AMESim requires a specific format for the isentropic and volumetric efficiency maps. The first line of the ASCII specifies the number of compressor speed data points and their corresponding compressor ratio values. The second line specifies the compressor speed data points and the third line specifies the pressure ratio data points. All of the subsequent lines specify the isentropic or volumetric efficiency values as a matrix of the compressor speed and pressure ratio values. For example, the fourth line specifies the efficiency for the different pressure ratio values for the first compressor speed, the fifth line specified the efficiency for the different pressure ratio values for the second compressor speed and so forth.

Compressor Isentropic Efficiency Map

```
5  5
1000 2000  3000  4000 5000
4.5 6 6.4 6.7 10
0.738 0.612 0.510 0.448 0.393
0.701 0.635 0.560 0.496 0.444
0.677 0.595 0.520 0.465 0.422
0.689 0.627 0.550 0.492 0.431
0.630 0.582 0.536 0.491 0.448
```

Compressor Volumetric Efficiency Map

```
5  5
1000 2000  3000  4000 5000
4.5 6 6.4 6.7 10
0.868 0.792 0.678 0.572 0.471
0.789 0.736 0.654 0.559 0.452
0.773 0.713 0.615 0.520 0.440
0.753 0.713 0.619 0.526 0.433
0.629 0.584 0.517 0.445 0.376
```

APPENDIX E Relevant AMESim Libraries

There are numerous libraries within AMESim that contain pre-established sub-models. The model for this thesis utilizes four different libraries.

1. Two-Phase Flow (TPF)
2. Thermal
3. Air Conditioning
4. Heat Exchanger Assembly Tool (HEAT)

A brief description of each of the libraries, their general capabilities, and their incorporation into the components of the full AC model are explained below. All of the descriptions below, summarize the documentation supplied by AMESim regarding the four libraries [28-31].

The two-phase flow library utilizes a lumped transient heat transfer approach. This library models heat transfer between the refrigerant and the walls of the ducts in which the refrigerant is flowing. There are pre-built components which include capabilities for modeling boundary conditions, sensors, ducts, pressure losses and internal and external flow. The capabilities of this library enable the user to model:[28]

- Energy transport;
- Internal convective heat exchange for condensation and boiling;
- External convective heat exchange;
- Pressure losses, temperature levels, mass flow rates, and enthalpy flow rates;
- Gas mass fraction of the fluid within the system;
- Mass transfer between the vapour and liquid phases.

The models in the present thesis utilize the Two-Phase Flow (TPF) library for the refrigerant piping in the AC system, specifying the refrigerant material properties, modeling the fins of the evaporator and incorporating sensors to measure pressures, enthalpy differences and temperatures within the AC system. For the AC refrigerant piping there are no bends included in the model, only straight line paths. The list below highlights the major assumptions for this library [28]:

- The refrigerant modeling is based on a homogeneous fluid model. When there are two phases present, the model assumes the flow as a single phase possessing mean fluid properties. There is no slip between the two phases and there is thermodynamic equilibrium between the phases. Thermodynamic equilibrium means that at the interface of the two boundaries the temperatures of the two states are equivalent;
- Internal flow is one-dimensional;
- Gravity is neglected for the calculation;
- External flow is zero-dimensional. The mass flow rates and their distributions are imposed with user-specified values and maps. This ensures that the model considers only the variation along the flow direction.

The Thermal Library models heat transfer between solid materials using the traditional heat transfer methods including conduction, free and forced convection and radiation. Modelling capabilities include transient heat transfer as well as the temperature evolution when exposed to a thermal source. There are two major sub-model types in the thermal library, thermal capacity and heat transfer sub-models. The thermal capacity sub-models calculate the temperature variation as a function of the simulation time and are representative of the mass of a material. The second type of sub-models calculate the energy transfer from traditional heat transfer methods due to a temperature difference.

The following list below highlights the major assumptions for this library: [29]

- Heat flow is one-dimensional where the model calculates variation in the fluid flow direction;
- All solid materials are isotropic, meaning uniform properties in all orientations;
- The temperature in the thermal capacity sub-models is homogeneous.

Included in the Thermal Library is the modeling capability for environmental moist air. The air for these sub-models are zero-dimensional, so the user specifies the mass flow rates and no pressure drops are computed. The focus of the modeling is on the evaluation of the heat transfer between the solid materials. These sub-models interact with the heat

transfer sub-models representing the fins of the evaporator [29]. See Section 3.2.6 for a more detailed description.

The Air Conditioning library contains pre-established sub-models for major AC components including the compressor, condenser, TXV, and evaporator. There is a sub-model to specify the type of refrigerant, which has many pre-built refrigerant material models including R134a, R1234yf, CO_2 and H_2O. The AC library has the capability of conducting transient and steady-state analyses accounting for the heat transfer of the refrigerant and the solid wall capacities. The AC model for the present thesis includes only the compressor, internal regulation control, TXV, condenser geometry and refrigerant material sub-models [30].

The Heat Exchanger Assembly Tool (HEAT) library provides the ability to model heat exchanger interactions within a closed environment. For example, this library allows the user to study the affect of the heat exchanger stacking in the front end of a vehicle. The amount of heat exchanged by the radiator is a direct effect of the capabilities of the trans-oil cooler, charge air cooler and condenser. The sub-models in this library have the capability of showing the 3D temperature distribution along the frontal area of the heat exchanger. The AC loop only includes the condenser sub-model from this library. By incorporating this sub-model, the automotive companies are able to use the AC model of the present thesis to study the effects of the air conditioning system coupled with the other front end heat exchangers [31].

APPENDIX F Air Conditioning Component Sub-Models

Studying the influence of an internal heat exchanger (IHX) on a system level, requires a calibrated and functional AC model. Using AMESim, this AC model is capable of simulating single and two-phase flow, steady-state and transient processes, as well as heat transfer by conduction, convection and radiation. The complete AC loop consists of the material models, compressor, condenser, TXV, evaporator, IHX, air recirculation model, vent model and the cabin model.

G.1 R134a Material Model

The refrigerant properties in the two-phase library are pre-established and the user does not have the ability to generate their own fluid properties. Figure F-1 shows the sub-model icon for TPF_FP01, which specifies the type of refrigerant for the AC model.

Figure F-1: AMESim icon for sub-model TPF_FP01. This icon is required when running simulations with two- phase materials. This sub-model contains all the refrigerant property data for all of the simulations in the present thesis.

AMESim uses the 32 coefficient Modified Benedict-Webb-Rubin (MBWR) equations of state model to calculate the refrigerant R134a properties [28]. To determine the initial fluid state of the simulation AMESim offers the user four different options. By selecting one of the options listed below and specifying their values, AMESim is able to calculate the initial refrigerant state for each component of the two-phase flow library.

- Pressure and specific enthalpy
- Pressure and temperature
- Pressure and gas mass fraction
- Pressure and superheat/sub-cooling

Ensuring the correct refrigerant charge and temperature helps reduce simulation time and unexpected results. For the refrigerant sub-model, the option "use load and temperature" offers two methods to specify the refrigerant charge and temperature. Specifying "no", AMESim initializes the refrigerant independently for each two-phase flow sub-model in the system. All simulations for this thesis use this option for initializing the refrigerant state in the AC system.

For the sake of future AMESim users, if "yes" is selected, the user specifies the refrigerant charge and initializing temperature. AMESim calculates the system volume from all of the individual components and uses this value to determine the refrigerant density. AMESim uses the initializing temperature to determine the initial pressure by assuming saturated liquid refrigerant properties.

Thermodynamic plots specify the refrigerant material properties within AMESim. These plots are used to determine the thermodynamic state of the refrigerant during the simulation. All of the plots involve different variations for pressure, temperature, enthalpy and specific volume variables at liquid and vapour saturation states for various temperatures, pressures and gas mass fractions.

G.2 Aluminum Material Model

Aluminum material represents the structural material of the heat exchangers. Defining the material for thermal calculations requires the density, specific heat and thermal conductivity. AMESim has the capability of defining these properties with respect to temperature using a 2^{nd} degree polynomial. However, the material card used in all simulations has density remaining constant for all temperature values.

The reference temperature, density and specific heat are 27^{o}C, 2702 kg/m^3 and 903 J/kg-K, respectively.

G.3 Compressor

All simulations, both steady-state and transient, have a variable displacement compressor with an internal control. The experimental AC system used an axial piston swash-plate compressor. Figure F-2, obtained from reference 19, shows a cross section as well as labelling for the important components for this type of compressor.

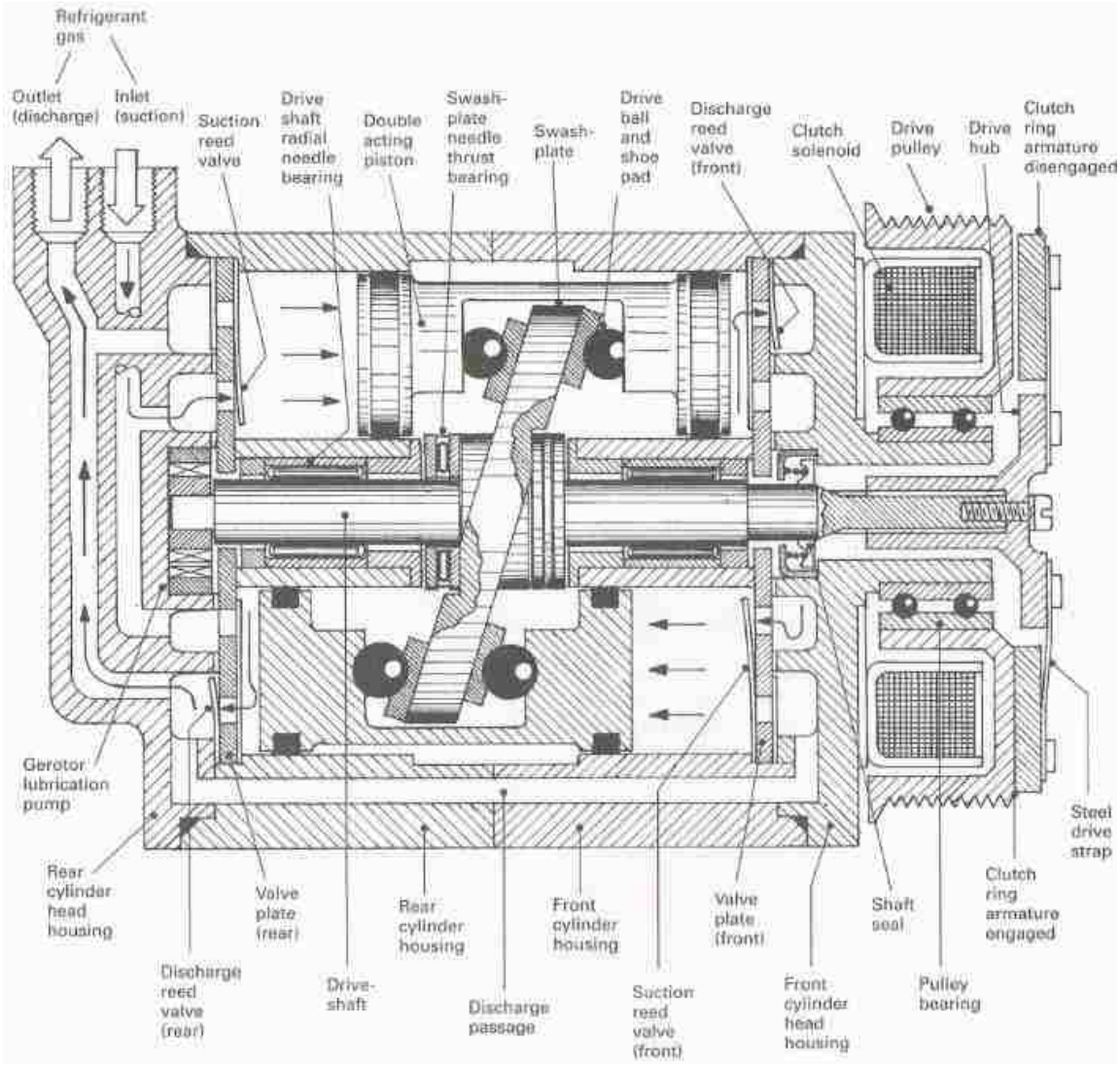

Figure F-2: Cross section of a double acting axial piston swash-plate driven compressor [22]. This schematic is for a fixed displacement compressor, whereas the compressor in the present thesis has an internal regulation valve which changes the angle of the swash plate. Increasing the angle increases the refrigerant volumetric displacement per revolution and decreasing does the opposite.

Within AMESim, the sub-model ACVDICCOMP00 coupled with the internal control sub-model ACVALVE00, from the AC library, represent the compressor for the simulations. It is necessary to include these two components together in order to have a variable displacement compressor with internal control.

Figure F-3 and Figure F-4 represent the inlet and outlet parameters for ACVDICCOMP00 and ACVALVE00, respectively.

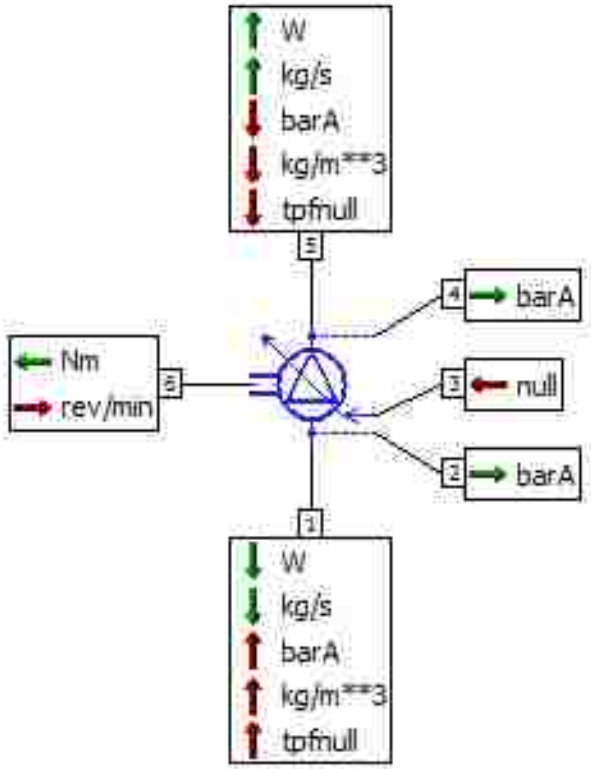

Figure F-3: Schematic representing the input and output parameters to the sub-model ACVDICCOMP00, the variable displacement compressor. The blue icon represents the sub-model as it appears within AMESim. The green arrows represent outgoing information to attached sub-models and the red arrows represent incoming information to represent sub-model ACVDICCOMP00. The variable W represents the measurement Watts as the enthalpy flow rate is exchanged with the connecting sub-models [24].

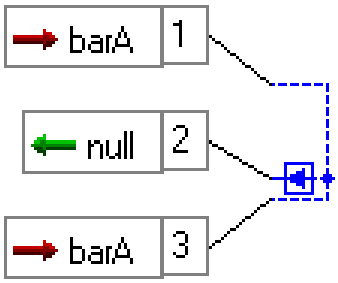

Figure F-4: Schematic representing the sub-model ACVALVE00 representing the internal control valve for the variable displacement compressor sub-model. The blue icon represents the sub-model as it appears within AMESim. The green arrow represents outgoing information to attached sub-models and the red arrows represent incoming information to the sub-models ACVALVE00 [24].

The components from the two-phase flow (TPF) and AC libraries exchange a special variable called *tpfnull*. This variable ensures that all of the components are using the same refrigerant index, for example R134a. Evaluation of the system volume and specific fluid properties are also sent to all the sub-models via this communication variable. This variable has no bearing on the heat transfer or the enthalpy flow rate of the refrigerant passed between the different sub-models.

The compressor sub-model has built-in start-stop capabilities. This feature is not utilized in the simulations of the present thesis, however having incorporated this sub-model into the AC system enables possible future analyses for vehicles with these capabilities. For example, incorporating this sub-model allows the user to study the effect of AC usage on vehicle fuel economy or the ability of the AC system to keep the cabin within comfortable temperatures when the compressor shuts off.

Normally, the regulation valve varies the force balance acting on the swash plate to change the displacement of refrigerant. The signal from the sub-model ACVALVE00 regulates the suction pressure of the compressor by following a user-specified regulation curve. The internal control sends a signal to the compressor, ACVDICCOMP00, with a value ranging between zero and one. The variable *redisp* represents the internal control signal sent from ACVALVE00, the internal control valve, to ACVDICCOMP00, the compressor.

The sub-model ACVALVE00 calculates the reduced displacement using the compressor suction and discharge pressures and four user-specified constants define the regulation curve for the suction pressure. Figure F-5, taken from the AMESim help files provides a graphic representation of the regulation curve and the user-specified constants.

- x_a corresponds to the critical compressor discharge pressure where the compressor displacement varies. Before this value, the suction pressure remains constant and after the suction pressure decreases linearly as the discharge pressure continues to increase.
- y_a the maximum average suction pressure value. It corresponds to the suction pressure during minimum displacement operation.
- k slope of the line relating suction pressure to discharge pressure once the discharge pressure exceeds the x_a specification.
- dp the allowable pressure differential tolerance for acceptable deviation above and below the user-specified pressure regulation curve.

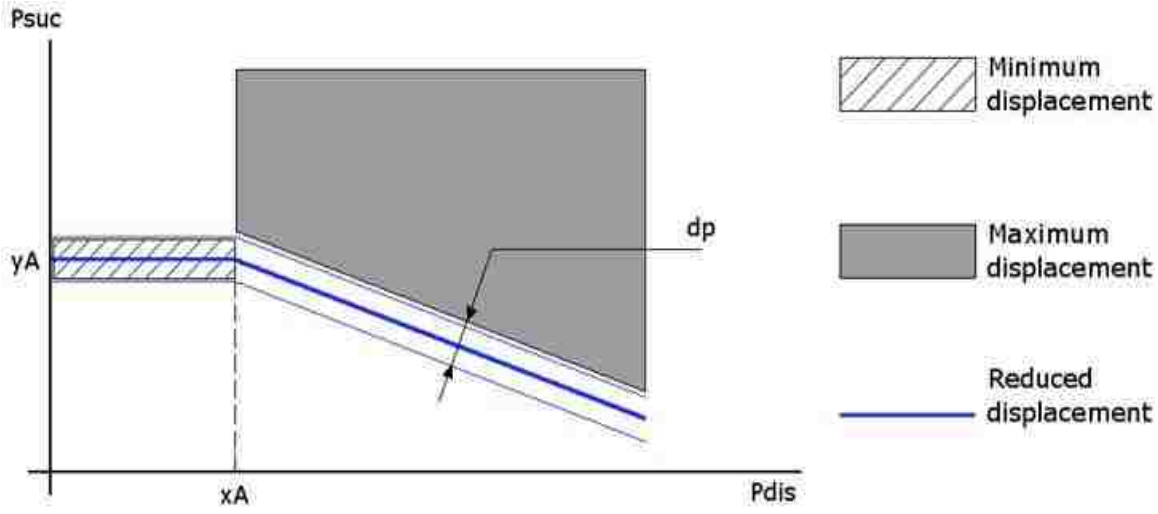

Figure F-5: Physical representation of the pressure regulation curve and user-specified parameters for the sub-model ACVALVE00 [24]. The AMESim software uses Equation (F.1), to calculate this curve. The parameter, *dp*, represents the pressure regulation offset. Once the pressure falls outside of this range, above or below the pressure regulation curve, a signal is sent to change the compressor displacement.

Equation (F.1) shows the equation describing the pressure regulation curve defined within AMESim. The list below displays the pressure regulation curve parameters used for all simulations in the present thesis.

$$p_{reg} = y_a - k \cdot (p_{dis} - x_a) \quad \textbf{(F.1)}$$

- x_a = 10.79 barA
- y_a = 2.914 barA
- k = 0.0491
- dp = 0.2451/8 barA

Calibration of the compressor sub-model involves specifying the volumetric, isentropic and mechanical efficiencies. For all three efficiencies, zero and one are the lowest and highest possible values respectively. The volumetric and isentropic efficiencies are input as functions of the compressor rotary speed. Please see Appendix D for the input map files for the volumetric and isentropic efficiencies and their corresponding formatting to meet the input requirements for the compressor sub-model. The mechanical efficiency remains constant for all simulations, with a value of 0.9.

The displacement signal sent from ACVALVE00 to the compressor sub-model, represented by the variable *sig* within the AMESim equations, enables the calculations for the compressor volumetric efficiency, displacement and consequently the refrigerant mass flow rate. Equation (F.2) shows the volumetric efficiency where $\eta_{vol_{min}}$ is the user-specified volumetric efficiency at minimum displacement and $\eta_{vol_{max}}$ is the maximum volumetric efficiency as specified in the American Standard Code for Information Interchange (ASCII) file in Appendix D. The variable *sig*, a normalized volumetric displacement, is obtained from the ACVALVE00 sub-model. The user-specified values for the variables $\eta_{vol_{min}}$ and $\eta_{vol_{max}}$ represent the minimum and maximum volumetric efficiency of the compressor. With the volumetric efficiency, the

sub-model calculates the refrigerant mass flow rate through the compressor, shown in Equation (F.3).

$$\eta_{vol} = (1 - sig) \cdot \eta_{vol_{min}} + sig \cdot \eta_{vol_{max}} \quad \textbf{(F.2)}$$

$$\dot{m}_{dis} = \eta_{vol} \cdot \rho_{suc} \cdot N \cdot V \quad \textbf{(F.3)}$$

The compressor displacement calculated by Equation (F.4) is shown below and the values are within the range of the minimum and maximum compressor displacement.

$$V = sig * (V_{max} - V_{min}) + V_{min} \quad \textbf{(F.4)}$$

AMESim uses the isentropic efficiency map to calculate the enthalpy difference between the compressor outlet and inlet, represented by h_d-h_s in Equation (F.5). The calculation for the isentropic discharge enthalpy, h_{d_s}, uses the discharge pressure and the suction enthalpy of the refrigerant. The variables, h_{dis} and h_{suc}, represent the discharge and suction enthalpy of the compressor, respectively. Multiplying the enthalpy difference by the mass flow rate gives the compressor power consumption. The user-specified compressor efficiency map files are located in Appendix D.

$$\eta_s = \frac{h_{d_s} - h_{suc}}{h_{dis} - h_{suc}} \quad \textbf{(F.5)}$$

Finally, the compressor sub-model calculates the torque with the user-specified mechanical efficiency. Equation (F.6) represents shows the equation used to calculate the compressor torque. The units of this equation are N-m/revolution.

$$T = \frac{\dot{m}_{dis} \cdot (h_{dis} - h_{suc})}{\eta_s \cdot N} \quad \textbf{(F.6)}$$

G.4 Condenser Geometry

All simulations in the present thesis model a parallel flow tube and fin condenser. Figure F-6, obtained from reference 21, shows a cross section for such a condenser along with labels for the important condenser parameters. There are three passes for the condenser shown in Figure F-6. They are the superheating, condensing and sub-cooling passes. The convention, first pass, second pass, etc., will be used instead for the explanations in the present thesis. The condenser for the simulations has a built in receiver/dryer, which helps reduce and simplify the system packaging requirements.

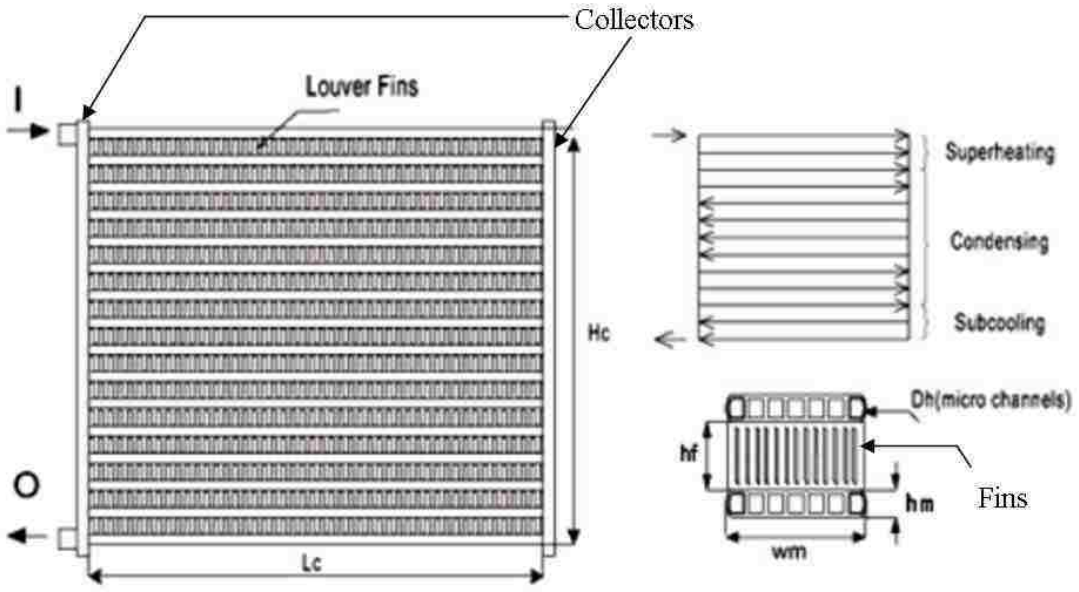

Figure F-6: Representation of a parallel flow micro channel condenser. The measurements in this figure are not relevant to the present thesis. This figure only serves to illustrate the concept of a parallel flow condenser with micro channel tubing for the refrigerant. Although not discussed in the present thesis, louvred fins serve to increase the turbulence of air flowing through the condenser, thus improving the condenser heat transfer capability[26]. On the left side of the figure, I and O represent the inlet and outlet of the refrigerant flowing through the condenser. L_c and H_c represent the width and height of the condenser. The measurements for the fins in the bottom right corner of the figure are not important, since AMESim has its own way of describing the fin geometry, which will be discussed in detail later on in this section.

As discussed in Section 3.1.2, the condenser sub-model was selected based on its compatibility with the engine related heat exchangers within AMESim. This allows for

easier integration with a model of the engine cooling system. Specifying the condenser location in 3D space allows for a thermal analysis of the air flow and cooling ability of the complete front end heat exchanger system. The components include the charge air cooler, transmission oil cooler, condenser and radiator. The following sections describe the modeling of the condenser geometry within AMESim, an explanation of the sub-models required and the modeling equations.

Figure F-7 and Figure F-8 show the parameters representing the condenser geometry as they are defined within AMESim. The simulation uses these parameters to determine liquid and air side cross-sectional areas and hydraulic diameters. Determining the Nusselt number, whose importance is discussed in Section 3.2.5, requires the knowledge of the air side cross-sectional area. The collector cross-sectional area is given by the supplier data sheet for the condenser sub-model.

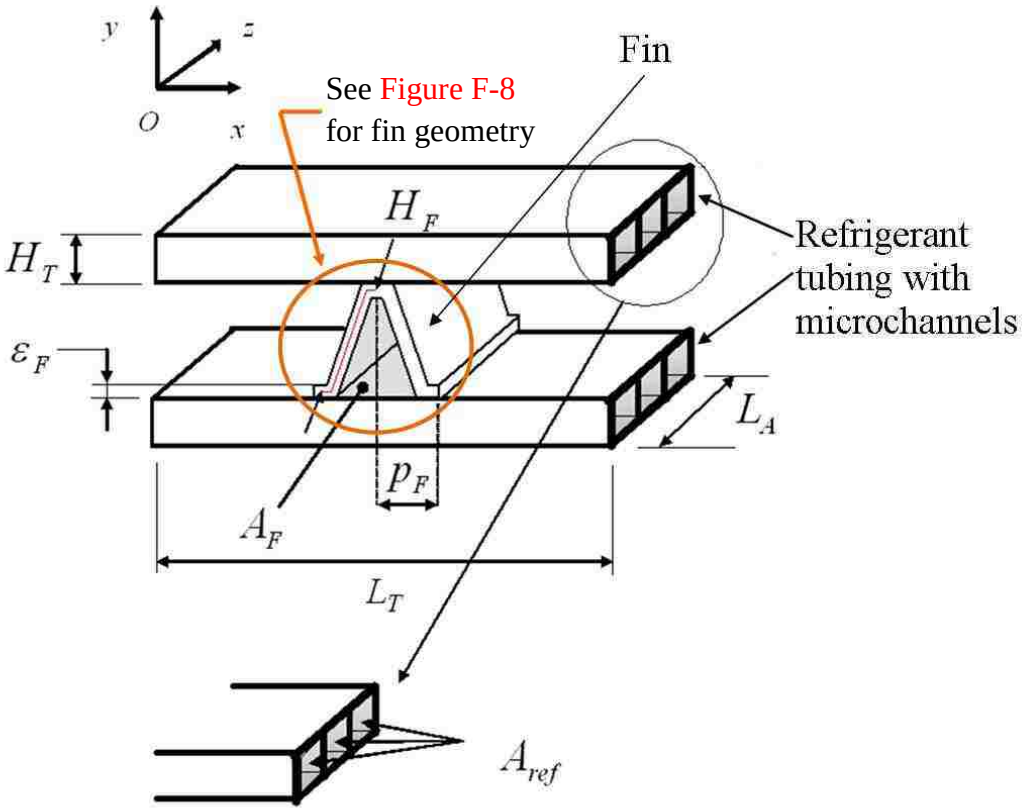

Figure F-7: AMESim model geometry specifications for a tube and fin condenser. This figure shows the structural configuration of the condenser and the parameters used by the commercial software, AMESim, to define the elementary geometry. Liquid refrigerant flows through the microchanneled tubes exchanging heat with the air flowing through the spaces between the fins. The top and bottom tubing represent two passes [24].

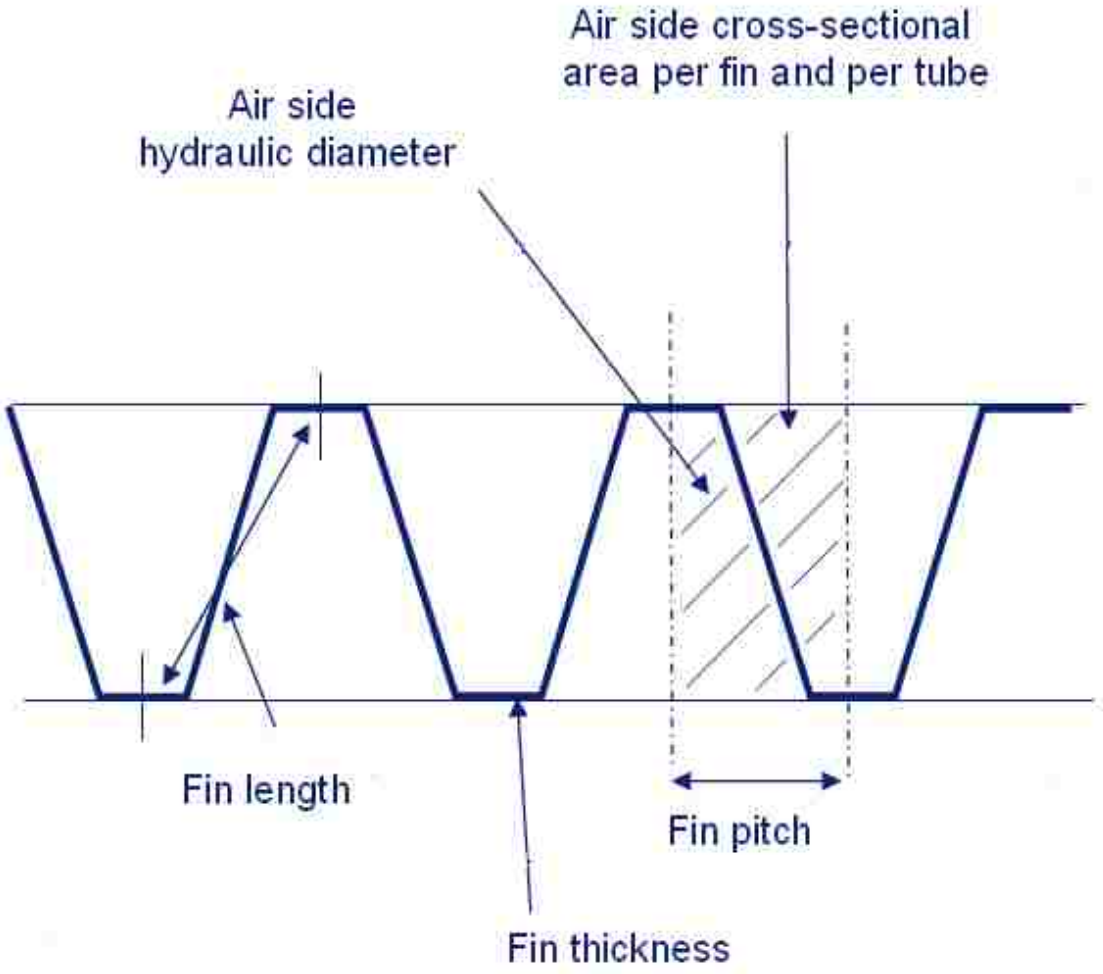

Figure F-8: AMESim model geometry specifications for the fins of a tube and fin condenser. This figure isolates the parameters used to describe the fin geometry from the rest of the condenser shown in Figure F-7. Note that AMESim defines the fin pitch differently from the normal convention [24].

A description of the parameters from Figure F-7 and Figure F-8 is included in the list below.

- H_T external tube height, which represents the vertical height of one tube.
- H_F fin length, measured as the distance between a valley and a peak of a fin, along the fin edge. This is an approximation, but due to the small size of the fin, the error is very small.
- L_A tube depth, which is equivalent to the depth of the condenser unit. The names tube depth, condenser depth and condenser thickness are interchangeable.
- L_T tube length or tube width. This neglects the extra length due to the collectors.

- A_F air side cross-sectional area per fin per tube. Figure F-8 shows this measurement more clearly than Figure F-7. This value is obtained by multiplying the vertical height of the fins between two tubes and the fin pitch. The vertical distance is obtained using the Pythagorean theorem with the fin pitch and vertical fin height forming two sides of the right triangle.
- p_F fin pitch. By standard convention, the distance from the centerline of one fin to another defines the fin pitch. However, the AMESim convention uses half the value of the standard convention.
- ε_F fin thickness
- A_{ref} refrigerant cross-sectional area per tube. In modern heat exchangers, the refrigerant tubing is made up of many micro channels to increase the heat transfer rate. The sum of the microchannel cross-sectional areas for one tube constitutes the total refrigerant cross-sectional area per tube.

G.5 Condenser Sub-models

This section focuses on the various sub-models required to model the condenser within AMESim. The discussion includes information on parameter specifications, important background equations as well as assumptions inherent in the sub models. Modeling of the condenser sub-model requires five different AMESim sub-models, which will be discussed below. The naming convention corresponds to the name of the sub-models as they appear within AMESim.

1. HEAT01

The sub-model, HEAT01, controls the external fluid flow interactions for the components from the Heat Exchangers Assembly Tool (HEAT) library. When using components from the library, the external fluid flow connections are not visible. Despite there only being one component from the HEAT library, the inclusion of this model is mandatory. Figure F-9 displays the icon for the sub-model as it appears within AMESim.

Figure F-9: Icon for the sub-model HEAT01 from the Heat Exchanger Assembly Tool Library. This sub-model is mandatory when using the pre-established AMESim sub-models.

2. TP_AIR

The second sub-model, PNGD004, specifies the properties of the external air passing through the condenser. The components from the HEAT library require the properties of dry air with zero humidity. The gas is completely defined using the perfect gas constant and three polynomial functions giving the absolute viscosity, the specific heat at constant pressure and the thermal conductivity [24]. Figure F-10 displays the icon for the sub-model as it appears within AMESim.

Figure F-10: Icon for the sub-model PNGD004 from the Pneumatic library. This defines the properties of dry air assuming it behaves as an ideal or semi-perfect gas.

3. HEATPFHE02

Modeling of the condenser requires geometrical information of the refrigerant flow, the air flow and the solid walls and fins. Single and two-phase flow correlations are also essential as they influence the heat transfer calculations for the condenser. The third sub-model, HEATPFHE02, contains the global geometrical and flow correlation information necessary to model the condenser passes. Figure F-11 displays the icon for the sub-model as it appears within AMESim.

Figure F-11: Icon for the sub-model HEATPFHE02 from the air conditioning library. This sub-model contains the condenser geometrical data and is responsible for calculating the internal and external pressure losses and internal convective heat exchange.

This sub-model is responsible for calculating the internal and external pressure losses and internal convective heat exchange. These calculations differ for the refrigerant depending on its state, that is, single or two-phased state. The following paragraphs and tables discuss the input parameters for this sub-model, which are separated into the categories: internal, external and structural dimensions of the tubes and fins.

The collector contains a volume of refrigerant at one end of the condenser. Here the refrigerant collects after flowing through one pass in the condenser. From Figure F-6 it can be seen that the collector is a cylinder with a cross-sectional area plane parallel to the refrigerant tubes. All simulations assume zero absolute roughness for the internal tubes of the condenser. For further clarification regarding the condenser geometry, please refer back to Section 3.2.4. Table F-1 summarizes the user-specified parameters for HEATPFHE02.

Table F-1: Displays the internal flow and convective heat exchange parameters for the sub-model HEATPFHE02.

INTERNAL FLOW PARAMETERS		
PARAMETER	**VALUE**	**NOTES**
Absolute roughness of the internal tube surface	0.0 mm	assumes the internal tube surface is completely smooth
Tube hydraulic diameter	0.81 mm	none
Tube cross-sectional area	10.9 mm^2	sum of the cross-sectional areas of the micro channels in one tube
Collector cross-sectional area	415.48 mm^2	none
Two-phase flow frictional pressure drop correlation	McAdams homogeneous flow model	Formulation calculating the friction factor for this type of flow
Condensation correlation	Shah formulation	computes the internal convective heat flow when the refrigerant is in the two-phase condition

Boiling correlation	VDI Heat Atlas for horizontal tubes formulation	computes the internal convective heat flow for two-phase conditions and boiling of the refrigerant
Refrigerant side single phase laminar Nusselt number	Nu = 2.976	value for a square cross-section, representing the micro channels, for laminar flow regime

The external flow and convective heat exchange parameters for HEATPFHE02 are shown in the Table F-2 below. These three parameters enable the computation of the external convective heat transfer and the airside cross-sectional areas. Refer back to Figure F-7 and Figure F-8, which provide a graphical representation of the condenser geometries. The hydraulic diameter is calculated from the rectangular crosshatched area shown in Figure F-8. The correlation for the hydraulic diameter of a rectangular duct is shown in Equation (F.7). The calculation to determine the fin height is explained for the variable A_F in Figure F-6.

Table F-2: Displays the external flow parameters for the sub-model HEATPFHE02

EXTERNAL FLOW PARAMETERS	
PARAMETER	**VALUE**
Air side cross-sectional area per fin and per tube	12.37 mm^2
Air side hydraulic diameter	2.59 mm
Condenser and fin thickness	16 mm

$$D_h = \frac{4 \cdot fin\ pitch \cdot fin\ height}{2(fin\ pitch + fin\ height)} \quad \textbf{(F.7)}$$

The parameters shown below are used to calculate areas, volumes and hydraulic diameters of the tubes and fin material. Determining the mass of the material is necessary to compute the thermal capacity of the solid walls. Having these dimensions allows AMESim to calculate the Reynolds and Prandtl number for the external air flow. Table F-3 below, summarizes the tube and fin geometrical data, as they are defined within AMESim.

Table F-3: Displays the geometry values for the tube and fin for the sub-model HEATPFHE02.

TUBE AND FIN GEOMETRIES		
PARAMETER	**VALUE**	**NOTES**
Tube height	1.6 mm	none
Tube length	622 mm	equivalent to the condenser length/width
Tube depth	16 mm	equivalent to the condenser depth/thickness
Fin pitch	3.2/2 mm	Recall AMESim defines the fin pitch has half the value of the conventional definition. Refer back to Figure F-8.
Fin thickness	0.07 mm	none
Fin length	7.96mm	none

The outputs of the HEATPFHE02 sub-model include:

- Condenser frontal area (external side)
- Condenser cross-sectional area (external side)
- Condenser heat exchange area (external side)
- Global heat flow rate (external side)
- Refrigerant volume
- Fin and tubing mass

4 & 5. HEATCONDREF120 & HEATCONDTOP120

The final two sub-models, HEATCONDREF120 and HEATCONDTOP120, represent the passes of the condenser. Within the HEAT library, only parallel cross-flow heat exchangers with "dry-air" as the external fluid are considered. HEATREF120 includes the geometrical data and boundary conditions, whereas HEATCONDTOP120 only specifies that there is a second pass of the condenser. Similar to the HEATPFHE02 sub-model, the AMESim condenser sub-model considers internal flow, external flow and solid walls and fins. Table F-4 shows a list of important user-specified parameters for the reference condenser sub-model.

Table F-4: Summary of the user-specified parameters for HEATCONDREF120. When discussing global heat exchanger dimensions the terms width and length are interchangeable for the horizontal measure of the front face. The term depth is interchangeable for condenser

thickness. The height (vertical distance) and width (horizontal distance) represent the frontal dimensions of the condenser. Refer back to Figure F-6 for further clarification.

PARAMETER	VALUE	NOTES
Height	0.2982 m	None
Width	0.622 m	None
Thickness	0.016 m	None
Inlet position	up and left	None
Number of tubes in first pass	27	None
Number of tubes in second pass	6	None
Velocity boundary condition	Map file	user-specified 2D data file for the air velocity along the condenser frontal area
Temperature boundary condition	Map file	user-specified 2D data file for the air temperature along the condenser frontal area

AMESim offers the user various options for specifying the velocity and temperature of the air side boundary conditions for the condenser, as noted in Table F-4 above. The map file format contains information along the front condenser profile for the air temperature and velocity in an ASCII file format. This option is utilized for the Cabin Cool-down (CCD) test cycle, discussed in Sections 1.1 and 3.7.1.

The homogeneous constant option is used for the steady-state simulations discussed in Section 3.6. Here, the air temperature and velocity remain at a constant user-specified value along the front condenser face. The values are sent to the HEATCONDREF120 sub-model via signal sources pre-existing within the AMESim libraries.

The NEDC, uses the homogeneous variable option. Here the air temperature and velocity are uniform along the front condenser face, but their values change as a function of simulation time utilizing a user-specified curve. The air temperature and velocity parameters are sent to the HEATCONDREF120 via signal sources that pre-exist within the AMESim libraries.

The following discussion of equations considers only the refrigerant side calculations. The two condenser sub-models, HEATCONDREF120 and HEATCONDTOP120, are responsible for the refrigerant side calculations. The pressure losses are computed using

correlations in the literature. The models use the Churchill friction factor correlation for the single phase refrigerant state, shown in Equation (F.8) below. Knowledge of the friction coefficient allows the determination of the refrigerant pressure drop along a pipe for laminar and turbulent flow. Note that *f* in this formula corresponds to the friction factor found on a Moody Chart. The variables ε and *D* represent the mean surface roughness and hydraulic diameter of the flow channel, respectively.

$$f = 8\left[\left(\frac{8}{\mathrm{Re}}\right)^{12} + \frac{1}{\left\{\left[2.457\, ln\left(\left(\frac{7}{\mathrm{Re}}\right)^{0.9} + 0.27\left(\frac{\varepsilon}{\mathrm{D}}\right)\right)\right]^{16} + \left[\frac{37350}{\mathrm{Re}}\right]^{16}\right\}^{3/2}}\right]^{1/12} \quad \textbf{(F.8)}$$

For a refrigerant in a two-phase state, the model uses the McAdams correlation. Recall the assumption of a homogeneous fluid model as explained in Section 3.1.2, which applies here. As a result, the two-phase refrigerant mixture is treated as a well-mixed pseudo-single-phase fluid with homogeneous mixture density and viscosity [32]. An in-depth discussion of the McAdams and other correlation models can be found in references [33] [34]. The McAdams correlation, shown in Equation (F.9), calculates the equivalent viscosity of the two-phase refrigerant. This correlation assumes a homogeneous fluid model. AMESim calculates the friction factor and corresponding pressure drop along the piping from the two-phase equivalent viscosity. This enables the simulation software to calculate the Reynolds number, friction factor and pressure loss along the refrigerant piping.

$$\frac{1}{\mu_{\mathrm{TPF}}} = \frac{x}{\mu_{\mathrm{v}}} + \frac{1-x}{\mu_{l}} \quad \textbf{(F.9)}$$

In Equation (F.9), the variable *x* corresponds to the refrigerant mass quality, defined as the ratio of the vapour mass to the total mixture mass. Quality has significance for saturated mixtures only. Its value ranges between 0 and 1 corresponding to saturated liquid and saturated vapour, respectively.

For the transient simulations, the boundary conditions of the condenser temperature and velocity are non-homogeneous. In other words, along the front face of the condenser, uniform velocity and temperature distribution are non-existent. Therefore, the user provides temperature and velocity profile maps for a discretized front condenser face. These conditions are specified in AMESim with map files. The origin of the frontal area coordinate system is located at the bottom left corner of the condenser. The temperature and velocity values are considered as cell-centered.

The refrigerant mass flow rate, shown in Equation (F.10), is derived from the Bernoulli formulation. The calculation of *f* depends on the type of flow, which includes:

1. Laminar regime
2. Turbulent regime
3. Single-phase flow
4. Two-phase flow

$$\dot{m}_R = \rho \cdot f \cdot A_{cross} \cdot \sqrt{\frac{2\Delta p}{\rho}} \qquad \textbf{(F.10)}$$

The enthalpy flow rate, equivalent to the capacity of the condenser, is calculated using the refrigerant mass flow rate and the specific enthalpy difference between the outlet and the inlet of the condenser. AMESim calculates the specific enthalpy at the inlet and

outlet using temperature and density to define the refrigerant state. Recall, the explanation given in Section 3.2.1 discussing the calculation of the refrigerant properties.

The external convective heat exchange is calculated from Equation (F.11). In this equation, the air thermal conductivity, air-side hydraulic diameter and external Nusselt number are used to calculate the external heat exchange coefficient, h_{ext}. A_{ex_sur} represents the external surface heat exchange area. AMESim conducts this calculation for each discretized section of one pass. The sum of the heat from one pass, and consequently all the other passes constitutes the total heat exchange from the external side of the condenser.

$$Q_{ext} = \hbar_{ext} \cdot A_{ex\_sur} \cdot (T_{air} - T_{wall}) \quad \textbf{(F.11)}$$

The internal heat exchange is calculated from Equation (F.12) below. Determining the value of the convection coefficient, h_{int}, experimentally is complex due to the refrigerant condensing process as it flows through the condenser tubes. The internal surface exchange area, A_{int_sur}, represents the internal surface area of all the micro channels that make up the condenser tubing. The process for calculating the total heat exchange from the internal side of the condenser is the same as the external side.

$$Q_{int} = \hbar_{int} \cdot A_{int\_sur} \cdot (T_{ref} - T_{wall}) \quad \textbf{(F.12)}$$

As stated in the previous caption, the calculation of the internal convection coefficient, h_{int} is difficult due to the condensing process within the condenser. During single-phase flow, the model considers two flow conditions:

1: Laminar regime
2: Turbulent regime

In the laminar regime, the Nusselt number is a user-specified constant value. Due to the microchannels, a Nusselt number of 3.66 was selected. Since the heat transferred as the refrigerant flows through the passes is transient, this value is difficult to specify with exact certainty. For the turbulent flow regime, AMESim uses the Gnielinski correlation shown in Equation (F.13). The friction factor corresponds to the Churchill correlation previously shown in Equation (F.8). The variables D_h and k represent the hydraulic diameter (a characteristic length) and thermal conductivity of the refrigerant, respectively.

$$\hbar_{int} = \left[\frac{\left(\frac{f}{8}\right)\cdot(\mathrm{Re}-1000)\cdot\mathrm{Pr}}{1+12.7\cdot\sqrt{\frac{f}{8}}\left(\mathrm{Pr}^{2/3}-1\right)} \right] \cdot \frac{k}{D_h} \qquad \textbf{(F.13)}$$

During two-phase refrigerant flow, the model considers two flow conditions:

1. Condensation
2. Boiling

An explanation of the correlations calculating the refrigerant convection coefficient, h_{int}, is beyond the scope of the present thesis. The AC model uses the Shah [35] and VDI Heat Atlas (horizontal tube) correlations to calculate the convection coefficient during condensation and boiling, respectively. For further information regarding the VDI boiling correlation, please see references [36] and [37].

G.6 Thermal Expansion Valve (TXV)

The purpose of a TXV is to regulate the refrigerant superheat leaving the evaporator. In a standard MAC system, the refrigerant exiting the evaporator passes through a feedback loop where it enters the thermal sensing bulb (TSB) of the TXV. There is fluid in the bulb, called the power fluid, which partially fills the TSB in Figure F-12. The pressure of the power fluid applies a force to the top of the diaphragm and the evaporator pressure applies a force on the bottom of the diaphragm. An increase in the refrigerant superheat, increases the temperature and pressure of the gas in the TSB. The pressure increase

causes the ball valve to open against the return spring, increasing the refrigerant flow rate through the evaporator. The increase in refrigerant superheat is usually an indication of either a decrease in the air velocity passing through the evaporator or an increase in the ambient air temperature. By increasing the refrigerant mass flow rate, this causes a discrete quantity of refrigerant to exchange less heat with the passing air as it passes through the evaporator. This reduces the refrigerant exiting temperature if it is superheated and the refrigerant quality if it exits in a saturated mixture state. However, overall the amount of heat transferred will increase since more refrigerant is passing through the evaporator. The refrigerant exiting as a saturated mixture will only occur when the IHX is introduced into the AC system because the compressor is not designed to handle a saturated mixture.

Figure F-12 displays a cross-sectional diagram of a TXV and includes labelling of the important components. In the figure, the outlet component screws into the main housing providing a method to calibrate the TXV. Screwing the outlet component up or down will change the super heat spring tension, thus changing the opening and max opening points of the ball valve. The super heat spring is calibrated to open at a specific refrigerant pressure from the evaporator outlet to control the temperature of the liquid refrigerant entering the evaporator. It is crucial that the temperature of the refrigerant is firstly low enough to be able to meet the cooling requirements of the refrigerated space, and secondly not too high which would deteriorate the compressor life.

A sample of the refrigerant exiting the evaporator is brought to the TXV through the inlet feed from the sensing bulb. As the superheated refrigerant temperature increases, the pressure applied to the diaphragm increases. This forces the diaphragm to push the diaphragm stem down, consequently opening the ball valve orifice. Further opening of the ball valve orifice decreases the pressure drop, and increases the refrigerant mass flow rate through the evaporator. The temperature of the refrigerant increases slightly from the decreased pressure drop. However as mentioned in the beginning paragraph of this section, the overall amount of heat transferred will increase since more refrigerant is passing through the evaporator.

The screen serves to help clean the refrigerant of any impurities before it passes through the valve orifice. It is crucial that only liquid refrigerant passes through the valve due to the extreme pressure change after the refrigerant passes through. If there is any vapour particles in the refrigerant, they will change the refrigerant volume passing through the valve and the TXV will not be able to regulate the refrigerant flow through the evaporator. As discussed in Section 1.1, the receiver/dryer serves to clean the refrigerant of impurities, remove water and ensure that only liquid refrigerant flows to the TXV.

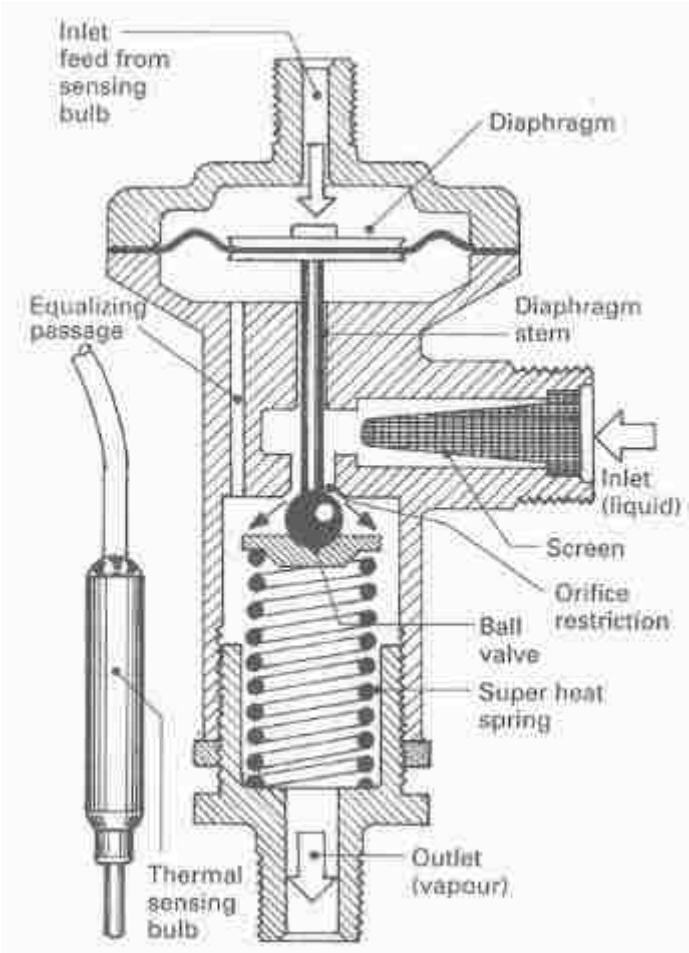

Figure F-12: Schematic of TXV cross-section. The refrigerant that enters the inlet feed from the sensing bulb acts to change the pressure acting on the diaphragm. The refrigerant enters the TXV in a liquid state and exits in a saturated liquid-vapour state. It is important that the amount of vapour exiting the TXV is limited, as this will decrease the evaporator capacity.

Sometimes the engineering schematic of a component does not provide a complete understanding of how it works. Therefore, Figure F-13 is included to compliment the schematic shown previously and provides the reader with a different perspective to assist in better understanding how a TXV functions.

Figure F-13: Cutaway of an actual TXV. The TXV geometry does not correspond directly to Figure F-12, but it serves to compliment the schematic previously shown.

The TXV sub-model within AMESim acts to mimic the performance of a real TXV with an internal TSB. Figure F-14 shows the TXV sub-model, ACTEVSB00, used for the AC model. Ports four and one represent the refrigerant entering the evaporator and ports two and three represent the refrigerant flowing past the TSB. TXV manufacturers normally provide TXV performance in the form of a four-quadrant graph with the following relationships [24]:

1. The refrigerant saturation curve and saturation curve of the thermal sensing bulb fluid
2. The evaporator outlet pressure as a function of the valve lift for different constant sub-cooling values
3. The evolution of the reference mass flow rate as a function of the valve lift
4. The evolution of the reference mass flow rate as a function of the evaporator outlet temperature.

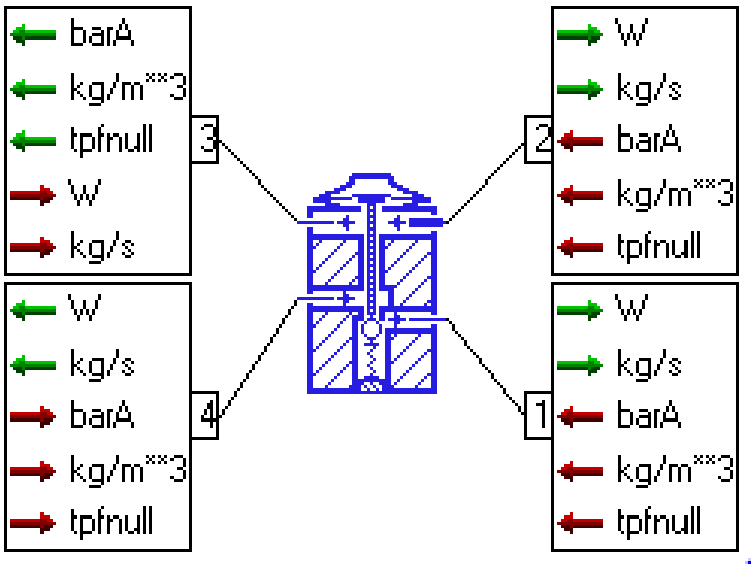

Figure F-14: AMESim TXV sub-model showing the incoming and outgoing parameters in the four ports. The green and red arrows represent outgoing and incoming information exchange. Ports 2 and 3 represent the refrigerant flowing into the thermal sensing bulb. Ports 4 and 1 represent the refrigerant flowing through the ball valve of the TXV and into the evaporator. Recall from Figure F-3 and Figure F-4, the explanation for the variables *W* and *tpfnull* [24].

With this TXV sub-model, the user specifies the saturation pressure curve of the bulb gas as well as the opening and full-opening temperature. The following discussion will highlight the equations that govern the TXV model within AMESim. The model considers the pressure acting on the TSB, the opening of the ball valve orifice and the refrigerant mass flow rate that passes through the valve.

The user-specified values for this sub-model are displayed in Table F-5 below:

Table F-5: Parameters that specify the AMESim thermal expansion valve sub-model. The significant variables such as the critical flow number and the *m* coefficient are explained in the discussion that follows.

TXV PARAMETERS		
PARAMETER	**VALUE**	**NOTES**
Maximum hydraulic diameter	2.05 mm	
Critical flow number	1000	Another way to express the Reynolds number. It is a function of the hydraulic diameter and pressure drop across the flow path. See Equation (F.21).
Maximum mass flow rate at reference conditions	0.1 kg/s	None
m coefficient	1	See Equation (F.26).
Bulb saturation pressure at 0°C	3.013 barA	None
Bulb saturation pressure at 10°C	3.5013 barA	None
Reference pressure	30 barA	None
Valve opening temperature at $P_{0°C}$	5°C	None
Valve full-opening temperature at $P_{10°C}$	35°C	None
Reference sub-cooling	5°C	None
Time constant	3 s	Accounts for the delay in TXV response due to inertia

Equation (F.14) calculates the bulb pressure of the gas. P_0, P_{10} and T_E represent the gas pressure at 10^oC, 0^oC and the refrigerant temperature exiting the evaporator, respectively. P_B represents the bulb pressure.

$$P_B = P_{0°C} + \frac{T_{evap}}{10} \cdot (P_{10°C} + P_{0°C}) \quad \textbf{(F.14)}$$

Equation (F.15) calculates the displacement of the rod controlling the opening of the ball valve previously shown in Figure F-12. The equation is given as a function of the refrigerant temperature and pressure exiting the evaporator. The parameters *A*, *k*, l_o and *h* represent the cross-sectional area of the rod, the spring stiffness, length of the spring with

no load and the rod displacement, respectively. AMESim calculates the rod displacement as a percentage of the maximum valve opening, represented by the variable $x_{\%}$.

$$x_{\%}\left(T_{evap}, P_{evap}\right) = \frac{A}{k} \cdot \left(P_{0°C} - P_{evap} + \frac{T_{evap}}{10} \cdot \left[P_{10°C} - P_{0°C}\right]\right) - l_0 \qquad \textbf{(F.15)}$$

Setting Equation (F.15) to the valve opening condition (T_{op}, $P_{0°C}$) and fully opened condition (T_{cl}, $P_{0°C}$) allows for the determination of the normalized valve displacement, represented by the term $x_{\%} / x_{max}$. The parameters T_{op} and T_{cl} represent the temperature values at the open and full opened valve position, respectively. Note that the valve opening and fully opened conditions correspond to the values zero (0) and x_{max}, respectively. The resulting two equations are shown below as Equation (F.16) and Equation (F.17), respectively:

$$0 = \frac{A}{k}\left(P_{0°C} - P_{0°C} + \frac{T_{op}}{10} \cdot \left(P_{10°C} - P_{0°C}\right)\right) - l_0 \qquad \textbf{(F.16)}$$

$$x_{max} = \frac{A}{k}\left(P_{0°C} - P_{0°C} + \frac{T_{cl}}{10} \cdot \left(P_{10°C} - P_{0°C}\right)\right) - l_0 \qquad \textbf{(F.17)}$$

The normalized valve displacement is obtained by first performing two equation subtractions {(F.15)-(F.16) and {(F.17)-(F.16)}. Second, perform a division of the equations {(F.15)-(F.16) }/ {(F.17)-(F.16)} Equation (F.18) shows the result of the equation manipulation.

$$x = \frac{x_{\%}}{x_{max}} = \frac{T_{evap} - T_{op}}{T_{cl} - T_{op}} + 10\left(\frac{P_{0°C} - P_{evap}}{P_{10°C} - P_{0°C}}\right) \cdot \left(\frac{1}{T_{cl} - T_{op}}\right) \qquad \textbf{(F.18)}$$

Equation (F.19) presents the refrigerant mass flow rate through the TXV. This equation is very similar to Equation 2.1, however the calculation for the friction factor, C_q is different for the TXV than the friction factor, f for the internal flow. AMESim calculates the mass flow rate as a normalized value with respect to the maximum mass flow rate at reference conditions. The max flow rate at reference conditions, shown in Equation (F.20), is computed by inserting the values of the variables at reference conditions into

Equation (F.19). The user specifies the reference pressure P_c^{ref} at a reference sub-cooling temperature. This value is obtained from the experimental testing conducted by the manufacturer supplying the TXV to the automotive manufacturer. The variable C_q represents the flow coefficient of the flow through the ball orifice valve.

$$\dot{m} = \rho \cdot C_q \cdot A \cdot \sqrt{\frac{2 \cdot \Delta P}{\rho}} \quad \textbf{(F.19)}$$

$$\dot{m}_{max} = \rho_{ref} \cdot C_{q_{max}} \cdot A_{max} \cdot \sqrt{\frac{2 \cdot (P_c^{ref} - P_0)}{\rho_{ref}}} \quad \textbf{(F.20)}$$

The following two equations show the calculation for C_q as well as an important assumption relating A to A_{max}. The parameters λ and λ_{crit} in Equation (F.21), represent the flow number calculated by the TXV sub-model and the critical flow number specified by the user, respectively. The critical flow number specifies when the transition of laminar to turbulent flow occurs [28]. Equation (F.21) serves to relate the flow coefficient, C_q, to the flow number, λ, thereby reducing the number of variables in Equation (F.27). In doing so, AMESim replaces an empirically determined value with a variable that depends on the hydraulic diameter and pressure drop of the flow through the ball valve orifice.

$$C_q = C_{q_{max}} \cdot \tanh\left(\frac{2\lambda}{\lambda_{crit}}\right) \quad \textbf{(F.21)}$$

The flow number is another way of expressing the Reynolds number of the flow through the ball valve orifice and is dependent upon the hydraulic diameter and pressure drop. It relates the pressure drop across the ball valve of the TXV to the refrigerant flow rate. Within the TPF library, singular pressure drop components, such as the TXV, the pressure drop and laminar-turbulent transition are expressed by the friction coefficient, K, and the critical Reynolds number, Re_{crit}. These two variables are related to the maximum

flow coefficient and critical flow number [28]. The four equations below describe the relationship between the friction coefficient, K, flow coefficient, C_q, Reynolds number, Re, and the flow number, λ.

$$C_{q\,max} = \frac{1}{\sqrt{K}} \quad \textbf{(F.22)}$$

$$Re_{crit} = C_{q\,max} \cdot \lambda_{crit} \quad \textbf{(F.23)}$$

Consequently, from the definitions shown in Equation (F.22) and Equation (F.23), the relationship between the Reynolds number and flow number can be expressed by Equation (F.24). This relationship was previously explained in the paragraph above, and is a consequence of the relationship in Equation (F.23). The flow number is a way of describing the type of flow through the ball valve of the TXV [28].

$$Re = C_q \cdot \lambda \quad \textbf{(F.24)}$$

Equation (F.25) displaying the calculation for the flow number, shows how the flow number is another expression of the Reynolds number. It is a ratio of the pressure drop to the flow rate across the ball valve of the TXV [28]. The term $2\Delta P/\rho$ is the velocity of the fluid squared. By comparing Equation (F.25) to Equation (2.7), it is clear that the same calculation is being conducted, but in a different way.

$$\lambda = \frac{dD_h}{\upsilon} \cdot \sqrt{\frac{2\Delta P}{\rho}} \quad \textbf{(F.25)}$$

In Equation (F.26), the power variable *m* represents a correlation parameter relating the normalized rod displacement, Equation (F.18), to the normalized flow cross-sectional area. The parameter, *x* below, represents the normalized displacement of the valve rod as derived by Equation (F.8).

$$\frac{A}{A_{max}} = x^m \qquad \textbf{(F.26)}$$

Equation (F.27), shows the final equation for the normalized mass flow rate. The normalized mass flow rate is a function of the normalized rod displacement, flow number, and pressure drop across the ball valve orifice. To obtain this equation, perform the equation division (F.19)/(F.20) and substitute {(F.25)} and {(F.26)}.

$$\frac{\dot{m}}{\dot{m}_{max}} = x^m \cdot \tanh\left(\frac{2\lambda}{\lambda_c}\right)\left(\frac{\rho}{\rho_{ref}}\right)\sqrt{\frac{\Delta P}{P_c{}^{ref} - P_0} \cdot \frac{\rho_{ref}}{\rho}} \qquad \textbf{(F.27)}$$

G.7 Evaporator

Unlike the compressor, TXV and condenser sub-models previously described, the evaporator does not use a pre-established AMESim model. The model was developed by Fiat to predict the performance of a four pass vertical tube and fin evaporator with micro channels.

The model concept treats the evaporator as a rectangular prism discretized into four passes, with each pass discretized by a user-specified number. The tube and air side equations are designed to account for different degrees of discretization. Figure F-15 shows a conceptual representation of the evaporator discretization, including the refrigerant and air flow paths. In Figure F-15, each column represents one pass of the evaporator and the number of rows shows the degree of discretization for each pass. The degree of discretization refers to the number of thermal masses representing one pass.

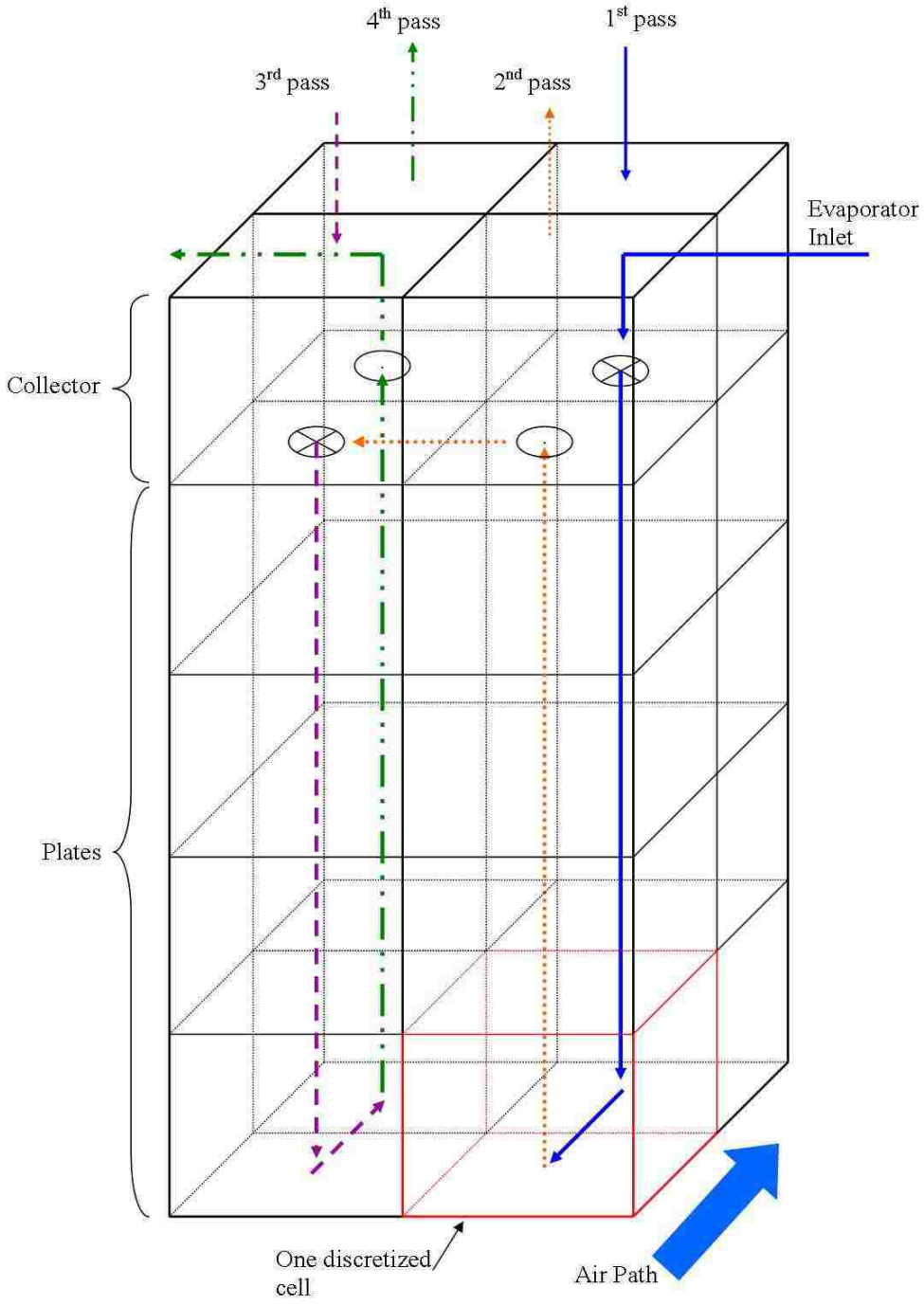

Figure F-15: Representation of the discretized evaporator model. This figure demonstrates how the AMESim evaporator model was organized and constructed. This model mimics a four pass vertical tube and fin evaporator with the plates and collectors treated separately. The air transfers heat to the plates containing saturated liquid-vapour and possibly superheated mixture. In this figure, the plates are discretized into four thermal masses; the red box, bottom right corner of the figure, highlights one discretized cell.

Figure F-15 shows the full evaporator model created in AMESim. The black and purple circled portions represent one pass for the refrigerant and one discretized cell, respectively. An explanation of the sub-models used to represent one evaporator pass will follow in the next section. For further information regarding the appropriate degree of discretization for the evaporator model, please see Appendix K.

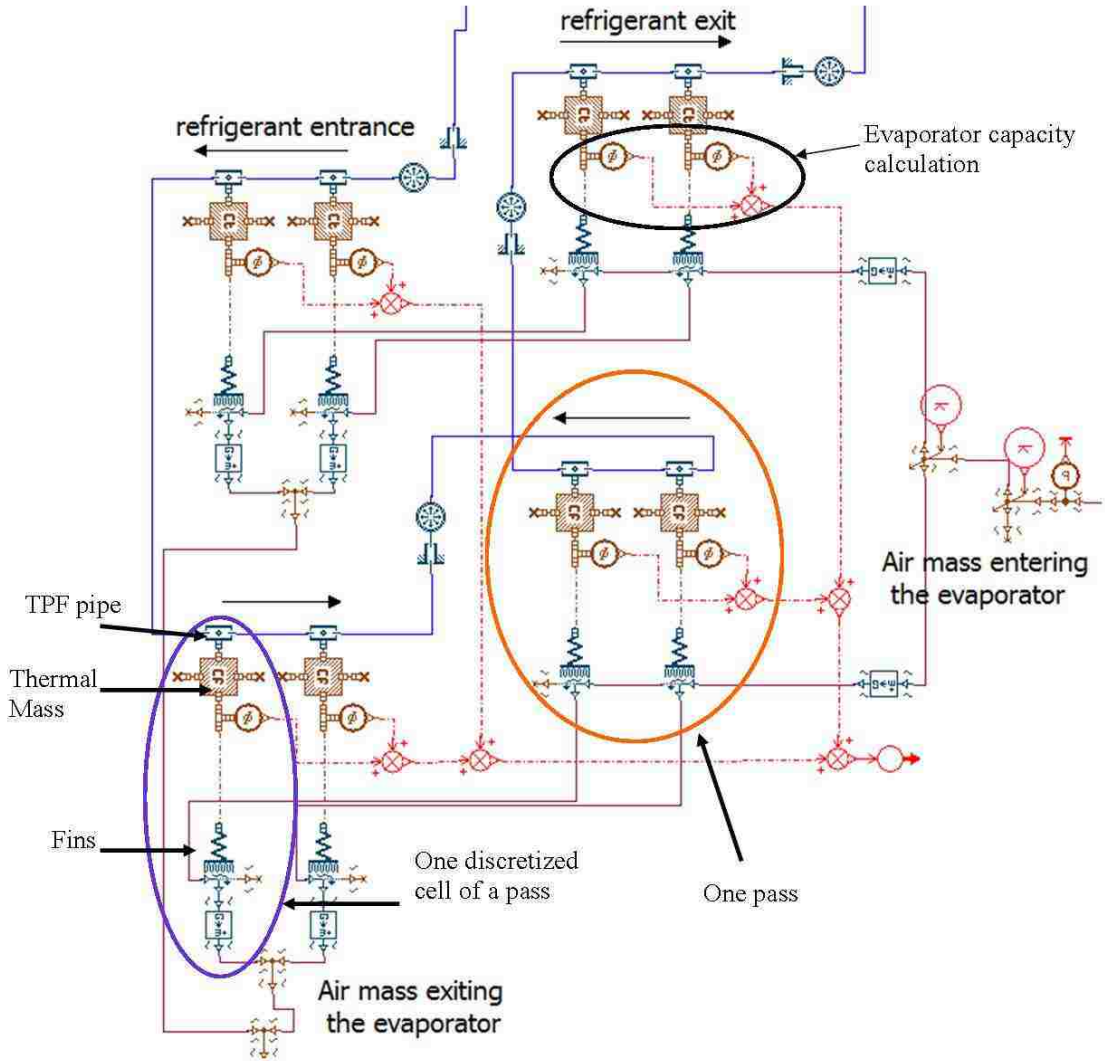

Figure F-16: AMESim evaporator model created from the conceptual model shown in Figure F-15. The black and purple circled portions represent one pass for the refrigerant and one discretized cell, respectively. This evaporator model has four refrigerant passes with a degree of discretization of two for each pass. Section 4.4 provides a further explanation for the chosen degree of discretization.

Tube Side Modeling - Evaporator

The tube side modeling consists of three sub-models: TPFHE0001 to model a pipe for two-phase flow, and TPFCH000 and TPFPIN00 for modeling the collectors. The former is a pipe capable of handling two-phase flow and exchanging heat with a thermal mass.

The methods AMESim uses for calculating the fluid properties depends on the refrigerant phase. Recall from Section 1.3 that the calculations are based on a homogeneous fluid model and the two phases, liquid and vapour, are treated as a single phase possessing mean fluid properties. AMESim uses the state variables pressure and density when determining the refrigerant phase, which was previously discussed in Section 3.2.1.

The calculation of the pressure drop and heat transferred within the pipe sub-model TPFHE0001 depends on the refrigerant phase. In single phase flow the Churchhill correlation, previously described in Section 3.2.5, is used to calculate the friction coefficient of the inner pipe surface. The convection coefficient is calculated from the Nusselt number for laminar flow, 3.66, and the Gnielinski correlation, Equation (F.13), for the turbulent regime. In two phase flow the friction coefficient is calculated using the McAdams correlation, see Equation (2.13), homogeneous correlation model.

AMESim uses different convection coefficient correlations depending on whether the refrigerant is boiling or condensing within the tubes. This is determined by checking the sign of the temperature difference between the pipe outlet, for one discretized cell, and the wall temperature of the same discretized cell. If the sign is negative, AMESim uses the VDI for vertical tube boiling correlation and if positive the Shah condensation correlation [24]. Figure F-17 displays the AMESim icon for the two-phase flow (TPF) pipe, previously labelled in Figure F-16.

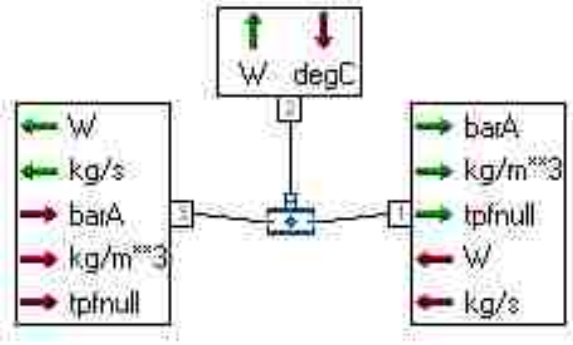

Figure F-17: Icon representing the two-phase pipe sub-model, TPFHE0001, within AMESim. Port 3 and 1 represent the entrance and exit of the pipe, respectively. The heat transfer between the pipe and thermal mass occurs at port 2. The green and red arrows represent outgoing and incoming information to the sub-model, respectively. See Figure F-3 and Figure F-4 for the explanation of for the variables *W* and *tpfnull* [24].

The sub-model TPFCH000 is an adiabatic chamber and represents volumes where the refrigerant collects before flowing through the subsequent evaporator passes. The purpose of this sub-model is to calculate the pressure and density time derivatives. The coupling of TPFCH000 with the TPF pipe sub-model, TPFHE0001, dictates the transient system behaviour. The adiabatic chamber sub-model is an element which has energy storage of a fluid volume. The TPF pipe sub-model is an element which computes energy dissipation, typically in the form of a pressure loss [28]. The last sub-model, TPFPIN00 is present only as a connection between the pipe and chamber sub-models previously mentioned [24]. Figure F-18 and Figure F-19 display the AMESim icons for the adiabatic chamber and pipe connection.

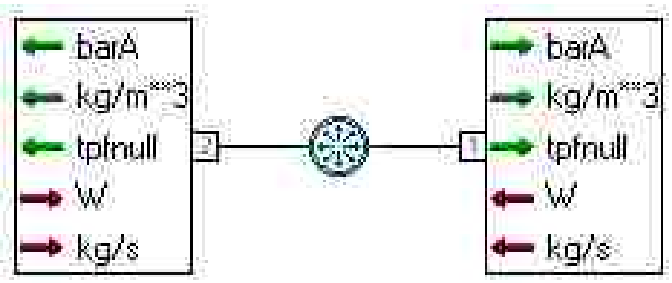

Figure F-18: Icon representing the adiabatic chamber sub-model, TPFCH000, within AMESim. The green and red arrows represent outgoing and incoming information to the sub-model, respectively [24].

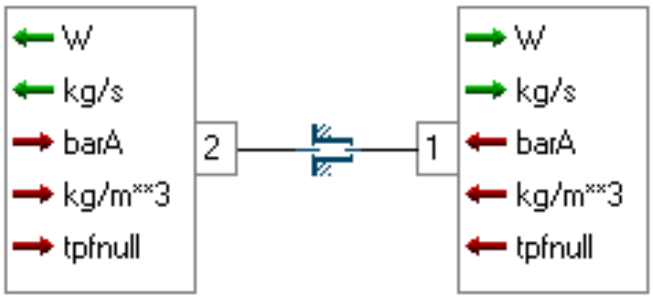

Figure F-19: Icon representing the pipe connection sub-model, TPFPIN00. The green and red arrows represent outgoing and incoming information to the sub-model, respectively[24].

Air Side Modeling

The air side modeling incorporates one sub-model, TPFCVMAFW001, which simulates the thermal convective heat exchange between moist air and a finned wall. Figure F-20 and Figure F-21, obtained from the AMESim help files, show the fin geometry definitions for the evaporator [24]. These definitions are very similar to the condenser geometry specifications in Figure F-6 and Figure F-7. Recall that the fin pitch definition within AMESim is half the value of the conventional definition. The two figures below show a horizontal tube and fin configuration, even though the experiments used a vertical tube and fin evaporator. Appropriate considerations were made when specifying the evaporator width, height and correlations for vertical tube layouts.

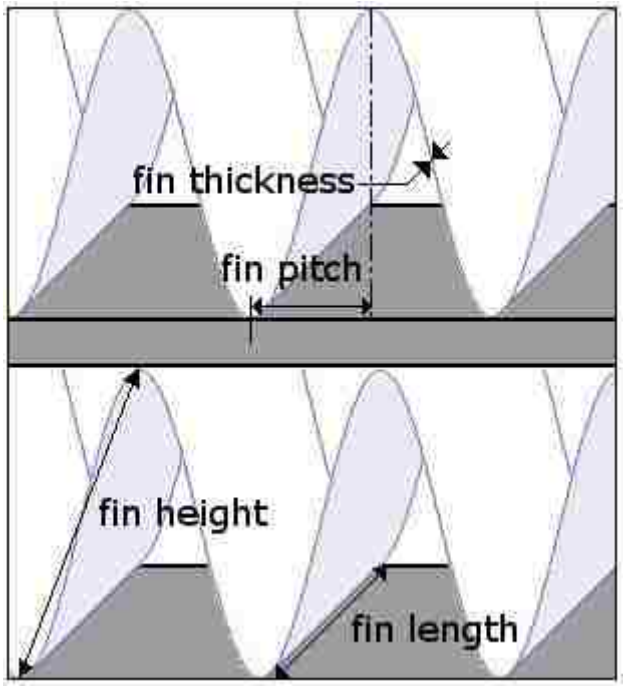

Figure F-20: Fin geometry specifications for the sub-model TPFCVMAF001 [24]. The fin pitch definition within AMESim is half the value of the conventional definition. The fin length is equivalent to the evaporator depth or thickness.

In Figure F-21, the variables represent the following dimensions:

- D evaporator depth, also called the evaporator thickness
- W evaporator width, also called the evaporator length
- H evaporator height
- L the distance between the bottom and top surfaces of the upper and lower refrigerant pipes, respectively.

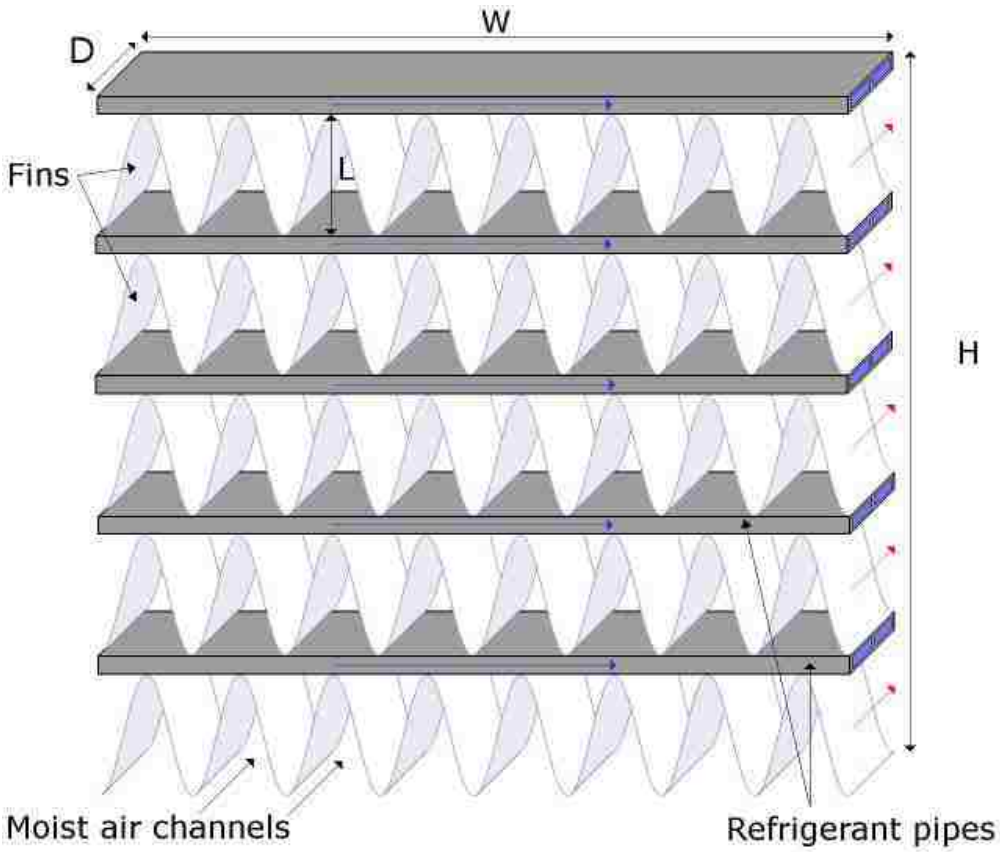

Figure F-21: Overall evaporator dimensions for the sub-model TPFCVMAF001 [24]. Specification of the evaporator width, height and correlations consider a vertical tube and fin layout contrary to the setup shown in the figure above. The number of microchannels is a user-specified value, and is not limited to only two.

The heat transfer between the moist air and the evaporator fins is affected by condensation of the cooled air. By comparing the air inlet absolute humidity (ah_{in}) to the saturation absolute humidity of air at the wall temperature ($ah_{w,sat}$) AMESim determines whether condensation occurs. Condensation occurs if the following relation is true:

$$ah_{w_{sat}} < ah_{in}$$

The capacity of the evaporator is measured using heat flow sensors placed between the aluminum mass, representing the fin and tubing, and the air side convection model. The sum of the heat flow from all of the passes represents the evaporator capacity.

Table F-6 below displays the parameters for the evaporator model. The *A*, *B* and *C* coefficients for the Nusselt equation are calibrated using optimization simulation software within AMESim. AMESim determines these values by ensuring that the simulation error of the evaporator capacity and pressure drop is minimal compared to the experimental values.

Table F-6: Tube and fin evaporator parameters. These values correspond to one discretized cell using one pass. In the case of the evaporator in the present thesis, the final evaporator model has four passes and two discretized cells per pass.

PARAMETER	VALUE	UNIT	NOTES
TUBE SIDE PARAMETERS			
Length	0.0925	mm	None
Cross-sectional area	196.67	mm^2	None
Hydraulic diameter	0.9865	mm	None
Absolute roughness	0	---	None
Regular pressure drop gain	1	---	None
Heat transfer gain	1	---	None
Single-phase laminar Nusselt number	3.66	---	None
ALUMINUM MATERIAL PROPERTIES			
mass	0.129	kg	None
AIR SIDE PARAMETERS			
Convective exchange area	257250	mm^2	None
Cross-sectional area	7075.58	mm^2	None
Ratio cross-sectional to frontal area	0.759	---	None
Characteristic length of the exchange	3.252	mm	None
Relative finned area	83.6	%	None
Fin length	29	mm	parallel to the air flow
Fin height	10	mm	perpendicular to the air flow
Fin thickness	0.08	mm	None
A coefficient	0.96	---	These three parmameters relate to the Nusselt calibration equation previously shown for sub-model HEATPFHE02 in Section 3.2.5.
B coefficient	0.421	---	
C coefficient	0.4	---	

APPENDIX G Cabin Model Description

Since the complete AC loop was calibrated using a Cabin Cool-Down (CCD) test, the ability to predict the heat transfer processes within the cabin is critical. The other transient test cycles use the feedback cabin air temperature to control the volume flow rate of fresh air through the blower model. Thus, the cabin model is an important component, and requires accurate calibration to predict the air temperature profile. The development of the cabin model follows the Lumped Capacitance Method described in the literature [38-41]. Figure G-1 shows the AMESim model for the cabin. A breakdown of each lumped mass will follow in the discussion to provide a complete understanding of the model development. The current model includes the following lumped masses: roof, front windshield, dashboard, side windows, rear windshield, front seats, doors and side paneling.

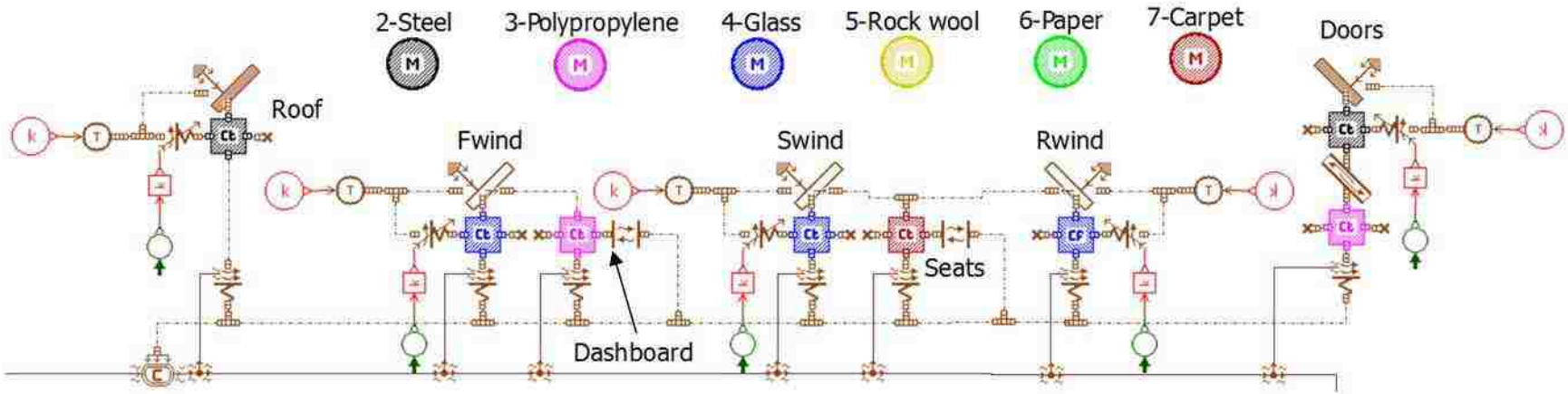

Figure G-1: AMESim cabin model. This uses the Lumped Capacitance Method, which treats the lumped masses for averaged state variables. The model is broken down into the following lumped masses, from left to right in the figure above: roof, front windshield and dashboard, side windows and seats, rear windshield and seats, and doors and interior plastic paneling. The lumped masses transfer heat to the moist cabin air independently of one another. The green arrows with a circle represent the user-specified velocity profile of the vehicle for constant ambient conditions. The cabin model is very important as the operational controls for other AC components in the transient simulations utilize the value of the cabin air feedback temperature.

The air is treated as a single lumped mass, with properties at the average interior air temperature. Normally the air temperature varies from front to rear, side to side and top to bottom within the cabin, however this effect is ignored with this model. All of the lumped masses transfer heat to or from the interior air. Each heat transfer process is calculated in parallel, so each case acts independent of the others.

In theory, adding more lumped masses to the model increases the prediction accuracy. However, this increases the complexity of the model and the number of unknown parameter values such as convection coefficients, characteristic lengths and heat transfer areas. Thus, the engineer must decide between the importance of minimal simulation error and large computation times.

Appendix A contains a table showing the significance of each thermal mass of the cabin model. Thus in the following sub-sections, for any general statements regarding the significance of a specific sub-model, please see the results of Appendix A.

G.1 Roof System

The roof accounts for a significant portion of the total heat transferred to the cabin. The model consists of the following heat transfer processes:

1. solar radiation for opaque materials;
2. external convection;
3. internal convection;
4. an ambient temperature source.

The roof model is simplified to simulate the heat transfer of a flat plate; the heat transfer effects of the interior roof liner are not included. The roof material uses the default steel properties of AMESim. The heat transfer processes associated with the roof liner are ignored since it was found to have a negligible effect on the model's ability to predict the experimental cabin air temperature. The opaque solar radiation model accounts only for

the absorptivity and reflectivity of the roof material. Figure G-2 displays the heat transfer processes considered in the roof system.

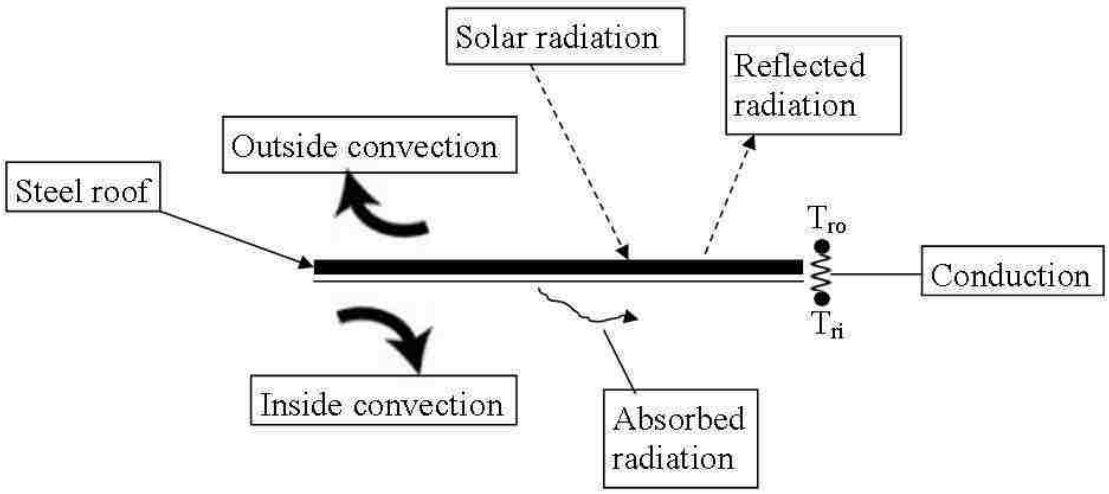

Figure G-2: Conceptual representation of the roof heat transfer system.

G.2 Front Windshield and Dashboard

The front windshield is another area of the vehicle from which a large amount of heat enters the cabin. The model consists of the following heat transfer processes:

1. solar radiation for transparent materials;
2. external convection;
3. internal convection for the front windshield and dashboard;
4. internal radiation heat transfer;
5. an ambient temperature source.

Due to the configuration of the solar lamps in the testing chamber, the model assumes all solar radiation transmitted from the front windshield is absorbed by the dashboard. See Section 3.7.1 for further clarification. The dashboard material uses the default properties of polypropylene within AMESim.

Any heat transfer between the cabin air and the dashboard is represented by radiation heat exchange sub-model occurring between two surfaces. This effect of this sub-model on the CCD calibration is considerable toward the end of the simulation. By neglecting radiation heat transfer between the interior surfaces of the vehicle with the cabin air, the model predicts a much cooler cabin air temperature at the end of the test. However, the parameters of this radiation exchange sub-model are uncertain and thus depend highly on calibration with the CCD test. See Appendix A for the significance of the radiation heat transfer from the front and rear seats. Figure G-3 displays the heat transfer processes considered in the front windshield and dashboard system.

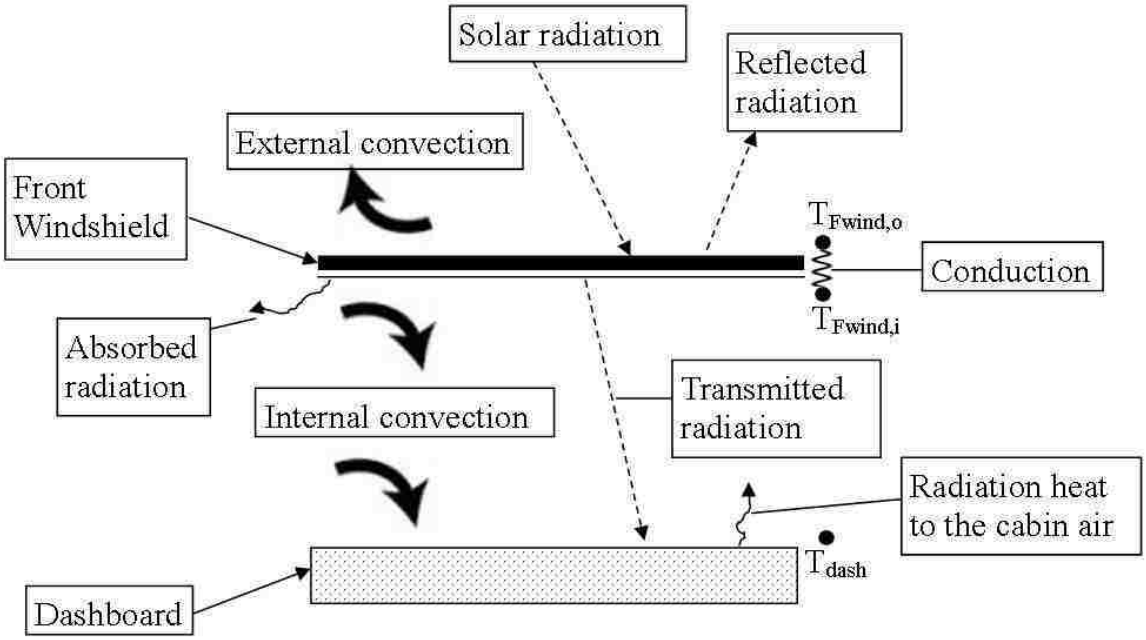

Figure G-3: Conceptual representation of the front windshield and dashboard system. This figure compliments Error! Reference source not found.

G.3 Side Windows and Seats

The heat exchange processes of the side windows and seats are identical to ones used for the front windshield and dashboard. The model consists of the following heat transfer processes:

1. solar radiation for transparent materials;
2. external convection;
3. internal convection for the side windows and seats;
4. internal radiation heat transfer;
5. an ambient temperature source.

Despite the configuration of the solar lamps relative to the vehicle, the model assumes that the seats absorb all of the heat transmitted from the side windows and rear windshield. The side windows and seats are represented by two thermal capacity sub-models.

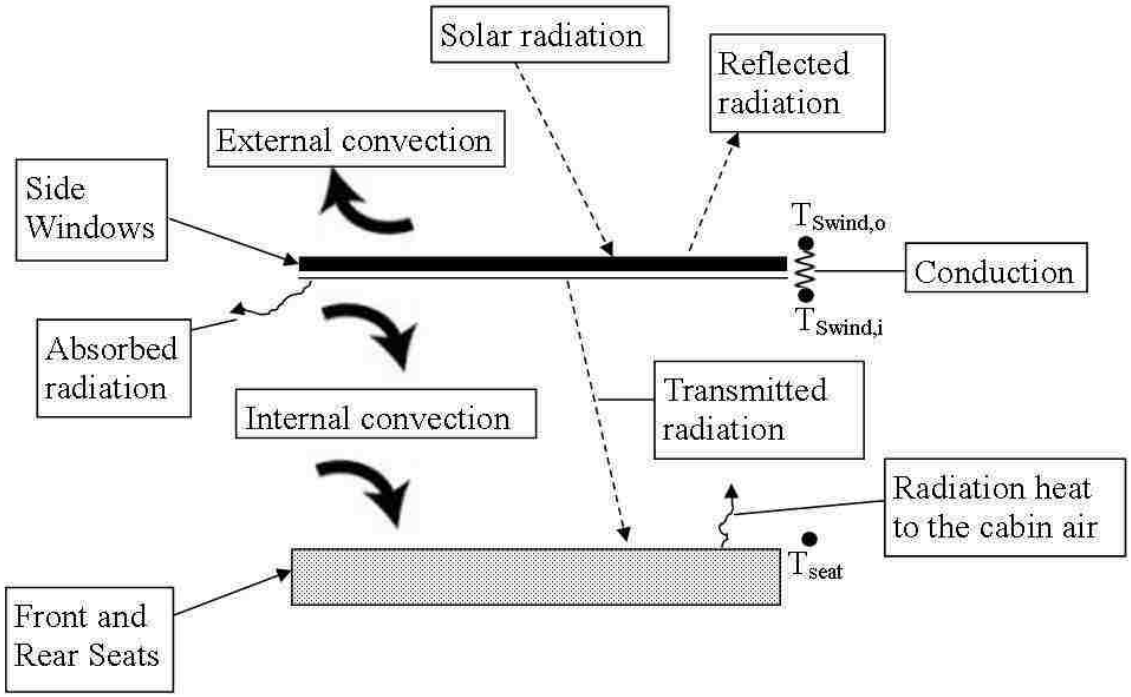

Figure G-4: Conceptual representation of the side windows and seats system. This figure compliments

G.4 Rear Windshield

As with the front windshield and side windows, the heat transfer processes of the rear windshield are identical. Absorbed radiation by the rear windshield transfers heat to the cabin via an internal convection sub-model, and transmitted radiation is absorbed by the

seats. The seats also emit radiation heat to the cabin. Please refer back to Figure G-3 and Figure G-4 for the heat transfer processes considered and the model created in AMESim. The seat parameters are the same for this system and are not repeated in the appendix.

G.5 Doors and Interior Side Paneling

Due to the large surface area, the doors contribute significantly to the heat transferred to and from the interior. The model consists of the following heat transfer processes:

1. solar radiation for opaque materials;
2. external convection;
3. convection heat transfer for a small enclosure (air gap);
4. internal convection;
5. an ambient temperature source.

The third heat transfer process models free convection of an air gap. Neglecting this process significantly alters the simulated interior air temperature curve. The air gap acts as a layer of insulation between the steel doors and the plastic paneling of the interior. The geometry of this area is very complex due to the varying side paneling shapes, electronic equipment and exterior profiling. Thus, a simplified heat transfer process is considered where a continuous air gap is assumed between the doors and the paneling.

The calculated heat transfer is dependent upon the Nusselt number shown in Equation (G.1). The variables C, n, m and p are all calibration coefficients to approximate the real Nusselt number and are dependent upon the aspect ratio *t/l*. The variable *t* and *l* represent the thickness and length of the enclosed gap. The accuracy of the Nusselt number directly affects the accuracy of the convection heat transfer coefficient and the model's ability to predict the heat transfer process.

$$Nu = C * Ra^n \cdot Pr^m \cdot \left(\frac{t}{l}\right)^p \qquad \textbf{(G.1)}$$

Figure G-4 displays the heat transfer processes considered in the side windows and seats system.

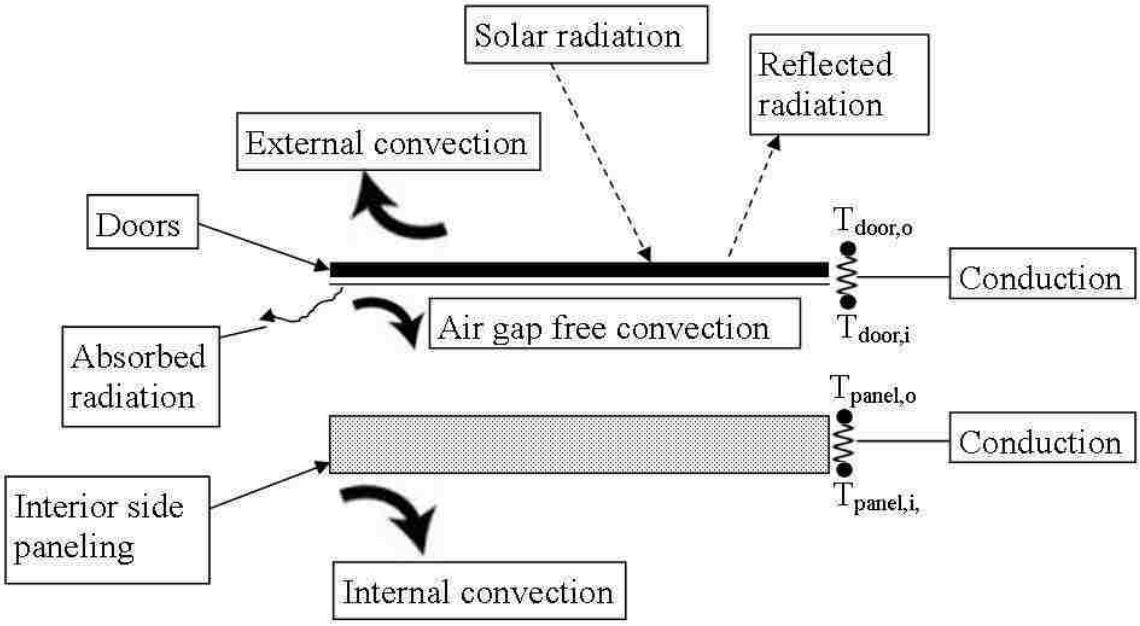

Figure G-5: Conceptual representation of the doors and side paneling system. This figure compliments.

APPENDIX H Vent Model Setup

This model is located between the air outlet of the evaporator and the air inlet of the cabin. It simulates the temperature change of the air as it travels through the plastic pathways of the heating, ventilation and air conditioning (HVAC) system of the vehicle. The air temperature increases as it flows through the pathways since the temperature of the evaporator air outlet would be uncomfortable for passengers. Figure H-1 shows the vent model created in AMESim.

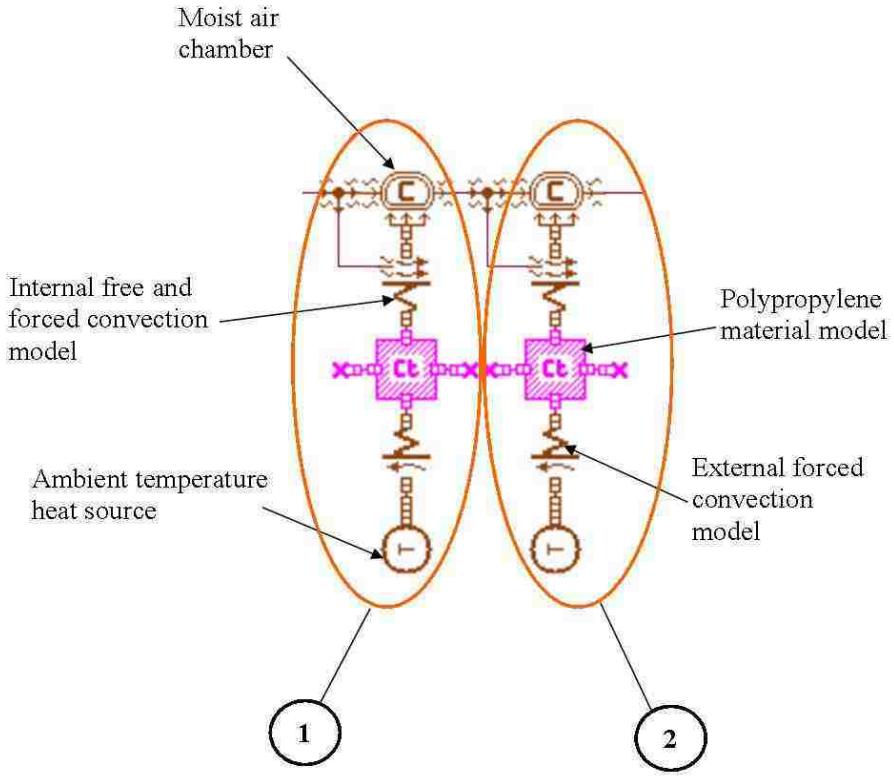

Figure H-1: AMESim HVAC venting system. This system represents the flow of air that exits the evaporator and travels through the HVAC channels to the cabin model. As the air travels through the channels it is heated slightly because there is a large temperature difference between the air just exiting the evaporator and the ambient/underhood air temperatures.

From Figure H-1, the vent system is divided into two heat transfer processes with two different ambient temperatures. The first process involves internal convection, accounting for forced and free convection heat transfer between the air exiting the

evaporator and the plastic channelling. There is also an external free convection model between the ambient air and the plastic channelling. The volume of the plastic channelling, labelled in Figure H-1 as the moist air chamber, is 0.01 m^3. This sub-model computes the temperature and absolute humidity of the air within the volume. The water production rate for this sub-model is zero (0) g/h. The temperature of the air outside the plastic channelling is set to the ambient air temperature of the climatic test chamber.

The second heat transfer process is similar to the first. The only difference lies in the characteristic length of heat exchange, where the length is half of the first heat transfer process.

Table H-1 displays the parameter values for the AMESim generated internal and external convection sub-models for the first heat transfer process. These models are specifically for moist air processes since the relative humidity of the air leaving the evaporator is usually close to 100%.

Table H-1: Parameters for the internal and external AMESim convection sub-models for the first heat transfer process of the venting system.

PARAMETER	VALUE	UNIT	NOTES
MOIST AIR CHAMBER			
Chamber volume	0.01	m^3	
Water production	0	g/h	
INTERNAL FORCED AND FREE CONVECTION			
Convection heat exchange area	3.50E+05	mm^2	
Characteristic length of heat exchange	50	mm	This value is 25mm for the second heat transfer process, see Figure H-1 for further clarification
Cross-sectional area	1.00E+04	mm^2	None
Free convection inclination angle	0	deg	None
Gain of heat forced convection coefficient	1	---	None
Gain of heat free convection coefficient	1	---	None
Forced Nusselt number	$Nu_{forced} = 0.037 \cdot Re^{(0.8+0.2)} \cdot Pr^{0.33}$		
Free Nusselt number	$Nu_{free} = 0.68 + \frac{(0.67 \cdot (Pr \cdot Gr)^{0.25})}{\left(1 + \left(\frac{0.492}{Pr}\right)^{9/16}\right)^{4/9}}$		

EXTERNAL FREE CONVECTION			
Convective heat exchange area	5.00E+05	mm^2	None
Characteristic heat exchange length	25	mm	None
Wall inclination angle	0	deg	w.r.t the horizontal
fluid pressure	1.03	barA	set to ambient pressure of the climatic chamber
Moist air relative humidity	30	%	set to ambient relative humidity of the climatic chamber
Free Nusselt number	$Nu_{free} = 0.68 + \frac{(0.67 \cdot (Pr \cdot Gr)^{0.25})}{\left(1 + \left(\frac{0.492}{Pr}\right)^{9/16}\right)^{4/9}}$		

APPENDIX I Blower and Air Recirculation Model Setup

This model is located between the cabin system and the evaporator. To make the explanation of this model easier, it is broken down into four different sections. Please see Figure I-1 for further clarification.

The first section calculates the temperature, pressure, relative humidity and volume flow rate of fresh air brought into the car by the blower. The fresh air intake depends on the value of the recirculation signal source, labelled in Figure I-1. The signal source curve is specified by the user. The volumetric flow rate of the blower ranges from zero to 400 m^3/h. The user also specifies this signal source to correspond to the experimental blower volumetric rates.

The air mass flow rate of the blower, and consequently the air that flows over the evaporator, is shown in Equation (I.1) below. The model uses this equation to calculate the mass flow rate of the fresh air intake. The blower and air recirculation model also uses this equation to calculate the relative humidity and temperature of the re-circulated/fresh air mixture in the third section.

$$\dot{m}_b = y * \frac{z}{100} + x * \frac{100-z}{100} \qquad \textbf{(I.1)}$$

In the equation above, *x* represents the mass flow rate of fresh air, *y* represents a cabin air property and *z* represents the recirculation percentage. In the first part of the blower and air recirculation model, the value of *y* is zero. The reason for the inclusion of the variable y, is because this equation is used in the third part of the blower and air recirculation model. The variable *y* is redundant in Equation (I.1). The sub-model containing the function that performs this calculation is labelled in Figure I-1.

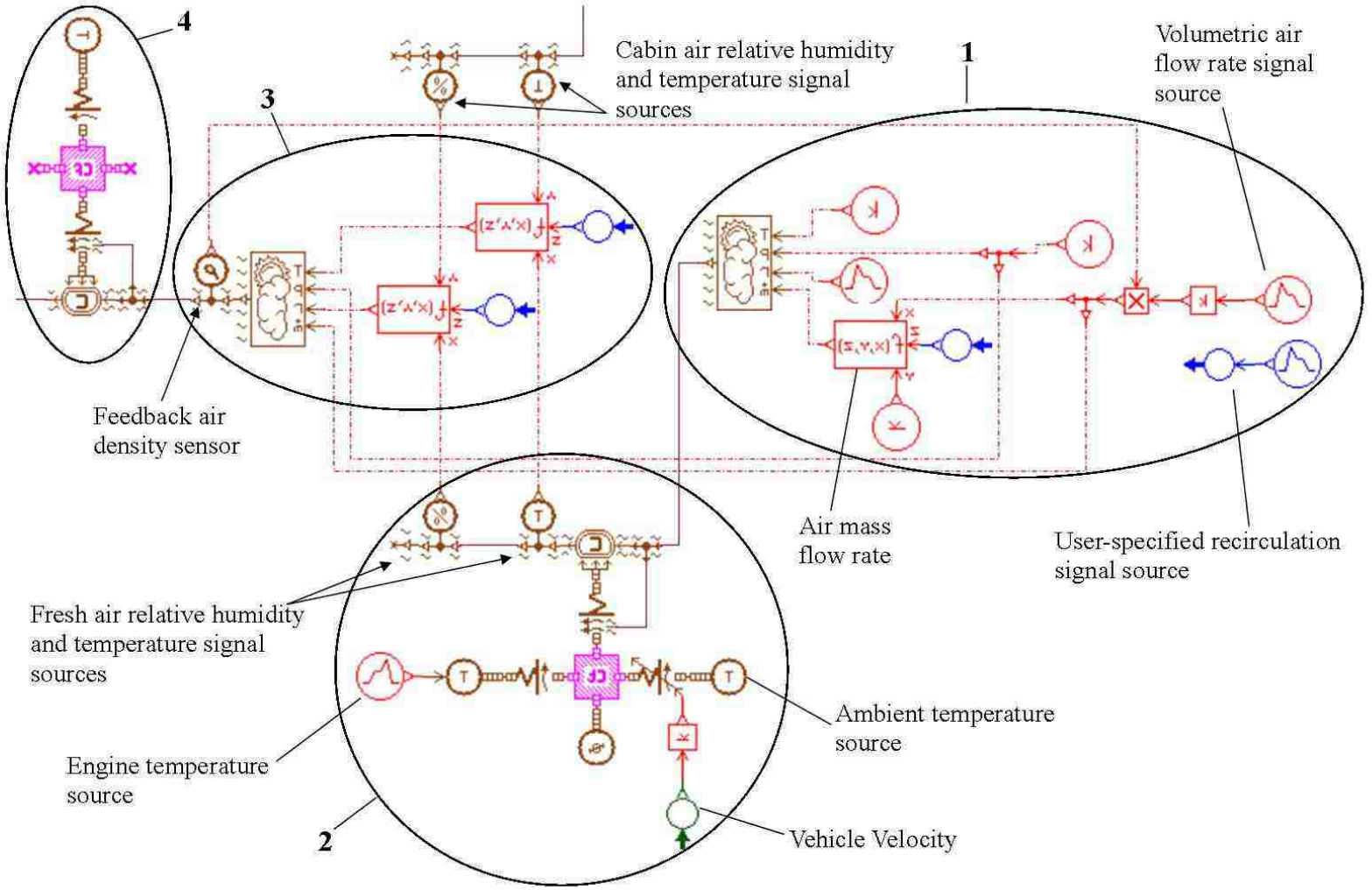

Figure I-1: Blower and Air Recirculation model as it appears within AMESim.

The second stage of the model, simulates heat transfer to the fresh air from the engine, vehicle velocity at ambient air temperature, and a solar radiation source. The air mixture and plastic intake channels exchange heat via an internal convection sub-model. The thermal mass for the plastic intake channels uses polypropylene material properties. An external convection sub-model simulates the heat transfer due to the vehicle velocity in ambient air. An internal convection sub-model simulates the heat transfer from the engine to the external air intake, in an effort to mimic the heat transfer process under the vehicle hood. Table I-1 summarizes important parameters for the second stage of the blower and air recirculation model.

Table I-1: Parameters for the internal and external convection sub-models in the second stage.

PARAMETER	VALUE	UNIT	NOTES
VEHICLE VELOCITY IN AMBIENT AIR			
Convective heat exchange area	400000	mm^2	None
Characteristic length of the heat exchange	10	mm	None
Gain of forced heat convection coefficient	1	---	None
Forced Nusselt number	$Nu_{forced} = 0.037 \cdot Re^{(0.8+0.2)} \cdot Pr^{0.33}$		
Free Nusselt number	$Nu_{free} = 0.68 + \frac{(0.67 \cdot (Pr \cdot Gr)^{0.25})}{\left(1 + \left(\frac{0.492}{Pr}\right)^{9/16}\right)^{4/9}}$		
SOLAR RADIATION SOURCE			
Heat Flow	90	W	None
ENGINE HEAT SOURCE			
Convective heat exchange area	2000000	mm^2	None
Charactistic length of heat exchange	5	mm	None
Wall inclination angle	0	deg	w.r.t. the horizontal
Free Nusselt number	$Nu_{free} = 0.68 + \frac{(0.67 \cdot (Pr \cdot Gr)^{0.25})}{\left(1 + \left(\frac{0.492}{Pr}\right)^{9/16}\right)^{4/9}}$		
POLYPROPYLENE THERMAL MASS			
Mass	10	kg	None

Moist air property sensors send the temperature and relative humidity for re-circulated air and fresh air to the third stage of the model. Here, the re-circulated/fresh air mixture properties are calculated using the same form as Equation (I.1). However, instead of calculating the mass flow rate, the equation calculates the relative humidity and the temperature of the fresh/re-circulated air mixture. The variable *y* represents the feedback signal for the cabin air temperature and relative humidity. The variables *x* and *z* represent the fresh air properties and recirculation percentage, respectively.

Finally, the air properties are sent to the fourth stage of the model. Similar to the method used in the vent model (refer back to Section 3.4) the air is heated or cooled as it travels from the blower to the evaporator. Table I-2 below summarizes important parameters for the internal and external convection sub-models for the last stage of this model.

Table I-2: Parameters for the internal and external convection sub-models in the fourth stage of the blower sub-model

PARAMETER	VALUE	UNIT	NOTES
EXTERNAL CONVECTION			
Convective heat exchange area	1.50E+06	mm^2	None
Characteristic length of heat exchange	50	mm	None
Wall inclination angle	0	deg	None
Free Nusselt number	$Nu_{free} = 0.68 + \frac{(0.67 \cdot (Pr \cdot Gr)^{0.25})}{\left(1+\left(\frac{0.492}{Pr}\right)^{9/16}\right)^{4/9}}$		
POLYPROPYLENE THERMAL MASS			
Mass	5.07	kg	None
INTERNAL CONVECTION			
Convective heat exchange area	1.50E+06	mm^2	None
Characteristic length of heat exchange	25	mm	None
Cross-sectional area	2000	mm^2	None
wall inclination angle	0	deg	w.r.t. the horizontal for free convection
Gain of forced convection coefficient	1	---	None
Gain of free convection coefficient	1	---	None
Forced Nusselt number	$Nu_{forced} = 0.037 \cdot Re^{(0.8+0.2)} \cdot Pr^{0.33}$		
Free Nusselt number	$Nu_{free} = 0.68 + \frac{(0.67 \cdot (Pr \cdot Gr)^{0.25})}{\left(1+\left(\frac{0.492}{Pr}\right)^{9/16}\right)^{4/9}}$		
MOIST AIR CHAMBER			
Chamber volume	0.01	mm^3	None
Water production	0	g/h	None

APPENDIX J Cabin Cool-down (CCD) Test Cycle

The vehicle velocity is a controlled input parameter as a function of the simulation time. Since the compressor is mechanically connected to the engine, it is proportional to the engine revolutions per minute (RPM) and vehicle velocity. The pulley ratio for the compressor is 1.277. The compressor revolutions per minute (RPM) map is a user-controlled input as a piecewise signal source. This map corresponds to the experimental compressor RPM map. Note from Figure J-1, that the effect of changing gears on the compressor RPM map is not included for this testing cycle. This is a transient testing cycle since the cabin air temperature is being measured as a function of time, however each vehicle and compressor RPM setting is constant for long intervals.

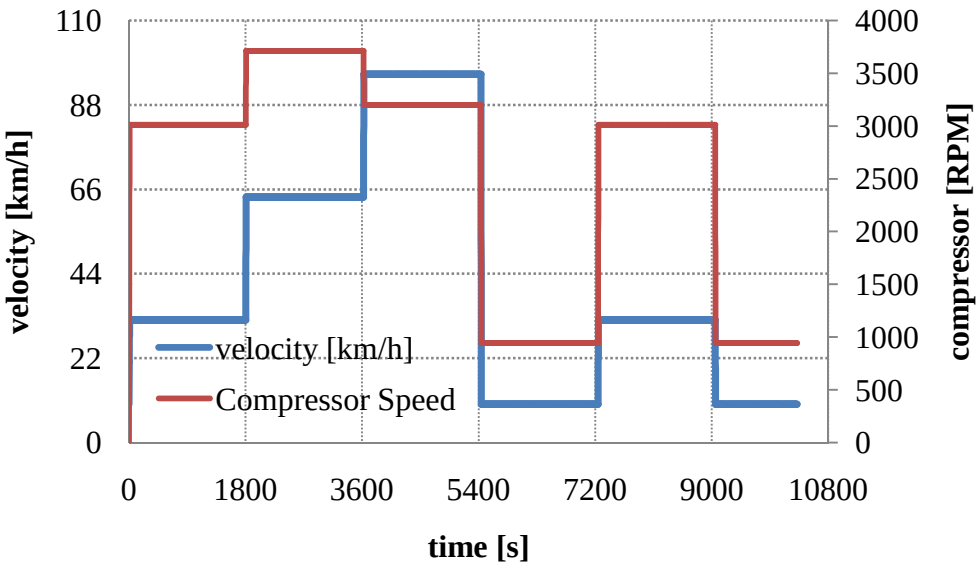

Figure J-1: Vehicle velocity and compressor RPM map for the cabin cool-down (CCD) test cycle. The left ordinate axis corresponds to the vehicle velocity and the right ordinate axis corresponds to the compressor RPM. This is a user-specified input curve, and does not account for acceleration times, or fluctuation in compressor RPM from gear changing.

There is a secondary control for the compressor to prevent ice formation from moisture condensing out of the cooled air. Once the air temperature entering the vents drops below the minimum allowable value, set to -2^{o}C, the compressor shuts off. Figure J-2 below highlights the two compressor controls.

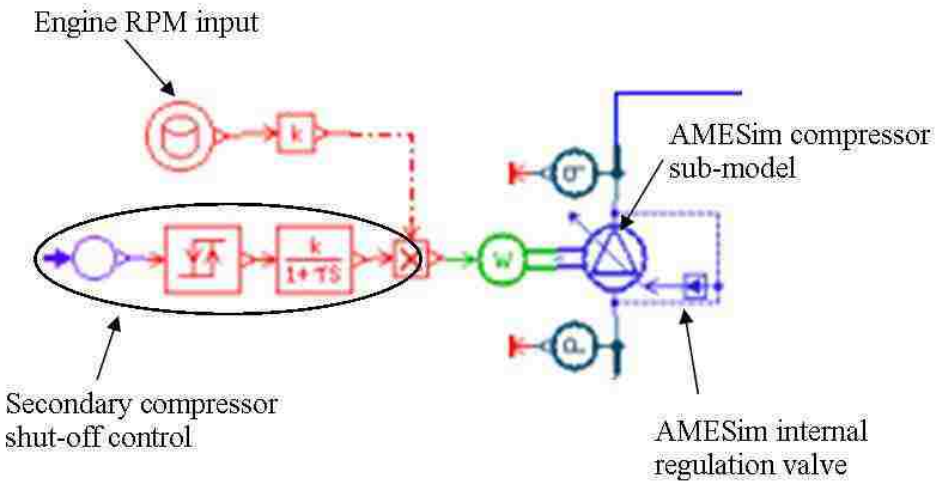

Figure J-2: compressor control for the CCD model.

Simulation of the vehicle velocity in the climatic chamber occurs by blowing air over an idle vehicle. The vehicle speeds for the Fiat experiment differ slightly from the standard vehicle speed schedule outlined by the test procedure. Table J-1 below, displays the standard and experimental interval times for the cool-down cycle. For the first 7200 seconds the air conditioning is in 100% recirculation mode and in 100% fresh air mode for the last 3600 seconds of the cycle.

Table J-1: Comparison of the vehicle speed interval times for the Fiat experiment and the standard schedule.

Vehicle Speed Range [km/h]	Standard Time [s]	Actual Time [s]
100% Recirculation		
32	1800	1800
64	1800	1820
96	1800	1810
10	1800	1810
100% Fresh Air Mode		
32	1800	1810
10	1800	1260

During the experimental test conducted at Fiat, an error was made which influenced the cool-down air temperature curve. This error occurred during last two phases of the CCD test, where the AC operates in fresh air mode. In the experiment conducted by Fiat the switch from recirculation to fresh air mode did not occur at the second last cycle. Instead

of making the switch from recirculation to fresh air at 7240 seconds, the operator made the switch at 8660 seconds. This difference in the conduction of the experiment is mimicked by the AC model for the CCD simulation

Previously described in Section 3.2.5, the implementation of the AMESim condenser model allows for different ways of specifying the velocity and temperature data. For the CCD test, velocity and temperature maps of the condenser frontal area are inputted into the reference condenser sub-model, HEATCONDREF120.

The blower inlet conditions, shown in Table J-2 are defined by the temperature, pressure, relative humidity and mass flow rate of the inlet ambient air. The recirculation is set to 100% for 7260 seconds and 0% for the remainder of the CCD test. The volumetric air flow rate is set to the maximum capacity for the entire CCD test. The input is a volumetric air flow rate which is converted into a mass flow rate based on the density of the incoming air.

Table J-2: Cabin Cool Down (CCD) inlet air conditions for the blower.

Parameter	Value	Constant or Variable
Temperature	43 ^{o}C	Constant
Pressure	1.01 kPa	Constant
Relative Humidity	30%	Constant
Mass Flow rate	400 m^3/h	Constant

The vehicle test took place in a climatic controlled chamber, however the ambient conditions vary slightly with respect to time. Figure J-3 displays the variation of the ambient relative humidity for the experimental testing. This curve is an input to the blower and air recirculation model using a pre-existing signal source within the AMESim library. This signal source is located in section one of the blower and air recirculation model shown previously in Figure I-1.

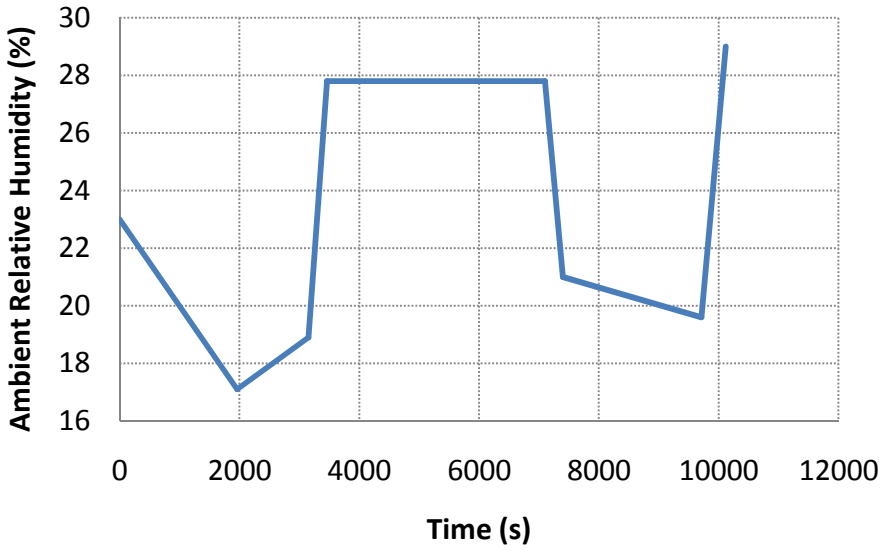

Figure J-3: Relative humidity of the inlet air to the blower for the CCD test cycle.

The other user-specified inputs to the CCD model include the vehicle speed, compressor isentropic efficiency map and compressor volumetric efficiency map. The model uses the vehicle speed signal in the cabin, reference condenser and the blower and air recirculation models. The isentropic and volumetric efficiencies are defined by two-dimensional ASCII file formats and are a function of the compressor RPM.

Verification shows how closely the simulated CCD results match experimental data. Measurement of the following parameters by Fiat during the CCD test allows for verification of the simulation model:

- Low-pressure line entering the compressor
- High-pressure line exiting the compressor
- Inlet refrigerant temperature entering the condenser
- Outlet refrigerant temperature exiting the condenser
- Outlet refrigerant temperature exiting the evaporator
- Air temperature exiting the vents
- Lumped average air temperature of the cabin
- Air temperature entering the evaporator

Ideally, when creating a model, each component is created and calibrated to experimental data. This process is conducted by the supplier to a major automotive company. Automotive companies use this experimental data and insert the equivalent computer model and conduct a series of simulations. This process helps the automotive manufacturer select the most suitable component. It also helps to piece together a simulation model from component level data to mimic system level performance. This system is not practical for the cabin model due to the complex geometries of the vehicle and the variety of materials that make up the vehicle interior. Thus a simplified cabin model, previously discussed in Section 3.3 is created and calibrated using the CCD test.

Calibrating the cabin model from a transient cycle is not necessarily the most accurate method due to unknown material properties, geometries, window glazing and solar radiation interaction, inertial thermal load of the soaked materials, and heat transfer coefficients. Calibrating the parameters requires many different steady-state tests, such as cool-down tests with no solar load, occupants, no AC operation, and full recirculation mode. This would allow the engineer to tune specific parameters related to each specific steady-state test. This would result in an accurate cabin model, however this method is not practical in the automotive industry as these tests are very expensive, and other vehicle systems require the climatic chamber to conduct higher priority tests. For these reasons the CCD test provides a cabin model that works, and is able to predict the performance with minimal error. This test allows Fiat, and any other automotive company to calibrate the vehicle cabin model. This is essential when determining if the cabin temperature is within the comfortable range for the passengers as well as modeling the AC in recirculation mode.

The test also ensures that the calibration of the AC system coupled with the cabin model. Comparing the pressure and temperature of the refrigerant before the main AC components ensures that the model accurately reflects the experimental measurements. Comparing the air entering the evaporator and leaving the vents shows that the model is accurately predicting the evaporator capacity. This data is shown in Appendix K.

APPENDIX K Cabin Cool-Down (CCD) Calibration

The calibrated parameters for the CCD test are the following:

- Evaporator R134a outlet pressure
- Evaporator R134a outlet temperature
- Condenser R134a inlet pressure
- Condenser R134a inlet temperature
- Condenser R134a outlet temperature
- Vent air outlet temperature
- Recirculation air temperature (air entering the evaporator inlet)
- Cabin cool-down curve

In an effort to describe the agreement between the computational results and experimental data, two calculations are included in this section. The first calculation is the average relative error between the simulation and the experiment. Equation (K.1) below shows the calculation for the average error. Where *y* and *Y* correspond to the simulation and experiment values at a specific time, t_i. This value is a dimensionless number, but if the calculation is for a temperature error, the final value corresponds to the temperature error.

$$\text{Average Relative Error} = \frac{1}{t}\int_0^t \left|\frac{y(t_i)-Y(t_i)}{Y(t_i)}\right| \quad \textbf{(K.1)}$$

The second calculation is a measure of the agreement between the computational results and the experimental data in such a way that positive and negative errors cannot cancel [42]. It is a validation metric model proposed by Oberkampf et al. and is given by Equation (K.2) below.

$$V = 1 - \frac{1}{t}\int_0^t \tanh\left|\frac{y(t_i)-Y(t_i)}{Y(t_i)}\right| \quad \textbf{(K.2)}$$

The choice of the *tanh* function for the metric sets the value to be unity when perfect agreement is attained and an exponential decrease toward zero for very poor agreement of the computational results and the experimental data [42]. Figure K-1 shows how the validation metric given by Equation (K.2) varies as a function of constant values of the relative error from Equation (K.1). The validation metric values for the calibration parameters in this sub-section may not necessarily correspond to the curve outlined in Figure K-1 because the average relative error is calculated rather than just the absolute value of the relative error.

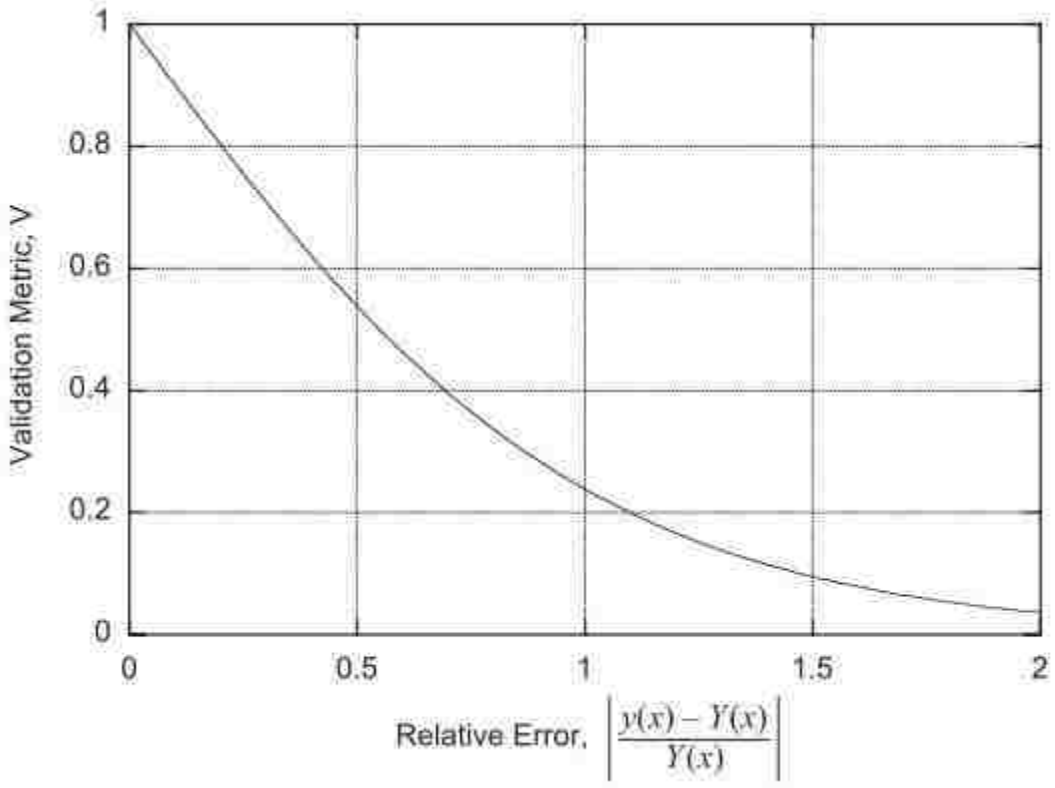

Figure K-1: Relationship between a constant value for the relative error and the corresponding validation metric value. This curve is calculated based on Equation (K.2) [42].

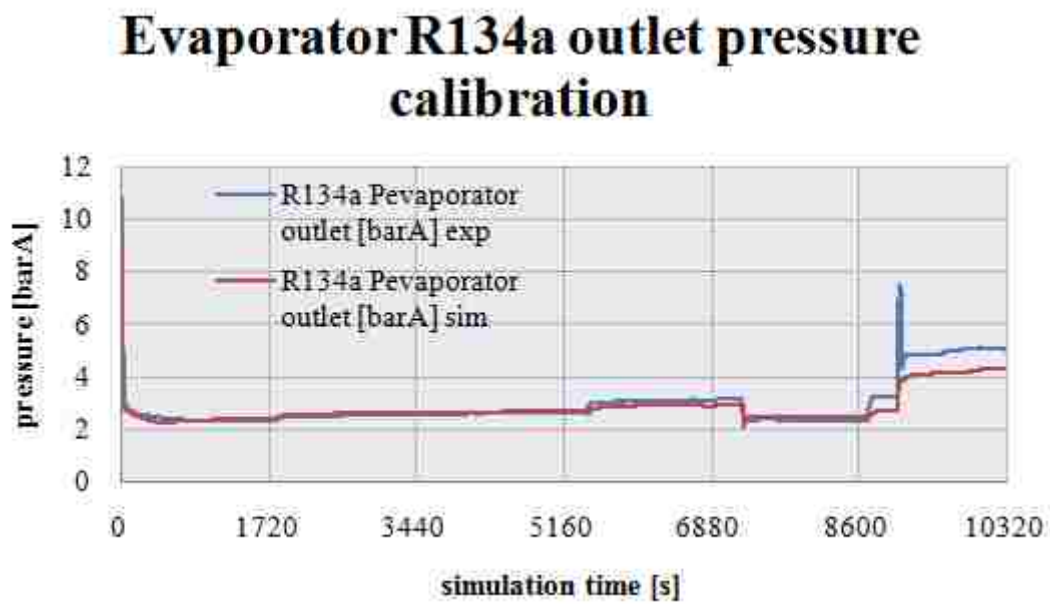

Figure K-2: Calibration curve for the refrigerant pressure at the evaporator outlet. While operating in recirculation mode, the model predicts the pressure with acceptable accuracy, however at the switch from recirculation to fresh air mode there is a large deviation from the experimental data. The average relative error and the validation metric values are located in Table K-1.

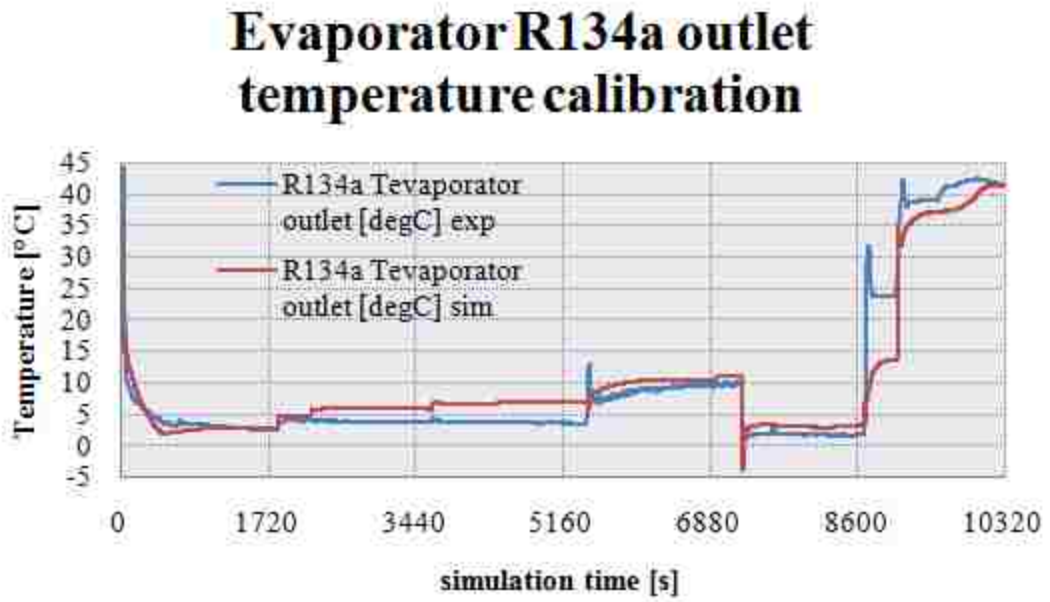

Figure K-3: Calibration curve for the refrigerant temperature at the evaporator outlet. The simulation does not do a good job predicting the spike in the refrigerant temperature when the AC system is switch from recirculation to fresh air mode. The average relative error and the validation metric values are located in Table K-1.

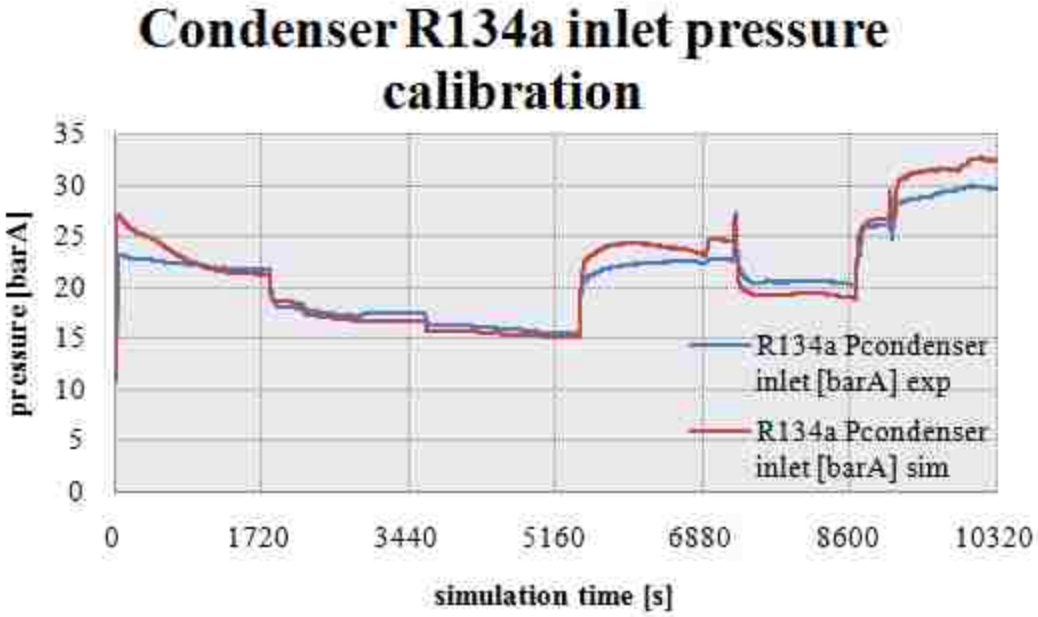

Figure K-4: Calibration curve for the refrigerant pressure at the condenser inlet. The average relative error and the validation metric values are located in Table K-1.

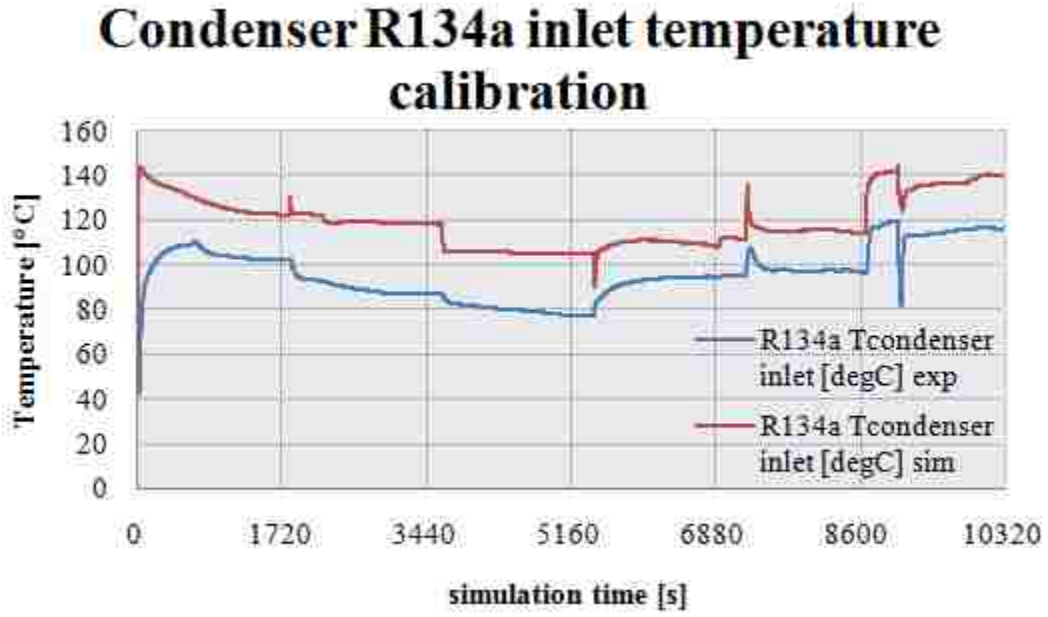

Figure K-5: Calibration curve for the refrigerant temperature at the condenser inlet. There is a significant difference for the refrigerant temperature entering the condenser. However, this difference remains relatively constant over the entire test time. The average relative error and the validation metric values are located in Table K-1.

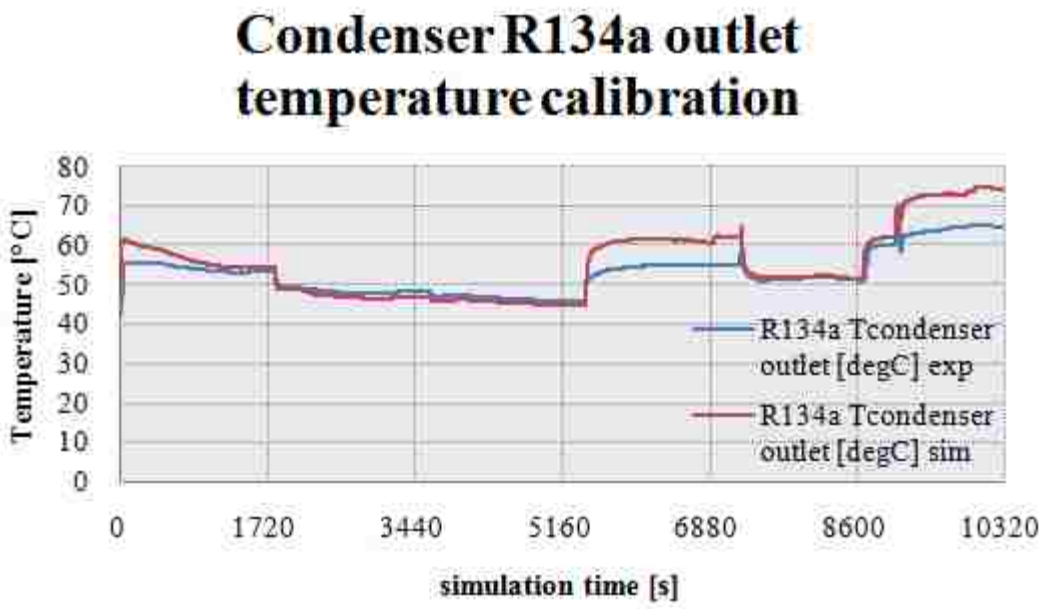

Figure K-6: Calibration curve for the refrigerant temperature at the condenser outlet. The average relative error and the validation metric values are located in Table K-1.

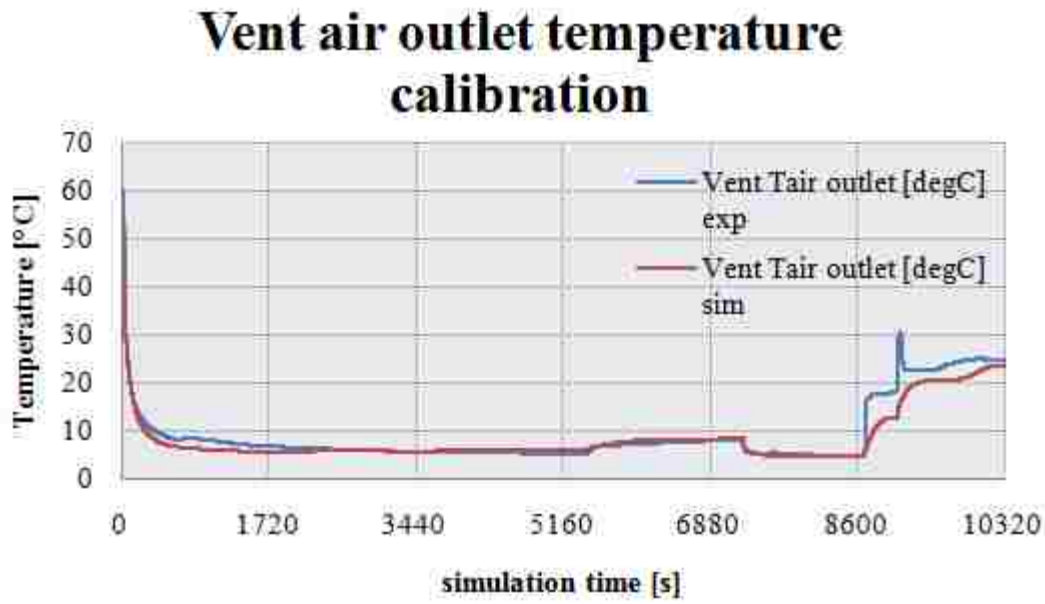

Figure K-7: Calibration curve for the air temperature at the outlet of the vents. This is the temperature of the air that enters the cabin from the HVAC system. The average relative error and the validation metric values are located in Table K-1.

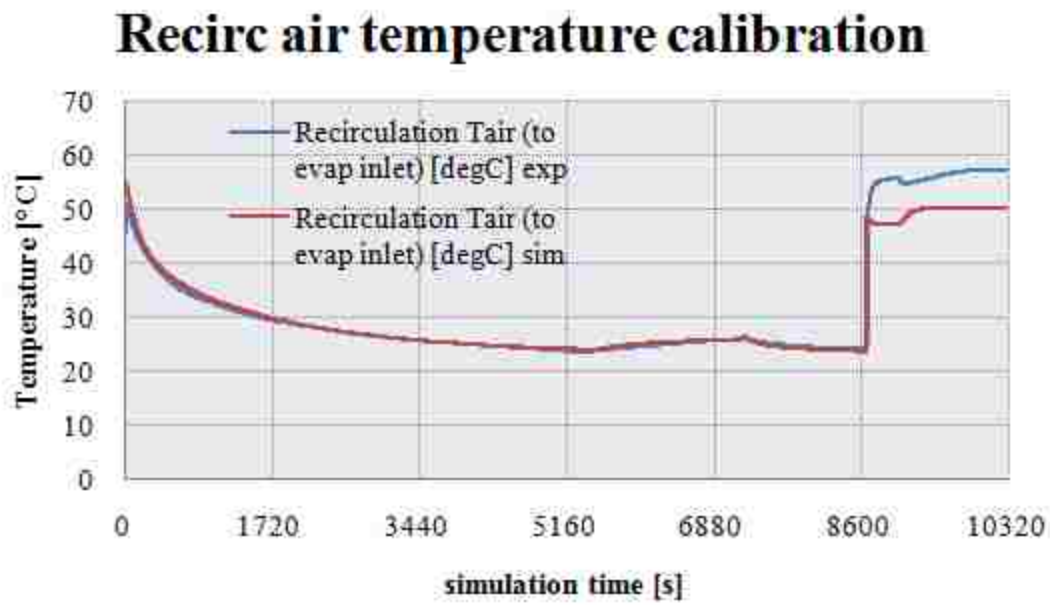

Figure K-8: Calibration curve for the air recirculation temperature that enters into the blower sub-model. It is important that the model correctly predicts this value correctly to ensure the model's ability to handle AC operation in recirculation mode. The average relative error and the validation metric values are located in Table K-1.

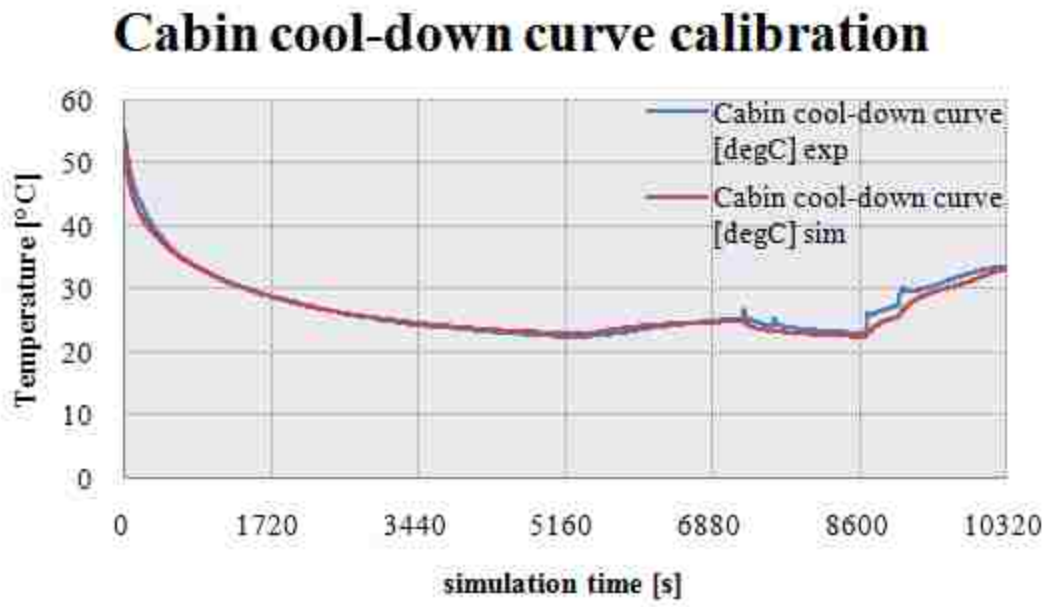

Figure K-9: Calibration curve for the cabin air temperature. The simulation shows good agreement with the experimental results. There is some slight deviation in the air temperature while the AC is operating in fresh air mode. The average relative error and the validation metric values are located in Table K-1.

Table K-1: Values for the relative error and validation metric for the cabin cool-down test calibration. These values in the table correspond to the results shown from Figure K-2 to Figure K-9, respectively.

CALIBRATED PARAMETER	AVERAGE ERROR [%]	VALIDATION METRIC
Evaporator R134a outlet pressure	0.227	0.9394
Evaporator R134a outlet temperature	2.27	0.6311
Condenser R134a inlet pressure	1.20	0.946
Condenser R134a inlet temperature	23.3	0.758
Condenser R134a outlet temperature	3.19	0.944
Vent air outlet temperature	1.19	0.898
Recirc air temperature	1.4	0.97
cabin cool-down curve	0.589	0.979

With the CCD test, the most important calibration parameter is the cabin cool-down curve. From the curve in Figure K-9 as well as the average error and validation metric values from Table K-1 the AC model predicts this value within an acceptable level. The simulation underpedicts the cabin air temperature while operating in fresh air mode, from the time interval 8665 to 10320 seconds. This error can be attributed to the model's error in modeling the thermal mass of all the internal components of the cabin. By increasing the thermal mass of the cabin model, the amount of inertial heat released by these internal components will increase, thus increasing the cabin air temperature. However, increasing this value too much will result in an inaccurate prediction of the initial stages of the cabin air temperature. The air temperature exiting the vents sub-model and the recirculation air temperature also have low error values, with high validation metric values. This indicates that the simulation predicts the experimental data within a acceptable accuracy and there is a general agreement between the simulation and experimental values.

The CCD results show that the model predicts the refrigerant condenser inlet temperature with very poor accuracy. The average error between the simulation and the experiment is 23.3 degC. This will significantly affect the error with the condenser capacity, however it does not change the other calibrated temperatures and pressures.

Another important calibration parameter is the refrigerant pressure at the evaporator outlet. From the literature, the suction line pressure significantly affects the compressor power consumption. A larger pressure drop means the compressor will have to work harder to compress the liquid and reach the required liquid line pressure. The results from Figure F-5 and the error results from Table 3-2 indicate that the AC model predicts this value within with acceptable accuracy.

APPENDIX L Condenser Heat Transfer Analysis

The condenser sub-model in AMESim requires the specification of the condenser type and size. With this information the condenser sub-model calculates the heat transfer rate and the outlet temperatures of the air and refrigerant. Since the outlet temperatures are not known, there exists a simple method to calculate the heat exchanger performance. This method is known as the Number of Transfer Units method, or more commonly, the effectiveness-NTU method.

To calculate the heat transfer, the NTU-method requires the definition of a dimensionless parameter called the heat transfer effectiveness, ε, defined in Equation (L.1) below.

$$\varepsilon = \frac{\dot{Q}}{\dot{Q}_{max}} = \frac{\text{Actual heat transfer rate}}{\text{Maximum possible heat transfer rate}} \quad \textbf{(L.1)}$$

The actual heat transfer rate is defined by Equation (L.2). The variables C_a and C_{ref} represent the heat capacity rate of the air and refrigerant, which are determined by Equation (L.3). In Equation (L.3), the variable c_p is the constant pressure specific heat.

$$\dot{Q} = C_a\left(T_{a,out} - T_{a,in}\right) = C_{ref}\left(T_{ref,out} - T_{ref,in}\right) \quad \textbf{(L.2)}$$

$$C_a = \dot{m}_a c_{p,a} \;;\; C_{ref} = \dot{m}_{ref} c_{p,ref} \quad \textbf{(L.3)}$$

Equation (L.2) and Equation (L.3) presents a very important concept with respect to the heat transfer process between the two fluids. The fluid with the smaller heat capacity rate will experience a larger temperature change, and thus it will be the first to experience the maximum temperature, at which point the heat transfer will come to a halt [25]. Therefore, the maximum possible heat transfer rate in a heat exchanger is given by Equation (L.4), below. The heat transfer with this equation assumes a heat exchanger efficiency of 100% or an effectiveness of 100%.

(L.4)

$$\dot{Q}_{max} = C_{min}\left(T_{h,in} - T_{c,in}\right)$$

The actual heat transfer rate is determined by combining Equation (L.1) and Equation (L.4). Therefore, the knowledge of the heat exchanger effectiveness enables the determination of the actual heat transfer rate. The effectiveness is a function of the geometry of the heat exchanger, as well as the flow path of the refrigerant through the heat exchanger. A dimensionless quantity called the number of transfer units (NTU) allows for effectiveness relations of the heat exchanger for certain capacity ratios. The NTU and capacity ratio are given by Equation (L.5) and Equation (L.6). With these two dimensionless parameters, the effectiveness is determined from charts previously established for specific heat exchanger geometries.

$$NTU = \frac{UA_s}{C_{min}} = \frac{UA_s}{\left(\dot{m}c_p\right)_{min}} \quad \textbf{(L.5)}$$

$$c = \frac{C_{min}}{C_{max}} \quad \textbf{(L.6)}$$

APPENDIX M Evaporator Discretization

There is always a balance between the desired accuracy of the simulation and the time required to complete the calculation. In most cases, there is a trade-off between these two desirable outputs from a simulation. The initial evaporator model used to calibrate the AC system with the Cabin Cool-down (CCD) test utilized four degrees of discretization for each pass. Recall that there are four passes for the evaporator in the present thesis. This degree of discretization led to longer simulation times, thus an investigation was conducted to see if the evaporator model could be simplified without sacrificing the model accuracy.

This investigation compares the evaporator capacity and the temperature of the air exiting the evaporator to the original calibrated model with four degrees of discretization. Similar to the naming convention for the IHX discretization degree study, Section 4.1, three other models with three, two then one discretization degree(s) are compared with the names 3mass, 2mass and 1mass, respectively. The evaporator is calibrated based on seven operating points outlined in Table M-1 below. The refrigerant exiting pressure and specific enthalpy are kept constant at 3.6 barA and 406.57 kg/m^3 for all of the operating points.

Table M-1: Operating conditions for the AMESim evaporator degree of discretization comparison. These operating points are used in the calibration of the evaporator model.

Air Mass Flow Rate [kg/s]	Refrigerant Mass Flow Rate [kg/h]	Refrigerant Inlet Quality	Refrigerant Inlet Pressure [barA]
200	110.24	0.43	4.152
250	129.69	0.42	4.325
300	150.77	0.41	4.54
350	168.6	0.4	4.74
400	181.57	0.4	4.9
450	192.92	0.39	5.05
500	204.27	0.38	5.2

Figure M-1 and Figure M-2 display the results of the comparison to the 4mass evaporator model. Recall that the percent difference between the IHX configurations is calculated using the results from the 4mass model as the base comparison. The percent difference

calculation is given by Equation (M.1) below, where the variable *Gen* represents any possible general variable comparison.

$$\%\ Difference = \left|\frac{Gen_{4mass} - Gen_{i^{th}mass}}{Gen_{4mass}}\right| * 100 \qquad \textbf{(M.1)}$$

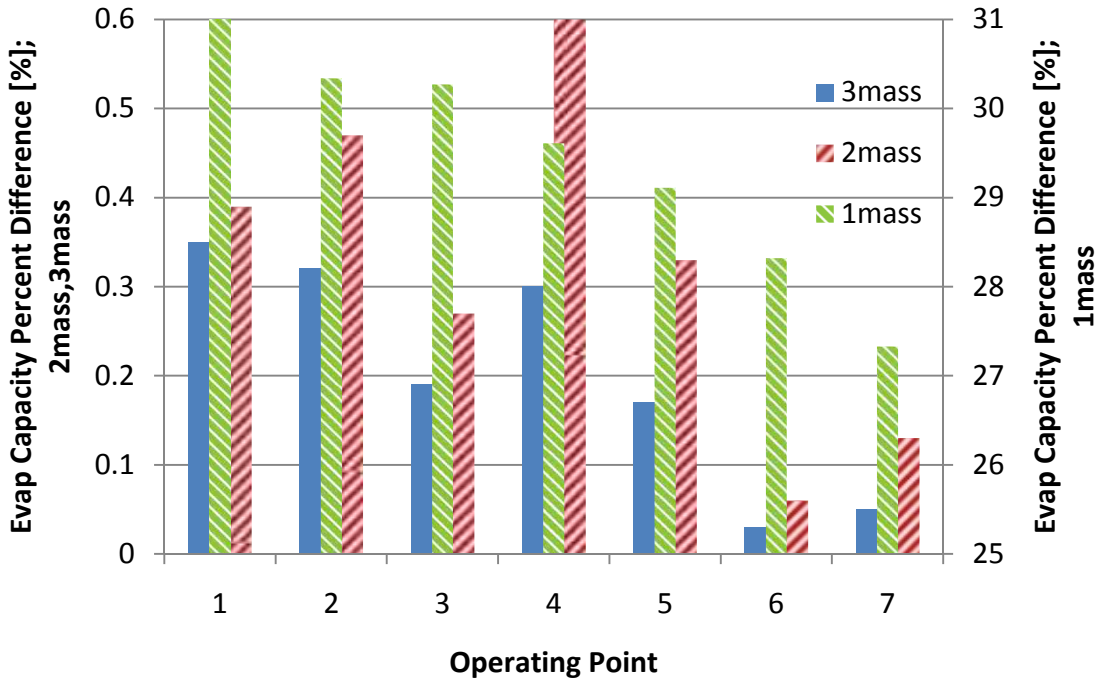

Figure M-1: Comparison of the evaporator capacity of the 3mass, 2mass and 1mass evaporator models to the 4mass model. The comparison is based on the percent difference from the 4mass model. The left ordinate axis corresponds to the 2mass and 3mass results. The right ordinate axis corresponds to the 1mass results.

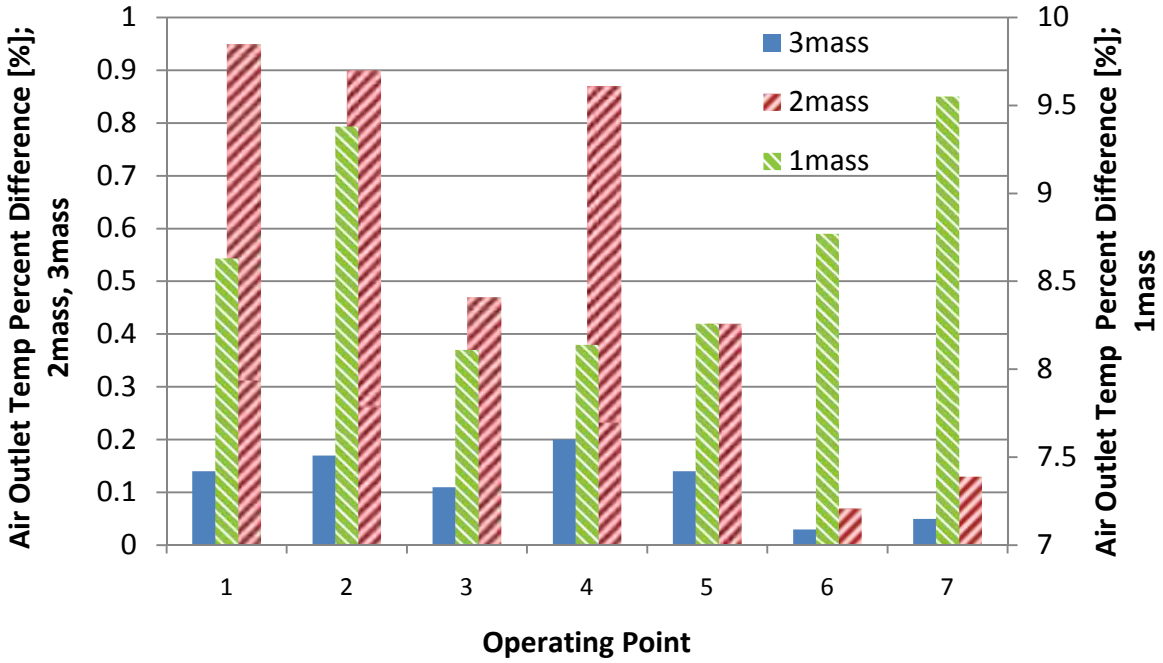

Figure M-2: Comparison of the air outlet temperature of the 3mass, 2mass and 1mass evaporator models to the 4mass model. The comparison is based on the percent difference from the 4mass model. The left ordinate axis corresponds to the 2mass and 3mass results. The right ordinate axis corresponds to the 1mass results.

The results from Figure M-1 and Figure M-2 show that both the 3mass and 2mass models yield an evaporator capacity and air outlet temperature that are within 1% of the 4mass model. The error associated with the 1mass model is very large showing that this degree of discretization is too small. The average simulation time of all the operating points for each model is shown in Table M-2 below.

Table M-2: Simulation time for all of the discretized evaporator models. This highlights the relationship between the increasing complexity of a model and the increasing simulation time.

Model	Simulation Time (seconds)
4mass	30.1
3mass	23
2mass	18
1mass	15.3

From Table M-2, it is clear that as the degree of discretization increases, the simulation time increases. The times are small because only the evaporator model is considered in this sub-section. When this model is introduced into the full AC loop, the effect of the extra discretization is compounded. An example will be included in Section 4.6.1, to highlight this effect.

Based on the results of this investigation, the 2mass model is implemented for the steady-state and transient tests in the following sections. This degree of discretization offers performance that is within 1% of the 4mass model with a simulation time reduction of 40%.

APPENDIX N Internal Heat Exchanger Length

N.1 Effect of Internal Heat Exchanger (IHX) Length for Component Level Testing

The IHX is a trade-off between the benefit of the additional heat transfer from the HP to the LP line and the detriment due to increased suction line pressure drop. This component level simulation investigates the IHX length that provides the best heat transfer to IHX suction side pressure drop ratio. This ratio was previously shown in Equation (2.4) as the component level Absolute Efficiency Ratio. This allows for a comparison of different IHX types and geometries on a normalized basis. Figure N-1 below shows the heat transferred by the IHX with respect to IHX length.

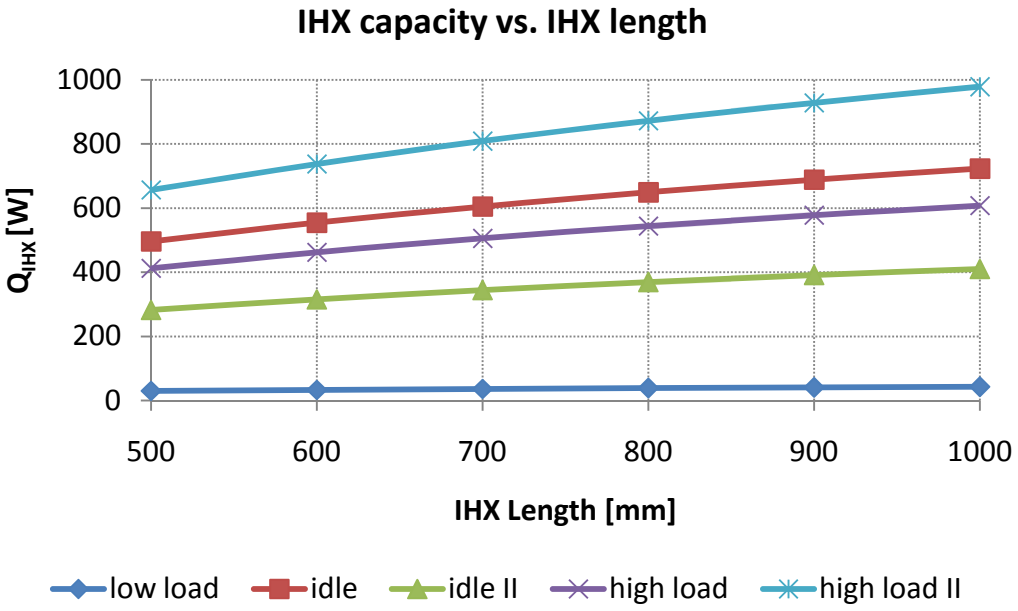

Figure N-1: IHX capacity vs. length for component level simulations at five different loading conditions.

As the IHX length increases so does the amount of heat transferred from the HP to LP side. However, the heat transfer is a decreasing function with the IHX length. That is to say that increasing the IHX length leads to diminished increases in the corresponding heat transfer capability. The Low Load condition transfers the least amount of heat, rendering the impact of an IHX on the AC system for this operating condition to be negligible. Low Load is equivalent to the use of an AC system for cooler ambient

conditions, while it is not in idle condition. The effect of ambient conditions is explored in further detail in Section 4.2.4.

Figure N-2 below shows the pressure drop on the LP side as a function of increasing the IHX length. From Figure N-2 there is a linear relationship between the LP pressure drop and the IHX length. This is an expected result due to the direct linear relationship between the pressure drop along a pipe and the pipe length. For further clarification, refer back to Equation (2.1). The pressure drop is equivalent for the idling conditions since the mass flow rate is the same for both operating points. The parameters of the IHX experimental tests conducted by the OEM are shown in Appendix C.

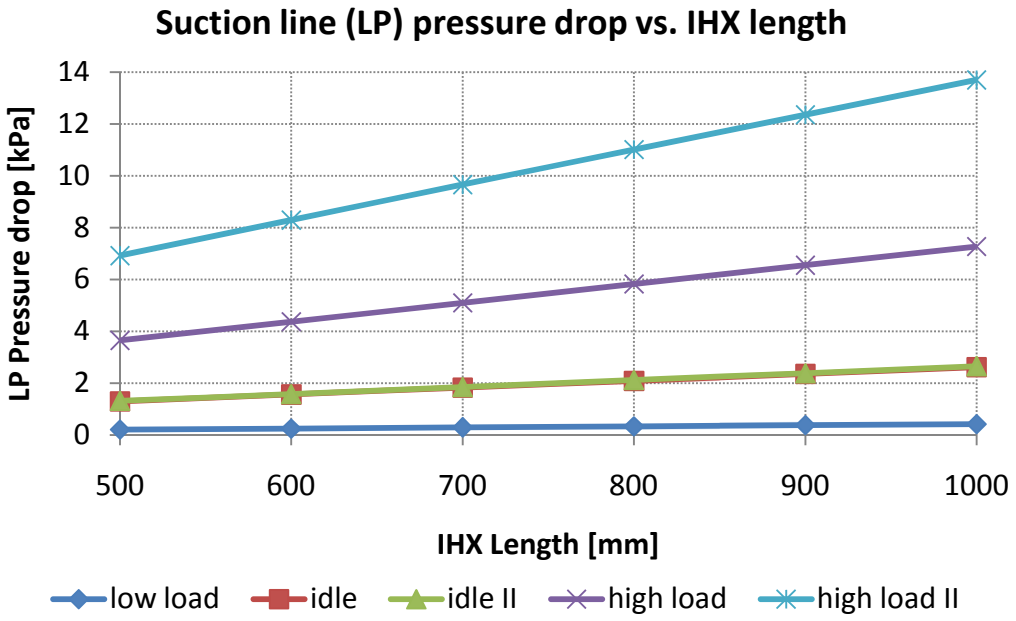

Figure N-2: IHX LP pressure drop vs. length for component level simulations at five different loading conditions

Another point of interest for Figure N-2 is the increased pressure drop with increasing load as evidenced by the increased line slope with each increase in load demand. From Figure N-1 the IHX capacity increases with IHX length and load condition and from Figure N-2 the suction line pressure drop increases with increasing IHX length and load condition. This is because the high load conditions correspond with increased compressor speeds and refrigerant mass flow rates. Increasing the mass flow rate corresponds to increased heat transfer and increased pressure drop. For the IHX to have

a positive impact, the increase in heat transfer must be greater than the relative increase in the suction side pressure drop.

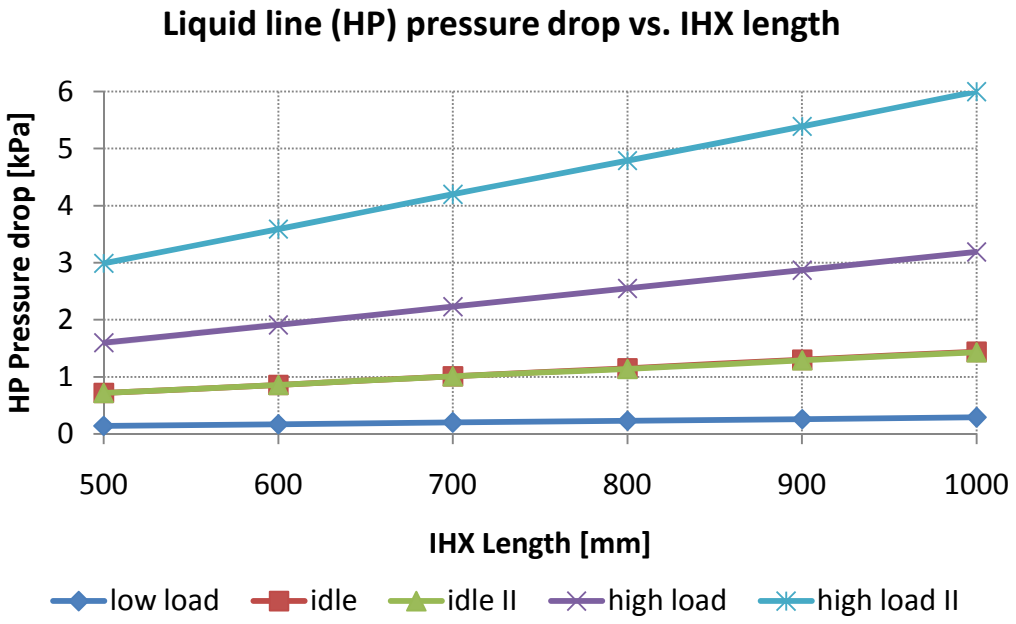

Figure N-3: IHX HP pressure drop vs. length for component level simulations at five different loading conditions

Figure N-3 above, displays the HP pressure drop as a function of increasing IHX length. This parameter does not significantly influence the AC power consumption; however, it is interesting to note the pressure drop difference between the IHX liquid and suction sides due to the two different refrigerant phases present in the two lines. Specifically, that the suction line pressure drop is approximately double the magnitude of the liquid line pressure drop. The liquid side pressure drop requires consideration to ensure that none of the sub-cooled refrigerant vaporizes before entering the thermal expansion valve (TXV). The TXV is not able to operate properly with gas present in the refrigerant due to its compressibility, which will affect the pressure drop across the TXV.

From these simulations, only three parameters will influence the pressure drop differences between the liquid and suction sides: the refrigerant density, pipe diameter

and friction factor. The liquid side refrigerant density and pipe diameter values are both larger than the suction side, which leaves the only influencing parameter to be the friction factor. From Equation (F.8), representing the Churchill correlation for the friction factor, the only influencing parameter is the Reynolds number, (Re). Finally, from Equation (2.7) describing the Reynolds number there is a significant difference between the absolute viscosities of the two refrigerant states. As an example, for the High Load operating point, the liquid and suction densities, pipe diameters and absolute viscosities are shown in Table N-1 below. The densities and absolute viscosities are averaged between the inlet and exit values for the HP and LP sides.

Table N-1: Table showing the liquid and suction densities, pipe diameters and absolute viscosities for the liquid (high pressure) side and suction (low pressure) side of the internal heat exchanger

LIQUID SIDE			
PARAMETER	**INLET**	**OUTLET**	**UNITS**
Density	1105.1	1145.7	kg/m3
Pipe Diameter	2.05		mm
Dynamic Viscosity	1.43E-04	1.61E-04	kg/m-s
Re	14082.5	12907.5	---
SUCTION SIDE			
Density	14.6	13.1	kg/m3
Pipe Diameter	9.3		mm
Dynamic Viscosity	1.12	1.18	kg/m-s
Re	440158	422523	---

The key parameter from Table N-1 is the Reynolds number. The suction side Reynolds number is significantly higher than the liquid side, leading to a much higher friction factor, explained by the Churchill correlation in Equation (F.8).

Figure N-4 below shows the absolute efficiency ratio as a function of IHX length. From Figure N-4, the efficiency of the IHX is highest in idle and high load conditions. The efficiency is very low for low load AC conditions. From Figure N-4 an IHX length of 700mm or more negligibly changes the absolute efficiency ratio. It is difficult to see the relative change of the Absolute Efficiency Ratio as the IHX length changes. Therefore,

the percent difference is displayed in Figure N-5, which shows the percent difference of the IHX absolute efficiency ratios using the 900mm IHX as the baseline for the comparison.

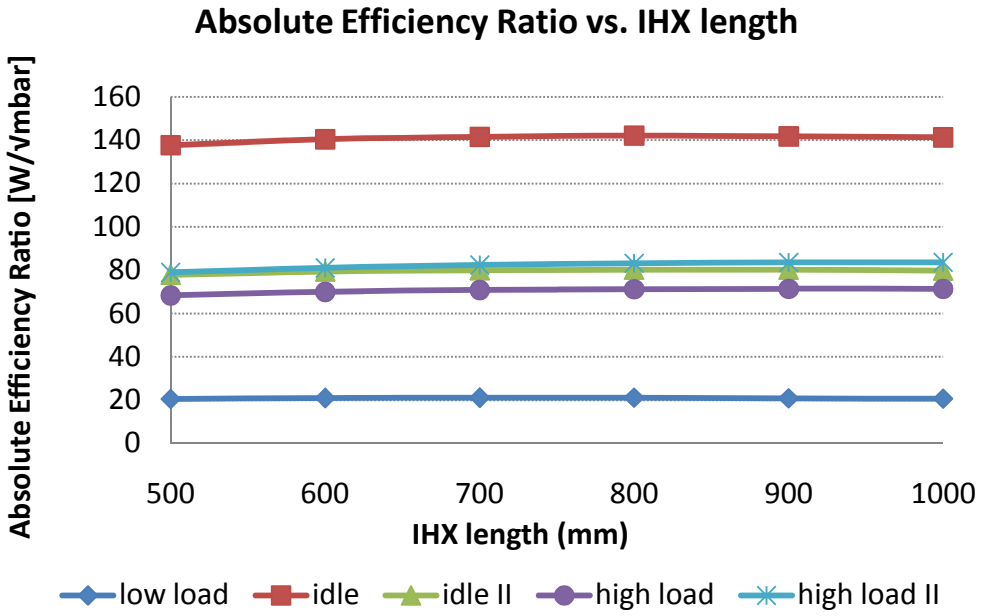

Figure N-4: IHX Absolute Efficiency Ratio vs. length for component level simulations at five different loading conditions

From Figure N-5, as the IHX length increases past 700mm, the increased benefits become negligible. After 800mm, increasing the IHX length yields little benefits in terms of the Absolute Efficiency Ratio, relative to the baseline 900mm IHX. The equation for the percent difference calculation for Figure N-5 is given in Equation (N.1) below.

$$\%\ Difference = \frac{A.E.R.\ @\ IHX_{length} - A.E.R.\ @\ IHX_{900mm}}{A.E.R.\ @\ IHX_{900mm}} * 100 \qquad \textbf{(N.1)}$$

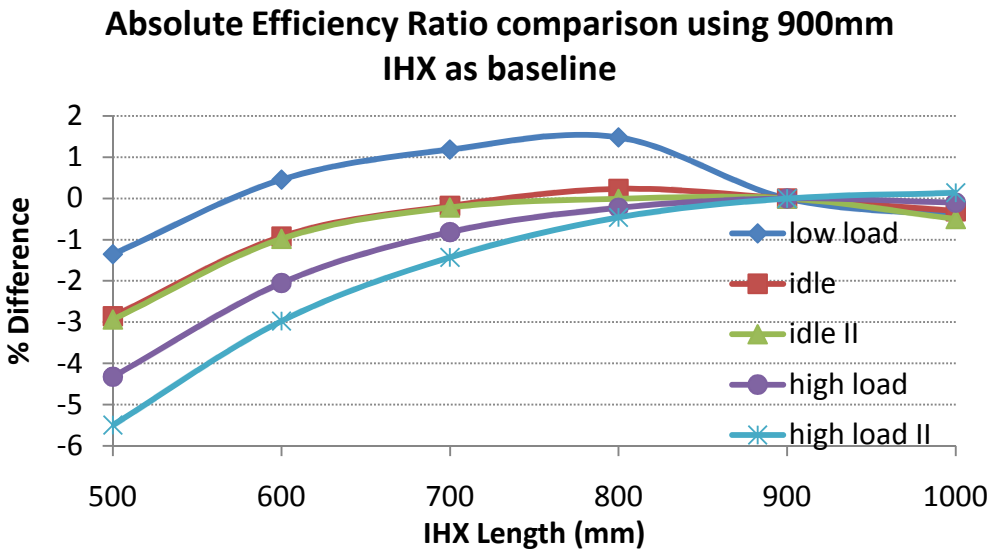

Figure N-5: Absolute Efficiency Ratio percent difference vs. IHX length for component level simulations at five different loading conditions. 900mm IHX is the baseline for the comparisons

From the results of component level testing of Figure N-5, the steady-state AC and transient tests will also study the effect of an IHX with lengths of 500mm and 700mm. There is no experimental data available for these IHX lengths, however the model is already calibrated for the 900mm IHX length. The purpose is to understand how changing the IHX length, with the same calibrated geometries, will affect the system performance. A shorter IHX length that provides the same improvement in system performance, will make packaging and implementation easier for automotive manufacturers.

N.2 Effect of Internal Heat Exchanger Length for System Level Testing

This section investigates the effect of the IHX length on the AC system level performance. Only the IHXa configuration is considered for this investigation, because based on the desired requirements of reduced compressor power consumption in the present thesis, IHXa outperformed IHXb. First the evaporator capacity ratio is plotted against the compressor power ratio. This serves as a visual aid to see the benefit of increased evaporator capacity to the drawback of increased compressor power

consumption. Second, the variation in compressor discharge temperature for the three IHX lengths for the eleven operating points from Table 3-4.

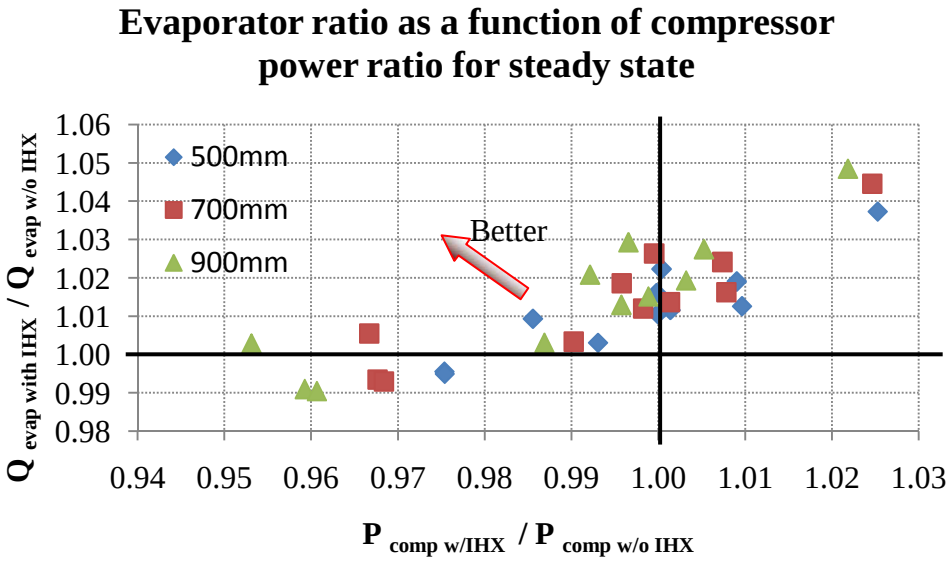

Figure N-6: Evaporator capacity ratio vs. compressor power ratio for different IHX lengths. The points correspond to the steady-state operating conditions from Table 3-4 in Section 3.7.2.

Figure N-6 displays the system response of the evaporator capacity relative to the compressor power consumption due to the introduction of an IHX. The ideal scenario from the introduction of an IHX is increased evaporator capacity with decreased compressor power consumption. The results from Figure N-6 display that the compressor power consumption increases with increasing evaporator capacity. Increasing the IHX length leads to decreased compressor power consumption, with similar evaporator capacity magnitudes.

The points with a low compressor power ratio and low evaporator capacity ratio correspond to the operating conditions with 25^{o}C ambient temperature at 2500 and 4000 RPMs. The points in the top right hand corner of Figure N-6, with high compressor power and evaporator capacity ratios correspond to the operating condition of 45/25/6000. For the rest of the steady-state operating conditions, the compressor power

consumption remains relatively unchanged compared to the increase in the evaporator capacity.

Figure N-7 displays the compressor discharge temperature difference for the three different IHX lengths. For this figure, the AC system without an IHX is used as the base comparison. As the IHX length increases, the discharge temperature increases. Also, increased compressor speeds drastically increases the refrigerant discharge temperature. An exception to this case is the operating point 35/40/4000, however, the internal valve engages during this test so the compressor is not operating at maximum displacement. The magnitude of the increasing refrigerant temperature with increasing compressor speeds is influenced by the ambient air temperature.

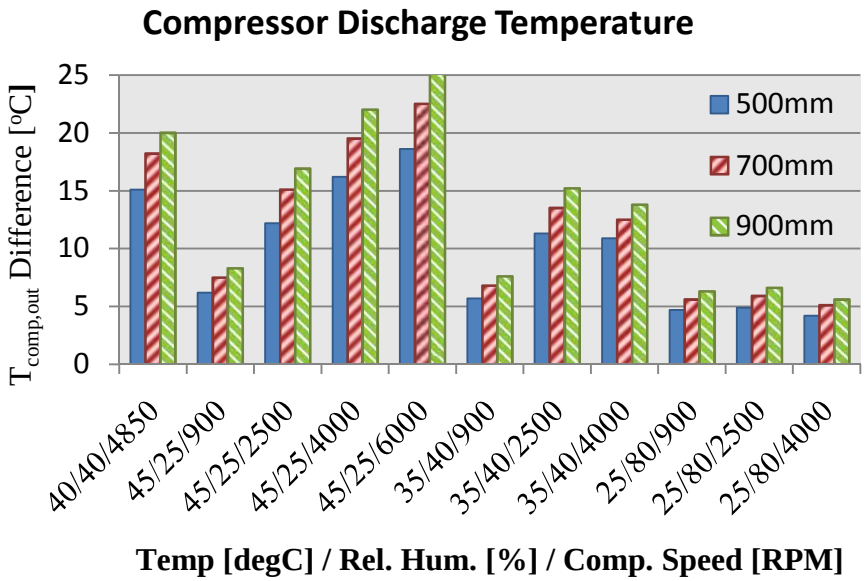

Figure N-7: Effect of IHX length on compressor discharge temperature for an IHXa AC configuration. The compressor discharge temperature of an AC system without an IHX is subtracted from the discharge temperature of the IHXa configuration. With increasing IHX length the compressor discharge temperature increases. This effect stacks as the ambient air temperature increases.

The next six figures, Figure N-8, Figure N-9, Figure N-10, Figure N-11, Figure N-12, and Figure N-13 will investigate the evaporator capacity, compressor power consumption, COP, suction line pressure drop and absolute efficiency ratio (A.E.R.).

Figure N-8 shows a plot of the evaporator capacity for different compressor speeds as a function of the IHX length. For the three higher compressor RPM cases, there are diminishing returns as the IHX length is increased. For the low loading condition, there is a weak linear relationship between the evaporator capacity and the IHX length.

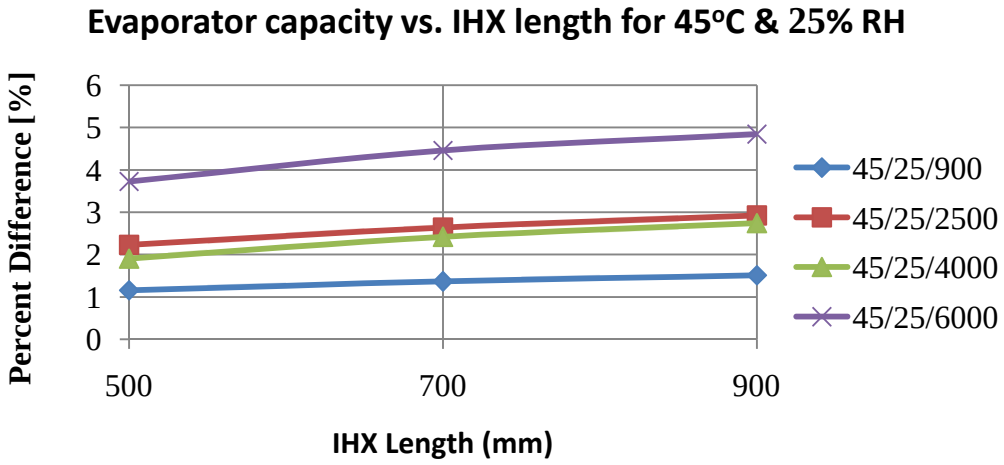

Figure N-8: Effect of the internal heat exchanger (IHX) length on evaporator capacity for an IHXa configuration. An air conditioning system without an IHX is used as the baseline comparison. With increasing IHX length and compressor speed the IHXa evaporator capacity increases.

From Figure N-9 the compressor power consumption increases for all of the operating conditions due to the introduction of an IHX. Interestingly, there is a slight decrease as the IHX length increases. This relationship is the opposite from the expected result. As the IHX length increases, it will increase the superheat of the refrigerant entering the compressor. Increasing the superheat, decreases the refrigerant density and consequently the amount of refrigerant the compressor is able to displace per revolution.

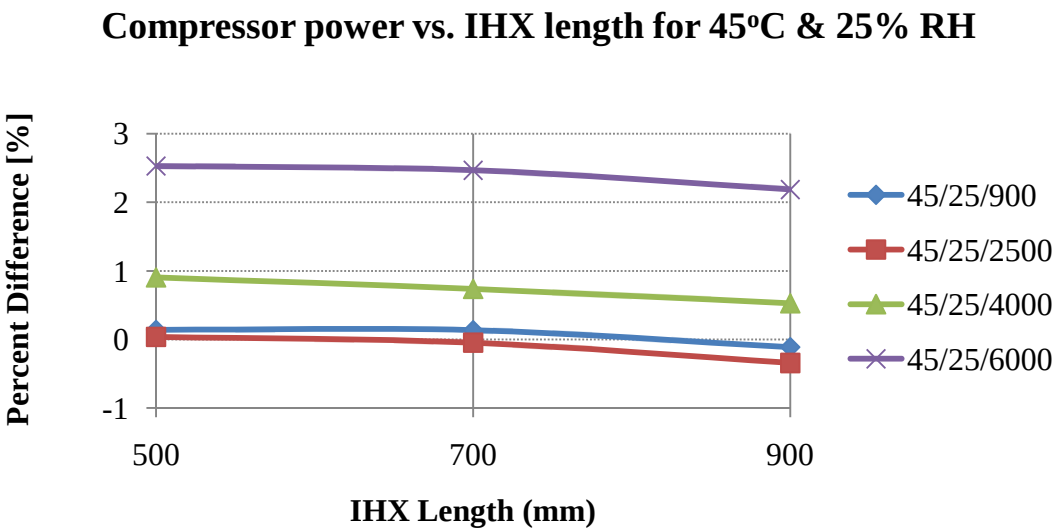

Figure N-9: Effect of the internal heat exchanger (IHX) length on compressor power consumption for an IHXa configuration. An air conditioning system without an IHX is used as the baseline comparison. With increasing IHX length, the compressor power consumption decreases slightly. As the compressor speed increases the power consumption increases.

Figure N-10 displays the COP as a function of IHX length for different compressor speeds. Figure N-10 demonstrates that increasing the IHX length increases the AC system COP. There is a linear relationship between the system COP and the IHX length. The system is most efficient for a compressor speed of 2500 RPM and least efficient at 900 RPM. At an IHX of 500mm, the cases 45/25/4000 and 45/25/6000 have low COP values due to the high compressor power consumption relative to the evaporator capacity. The results from Figure N-10 indicate that increasing the IHX length does not correspond with diminishing system efficiency. From this relatively small IHX length sample size, there is no saturation point showing an optimal IHX length.

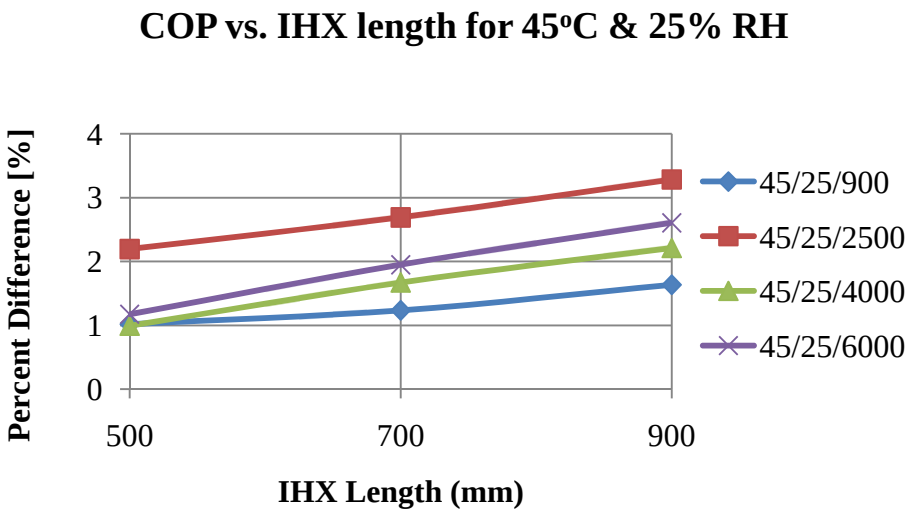

Figure N-10: Effect of the internal heat exchanger (IHX) length on the air conditioning (AC) coefficient of performance (COP) for an IHXa configuration. An air conditioning system without an IHX is used as the baseline comparison. With increasing IHX length the COP increases.

Figure N-11 and Figure N-12 show the suction line pressure drop and refrigerant mass flow rate as a function of the IHX length for different compressor speeds. The results from the steady-state simulations do not follow the expected pressure drop relationship with the IHX length. The suction line pressure drop, which spans from the evaporator inlet to the compressor inlet, decreases with increasing IHX length. For the operating point 45/25/900 there is a saturation point an IHX length of 700mm, after which, the there is a slight pressure drop increase for the 900mm length. The pressure drop decrease from the baseline AC system without an IHX is much for the higher compressor speed operating points

The unexpected result for the suction line pressure drop can be explained by the refrigerant mass flow rates from Figure N-12. The refrigerant mass flow rate decreases with increasing IHX length. The decrease is due to the increased cooling capacity of the AC system with the IHX, recall the results from Figure N-8 as well as Figure 4-22 from Section 4.2.3. The higher compressor speed operating points experience a significant decrease in the mass flow rate compared to the 900 RPM case. From Equation (2.1) in

Chapter 2, the pressure drop is proportional to the square of the fluid velocity. Therefore the effect of the lower refrigerant mass flow rate influences the suction line pressure drop greater than the increase in the IHX length.

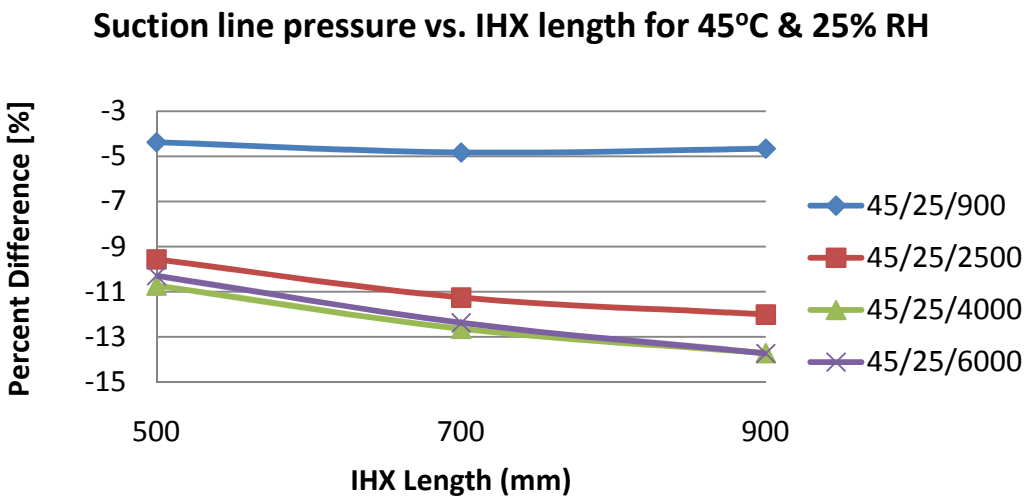

Figure N-11: Effect of the internal heat exchanger (IHX) length on the suction line pressure drop for an IHXa configuration. An air conditioning system without an IHX is used as the baseline comparison. With increasing IHX length the suction line pressure drop decreases.

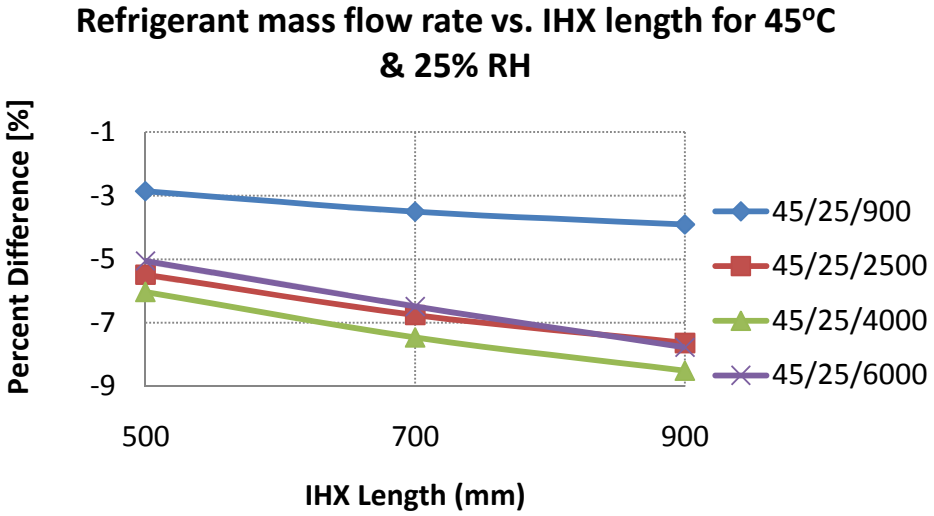

Figure N-12: Effect of the internal heat exchanger (IHX) length on the refrigerant mass flow rate for an IHXa configuration. An air conditioning system without an IHX is used as the baseline comparison. The refrigerant mass flow rate directly affects the results for the suction line pressure drop in Figure N-11.

Figure N-13 shows the system level absolute efficiency ratio (A.E.R.) as a function of IHX length for different compressor speeds. There appears to be a weak decreasing quadratic relationship between the A.E.R. and the IHX length, however a linear relationship seems more realistic. The 900 RPM experiences little change with increasing IHX length. This result can be attributed to the low evaporator capacity from Figure N-8 and the high suction line pressure drop from Figure N-11.

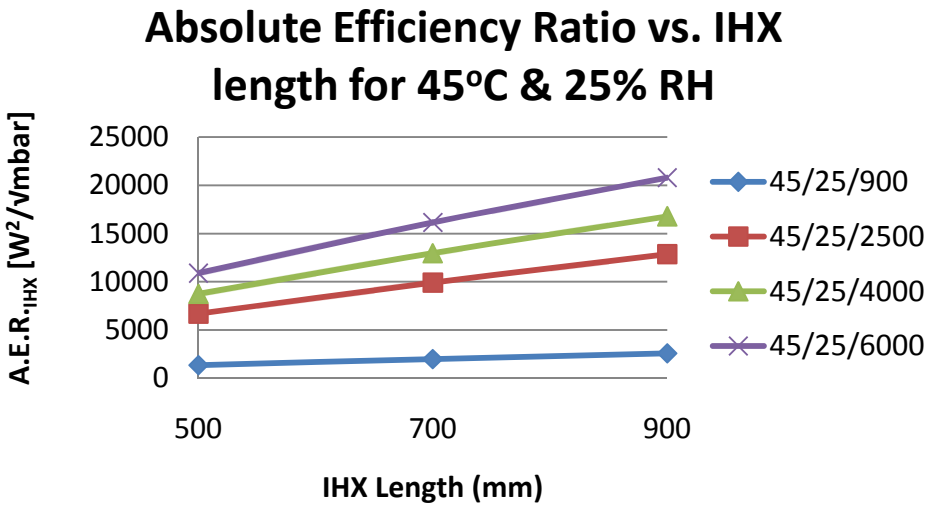

Figure N-13: Effect of the internal heat exchanger (IHX) length on the system level absolute efficiency ratio (A.E.R.) for an IHXa configuration. An air conditioning system without an IHX is used as the baseline comparison. With increasing IHX length and compressor speed the system A.E.R. increases.

The folling four figures, Figure N-14, Figure N-15, Figure N-16, and Figure N-17 display the evaporator capacity, compressor power ratio, suction line pressure drop and refrigerant mass flow rate for steady-state operation with ambient air at 25°C and 80% RH. These four figures serve to highlight the AC performance under different ambient air conditions. They reinforce the relationship between the suction line pressure drop and the refrigerant mass flow rate for different operating conditions previously shown for Figure N-11 and Figure N-12.

The internal compressor control is engaged for the two operating points 25/80/2500 and 25/80/4000. The reason for this occurring for these two operating points has been previously discussed in Section 4.2.2. The reduced volumetric displacement for these operating points significantly affects the evaporator capacity. In Figure N-8 the

evaporator capacity increased with increasing compressor speed, however this is not the case in Figure N-14.

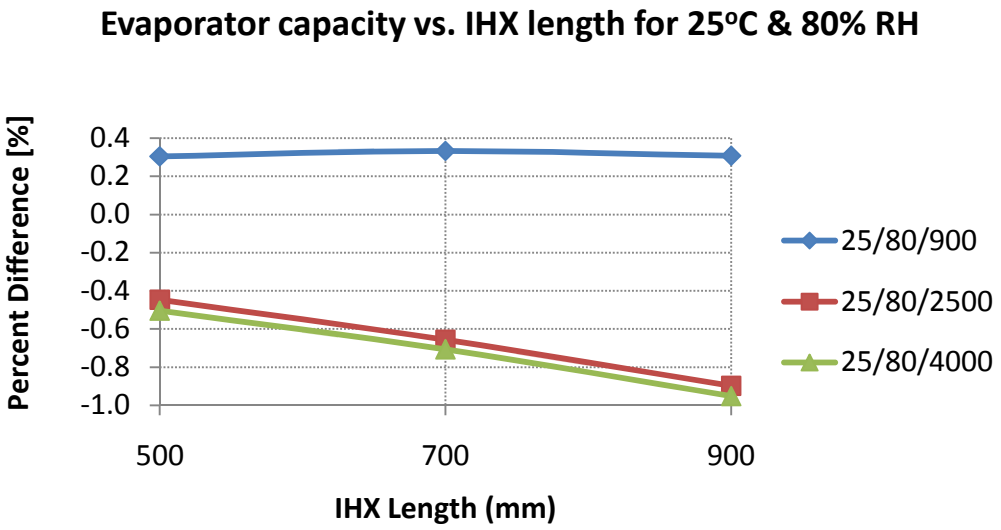

Figure N-14: Effect of the internal heat exchanger (IHX) length on evaporator capacity for an IHXa configuration. An air conditioning system without an IHX is used as the baseline comparison. The engagement of the internal compressor valve control changes the evaporator capacity response pattern previously shown in Figure N-8.

The engagement of the internal control valve also leads to decreased compressor power consumption as seen in Figure N-15. This result is expected since the compressor is not operating to its full capacity. The results in Figure N-16 and Figure N-17 display the relationship between the suction line pressure drop and the refrigerant mass flow rate. A smaller refrigerant mass flow rate corresponds to a smaller suction line pressure drop.

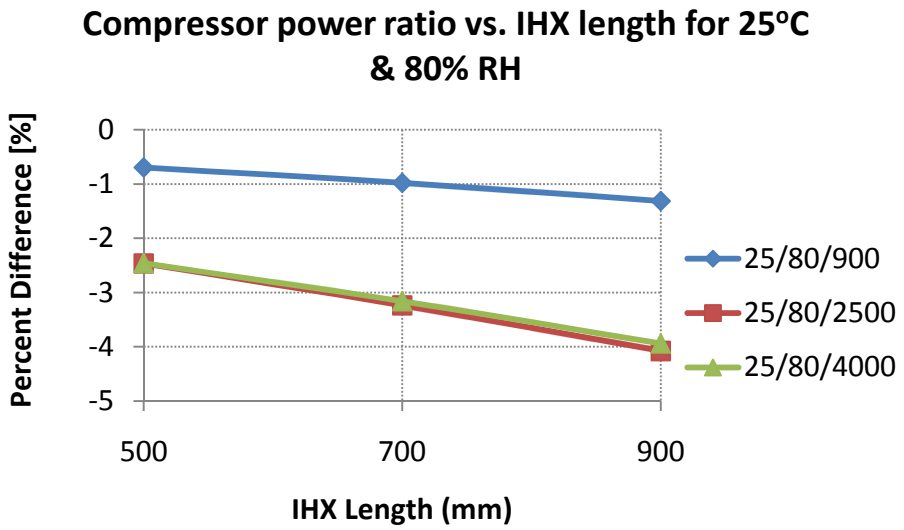

Figure N-15: Effect of the internal heat exchanger (IHX) length on compressor power consumption for an IHXa configuration. An air conditioning system without an IHX is used as the baseline comparison. With increasing IHX length, the compressor power consumption decreases slightly. The engagement of the internal compressor valve control changes the power consumption response pattern previously shown in Figure N-9.

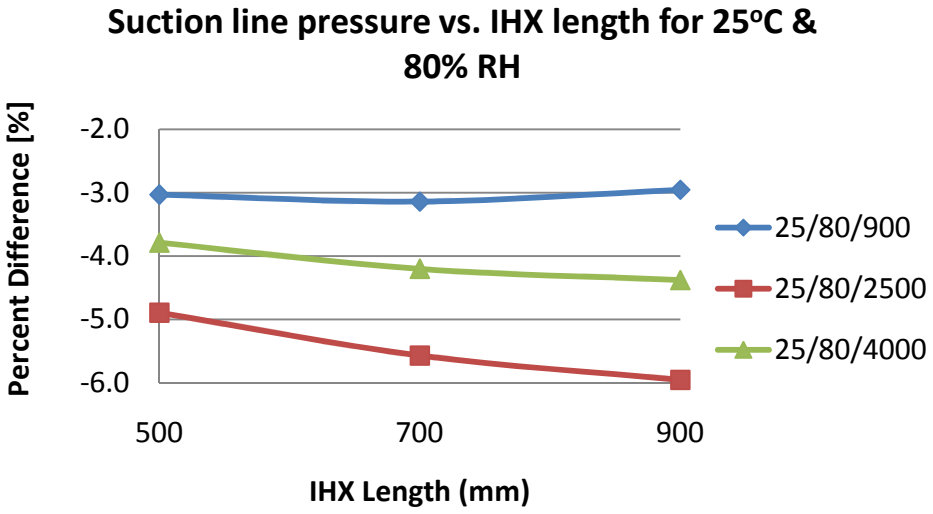

Figure N-16: Effect of the internal heat exchanger (IHX) length on the suction line pressure drop for an IHXa configuration. An air conditioning system without an IHX is used as the baseline comparison.

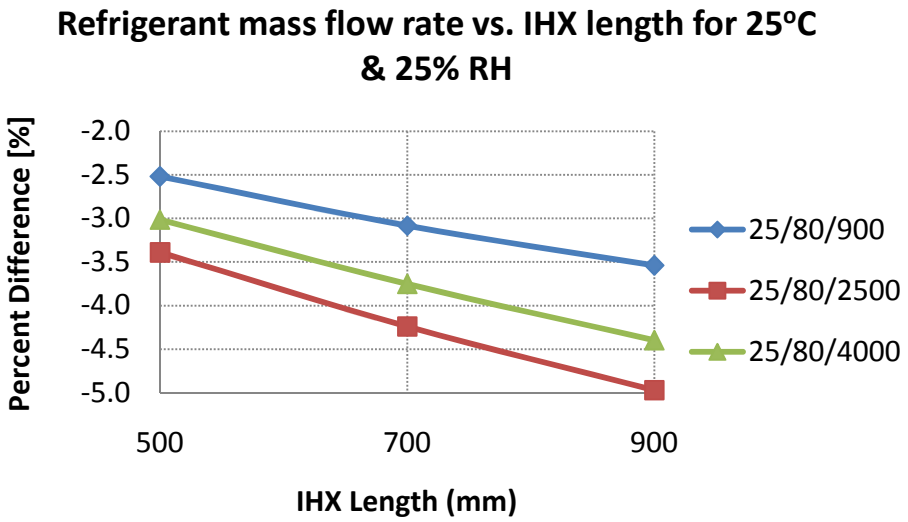

Figure N-17: Effect of the internal heat exchanger (IHX) length on the refrigerant mass flow rate for an IHXa configuration. An air conditioning system without an IHX is used as the baseline comparison. The refrigerant mass flow rate directly affects the results for the suction line pressure drop in Figure N-16.

This section outlines the benefits and drawbacks of increasing the IHX length. One parameter that is not considered is the effect of the increased IHX length on packaging constraints. This issue is unique to every vehicle that utilizes the IHX technology in its HVAC system.

Increasing the IHX length increases the compressor discharger temperature, evaporator capacity, COP and system level A.E.R. The compressor power consumption, suction line pressure drop and refrigerant mass flow rate decrease with increasing length as well. For all three of the lengths investigated, it appears that increasing the IHX length further will continue to improve the AC system performance. The 900mm IHX outperforms the 500mm and 700mm lengths.

References

1. **Administration, National Highway Traffic Safety.** CAFE - Fuel Economy.

2. **(EPA), United States Environmental Protection Agency.** *Cars and Light Trucks.* 1996.

3. **Register, Federal.** *Light-Duty Vehicle Greenhouse Gas Emission Standards and Corporate Average Fuel Economy Standards.* May 7, 2010.

4. **Huff, S., West, B., Thomas, J.,.** *Effects of Air Conditioner Use on Real-World Fuel Economy.* s.l. : Sae Technical Paper, 2013. 2013-01-0551.

5. **Han, T., Chen, K., Khalighi, B., et all.** *Assessment of Various Environmental Thermal Loads on Passenger Thermal Comfort.* s.l. : SAE International, 2010. 2010-01-1205.

6. **Johnson, V.** *Fuel Used for Vehicle Air Conditioning: A State-by-State Thermal Comfort-Based Approach.* s.l. : SAE Technical Paper, 2002. 2002-01-1957.

7. **Nadamoto, H., Kubota, A.** *Power Saving with the Use of Variable Displacement Compressors.* s.l. : SAE Technical Paper, 1999. 1999-01-0875.

8. **Zilio, C., Brown, J.S., Schiochet, G., Cavallini, A.,.** *The Refrigerant R1234yf in Air Conditioning Systems.* s.l. : Energy, 2011. Vol. 36. pgs. 6110-6120.

9. **Preissner, M., Radermacher, R., Zhang, C., Dickson, T.,.** *R134a Suction Line Heat Exchanger in Different Configurations of Automotive Air-Conditioning Systems.* s.l. : SAE Technical Paper, 2001. 2001-01-1694.

10. **Kurata, S., Suzuki, T., Ogura, K.,.** *Double-pipe Internal Heat Exchanger for Efficiency Improvement in Front Automotive Air Conditioning System.* s.l. : SAE Technical Paper, 2007. 2007-01-1523.

11. **Seybold L., Hill W., Zimmer C.,.** *Internal Heat Exchanger Design Performance Criteria for R134a and HFO-1234yf.* s.l. : SAE Technical Paper, 2010. 2010-01-1210.

12. **Seybold, L., Hill, W., Robin, J.J.,.** *Internal Heat Exchanger System Integration for R1234yf Refrigerant.* s.l. : SAE Technical Paper, 2011. 2011-01-0128.

13. **Seybold, L., Hill, W., Pietsch, K.O., Lazaridis, I.,.** *Comparison of Coaxial and Non-Coaxial Internal Heat Exchangers.* s.l. : SAE Technical Paper, 2012. 2012-01-0319.

14. **Zhang, C.A., Graham, B.L., Dickson, T.R.,.** *How to Improve Vehicle R134a A/C System Performance with a Liquid Line Suction Line Heat Exchanger (IHX).* s.l. : SAE Technical Paper, 2002. 2002-01-0507.

15. **Mastrullo, R., Mauro, A.W., Tino, S., Vanoli, G.P.,.** *A Chart for Predicting the Possible Advantage of Adopting a Suction/Liquid Heat Exchanger in Refrigerating System.* s.l. : Applied Thermal Engineering, 2007. Vol. 27. pgs. 2443-2448.

16. **Meyer, J.,.** *Internal Heat Exchanger Heat Transfer and Pressure Drop Effect on System Performance and Compressor Discharge Temperature.* s.l. : SAE Technical Paper, 2012. 2012-01-0318.

17. **Mathur, G.D.,.** *Enhancing AC System Performance with a Suction Line Heat Exchanger with Refrigerant HFO-1234yf.* s.l. : SAE Technical Paper, 2011. 2011-01-0133.

18. **Sciance, F.** *The Transition from HFC-134a to a Low-GWP Refrigerant in Mobile Air Conditioners.* s.l. : General Motors Public Policy Center, 2013.

19. **Cengel, Y.A., Boles, M.A.,.** *Thermodynamics: An Engineering Approach.* New York : McGraw Hill, 2008. 978-0-07-352921-9.

20. **Cengel, Y.A., Cimbala, J.M.** *Fluid Mechanics Fundamentals and Applications.* s.l. : McGraw-Hill, 2006. 0-07-247236-7.

21. **Stoecker, W.F., Jones, J.W.,.** *Refrigeration and Air Conditioning.* s.l. : McGraw-Hill, Inc., 1982. 0-07-061619-1.

22. **Heisler, H.** *Vehicle and Engine Technology 2nd edition.* s.l. : Butterworth, 1999. 0-340-69186-7.

23. Photo Gallery. *CarBase.com.* [Online] Available:http://www.carsbase.com/photo/photo_full.php?id=33832.

24. **Imagine.Lab, LMS.** *AMEHelp.* Rev11.

25. **Cengel, Y.A.,.** *Heat and Mass Transfer; A Practical Approach 3rd Edition.* s.l. : McGraw-Hill, 2007.

26. **Jabardo, J.M.S., Mamani, W.G.,.** *Modeling and experimental evaluation of parallel flow micro channel condensers.* Rio de Janeiro : J. Braz. Soc. Mech. Sci. & Eng., Apr./June 2003. Vol. vol.25.

27. **Navarro-Esbrí, J., Molés, F., Barragán-Cervera, Á.,.** *Experimental Analysis of the Internal Heat Exchanger Influence on a Vapour Compression System Performance*

Working with R1234yf as a drop-in replacement for R134a. s.l. : Applied Thermal Engineering, 2013. Vol. 59. pg. 153-161.

28. **LMS Imagine.Lab.** *Two Phase Flow Library Rev 11, Users Guide.* 1995-2012.

29. —. *Thermal Library Rev 11, Users Guide.* 1995-2012.

30. —. *Air Conditioning Library Rev 11, User's Guide.* 1995-2012.

31. —. *Heat Library Rev 11, User's Guide.* 1995-2012.

32. **Yue, J., Chen, G., Yuan, Q.,.** *Pressure drops of single and two-phase flows through T-type microchannel mixers.* s.l. : Chemical Engineering Journal, 2004. Vol. 102.

33. **Wallis, G.B.,.** *One Dimensional Two-phase Flow.* New YHork : McGraw-Hill, 1969.

34. **McAdams, W.H., Woods, W.K., and Bryan, R.L.:.** *"Vaporization inside horizontal tubes -II- Benzene-oil mixtures,".* s.l. : Trans. ASME, 1942. Vol. Vol. 64.

35. **Shah, M.M.:.** *"A general correlation for heat transfer during film condensation inside pipes",.* s.l. : International Journal of Heat and Mass Transfer, 1979. Vol. Vol. 22.

36. **Verein Deutscher Ingenieure, VDI-Gesellschaft Verfahrenstechnik und Chemieingenieurwesen.** *VDI Heat Atlas.* s.l. : VDI, 2010. 2nd edition.

37. **Steiner, D., Taborek, J.:.** *"Flow boiling heat transfer in vertical tubes correlated by an asymptotic model",.* s.l. : Heat Transfer Engineering. Vol. Vol. 13.

38. **Yang, S.L., Arci, O., Huang, D.C.,.** *A dynamic computer aided engineering model for automobile climate control system simulation and application, part 2: Passenger compartment simulation and application.* s.l. : SAE paper, 1999. 1999-01-1196.

39. **Sanaye, S., Dehghandokht, M.,.** *Thermal Modeling for Predication of Automobile Cabin Air Temperature.* s.l. : Int. Journal of Automobile Engineering, 2011. Vol. 1.

40. **Zheng, Y., Brown, M., Youmans, H.,.** *A Simple Method to Calculate Vehicle Heat Load.* s.l. : SAE International, 2011. 2011-01-0127.

41. **Shimizu, S., Hara, H. and Asakaw, F.** *Analysis on air-conditioning heat load of a passenger vehicle.* s.l. : Int. J. of Vehicle Design, (1983). Vol. vol. 4. pp. 292-311.

42. **Oberkampf, W.L., and Trucano, T.G.** *Verification and validation in computational fluid dynamics.* s.l. : Progress in Aerospace Sciences, 2002. Vol. 38. pp. 209-272.

43. **Natarajan, S., Sathish, K.S., Amaral, R., and Rahman, S.,.** *1D Modeling of AC Refrigerant Loop and Vehicle Cabin to Simulate Soak and Cool Down.* s.l. : SAE Technical Paper, 2013. 2013-01-1502.

Vita Auctoris

Name:	Stephen Gemin
Place of Birth:	Windsor, Ontario
Year of Birth:	1988
Education:	University of Windsor, B.Sc. in Mechanical Engineering, Windsor, ON
	University of Windsor, M.A.Sc. in Mechanical Engineering, Windsor, ON